To the Graduate Council:

I am submitting herewith a dissertation written by Michael Bruce Wyatt entitled "Analysis of Terrestrial and Martian Volcanic Compositions using Thermal Emission Spectroscopy." I have examined the final paper copy of this dissertation for form and content and recommend that it be accepted in partial fulfillment of the requirements for the degree of Doctor of Philosophy, with a major in Geology.

Harry Y. McSween, Jr., Major Professor

We have read this dissertation
and recommend its acceptance:

Theodore C. Labotka

Jeffrey E. Moersch

Kenneth H. Orvis

Lawrence A. Taylor

Acceptance for the Council:

Vice Provost and Dean of
Graduate Studies

ANALYSIS OF TERRESTRIAL AND MARTIAN VOLCANIC COMPOSITIONS USING THERMAL EMISSION SPECTROSCOPY

A Dissertation
Presented for the
Doctor of Philosophy
Degree
The University of Tennessee, Knoxville

Michael Bruce Wyatt
May 2002

Thesis
2002b
.W93

DEDICATION

The four parts of this dissertation are dedicated to four individuals to whom I owe everything. To my mother and father, Elaine and Bruce Wyatt, for unquestionable love and support. To my grandfather, Stanley Rockey, who is an inspiration and model for the benefits of hard work. To my dog Rocky, a chocolate lab, who is always too excited and eager to play at always the wrong times; it is for this that he makes the list.

ACKNOWLEDGMENTS

Completing this degree would not have been possible without the help and encouragement of many. The person to whom I owe the most recognition and gratitude is my major advisor, Dr. Hap McSween. As his student I have learned that personal and professional integrity is what truly makes good science. I would also like to thank my Dissertation Committee members, Dr. Jeff Moersch, Dr. Larry Taylor, Dr. Ted Labotka, and Dr. Ken Orvis, and others at UT, who helped me tremendously through meaningful discussions and by steering me in the right directions. Among these are Dr. Jim Greenwood, Dr. Amitabha Ghosh, Dr. Marvin Bennett, Dr. Rachel Lentz, Dr. Greg Snyder, and Allan Patchen. I thank the Department secretaries (Melody, Denise, and Teresa) for not letting me forget my head and for their kind smiles every day.

Several people outside the University of Tennessee also helped immensely through reviews, discussions, and technical assistance. Among these are Dr. Vicky Hamilton, Dr. Josh Bandfield, and Dr. Phil Christensen at the Department of Geology at Arizona State University, and Trent Hare at the United States Geological Survey at Flagstaff, Arizona. I would also like to acknowledge the entire MGS-TES team for making the possibility of this dissertation a reality.

I extend my most heartfelt thanks to fellow graduate students, family, and friends that helped me through all the hoops during my roller coaster Ph.D. ride. Valerie, Jeff, Elizabeth, Brett, Chris, Jen, Brendan, Keith, Doug, Matt, and Katie, I thank you.

Finally, I would like to acknowledge the Department of Geological Sciences at the Unviersity of Tennessee, and the NASA Graduate Student Researchers Program, for supporting my research

ABSTRACT

This dissertation comprises four separate parts, revised from individual research papers, which address the Mars Global Surveyor (MGS) Thermal Emission Spectrometer (TES) investigation objective of determining and mapping the composition and distribution of surface minerals and rocks on Mars from orbit. Each part is self-contained and addresses a specific aspect of this objective while collectively building on results of the previous studies.

In Part 1, laboratory thermal infrared spectra (5–25 μm, at 2 cm^{-1} spectral sampling), deconvolved modal mineralogies, and derived mineral and bulk rock chemistries of basalt, basaltic andesite, andesite, and dacite were used to evaluate and revise volcanic rock classification schemes. Modal mineralogies derived from linear deconvolution of terrestrial volcanic rocks were compared to modes measured by an electron microprobe phase-mapping technique to determine the accuracy of linear deconvolution in modeling specific mineral abundances. One-σ standard deviations of the absolute differences between modeled and measured mineral abundances range from 2.4 to 12.2 vol %, with an average standard deviation of 4.8 vol % being in agreement with average uncertainties calculated in previous studies. Weighted average compositions of feldspars in the deconvolution generally overlap the measured ranges of plagioclase compositions and the presence of low-calcium and high-calcium pyroxenes was correctly identified. Bulk chemistries of volcanic rocks were derived with a reasonable degree of accuracy (one-σ standard deviations ranging from 0.4 to 2.6 wt %) by combining the compositions of spectrally modeled phases in proportion to their relative abundances in a particular sample. No single classification scheme was effective in accurately classifying

all samples. Multiple steps of classification were required to distinguish volcanic rocks, reflecting the mineralogic diversity and continuum of compositions that exists in volcanic rock types.

In Part 2, laboratory spectral data were convolved to TES 10 cm^{-1} sampling to ascertain whether adequate results for volcanic rock classification can be obtained with lower spectral resolution, comparable to that obtained from Mars orbit. Convolution of terrestrial laboratory data to the lowest spectral resolution of the TES instrument does not produce significantly degraded results. Modeled spectra, modeled modal mineralogies, and derived bulk rock chemistries at low (10 cm^{-1}) spectral sampling provide good matches to measured and high (2 cm^{-1}) spectral sampling modeled values. These results demonstrate the feasibility of using similar techniques and classification schemes for the interpretation of terrestrial laboratory samples and TES-resolution data. The classification schemes from Part 1 were applied to atmospherically corrected TES spectra of large regions of the martian surface previously interpreted as representing basalt (Surface Type 1) and andesite (Surface Type 2) compositions. Results substantiate the previously proposed hypothesis that two spectral classes on the martian surface represent volcanic compositions with distinguishable differences in silica content ranging from basalt to andesite.

In Part 3, new deconvolved mineral abundances from TES data and terrestrial basalts using a spectral end-member set representing minerals common in unaltered and low-temperature aqueously altered basalts were used to reclassify martian surface lithologies. The new formulations maintain the identification of Surface Type 1 basalt, but indicate Surface Type 2 andesite can be equally well interpreted as weathered basalt.

The coincidence between locations of altered basalt and a suggested northern ocean basin implies that lowland plains materials on Mars may be basalts weathered under submarine conditions and/or aqueously weathered basaltic sediment transported into this depocenter.

In Part 4, results from the previous parts are applied to examine the distribution of TES-derived surface compositions in the Oxia Palus region on Mars through high-spatial resolution mapping. The Mars Orbiter Camera (MOC) and Mars Orbiter Laser Altimeter (MOLA) datasets are integrated for a detailed description of the martian surface. Interpretations of the TES basalt and andesite/weathered basalt derived surface compositions are fit into multiple working hypotheses to describe the origin of surface materials on local and regional scales. Local regions of interest include volcanic/sedimentary materials in southern Acidalia Planitia, low-albedo crater floors and wind streaks in western Arabia Terra, and the channel outflow deposits of the Mars Pathfinder (MP) landing site in Chryse Planitia. Regionally, Surface Type 1 materials dominate the low-albedo southern highlands and Surface Type 2 materials dominate the low-albedo northern lowlands. A mixing/transition from Surface Type 1 to Type 2 compositions is observed in the low-albedo regions of southern Acidalia Planitia. This gradational boundary may represent either (1) an influx of basaltic sediment from the southern highlands, deposited on and mixed with andesitic volcanics; (2) an influx of water-transported basaltic sediment from the southern highlands that was altered and later deposited as a thin sedimentary veneer; or (3) different degrees of weathering of basalt marking the geographic extent of submarine alteration of basaltic crust. The MP landing site and Ares and Tiu Valles source regions are sufficiently blanketed by fine-grained dust to prohibit the analysis of surface rock compositions. Despite the fact that the MP

site is one of the rockiest places on the planet and that dust apparently covers only the upper surfaces of rocks, spectral observations at multiple emission angles remain obscured by dust in the atmosphere. Deconvolved TES spectra of low albedo intracrater materials in western Arabia Terra reveal both Surface Type 1 and 2 compositions within individual craters where complete TES coverage is available. Surface Type 1 compositions form a central core in dark features on crater floors while Surface Type 2 compositions form a surrounding arc on the dark downwind sides of crater walls. The transition between these compositions appears to occur near the floor-wall interface within some impact craters. The compositional transition coincides with decreasing thermal inertia values that are interpreted to reflect decreasing particle sizes, possibly controlled by mineralogic differences between a largely unweathered basalt component and an andesite/altered basalt component. Intracrater floor materials are interpreted as eolian sediment blown into impact craters. Intracrater wall materials are interpreted as either eolian sediment sorted by particle size, or eroded material from in-place crater wall lithologies. Surface Type 1 and 2 compositions are also observed in adjacent low albedo wind streaks; however, a mixing trend is not as evident as within the impact craters. There does not appear to be a discernable compositional difference across (east-west) dark wind streak material and the often-observed bright red deposits along their margins. This distribution may support both deflation and erosional models for the formation of wind streaks.

TABLE OF CONTENTS

Introduction.....1
References.....7

Part 1

Analysis of terrestrial and martian volcanic compositions using thermal emission spectroscopy: 1. Determination of mineralogy, chemistry, and classification strategies

Abstract.....11
1. Introduction.....12
2. Rock Samples.....16
2.1. Basalt.....16
2.2. Basaltic Andesite.....17
2.3. Andesite.....18
2.4. Dacite.....19
3. Experimental and Analytical Techniques.....19
3.1. Thermal Emission Spectroscopy.....19
3.2. Electron Microprobe Phase Mapping.....20
3.3. Linear Deconvolution.....22
3.3.1. Description.....22
3.3.2. End-member selection.....25
3.3.3. Application.....27
4. Results.....28
4.1. Measured and Modeled Spectra.....29
4.2. Mineralogy.....30
4.3. Derived Chemistry.....35
4.3.1. Plagioclase chemical compositions.....35
4.3.2. Pyroxene chemical compositions.....37
4.3.3. Derived bulk rock chemistry.....38

5. Volcanic Rock Classification.....40
5.1. Spectral Discrimination..... 41
5.2. Deconvolved Modal Mineralogy and Mineral Compositions..... 42
5.3. Derived Bulk Chemistries..... 44
5.4. Summary of Classifications..... 46
6. Implications for Determination of Martian Volcanic Rock Lithologies.....48
7. Conclusions.....48
References.....50
Appendix.....56
Tables.....57
Figures..... 69

Part 2

Analysis of terrestrial and martian volcanic compositions using thermal emission spectroscopy: 2. Application to martian surface spectra from the Mars Global Surveyor Thermal Emission Spectrometer

Abstract.....87
1. Introduction.....88
2. Data and Methods..... 89
2.1. Laboratory Rock and Mineral Spectra.....89
2.2. TES Martian Surface Spectra.....90
2.3. Linear Deconvolution..... 92
2.4. Calculation of Bulk Oxides from Deconvolution Results..... 94
3. Deconvolution of Terrestrial Volcanic Compositions at Reduced Spectral Resolution.....95
4. Martian Surface Compositions..... 98
4.1. Spectral Classification..... 99
4.2. Deconvolution of Martian Surface Mineralogies..... 100
4.2.1. Modeled spectra..... 101

4.2.2. Modal mineralogy..... 101
4.3. Normative Plagioclase Composition versus Color Index..... 104
4.4. Derived Bulk Chemistries of the Martian Surface..... 106
4.5. Summary of Classifications..... 106
5. Comparison to Martian Meteorite Compositions and Previous Results..... 107
5.1. Comparison to Martian Meteorite Compositions..... 108
5.2. Comparison to Previous Remote Sensing Results..... 110
6. Conclusions..... 113
References..... 116
Appendix..... 123
Tables..... 124
Figures..... 130

Part 3

Spectral evidence for weathered basalt as an alternative to andesite in the northern lowlands of Mars

Abstract..... 139
1. Introduction..... 140
2. Results..... 141
3. Discussion..... 146
4. Conclusions..... 148
References..... 149
Appendix..... 152
Methods..... 153
Tables..... 155
Figures..... 158

Part 4

Analysis of Surface Compositions in the Oxia Palus Region on Mars from Mars Global Surveyor Thermal Emission Spectrometer Observations

Abstract..... 165

1. Introduction..... 167

2. Geologic Setting..... 168

3. Datasets..... 170

    3.1. Thermal Emission Spectrometer..... 170

    3.2. Mars Orbiter Camera..... 173

    3.3. Mars Orbiter Laser Altimeter..... 174

    3.4. Dataset Registration..... 174

4. Distribution of TES Surface Compositions..... 174

    4.1.Regional View..... 174

    4.2. Southern Acidalia Planitia..... 176

    4.3. Low-Albedo Crater Floors and Wind Streaks..... 177

    4.4. Mars Pathfinder Landing Site and Source Regions..... 180

5. Discussion..... 182

    5.1. Southern Acidalia Planitia..... 182

    5.2. Low-Albedo Intracrater Materials and Wind Streaks..... 187

6. Summary..... 192

References..... 194

Appendix..... 199

    Figures..... 200

Summary..... 213

References..... 218

Future Work..... 219

1. 2001 Mars Odyssey..... 219

2. 2003 Mars Exploration Rovers.....221
3. 2005 Mars Reconnaissance Orbiter..... 223
4. Summary.....224
References.....225

Vita.....227

LIST OF TABLES

Part 1

1. Major and Minor Element Analyses of Basalts, Basaltic Andesites, Andesites, and Dacites.....57
2. Concentration Criteria Used to Classify Minerals and Glasses.....59
3. Major Element Analyses of Glasses Added to Mineral Library.....60
4. End-member Mineral Compositions Used in Deconvolution.....61
5. Electron Microprobe Bulk Mineralogy of Basalt, Andesite, and Dacite.....63
6. Deconvolved Bulk Mineralogy of Basalt, Basaltic Andesite, Andesite, and Dacite.....64
7. Major Mineralogy and Bulk Chemistry Error Analysis.....66
8. Summary of Volcanic Rock Classifications.....67

Part 2

1. Measured and Modeled Modal Mineralogies of Laboratory Samples.....124
2. Uncertainties with Derived Modal Abundances and Bulk Oxides.....126
3. Modal Mineralogies Derived from Martian Surface Spectra.....127
4. Measured and Modeled Average Feldspar Compositions.....128
5. Summary of Classification Results for Martian Surface Spectra.....129

Part 3

1. Mineral Library Spectral End-member Set used for the Deconvolution of Martian Surface Type 1 and 2 Spectra.....155
2. Modeled Mineral Abundances Retrieved by Deconvolution for Martian Surface Type 1 and 2 Spectra.....156
3. Modeled Mineral Abundances Retrieved by Deconvolution for Columbia River Basalt (CRB) Fresh Cut and Natural (Weathered) Surfaces.....157

LIST OF FIGURES

Part 1

1. Chemical compositions of subalkaline volcanic rocks examined in this study....69
2. Crossed polar photomicrographs of volcanic rocks displaying variable textures.....70
3. Normative recalculation of microprobe analyses of (a) interstitial glasses in Hakone and Medicine Lake andesite and Columbia River flood basalt and (b) Measured normalized emissivity spectra of obsidian, silica- K_2O glass, silica glass, and quenched basalt.....71
4. Measured and modeled emissivity spectra of basalt and basaltic andesite.....73
5. Measured and modeled emissivity spectra of andesite and dacite.....74
6. Comparison of electron microprobe and deconvolved bulk mineralogies for (a) basalt and (b) andesite/dacite.....75
7. Measured and modeled emissivity spectra of Hakone andesite sample Hk-5 and quartz showing misfit between measured and modeled spectra at 1150 cm^{-1}.....77
8. Or-Ab-An ternary diagram showing deconvolved feldspar compositions (mol % An) for basalt, basaltic andesite, andesite, and dacite.....78
9. Deconvolved and maximum and minimum measured mol % An values in plagioclase for basalt, basaltic andesite, andesite, and dacite.....79
10. Deconvolved and measured pyroxene compositions for basalts and andesites in the diopside-enstatite-hedenbergite-ferrosilite system.....80
11. Isotherms for pyroxene compositions in the Di-En-Hd-Fs system at atmospheric pressure.....81
12. Measured versus derived oxide data (wt %) for all basalt, basaltic andesite, andesite, and dacite rocks.....82
13. Overlapping but distinct composite spectral fields for basalt, andesite, and dacite.....83

14. Measured mineralogy classification scheme for distinguishing andesite/dacite from basalt using SiO_2-rich glasses + quartz versus high-calcium pyroxene.....84
15. Normative plagioclase composition versus normative color index for separating subalkaline volcanic rocks.....85
16. Derived silica versus alkalis superimposed on chemical classification scheme for volcanic rocks.....86

Part 2

1. Example measured and modeled terrestrial rock spectra at 10 cm^{-1} spectral sampling..... 130
2. Scatterplot of mineral abundances deconvolved from terrestrial rock spectra at 2 versus 10 cm^{-1} spectral sampling.....131
3. Scatterplot of measured versus modeled wt % SiO_2 for all terrestrial rocks at 2 and 10 cm^{-1} spectral sampling..... 132
4. Martian surface spectra acquired by TES overlaid on the spectral field classification diagram..... 133
5. TES martian surface spectra and modeled spectra derived using the end-member set described in Part 1..... 134
6. Modal mineralogy classification diagram from Part 1..... 135
7. Comparison of average plagioclase An# derived from deconvolution of terrestrial spectra at 2 and 10 cm^{-1} sampling..... 136
8. Normative plagioclase composition versus normative color index for 32 terrestrial rocks and martian spectra..... 137
9. Chemical classification diagram showing model-derived chemistries for terrestrial 10 cm^{-1} data and martian spectra..... 138

Part 3

1. Comparison of martian surface spectra and modeled spectral fits. (a) Martian Surface Type 1 and (b) Type 2 spectra and modeled spectral fits and mineral abundances produced by linear deconvolution.....158
2. Spectral comparisons of glass, clays, terrestrial basalt, and martian surface spectra. (a) High-silica glass and two clays, and (b) fresh-cut and weathered surface of a CRB sample compared to Surface Type 1 and 2 spectra, respectively..... 160
3. Global distribution of Surface Type 1 and 2 and global topography determined from MOLA data..... 162

Part 4

1. Composite MOC image of Oxia Palus quadrangle.....200
2. TES compositional map of the Oxia Palus quadrangle (8 pixels/degree)..... 201
3. TES compositional maps, MOLA shaded relief map, and MOC composite image of the Surface Type 1 and Type 2 transition in southern Acidalia Planitia.....202
4. Average atmospherically corrected thermal emissivity spectra of the northern and southern transition bands in Acidalia Planitia compared to Surface Type 1 and 2 spectral end-members.....203
5. Composite MOC image, TES compositional and thermal inertia maps of Radau and Marth impact craters.....204
6. Composite MOC image of Radau Crater with superimposed TES composition pixels draped over MOLA topography.....205
7. Average atmospherically corrected thermal emissivity spectra of low-albedo intracrater materials compared to Surface Type 1 and 2 spectral end-members.....207
8. TES 16 pixels/degree compositional coverage superimposed over a composite MOC image of Chryse Planitia with Mars Pathfinder landing site and Ares and Tiu Valles source regions..... 208

9. High-resolution NA MOC image of Mars Pathfinder landing site (a) with thermal emissivity spectra of landing site and source regions (b) compared to Surface Type 1 and 2 spectra end-members..... 209
10. Plot of albedo versus ICK for an EPF mosaic of the Mars Pathfinder landing site..... 210
11. Composite MOC, MOLA, and TES map showing distribution of Surface Type 1 and 2 materials in southern Acidalia Planitia and southern highlands..... 211

Introduction

The Mars Global Surveyor (MGS) spacecraft was launched on November 7, 1996, arrived at Mars on August 11, 1997, and began mapping on April2, 1999 after an extended aerobraking phase. The Thermal Emission Spectrometer (TES) investigation on MGS addresses a wide range of topics using thermal infrared spectra measured from orbit. The objectives of the TES experiment are to (1) determine and map the composition and distribution of surface minerals, rocks, and ices; (2) study the composition, particle size, and spatial and temporal distribution of atmospheric dust; (3) locate water-ice and CO_2 condensate clouds and determine their temperature, height, and abundance; (4) study the growth, retreat, and total energy balance of the polar cap deposits; and (5) measure the thermophysical properties of martian surface materials [*Christensen et al.*, 1992]. To meet these objectives, the TES instrument was designed to have high spectral resolution (5 and 10 cm^{-1}) and broad spectral range (~6 to 50 μm or 1655 to 200 cm^{-1}), combined with high spatial resolution (~3 x 6 km) and eventual complete global coverage [*Christensen et al.*, 1992]. A complete description of the TES interferometer/spectrometer, calibration, and instrument-related errors is found in *Christensen et al.* [2002].

The remote sensing of martian surface compositions using TES is based on vibrational spectroscopy. Within the thermal infrared (~5 to 100 μm), vibrational motions within the crystal lattices of geologic materials occur at fundamental frequencies that are directly related to the crystal structure and elemental composition (i.e. mineralogy) [*Wilson et al.*, 1955; *Farmer*, 1974; *Christensen et al.*, 2002]. These vibrations interact with electromagnetic transmitted energy to produce spectral

absorptions. The relative strength, number, and wavelength positions of the spectral absorptions are unique for different silicate minerals, which can be used to identify a particular phase. In complex mixtures, such as rocks and coarse particulates, spectral features of the component minerals add linearly to produce the mixture spectrum [*Christensen et al.*, 1986; *Thomson and Salisbury*, 1993]. Conversely, complex mixtures can be deconvolved into abundances of their component minerals using a spectral end-member library of known mineral compositions [*Johnson et al.*, 1983, 1992; *Hamilton et al.*, 1997; *Ramsey and Christensen*, 1998; *Feely and Christensen*, 1999; *Hamilton and Christensen*, 2000]. Individual minerals and phases can thus be identified, and rock types distinguished, allowing the bulk modal mineralogy and petrology to be determined.

Previous remotely acquired measurements have led to a variety of interpretations of the mineralogic composition of the martian surface. Mars Pathfinder rocks were determined to be chemically similar to andesite on the basis of alpha proton X-ray spectrometer (APXS)-measured element abundances [*Rieder et al.*, 1997], but textural and visible/near-infrared multispectral evidence supporting the hypothesis that these rocks are volcanic is more ambiguous [*McSween et al.*, 1999]. The silica-rich composition of the rocks was unanticipated because, previously, several lines of evidence suggested that a large portion of the martian surface is covered by basalt. Near-infrared spectroscopic investigations of low-albedo regions on Mars, interpreted to be composed of rock and residual dark soil, suggest the surface material contains clinopyroxenes with compositions similar to those in basaltic shergottites [*Singer and McSween*, 1993; *Mustard and Sunshine* 1995; *Mustard et al.*, 1997]. Furthermore, basaltic shergottite meteorites, commonly thought to be martian samples [*McSween*, 1994, and references

therein], have compositional similarities to martian soils [*Baird and Clark*, 1981], suggesting a globally extensive basaltic source for weathered materials [*McSween and Keil*, 2000]. However, much of the visible/near-infrared spectral evidence supporting a martian surface dominated by basaltic compositions is based on incomplete mineralogies and may not be unique in distinguishing basaltic andesite or even andesite compositions. It is important to be able to identify accurately and to distinguish basalt and andesite in remote sensing data because each rock type carries implications about planetary physical and chemical conditions and petrogenetic processes.

This dissertation comprises four separate parts, revised from individual research papers, that address the TES objective of determining and mapping the composition and distribution of surface minerals and rocks on Mars from orbit. Each part is self-contained and addresses a specific aspect of this objective while collectively building on results of the previous studies. The parts are presented in the order they have been published or submitted for publication.

The first part entitled "Analysis of terrestrial and martian volcanic compositions using thermal emission spectroscopy: 1. Determination of mineralogy, chemistry, and classification strategies" determined the accuracy to which laboratory thermal infrared spectra (5-25 μm, 2 cm^{-1} spectral sampling) and model-derived mineral assemblages and chemistries of unweathered terrestrial volcanic rocks can be used for petrologic classification. The Mattson Cygnus 100 Fourier transform infrared (FTIR) interferometric spectrometer at Arizona State University was used to measure emitted radiance of basalt, basaltic andesite, andesite, and dacite rocks. Modeled mineralogies of the rocks were derived from linear deconvolution of the rocks' infrared spectra and were

compared with modes obtained by an electron microprobe phase mapping technique for accuracy. Modeled mineral compositions and bulk rock chemistries, calculated from deconvolved mineralogies, were also determined and compared to laboratory-measured mineral and bulk rocks chemistries for accuracy. The thermal infrared spectral shapes, deconvolved mineralogies, and derived mineral and bulk rock chemistries of all the rocks were then examined for their effectiveness in classifying basalt, basaltic andesite, andesite, and dacite.

In the second part, "Analysis of terrestrial and martian volcanic compositions using thermal emission spectroscopy: 2. Application to martian surface spectra from the Mars Global Surveyor Thermal Emission Spectrometer," laboratory spectral data were convolved to TES 10 cm^{-1} sampling to ascertain whether adequate results for volcanic rock classification can be obtained with lower spectral resolution, equivalent to the bulk of spectra that are obtained from Mars orbit. The techniques and classification schemes developed in the first laboratory study were applied to examine martian surface compositions and to help constrain the surface lithologies of the martian crust. Results from this work are directly applicable to classifying martian surface compositions and were applied to assign petrologic classifications to martian surface materials.

The third part, entitled "Spectral evidence for weathered basalt as an alternative to andesite in the northern lowlands of Mars", took a different approach to all previous work and examined terrestrial unaltered and low-temperature aqueously altered basalts as candidate compositions for Mars. Mineral abundances derived from analysis of TES data were originally interpreted to indicate that the surface is composed of basalt and andesite [*Bandfield et al.*, 2000] with distributions divided roughly along the planetary dichotomy

that separates ancient, heavily cratered crust in the southern hemisphere from younger lowland plains in the north. The existence of such a large volume of andesite was difficult to reconcile with existing knowledge of the geologic evolution of the planet. New deconvolved mineral abundances in this study from TES data and terrestrial basalts using a spectral end-member set representing minerals common in unaltered and low-temperature aqueously altered basalts were used to reclassify martian surface lithologies. The new formulations maintain the dominance of unaltered basalt in the southern highlands, but indicate the northern lowlands can be interpreted as weathered basalt. The coincidence between locations of altered basalt and a previously suggested northern ocean basin implies that lowland plains materials may be basalts altered under submarine conditions and/or weathered basaltic sediment transported into this depocenter.

The fourth paper entitled, "Analysis of Surface Compositions in the Oxia Palus Region on Mars from Mars Global Surveyor Thermal Emission Spectrometer Observations," applied results from the previous papers to examine the distribution of TES derived surface compositions in the Oxia Palus region on Mars through high-spatial-resolution mapping. The Mars Orbiter Camera (MOC) and Mars Orbiter Laser Altimeter (MOLA) datasets are integrated for a detailed description of the martian surface. The diversity of observable landforms in Oxia Palus, which reflect both active geologic processes and remnants of paleoclimate effects, have made this one of the most studied regions on Mars. Features of interest within Oxia Palus include volcanic/sedimentary materials in southern Acidalia Planitia, low-albedo crater floors and wind streaks in western Arabia Terra, and channel outflow deposits of the Mars Pathfinder (MP) landing site in Chryse Planitia. Interpretations of the TES basalt and andesite/weathered basalt

derived surface compositions are fit into multiple working hypotheses to describe the origin of surface materials on local and regional scales.

The research papers presented here thus determine the accuracy of laboratory and TES thermal infrared spectra, deconvolved mineralogies, and derived chemistries for classifying terrestrial and martian volcanic rocks. By determining limits for discriminating volcanic lithologies, high-resolution maps of martian surface compositions have been completed and integrated with multiple data sources. The resulting detailed description of the martian surface allows for interpretations into the petrogenesis and geologic significance of observed volcanic compositions.

References

Baird, A. K., and B. C. Clark, On the original igneous source of martian fines, *Icarus*, 45, 113–123, 1981.

Bandfield, J.L., V.E. Hamilton, and P.R. Christensen, A global view of martian volcanic compositions, *Science*, *287*, 1626-1630, 2000a.

Christensen, P. R., H. H. Kieffer, S. C. Chase, and D. D. Laporte, A thermal emission spectrometer for identification of surface composition from Earth orbit, in *Commercial Applications and Scientific Research Requirements for Thermal Infrared Observations of Terrestrial Surfaces*, NASA-EOSAT joint report, pp. 119–132, Earth Obs. Satell. Co., Lanham, Md., 1986.

Christensen, P.R., D.L. Anderson, S.C. Chase, R.N. Clark, H.H. Kieffer, M.C. Malin, J.C. Pearl, J. Carpenter, N. Bandeira, F.G. Brown, and S. Silverman, Thermal Emission Spectrometer experiment: The Mars Observer Mission, *J. Geophys. Res.*, *97*, 7719-7734, 1992.

Christensen, P. R., J. L. Bandfield, V. E. Hamilton, S. W. Ruff, H. H. Kieffer, T. N. Titus, M. C. Malin, R. V. Morris, M. D. Lane, R. L. Clark, B. M. Jakosky, M. T. Mellon, J. C. Pearl, B. J. Conrath, M. D. Smith, R. T. Clancy, R. O. Kuzmin, T. Roush, G. L. Mehall, N. Gorelick, K. Bender, K. Murray, S. Dason, E. Greene, S. Silverman, M. Greenfield, The Mars Global Surveyor Thermal Emission Spectrometer experiment: Investigation description and surface science results, *J. Geophys. Res.*, 2002

Farmer, V.C., *The Infrared Spectra of Minerals*, 539 pp., Mineralogical Society, London, 1974.

Feely, K. C., and P. R. Christensen, Quantitative compositional analysis using thermal emission spectroscopy: Application to igneous and metamorphic rocks, *J. Geophys. Res.*, 104, 24,195–24,210, 1999.

Hamilton, V. E., P. R. Christensen, and H. Y. McSween Jr, Determination of martian meteorite lithologies and mineralogies using vibrational spectroscopy, *J. Geophys. Res.*, 102, 25,593–26,603, 1997.

Hamilton, V. E., and P. R. Christensen, Determining the modal mineralogy of mafic and ultramafic igneous rocks using thermal emission spectroscopy, *J. Geophys. Res.*, 105, 9717–9733, 2000.

Johnson, P. E., M. O. Smith, S. Taylor-George, and J. B. Adams, A semiempirical method for analysis of the reflectance spectra of binary mineral mixtures, *J. Geophys. Res.*, 88, 3557–3561, 1983.

Johnson, P. E., M. O. Smith, and J. B. Adams, Simple algorithms for remote determination of mineral abundances and particle sizes from reflectance spectra, *J. Geophys. Res.*, 97, 2649–2657, 1992.

McSween, H. Y., Jr., What we have learned about Mars from SNC meteorites, *Meteoritics*, 29, 757–779, 1994.

McSween, H. Y., Jr., et al., Chemical, multispectral, and textural constraints on the composition and origin of rocks at the Mars Pathfinder landing site, *J. Geophys. Res.*, 104, 8679–8715, 1999.

McSween, H. Y., Jr., and K. Keil, Mixing relationships in the martian regolith and the composition of globally homogeneous dust, *Geochim. Cosmochim. Acta.*, 64, 2155–2166, 2000.

Mustard, J. F., and J. M. Sunshine, Seeing through the dust: martian crustal heterogeneity and links to the SNC meteorites, *Science*, 267, 1623–1626, 1995.

Mustard, J. F., S. Murchie, S. Erard, and J. M. Sunshine, In situ compositions of martian volcanics: Implications for the mantle, *J. Geophys. Res.*, 102, 25,605–25,615, 1997.

Ramsey, M. S., and P. R. Christensen, Mineral abundance determination: Quantitative deconvolution of thermal emission spectra, *J. Geophys. Res.*, 103, 577–596, 1998.

Rieder, R., et al., The chemical composition of martian soils and rocks returned by the mobile alpha proton X-ray spectrometer: Preliminary results from the X-ray mode, *Science,* 278, 1771–1774, 1997.

Singer, R. B., and H. Y. McSween Jr., The igneous crust of Mars: Compositional evidence from remote sensing and the SNC meteorites, in *Resources of Near-Earth Space*, edited by J.S. Lewis, M. S. Matthews, and M. L. Guerrieri, pp. 709–736, Univ. of Ariz. Press, Tucson, 1993.

Thomson, J. L., and J. W. Salisbury, The mid-infrared reflectance of mineral mixtures (7–14 μm), *Remote Sens. Environ.*, 45, 1–13, 1993.

Wilson, E.B., Jr., J.C. Decius, and P.C. Cross, *Molecular Vibrations: The Theory of Infrared and Raman Vibrational Spectr*a, McGraw-Hill, 1955.

Part 1

Analysis of terrestrial and martian volcanic compositions using thermal emission spectroscopy: 1. Determination of mineralogy, chemistry, and classification strategies

This chapter is a revised version of a paper by the same name published in the *Journal of Geophysical Research* in 2001 by Michael B. Wyatt, Victoria E. Hamilton, Harry Y. McSween Jr., Philip R. Christensen, and Lawrence A. Taylor:

Wyatt, M.B., Hamilton, V.E., McSween, H.Y. Jr., Christensen, P.R., and Taylor, L.A. Analysis of terrestrial and martian volcanic compositions using thermal emission spectroscopy: 1. Determination of mineralogy, chemistry, and classification strategies. *JGR 106*, 14,711-14,732 (2001).

Abstract

We have examined and applied existing classification schemes for volcanic rocks and developed new schemes using thermal emission spectra of terrestrial volcanic rocks. Laboratory thermal infrared spectra (5–25 μm, at 2 cm^{-1} spectral sampling), deconvolved modal mineralogies, and derived mineral and bulk rock chemistries were used to distinguish basalt, basaltic andesite, andesite, and dacite. Modal mineralogies derived from linear deconvolution of terrestrial volcanic rocks were compared to modes measured by an electron microprobe phase mapping technique to determine the accuracy of linear deconvolution in modeling specific mineral abundances. One σ standard deviations of the absolute differences between modeled and measured mineral abundances range from 2.4 to 12.2 vol %, with an average standard deviation of 4.8 vol % being in agreement with average uncertainties calculated in previous studies. Weighted average compositions of feldspars in the deconvolution generally overlap the measured ranges of plagioclase compositions and the presence of low-calcium and high-calcium

pyroxenes was correctly identified. Bulk chemistries of volcanic rocks were derived with a relatively high degree of accuracy (1σ standard deviations ranging from 0.4 to 2.6 vol %) by combining the compositions of spectrally modeled phases in proportion to their relative abundances in a particular sample. These data were collectively used to examine existing and develop new volcanic rock classification schemes. However, no single classification scheme was effective in accurately classifying all samples. Multiple steps of classification were required to distinguish volcanic rocks, reflecting the mineralogic diversity and continuum of compositions that exists in volcanic rock types. In a companion paper [*Hamilton et al.*, 2001] these schemes are applied to the classification of martian surface compositions.

1. Introduction

The most abundant volcanic rock types on Earth are basalt and andesite, both of which have been suggested to occur on Mars on the basis of data collected prior to the arrival of Mars Global Surveyor (MGS) at Mars [e.g., *Baird and Clark*, 1981; *McSween*, 1994; *Rieder et al.*, 1997; *Mustard et al.*, 1997]. It is important to be able to accurately identify and distinguish basalt and andesite in remote sensing data because each rock type carries implications about planetary physical and chemical conditions and petrogenetic processes. However, questions and uncertainties arise in applying terrestrial volcanic rock classification schemes to extraterrestrial rocks analyzed by remote sensing techniques because of a frequent lack of textural and complete mineralogical data.

For example, Mars Pathfinder rocks were determined to be chemically similar to andesite based on alpha proton X-ray spectrometer (APXS)-measured element

abundances [*Rieder et al.*, 1997], but textural and visible/near-infrared multispectral evidence supporting the hypothesis that these rocks are volcanic is more ambiguous [*McSween et al.*, 1999]. The silica-rich composition of the rocks was unanticipated because, previously, several lines of evidence suggested that a large portion of the martian surface is covered by basalt. Near-infrared spectroscopic investigations of low-albedo regions on Mars, interpreted to be composed of rock and residual dark soil, suggest the surface material contains clinopyroxenes with compositions similar to those in basaltic shergottites [*Singer and McSween*, 1993; *Mustard and Sunshine* 1995; *Mustard et al.*, 1997]. Furthermore, basaltic shergottite meteorites, commonly thought to be martian samples [*McSween*, 1994, and references therein], have compositional similarities to martian soils [*Baird and Clark*, 1981], suggesting a globally extensive basaltic source for weathered materials [*McSween and Keil*, 2000]. However, much of the visible/near-infrared spectral evidence supporting a martian surface dominated by basaltic compositions is based on incomplete mineralogies and may not be unique in distinguishing basaltic andesite or even andesite compositions.

The difficulty in classifying martian volcanic surface compositions is not surprising, as basalt and andesite can be difficult to discriminate even on Earth [*Chayes*, 1981]. Both rock types are typically fine-grained, usually with significant proportions of mesostasis or glass, so they may be nearly impossible to distinguish texturally. Most determinations of modal mineralogy consist only of optically counted phenocryst abundances, which may be unrepresentative of the bulk (phenocryst plus groundmass) mineralogies of the rocks and thus misleading for classification purposes. In fact, the distinction between basalt and andesite is formally made on the basis of bulk silica and

alkali oxide contents [*Le Bas et al.*, 1986]. The compositional spectrum between basalt (< 52% SiO_2) and andesite (> 57% SiO_2) is recognized in chemical classification schemes by a rock of intermediate composition, basaltic andesite (52–57% SiO_2).

Despite these similarities, it is petrologically important to distinguish basalts from andesites because the identification of each rock type on Mars may allow insight into magma source compositions within the crust and mantle. The relative abundances of mineral phases and differences in bulk chemistries can have implications in understanding issues such as degree of partial melting, fractionation processes, and crustal contamination.

The Thermal Emission Spectrometer (TES) aboard the MGS orbiting spacecraft measures the emitted thermal infrared energy of the martian surface (as well as atmospheric aerosols). Thermal infrared spectroscopy is sensitive to the chemistry and structure of virtually all minerals. Minerals (and even some glasses) exhibit unique thermal infrared (~5–50 μm) spectral signatures that arise from the vibrational motions of atoms in crystal lattices (e.g., Si-O stretching and bending in silicates), which occur at specific, quantized frequencies. These vibrations interact with electromagnetic transmitted energy to produce spectral absorptions. The relative strength, number, and wavelength positions of the spectral absorptions are different for each mineral or phase. In complex mixtures, such as rocks and coarse particulates, very high absorption coefficients result in few multigrain interactions, and spectral features of the component minerals add linearly to produce the mixture spectrum [*Christensen et al.*, 1986; *Thomson and Salisbury*, 1993]. Conversely, complex mixtures can be deconvolved into abundances of their component minerals using a spectral end-member library of known

mineral compositions [*Johnson et al.*, 1983, 1992; *Hamilton et al.*, 1997; *Ramsey and Christensen*, 1998; *Feely and Christensen*, 1999; *Hamilton and Christensen*, 2000].

In this study, we examine whether thermal infrared spectra of terrestrial basalts, basaltic andesites, andesites, and dacites can be used for petrologic classification. *Walter and Salisbury* [1989] presented a generalized classification of igneous rock compositions from mid-infrared spectra using statistical analysis of averaged band intensities versus a chemical parameter to characterize polymerization, which is the ratio of silica to silica plus the oxide abundances of Ca, Fe, and Mg (SCFM index). The Walter and Salisbury study examined 37 volcanic and plutonic rocks ranging from ultramafic to silicic and basic to alkalic and did not address the issue of discriminating between samples exhibiting lesser compositional variations; in addition, the SCFM parameter can only be used to describe unweathered samples. Our approach differs in that we focus on a narrower compositional range, and rather than using averaged band intensities, we use linear deconvolution to fit both the point-to-point intensity and curvature of the rock spectra. Modal mineralogies of our rocks are derived directly from the linear deconvolution of the rocks' infrared spectra; because the deconvolution utilizes a library of mineral end-member spectra, weathering and accessory phases can be included in the best fit model if they are present at detectable abundances. The deconvolved primary mineralogies are compared to modes obtained by an electron microprobe phase mapping technique and are examined for accuracy in classifying rock types using several different metrics. Mineral compositions and bulk rock chemistries, calculated from deconvolved mineralogies, are also determined. These modeled values are compared to laboratory-measured mineral and bulk rock chemistries to determine the accuracy of chemistries

calculated from modeled mineralogy and to determine if the derived chemistry can also be utilized for discriminating volcanic rock types. In a companion paper [*Hamilton et al.*, 2001], laboratory spectral data (2 cm^{-1} sampling) are convolved to TES 10 cm^{-1} sampling to ascertain whether adequate results for volcanic rock classification can be obtained with lower spectral resolution, comparable to that obtained from Mars orbit.

2. Rock Samples

Rock samples representing the diversity of chemistry, mineralogy, and texture found in subalkaline terrestrial basalts, basaltic andesites, and andesites were assembled from Kilauea volcano, Hawaii; Columbia River Flood Basalt Group (CRB), Washington; Deccan Traps, India; Mogollon Rim, central Arizona; Medicine Lake Highland volcano, California; Hakone volcano, Japan; and Mount Shasta, California (Table 1). The samples were chosen to help define ranges in mineralogy that can be distinguished by deconvolution of thermal infrared spectra. These samples, which are relatively unweathered and unaltered, include basalt, basaltic andesite, andesite, and dacite compositions that plot well within the chemical classes of *Le Bas et al.* [1986] as well as a few compositions that lie along the boundaries of each lithology (Figure 1). Major element analyses for rocks in this study as well as sources of data are given in Table 1. Photomicrographs illustrating representative mineral properties (e.g., zoned plagioclase) and textural variations within the volcanic rock suites are shown in Figure 2.

2.1. Basalt

Four geologic environments were sampled in an attempt to obtain rocks from diverse subalkaline basaltic provinces: oceanic and continental intraplate, continental

flood, and continental arc. The following petrographic descriptions are based on optical analyses of thin sections and hand sample descriptions.

Medicine Lake Highland (continental arc) samples 79-3b and 79-35i display intersertal-intergranular to subophitic textures with moderately abundant plagioclase phenocrysts in a groundmass of plagioclase and pyroxene [*Gerlach and Grove*, 1982]. Samples HCC4A and HCC4E of the Kane Nuio Hamo flows, on the southern flank of Kilauea volcano, are representative of tholeiitic basalts derived from ocean intraplate volcanism. Both samples display fine-grained hypocrystalline textures composed mostly of plagioclase and clinopyroxene phenocrysts with interstitial plagioclase in a glassy mesostasis. Columbia River flood basalt sample CRB-5 (Elephant Mountain Member, Saddle Mountain Formation) displays an intersertal texture composed of fine-grained plagioclase and clinopyroxene with minor amounts of olivine in a matrix of glassy material. Deccan flood basalt WAR-R1049 contains phenocrysts of plagioclase and pyroxene with minor amounts of olivine in a microcrystalline to glassy groundmass [*Hamilton and Christensen*, 2000]. Samples RSL-95-23 and RSL-94-41 from central Arizona (continental intraplate) are vesicular basalts that display intergranular to subophitic textures with abundant plagioclase and olivine phenocrysts in a groundmass of plagioclase and pyroxene [*Leighty*, 1997].

2.2. Basaltic Andesite

Columbia River Flood Basalt Group samples CRB-2, CRB-4, and CRB-6 are chemically classified as basaltic andesites. CRB-2 and CRB-4 of the Frenchman Springs Member, Wanapum Formation flows, are sparsely phyric with plagioclase phenocrysts in a microphyric groundmass of plagioclase and pyroxene. CRB-6 of the Grande Ronde

Formation is a fine-grained, aphyric rock composed of glass, plagioclase, and clinopyroxene with sparse amounts of olivine. Medicine Lake Highland samples 79-24c (Paint Pot Crater flow), 79-38k (Callahan flow), 79-38g (Callahan flow), and 79-4d (Burnt Lava flow) contain small amounts of plagioclase phenocrysts and lesser amounts of olivine and pyroxene. Glassy to microcrystalline-intergranular groundmasses are composed of the same phases [*Gerlach and Grove*, 1982]. Medicine Lake Highland sample 79-37j is an olivine-bearing rock with phenocrysts of plagioclase, augite, and olivine in a fine-grained intergranular to trachytic groundmass of plagioclase, pyroxene, and glass [*Gerlach and Grove*, 1982]. Samples RSL-94-36, RSL-94-8, and RSL-94-12 from central Arizona display intergranular-microcrystalline textures with plagioclase, pyroxene, and olivine phenocrysts in a groundmass composed of similar phases [*Leighty*, 1997].

2.3. Andesite

Medicine Lake Highland sample 79-39d (Schonchin Butte flow) contains small amounts of plagioclase phenocrysts and lesser amounts of olivine and pyroxene with a glassy to microcrystalline-intergranular groundmass composed of the same phases [*Gerlach and Grove*, 1982]. Medicine Lake Highland sample 79-9g is an olivine andesite with plagioclase, augite, and olivine phenocrysts set in a nearly cryptocrystalline trachytic to pilotaxitic groundmass [*Gerlach and Grove*, 1982]. Samples 82-5 and 82-69b (Burnt Lava flow, Medicine Lake Highland) are porphyritic rocks with phenocrysts dominantly of plagioclase and lesser amounts of pyroxene, olivine, and quartz in a glassy groundmass with microlites of plagioclase, pyroxene, and olivine. Samples Hk-1, Hk-3, and Hk-5 from the Hakone volcano (Old Soma lavas), are aphanitic-porphyritic rocks

containing phenocrysts of plagioclase and pyroxene in a glassy groundmass with microlites of plagioclase and pyroxene [*Kuno*, 1950]. Mount Shasta samples 82-102 and 82-85 (Sargents Ridge cone) are porphyritic andesites containing phenocrysts of plagioclase, orthopyroxene, and clinopyroxene with lesser amounts of amphibole and olivine. The fine-grained pilotaxitic to hyalopilitic groundmass consists of plagioclase, pyroxene, and glass [*Baker*, 1988].

2.4. Dacite

Mount Shasta samples 85-2b, 82-88b, 82-95 (Sargents Ridge cone), and 82-98 (Misery Hill) are porphyritic dacites containing phenocrysts predominately of plagioclase, orthopyroxene, and clinopyroxene set in a pilotaxitic to hyalopilitic groundmass of the same phases and glass [*Baker*, 1988]. These samples plot very close to the andesite-dacite boundary defined at 63 wt % SiO_2 (Figure 1); these rocks were included to increase the number of samples representing the boundary between andesite and dacite.

3. Experimental and Analytical Techniques

3.1. Thermal Emission Spectroscopy

The Mattson Cygnus 100 Fourier transform infrared (FTIR) interferometric spectrometer at Arizona State University measures emitted sample radiance. Detailed descriptions of the emission technique and the spectrometer are provided by *Ruff et al.* [1997]. Data for this study were collected over the wavelength range of 2000–400 cm^{-1} (5–25 μm) at a spectral sampling of 2 cm^{-1}. The TES covers the wavelength range of 1650–200 cm^{-1} at a spectral sampling of 10 cm^{-1}. Laboratory data >1650 cm^{-1} are thus

not pertinent to TES data. However, the laboratory spectrometer does not cover the 400–200 cm^{-1} wavelength region as TES does. By the completion of this study a new ASU spectrometer that additionally covers the 400–200 cm^{-1} wavelength region was operational, but a spectral library that covered the entire wavelength region was not yet available. Because there are no fundamental silicate features in the 2000–1400 cm^{-1} region and silicate minerals make up the vast majority of basaltic and andesitic rock modes, spectral data will only be shown from 1400 to 400 cm^{-1} (~7–25 μm).

Each sample was cut so that a fresh surface was analyzed, ensuring an accurate representation of bulk mineralogy. Samples were heated to 80°C prior to analysis to improve signal to noise during data acquisition. The radiances of large portions of the sample surfaces (3–4 cm diameter spots) were measured to reduce the likelihood of observing nonrepresentative areas in heterogeneous samples. Raw radiance data were converted to emission spectra following method 1 of *Christensen and Harrison* [1993], as modified by *Ruff et al.* [1997]. Sources of error in the acquisition of these data are described by *Ruff et al.* [1997]; total instrument-derived error for any given spectrum in this study is ~2–5% absolute emissivity.

3.2. Electron Microprobe Phase Mapping

The accuracy of the spectral deconvolution method in estimating phase abundances is determined by comparing the deconvolved values with modes measured by an electron microprobe phase mapping technique. Modes obtained by electron microprobe mapping analysis should be comparable to those derived from deconvolved spectra because both techniques report areal abundances (stated as vol %). Microcrystalline textures in rocks do not hinder either technique, unlike optical analyses

in which phases can be too small to identify. Electron microprobe modes are only limited by spot and step sizes, which in this study (1 μm spot and 3.8–7.6 μm step) were fine enough to identify virtually all phases within the mesostasis of the volcanic rocks.

Modal abundances were calculated using an image microanalysis technique (described by *Taylor et al.* [1996]) with an Oxford Instruments (LINK) Model eXL II energy dispersive spectrometer (EDS) mounted on a Cameca SX-50 electron microprobe at the University of Tennessee. The Feature Scan image analysis software package was used for the detection, measurement, and analysis of phase characteristics in a backscattered electron (BSE) image. Polished thin sections were initially studied with transmitted- and reflected- light optical microscopy to identify the minerals present. Backscattered electron signals, a function of average atomic number, were used to discriminate phases as well as between minerals/glasses and epoxy. Phases appear as distinct shades of gray and are easily identified for chemical analysis. User-defined "windows" of the energy dispersive spectrum (e.g., 1.38–1.60 keV for Al) were used to distinguish various phases in a sample and to establish identification criteria (Table 2). These parameters were determined after several analyses of each phase to establish their approximate chemical compositions. For example, high Al and Ca and low Fe and Mg are criteria indicative of plagioclase.

X-ray data by EDS were acquired using excitation potential (20 keV), beam current (3 nA), counting time (40–60 $\times$ 10^{-3}s), and sampling mode (1 μm beam size). An EDS spectrum was acquired at every second or fourth pixel (3.8 or 7.6 μm at 70X) depending on grain size and optimization of analysis time. This typically resulted in over 100,000 pixels per thin section being classified, vastly more than traditional optical point

counting techniques. Pixels that are unclassifiable (on average < 5%) because they straddle boundaries between phases were normalized back into the bulk mode in proportion to the measured abundances of identified phases. The microanalysis technique has an estimated precision of 5% of the amount of each phase present [*Taylor et al.*, 1996].

3.3. Linear Deconvolution

3.3.1. Description. Linear deconvolution of the spectra of complex mixtures is based on the principle that the energy emitted from the mixed material is equivalent to the emitted energy of each component phase in proportion to its observed areal percentage [e.g., *Thomson and Salisbury*, 1993; *Ramsey and Christensen*, 1998]. Assuming η isothermal end-members, the mathematical expression for a mixture spectrum ($\varepsilon(\lambda)_{mix}$) is stated by equation (1) with the constraint that the fractions must sum to unity [*Ramsey and Christensen*, 1998]:

$$\varepsilon(\lambda)_{mix} = \sum_{i=1}^{\eta} \zeta_i \varepsilon(\lambda)_i + \delta(\lambda); \qquad \sum_{i=1}^{\eta} \zeta_i = 1.0 \qquad (1)$$

where ζ_i is the areal fraction of the ith end-member ($\varepsilon(\lambda)_i$) and is equal to the mass divided by the product of the density and diameter.

Ramsey and Christensen [1998] presented a least squares algorithm using a chi-square minimization [*Ramsey*, 1996] for linear deconvolution of thermal infrared emission spectra. This algorithm, as applied by Bandfield (*pers. comm.*, 2002), and used here, requires three inputs: a spectrum (or spectra) to be deconvolved, a library of pure mineral spectra (end-members), and the wavelength range over which to perform the fit. The technique uses a linear regression analysis, assuming a normal distribution of data, to

solve for a matrix of unknown end-member fractions [*Press et al.*, 1988]. The derivation of the algorithm in matrix form reduces the solution shown in equation (2),

$$[\zeta]_{(\eta)} = \left([X]^{T}_{(\eta,\lambda)}[X]_{(\lambda,\eta)}\right)^{-1}[X]^{T}_{(\eta,\lambda)}[U]_{(\lambda)} \quad (2)$$

Where $[X]_{(\lambda,\eta)}$ is the end-member matrix of emissivity spectra at each wavelength (ε_λ) and is [λ wavelength channels by η end-members] in size [*Ramsey and Christensen*, 1998]. The unknown mixture spectrum $[U]_{(\lambda)}$ can be represented as a [λ wavelength channels by 1] column vector [*Ramsey and Christensen*, 1998]. The solution $[\zeta]_{(\eta)}$ is a column vector of fractions that each end-member contributes to the mixture spectrum and has a length equal to the number of end-members [η end-members by 1] [*Ramsey and Christensen*, 1998].

In this study, mineral spectra from the Arizona State University (ASU) thermal emission spectral library [*Christensen et al.*, 2000] were used as end-members, and the fitting was constrained to the 1300–400 cm^{-1} region, which contains all measured spectral features. Limiting the range to which end-members are fitted to 1300 cm^{-1} instead of 1400 cm^{-1} eliminates a portion of the spectral signature of water vapor at high wavenumbers and prevents a degradation of the fit over the rest of the spectrum. Outputs of the algorithm are a best fit model spectrum, the percentage of each end-member mineral spectrum used in the best fit model, and a root-mean-square (RMS) error value. The RMS value is best used as an indicator of goodness of fit for a particular iteration of the model for a given sample: it was not used to compare between fits of different samples [*Ramsey and Christensen*, 1998; *Hamilton and Christensen*, 2000]. A better means of examining the model accuracy is to generate a residual error spectrum, which is

simply the measured spectrum minus the modeled spectrum [*Adams et al.*, 1993; *Ramsey and Christensen*, 1998; *Hamilton and Christensen*, 2000]. Residual error spectra permit rapid identification of regions of the spectrum that may be poorly modeled (for a more detailed discussion of factors affecting deconvolution results, see *Hamilton and Christensen* [2000]). Application of the linear deconvolution technique to thermal emission spectra of coarse particulate samples is described by *Ramsey and Christensen* [1998], and application to solid rock samples has been described by *Hamilton et al.* [1997], *Feely and Christensen* [1999], and *Hamilton and Christensen* [2000].

Because the least squares algorithm is a purely mathematical expression, results can produce negative as well as positive values for modeled percentages of end-members. Two constraints are placed on the methodology described in detail by *Ramsey and Christensen* [1998] to produce results that are physically meaningful. First, if a spectral end-member phase is negatively modeled, it is presumed that the end-member phase is not present in the mixed spectrum and is removed. The entire model process is then repeated with a smaller spectral end-member list. Since negative end-members correspond to spectra that fall outside the area defined by the original end-members, these negative values are assumed not to be part of the mixture [*Ramsey and Christensen*, 1998]. A negative blackbody component is however permitted in final modeled results to compensate for possible differences in band-depths between spectral end-members and mixtures. The second constraint on least squares algorithm is that the modeled end-member values must sum to 100% for the most accurate solution and lowest RMS error [*Ramsey and Christensen*, 1998].

3.3.2. End-member selection. Accurate deconvolution of mixture spectra is largely dependent on the input of spectral end-members that represent the appropriate range of compositions in the mixture [*Hamilton et al.*, 1997; *Feely and Christensen*, 1999]. However, even with a robust group of end-member phases, it is unlikely that any end-member will have an identical composition to a particular phase in an unknown rock, particularly in the case of solid solution minerals. The lack of an exact match may be compensated for in the best fit model if several compositionally related end-members are included in different proportions to reproduce the spectral contribution of a phase in the unknown spectrum. *Hamilton et al.* [1997] and *Hamilton and Christensen* [2000] demonstrated that the compositions of plagioclase, pyroxene, and olivine could be modeled with some success by combining spectra of two or more solid-solution end-members to produce an intermediate composition. The end-members used here are from the ASU spectral library [*Christensen et al.*, 2000] and *Hamilton and Christensen* [2000]. A blackbody end-member is also included to accommodate variations in spectral contrast [*Hamilton et al.*, 1997; *Feely and Christensen*, 1999; *Hamilton and Christensen*, 2000].

However, the abundance of a phase in a rock cannot be accurately modeled if there is a complete absence of compositionally or structurally related phases in the mineral spectral endmember library. If this occurs, the abundance of some or all of the modeled phases in the deconvolved mode will be overestimated. This is due to redistribution of the percentage of the phase not modeled into the derived modes as the algorithm calculates fractional percentages that sum to 100 vol % (see *Ramsey and Christensen* [1998] for details). In this study, several new experimental and natural glass compositions and pigeonite were added to the mineral suite. These were previously not

present in the library but are common in volcanic rocks and are thus critical for accurately modeling phase abundances.

Prior to this study the ASU mineral spectral library contained only one glass sample, an obsidian. Figure 3a shows the normative compositions of interstitial glasses in Hakone and Medicine Lake andesites (this study) and Columbia River flood basalts [*Lambert et al.*, 1989] on a quartz-albite-orthoclase ternary diagram. The observed scatter in glass compositions reflects a chemical variability of 57–87% SiO_2. This wide range in glass compositions cannot be modeled accurately with one obsidian glass; therefore it was necessary to synthesize additional phases for this study. Three glasses were added to the end-member library: quenched Hawaiian basalt, silica-K_2O glass, and silica glass (Table 3). As shown in Figure 3a, glass compositions now cover a wider range of SiO_2 contents (50–100%), providing the deconvolution algorithm more end-members with which to model glasses in volcanic rocks. Figure 3b shows the spectra of the three new glass phases and obsidian. The silica-K_2O glass is essentially indistinguishable from obsidian [e.g., *Ramsey and Fink*, 1999] in shape and position, as might be expected on the basis of its composition; although the silica glass has a virtually identical shape, it is noticeably shifted toward shorter wavelengths relative to the silica-K_2O glass. The basaltic glass has reststrahlen features in the 1300–800 cm^{-1} region that are shifted to longer wavelengths than either of the silica-rich glasses, which is consistent with its greater mafic content [*Walter and Salisbury*, 1989; *Salisbury et al.*, 1991a]. The rounder shape of the basaltic glass is due to partial crystallization of the sample prior to quenching (described below).

The Hawaiian basalt glass was formed at the Kilauea volcano by R. Lentz by scooping basalt lava and quenching it with water. The silica glass is commercially pure silica glass tubing. The silica-K_2O glass was experimentally made by M. Wyatt and L. Anovitz at Oak Ridge National Laboratory. Dry oxide powder with a composition of 78% SiO_2, 13% Al_2O_3, 6% K_2O, and 4% Na_2O was evacuated and sealed in a platinum crucible and heated above its liquidus (~1200°C) for 15 min. The melt was then quenched, broken out of the crucible, and reground, remelted, and quenched at least twice to ensure homogeneity.

Pigeonite is a characteristic clinopyroxene in the groundmass of many basalts and andesites. Unfortunately, obtaining substantial quantities of pure pigeonite from a volcanic rock is a prohibitively difficult task, as it is usually found within only the mesostasis and never as large crystals. Therefore the ASU mineral spectral library does not and probably will never contain a wide variety of pigeonite samples. However, we were able to obtain a synthetic pigeonite sample (synthesized by D. Lindsley) for analysis, and this sample has been included in the end-member set (Table 4). To make the sample, MgO, SiO_2, Fe (iron metal), Fe_2O_3, and $CaSiO_3$ were weighed, ground together, placed in silver foil inside a silica glass tube which was then evacuated and sealed, and allowed to react for ~2 weeks at ~930°C (D. Lindsley, personal communication, 1999).

3.3.3. Application. The linear deconvolution algorithm was run twice for each sample to provide the best constraints on bulk modal mineralogy. Each rock spectrum was initially deconvolved using the full ASU spectral library (over 150 end-members) [*Christensen et al.*, 2000]. Model fits using the entire library can be difficult to interpret

because small amounts of the spectra of some end-members may be used to improve minor deviations between the model and measured spectra due to minor noise and differences in solid-solution minerals as discussed above. To better limit this potential confusion, a second deconvolution run used only a limited set of end-members representing the most abundant phases modeled in the first iteration for all samples; these are the results described in this paper. These phases, mainly plagioclase, orthopyroxenes and clinopyroxenes, olivine, and Si-rich glasses, represent the most common minerals generally found in basaltic to andesitic rocks. Serpentines and amphiboles were also included because they are common alteration products of olivine and pyroxene. Oxides, such as magnetite, hematite, chromite, and ilmenite, were not included because they are spectrally featureless over much of the wavelength region of interest. This gray body behavior could result in the modeling of an oxide component rather than a blackbody. The impact of the omission of oxide end-members is described below. The compositions of the end-member minerals used for the second deconvolution are listed in Table 4.

4. Results

Modal mineralogies of basalt, basaltic andesite, andesite, and dacite are derived from the linear deconvolution of the rocks' infrared spectra and compared to modes obtained by an electron microprobe phase mapping technique. Mineral compositions and bulk rock chemistries, calculated from deconvolved mineralogies, are also determined. These modeled values are compared to laboratory-measured mineral and bulk rock chemistries to determine the accuracy of chemistries derived from modeled mineralogies.

Table 1 shows the bulk chemistries of all samples. Table 5 shows electron microprobe-measured mineralogies of a subset of these samples which were selected to maximize compositional diversity. Blank spaces refer to phases that were not detected. There is an estimated precision of 5% of the amount of each phase present in Table 5 [*Taylor et al.*, 1996].

Plagioclase is the most abundant phase in all samples, variable concentrations of silica-K_2O glass are present in all groups, and silica glass and quartz are predominately found only in andesite and dacite. Orthopyroxene is most abundant in andesite, pigeonite is present in varying proportions in all groups, and high-Ca pyroxene (augite and/or diopside) is most abundant in basalt but still significant in andesite and dacite. Olivine is present in a significant proportion in only one basalt.

4.1. Measured and Modeled Spectra

Measured and modeled spectra of basalt, basaltic andesite, andesite, and dacite are shown in Figures 4 and 5. The positions and relative depths of individual absorptions are different between rock types owing to variations in the abundances and compositions of constituent phases. There are also noticeable spectral differences within each rock type owing to the fact that not all basalts are identical in their mineralogy. Overall, spectral fits produced by the linear deconvolution algorithm are extremely good (Figures 4 and 5), suggesting major rock phases are well represented in the end-member library and that they provide good fits to the rock types in this study. However, there are small noticeable misfits between measured and modeled spectra for several rocks at ~1150 and 945 cm^{-1}. The causes of these misfits are discussed in section 4.2 as modeled phase abundances are examined and compared to measured phase abundances for accuracy.

4.2. Mineralogy

Table 6 lists model-derived bulk mineralogies (total 100%) for all samples (abundances have been normalized to exclude blackbody percentages of 13–74% that were modeled [*Hamilton et al.*, 1997; *Feely and Christensen*, 1999; *Hamilton and Christensen*, 2000]). The physical justification for normalizing mineral abundances to exclude blackbody percentages is to account for differences in spectral contrast that can results from varying particle size effects. Blank spaces in Table 6 indicate phases that are not modeled in a given rock.

Plagioclase is modeled in high abundance for all samples. Silica-K_2O glass is also common among rock types, whereas silica glass and quartz are not modeled in high abundance in basalts and basaltic andesites. Orthopyroxene, pigeonite, olivine, and serpentine are present in all rock groups in varying abundances. High-Ca pyroxene is most abundant in basalt but still makes a significant contribution to basaltic andesite and andesite/dacite modes. Amphibole is modeled only in small amounts for one basaltic andesite and two andesite samples.

We have quantified the uncertainties in individual modeled mineral abundances (e.g., plagioclase and pyroxene groups) by calculating 1σ standard deviations of the absolute differences in mineral abundances as determined by the linear deconvolution and electron microprobe techniques. Assuming that they have a normal distribution, the 1σ standard deviations of the differences between each modeled and measured mineral phase abundance are shown in Table 7 (top). Standard deviations range from 2.4 to 12.2 vol %, with an average standard deviation of 4.8 vol %.

In previous studies a ± 5–10 vol % absolute error has been associated with all modeled mineral abundances based on small (0.5% daily to 4% over time) contributions to error in the measured spectra as a result of instrument noise and precision [*Ramsey and Christensen*, 1998] and by comparison with traditional petrographic point counting modes [*Feely and Christensen*, 1999; *Hamilton and Christensen*, 2000]. Traditional petrographic determinations of mineral abundances by point counting typically quote absolute errors of ± 5–15 vol % for major minerals and ~5 vol % for minor minerals. This additional uncertainty in mineral abundances creates further doubt in any error analysis of the linear deconvolution technique using point counted modes as "known" values. The error analysis completed in this study does not have the same degree of uncertainty because electron microprobe mineral abundances are the most accurate determinations of phase abundances possible (relative precision of 5 vol % [*Taylor et al.* 1996]). This allows for a calculation of error in modeled abundances for specific minerals, not simply an average error for all mineral abundances. The error calculation does not however take into account the possibility that phases with low-modal abundances in rocks may have larger modeled uncertainties compared to phases with high-modal abundances in rocks. This additional uncertainty is likely dependent not only on the abundance of a specific mineral in a rock, but also the abundances of other phases in a rock and thus the overall rock composition. Additional work is required to determine the affects of varying modal abundances of specific phases in combination with varying abundances of different phases as applied to error calculations.

By comparing modeled mineralogies to electron microprobe results, overestimations and underestimations of deconvolved abundances can be identified and

may indicate potential missing phases in the spectral end-member suite. Figures 6a and 6b show electron microprobe (measured) and spectrally deconvolved modal abundances for the subset of basalt, andesite, and dacite samples, respectively (no basaltic andesites were analyzed by electron microprobe). Error bars for individual modeled minerals are taken from the 1σ standard deviation error analysis values listed in Table 7 (top), and errors for measured abundances are a relative 5 vol % of the measured amount. Points that plot on the solid diagonal line have a 1:1 measured to modeled ratio. The dark gray field represents the average ~5 vol % uncertainty with deconvolved modal abundances determined in this study, and the light gray field with dashed lines represents the 5–10 vol % uncertainty determined in previous studies as stated above. Points that plot within the 5 vol % field are within the error determined in this study and thus represent accurate fits. Goodness of fits (i.e., underestimated or overestimated abundances) for deconvolved model modes are relative to electron microprobe measured abundances.

Figure 6a shows the vast majority of deconvolved phase abundances (28 of 32, or 87.5%) for basalt are within the 5 vol % uncertainty envelope considering the error associated with each phase. Only four phases (12.5%) are outside the 5 vol % uncertainty by an additional 1–9 vol %. Figure 6b shows that 85% (34 of 40) of modeled phase abundances for andesite and dacite are within the 5 vol % uncertainty envelope considering the error associated with each phase; of the remaining 15%, five of the samples are within 10 vol % of the known abundance, and only one sample is modeled at >15 vol % more than known values. These results are consistent with previously determined average accuracies of *Feely and Christensen* [1999] and *Hamilton and Christensen* [2000].

For this subset of rocks the silica-K_2O glass is not as well modeled as other phases and is consistently underestimated, while silica glass is slightly underestimated in andesite but overestimated in the dacite. The underestimation of silica-K_2O and silica glasses suggests they may not be representative of the exact composition and/or crystallinity of glasses identified by electron microprobe analyses in the samples. The silica-K_2O and silica glasses in the Hakone samples may be more crystalline than the synthetic glasses in the spectral library. It is known that the degree of crystallinity will affect the spectral shapes of two chemically identical glasses [e.g., *Kahle et al.*, 1988; *Crisp et al.*, 1990]. If the rock glasses are actually mostly microcrystalline silica phases, the more amorphous synthetic glass end-members probably will not provide good spectral fits.

Because the deconvolution algorithm calculates fractional percentages which sum to 100 vol % [*Ramsey and Christensen*, 1998], the misfit of silica-K_2O and silica glasses is redistributed throughout other phases. This may result in slightly overestimated modal abundances for one or more other phases. A likely substitute for glass phases would be a highly silicic mineral which would have absorption features at shorter wavelengths, like those of the glasses. Quartz is the most silicic library mineral available and its spectrum is included in small amounts in several of the best fit models where glass is known to be present.

In Hakone and Cascades samples the spectral contribution of the slightly overestimated quartz can be seen in the modeled fit. This is because quartz has a very diagnostic spectral shape. Figure 7 shows the measured and modeled spectra for Hakone andesite Hk-5, for which deconvolved silica-K_2O and silica glass abundances are 10 and

6 vol % below the measured values. Also plotted in Figure 7 is the emission spectrum of quartz. At ~1150 cm^{-1} a noticeable misfit between measured and modeled spectra is observed by a small peak in the modeled curve. The location of the modeled peak coincides with the strong spectral feature measured in quartz at the same wavenumber location. The deconvolution algorithm may have substituted quartz in place of silica-rich glasses, causing the misfit of the modeled spectra around 1150 cm^{-1} and the overabundance of quartz in modeled modes. However, because quartz has such a unique spectral shape, with the large peak at 1150 cm^{-1}, the deconvolution algorithm cannot completely substitute quartz for the missing glasses. Modeling too much quartz will cause the small misfit seen in Figure 7 to increase dramatically, resulting in an increased and unacceptable RMS error. The same misfit peak due to overestimated quartz observed in Hk-5 can be seen in the modeled spectra for Hakone andesites Hk-1 and Hk-3 and Cascades samples 82-95, 82-98, 82-102, and 85-2b (Figure 5). All of these samples have very little or no silica-K_2O glass modeled but do contain some quartz.

The remaining amount of glass abundance not replaced by substituting modeled quartz is redistributed into the other phases. Orthopyroxene, pigeonite, high-Ca pyroxene, and olivine are all slightly overestimated by the deconvolution algorithm for these samples. The same pattern is true for sample 82-98, except that silica glass is also overestimated. Overestimation of mafic phases can make up for some of the missing silica-K_2O and silica glass in Hakone samples and silica-K_2O glass in the Cascades sample. However, mafic minerals do not account for the total amount of glass phases underestimated, as their compositions and thus spectra are too different to substitute effectively in the model. The overestimation of modeled olivine causes the small

deviation between measured and modeled spectra at 945 cm^{-1} (Figures 4 and 5) as the misfit coincides with a strong spectral feature measured in olivine at the same wavenumber location.

Despite errors due to silica glasses, most other phases are modeled within the 5 vol % uncertainty. The redistribution of percentages from poorly modeled silica-K_2O and silica glasses does not greatly affect other phases outside the 5 vol % uncertainty, as errors are spread across all phases. This inspection of deconvolved modal abundances indicates that silicate phases common in basaltic to andesitic/dacitic rocks are indeed being modeled in plausible proportions, thus accounting for the good modeled spectral fits.

4.3. Derived Chemistry

Deconvolved mineral and bulk rock chemistries are derived from deconvolved modal mineralogies by combining the compositions (wt % oxides) of end-members in proportion to their relative modeled abundances (recalculated to wt %). Converting from deconvolved modes to a derived bulk chemistry is in essence a degradation of the data, as the derived chemistry is completely dependent on the end-member suite used, rather than the actual minerals in the rock. Here we describe how plagioclase, pyroxene, and derived bulk rock chemistries are compared to actual mineral and whole-rock compositions to examine their accuracy and usefulness in classifying volcanic rocks from thermal infrared spectra.

4.3.1. Plagioclase chemical compositions. Because volcanic rocks typically consist of chemically zoned plagioclase, it is probable that none of the plagioclase spectral end-members alone represents exactly the same composition as plagioclase in a

given sample. Multiple plagioclase end-members may be used in a model fit to reproduce the spectral contribution of zoned plagioclase in a rock. Deconvolved plagioclase compositions should be a good approximation to actual average plagioclase compositions in basalt, basaltic andesite, andesite, and dacite.

Figure 8 illustrates the Or-Ab-An ternary for feldspars including all compositional fields for the plagioclase (albite to anorthite) and alkali feldspar (albite to orthoclase) solid- solution series. The unlabeled field represents compositions that do not occur in nature. Deconvolved plagioclase compositions in andesite/dacite extend from labradorite into the more sodic-rich oligoclase and andesine fields, deconvolved plagioclase in basalt is confined to labradorite compositions, and deconvolved plagioclase in basaltic andesite ranges from labradorite to andesine.

Figure 9 compares deconvolved plagioclase compositions to measured phenocryst maximum (core) and minimum (rim and groundmass) values for rocks with known plagioclase compositions. Within this subset of 18 rocks, 14 have deconvolved plagioclase compositions that plot within the reported ranges. Only four deconvolved plagioclase compositions plot outside the reported ranges, with all being less than the minimum measured values and all occurring in andesites and dacites. The expected general trend of decreasing An content with increasing bulk rock SiO_2 wt % is observed with modeled An values plotted in Figure 9. This trend also exists with samples not shown in Figure 9 because of the lack of measured plagioclase compositions.

Another overall trend in Figure 9 is for deconvolved plagioclase to plot closer to the minimum than the maximum measured value. Normally, zoned plagioclase becomes more sodic (lower An) from core to rim, with rim compositions being close to the

average groundmass plagioclase composition. Thus modeled plagioclase probably reflects the average of total plagioclase chemistry in a rock in which phenocryst rims and groundmass grains are volumetrically more abundant than phenocryst cores. Error analysis between modeled and measured average plagioclase compositions, however, is not possible as measured average plagioclase compositions were not calculated for samples in this study. This is an ongoing study [*Milam et al.*, 2002]. The modeled plagioclase in the four samples that plot below the minimum measured value could reflect sodium-rich plagioclase compositions within the mesostasis that were not detected or measured during microprobe analyses.

4.3.2. Pyroxene chemical compositions. Deconvolved and measured pyroxene compositions for two basalts (79-35i and 79-3b) and three andesites (79-39d, Hk-3, and Hk-5) are compared in Figure 10 to examine the accuracy of the linear deconvolution algorithm in modeling pyroxene chemistries. Solid dots in Figure 10 represent deconvolved pyroxene compositions, while gray fields designate ranges in measured pyroxene compositions. Deconvolved compositions can represent a single pyroxene end-member (e.g., augite WAR-6474) or a combination of pyroxene end-members (e.g., augite WAR-6474 plus diopside WAR-5780) that make an intermediate composition.

For the basalts above, deconvolved and measured pyroxene compositions are similar in that when both orthopyroxene and clinopyroxene compositions are measured, both are modeled. However, deconvolved high-calcium pyroxenes consistently are more calcic than their measured values. Deconvolved and measured pyroxene compositions in andesites also show the same slight overabundance of calcium in clinopyroxenes. Another trend that appears in andesites and one basalt is the overestimation of

magnesium in orthopyroxene. The overestimation of calcium in clinopyroxenes and magnesium in orthopyroxenes can be explained by the compositions of available pyroxenes in the spectral library and the rocks from which they were obtained. The composition of high-calcium clinopyroxene is sensitive to the temperature at which the mineral equilibrates. Figure 11 shows isotherms for pyroxene compositions at atmospheric pressure. Shaded gray regions in Figure 11 are measured pyroxene compositions for samples in this study and solid dots are deconvolved pyroxene compositions from Figure 10. Shaded stars are the pyroxene end-member compositions available to the deconvolution algorithm. Because of particle size constraints on mineral library samples, almost all library standards are from plutonic rocks which equilibrated to lower temperatures than quenched pyroxenes in volcanic rocks. Thus deconvolving high-calcium pyroxene phases in volcanic rocks with plutonic pyroxene spectra probably results in the small errors in pyroxene chemistry observed in this study. Orthopyroxene compositions are not very sensitive to temperature changes, as is evident from the close spacing of the orthopyroxene isotherms in Figure 11; however, the orthopyroxenes in the library are generally more Mg-rich than the compositions measured in our volcanic rocks. There is a wider range of pyroxene compositions available in the ASU spectral library [*Hamilton and Christensen*, 2000; *Christensen et al.*, 2000]. Our results suggest that a wider range of pyroxene end-members may be necessary.

4.3.3. Derived bulk rock chemistry. Bulk chemistry for a given rock was derived by combining the compositions (wt % oxides) of modeled end-member phases in proportion to their relative abundances as determined by the deconvolution algorithm (recalculated to wt %). Table 7 (bottom) lists the mean absolute and mean relative

uncertainties and 1σ standard deviations of the differences between each derived and measured major oxide abundance. Figure 12 shows measured versus derived bulk rock oxide data for all basalt, basaltic andesite, and andesite/dacite samples with 1σ standard deviation errors on modeled oxides.

Overall, derived oxide contents exhibit a good correlation with measured values. Silica is fairly well modeled with absolute errors ranging from -4.4 (underestimation) to +4.3 wt % (overestimation). Derived abundances of Al_2O_3 and CaO have absolute errors ranging from –5.9 to +3.8 wt % and –2.2 to +3.0 wt %, respectively. Alkali abundances are also well modeled with Na_2O absolute errors ranging from only –1.6 to +1.3 wt % and K_2O absolute errors ranging from –1.9 to +0.2 wt %. Absolute errors in derived abundances for FeO and MgO range from –4.1 to + 2.7 wt % and –0.4 to +9.9 wt %, respectively. TiO_2 is underestimated in all samples by an average of 1.3 wt % with a maximum of –3.6 wt %.

The absolute and relative errors between derived and measured oxide abundances (Table 7) indicate that the most common oxides in silicate mineral phases (SiO_2, Al_2O_3, FeO, CaO, Na_2O, and K_2O) are well modeled. However, MgO and TiO_2 are not as well modeled, as indicated by relative errors of 74.5% and 94.7%, respectively. The greatest contribution to total MgO is likely to come from olivine as the vast majority of modeled olivine abundances come from the magnesium end-member forsterite. Overestimation of derived MgO is thus due to overestimations of olivine abundance, which is observed in the deconvolved modes of the subset of samples for which we have electron microprobe-measured phase abundances.

The source of the error in modeling wt % TiO_2 is a more complex issue. In the vast majority of basalt, basaltic andesite, and andesite/dacite samples selected for this study, oxide minerals comprise < 2% of the bulk modal abundance. Thus excluding oxides such as magnetite and ilmenite from the end-member suite for modeling these rocks should not have a significant negative effect on deconvolved modes and chemistry. However, CRB samples contain an appreciable amount of oxides, primarily ilmenite and magnetite in 5–10% total modal abundance, as determined by optical analyses of thin sections. For these rocks, the absence of oxides in the end-member set affects not only modeled TiO_2 contents but also SiO_2 contents. Because the deconvolution algorithm calculates modes that sum to 100%, any phase present in a rock but not represented in the end-member set causes an overestimation of deconvolved phase abundances as they compensate for the missing phase's spectral contribution. In the case of CRB rocks the only phases available to compensate for the missing oxide end-members are silicates, which causes an overestimation of SiO_2. The CRB samples possess some of the highest measured bulk TiO_2 contents (2.4–3.6 wt %) of all of our samples and also have the highest overestimated deconvolved SiO_2 contents with an average of +3.3 wt %.

5. Volcanic Rock Classification

Thermal infrared spectral shapes, deconvolved mineralogies, and derived mineral and bulk rock chemistries are all examined for their effectiveness in classifying basalt, basaltic andesite, andesite, and dacite. We address the data sets in order of least model dependent (measured spectra) to most model dependent (spectrally derived mineralogy and chemistry). Although chemical classification is the generally accepted method for

distinguishing volcanic rocks, the spectrally derived chemical values are the most model-dependent data set in this study. Therefore, if derived bulk chemistry provides a generally accurate means of classifying these rocks, we can have more confidence in the less model dependent results.

5.1. Spectral Discrimination

Figure 13 shows overlapping composite spectral fields for basalt (shaded) and andesite (open). Each field was created from measured spectra of basalt and andesite rocks and represents the ranges in spectral signatures. The fields are not defined by single rock spectra but, instead, by portions of several rock spectra that delineate maximum and minimum spectral ranges. The spectral field for dacite (dotted) is unique and does not overlap the basalt or andesite fields where shown. Basaltic andesites grade across the basalt and andesite spectral fields.

In the spectral fields of Figure 13, the Christiansen feature (the emission maximum on the short wavelength side of the Si-O stretching absorption) is located at higher wavenumbers (shorter wavelengths) in andesite than in basalt. The primary cause for this difference is the higher abundances of quartz and silica-rich glasses in the andesites. These phases display spectral absorption features at shorter wavelengths owing to their higher degree of polymerization, causing the spectra of rocks dominated by these phases to have a shorter-wavelength Christiansen feature [*Walter and Salisbury*, 1989; *Salisbury et al.*, 1991b]. Dacites have the highest abundances of quartz and silica glass, causing the Christiansen feature to occur at the highest wavenumbers (shortest wavelengths).

There is more overlap between spectral fields in the region of the reststrahlen bands (1200–800 cm^{-1}). As in the case of the Christiansen feature, silicate absorption features in this range move to lower wavenumbers owing to changes in the Si-O-Si stretching vibrations as a function of decreasing Si-O tetrahedral polymerization [*Walter and Salisbury*, 1989; *Salisbury et al.*, 1991b]. The spectral fields display absorption features that are at wavelengths comparable to features in minerals with a range of silica polymerization, such as plagioclase, pyroxene, amphibole, and olivine. The basalt spectral minimum shows a greater shift to lower wavenumbers compared to andesite and dacite. This observation coincides with the high deconvolved abundance of pyroxene and sometimes olivine in basalt. This shift can be explained by the overall higher average abundance of pyroxene and olivine in basalt (30 vol %) compared to andesite (13 vol %) and dacite (9 vol %).

Subalkaline basalts, andesites, and dacites can be distinguished using the spectral fields in Figure 13. However, basaltic andesites overlap with basalts and andesites in their classification.

5.2. Deconvolved Modal Mineralogy and Mineral Compositions

Measured mineral abundances, in various combinations, were examined for their effectiveness in classifying basalt and andesite and to develop a classification scheme that can accurately classify these rock types with modeled mineral abundances. The most effective scheme is shown in Figure 14 with SiO_2-rich glasses (silica glass and silica-K_2O glass) + quartz plotted versus high-calcium pyroxene (augite and diopside). The light gray basalt and andesite fields in Figure 14 were created using measured mineral abundances of basalt and andesite samples. Deconvolved mineral abundances of basalts

and andesites that plot in their respective fields are well classified. Basalt and andesite samples whose deconvolved mineral abundances plot outside their respective fields are misclassified. There is no basaltic andesite or dacite field in Figure 14. The dark gray fields in Figure 14 represent the entire range of all modeled basalt and andesite samples as plotted in this classification diagram.

Error bars in Figure 14 are taken from the 1σ standard deviations for modeled mineral abundances listed in Table 7. High-Ca pyroxene abundances have an error of ± 3.7 vol % while combined silica phases have an error of ± 7.3 vol %. The standard deviation error for silica phases was computed as a single total (i.e., standard deviation between the absolute difference of the total sum of modeled silica phases and total sum of measured silica phases). Reasons for computing the error of silica phases together are the following: (1) There is a tendency for errors to offset each other; that is, when one of these phases is over abundant, one or more of the others will be underestimated. (2) The unique spectral signatures of each silica phase are analogous to the unique spectral signatures of the high-Ca pyroxenes augite and diopside, which are reported as one high-Ca pyroxene phase. (3) Only the sum of these phases is used in classification of rock types.

All modeled basalts plot within the measured basalt field and are thus accurately classified. However, basalt samples 79-35i, CRB-5, and RSL-94-41 range outside the basalt classification field when error bars are applied. This results in their accurate classification as basalts being viewed with a lower degree of confidence. Four of nine modeled andesites (79-39d, 82-5, 82-69b, and 82-85) plot within the measured andesite field and are accurately classified. However, only sample 79-39d remains inside the

andesite classification field when error bars are applied. Of the remaining five andesites, three (Hk-1, Hk-5, and 82-102) plot between the basalt and andesite fields and two (79-9g and Hk-3) plot in the basalt field. However, the misclassification of these two andesites as basalt extends into the region between the basalt and andesite fields when error bars are applied, resulting in a more ambiguous classification instead of a wrong classification.

A second classification scheme by *Irvine and Baragar* [1971] (Figure 15) separates subalkaline volcanic rocks by plotting normative plagioclase composition (mol % An = 100An/(An+Ab)) versus normative color index (modal olivine + orthopyroxene + clinopyroxene). The shaded field shows typical volcanic compositions ranging from basalt to rhyolite. Volcanic rocks range from basalt through andesite and dacite to rhyolite with decreasing normative anorthite content and decreasing normative color index. The 1σ standard deviation for normative color index is shown in Figure 15, while no error calculation for normative plagioclase composition is possible, as previously discussed. Basalts and andesites are fairly well separated in Figure 15 with no basalts plotting in the andesite field but with a few andesites plotting in the basalt field. Some dacite samples plot as andesites; however, these dacites are borderline andesite.

5.3. Derived Bulk Chemistries

Figure 16 is a plot of derived silica versus alkalis superimposed on the chemical classification scheme for volcanic rocks [*Le Bas et al.*, 1986]. The 1σ standard deviation errors for SiO_2 and $Na_2O + K_2O$ are listed in Table 7. All rocks are accurately classified as being subalkaline.

Basalts plot as both basalt and basaltic andesite on the basis of derived SiO_2 contents. Samples 79-35i, 79-3b, HCC4E, HCC4A, and RSL-94-41 have almost perfectly modeled SiO_2 contents and are accurately classified as basalts. 79-35i is difficult to discriminate using the mineralogical classification scheme but is accurately represented using derived bulk SiO_2 content. Sample RSL-94-23 has a derived bulk SiO_2 content of 52 wt %, which straddles the classification boundary between basalt and basaltic andesite. Samples WAR-R1049 and CRB-5 are slightly overestimated in bulk SiO_2 to the extent that they are misclassified as basaltic andesite (recall that CRB samples contain relatively higher amounts of oxides and are expected to have slightly inflated SiO_2 values). Of the misclassified basalts, only CRB-5 does not extend into the basalt field when error bars are applied. No basalts are misclassified as andesites or dacites.

All but two basaltic andesites plot as basaltic andesite on the basis of derived bulk SiO_2 contents. Samples 79-24c and 79-38g have measured SiO_2 contents of 52.94 and 54.20 wt % near the basalt chemical classification field and are misclassified as basalts.

All but two andesites plot as andesite on the basis of derived bulk SiO_2 contents. Samples 82-69b and Hk-5 have measured SiO_2 contents of 57.80 and 59.52 wt % near the basaltic andesite chemical classification field and are misclassified as basaltic andesites. However, both samples extend into the andesite field when error bars are applied. Four andesites (82-5, 79-39d, Hk-3, and 82-102) extend into the basaltic andesite field when error bars are applied. Two of four dacites (85-2b and 82-98) are accurately classified as dacite based on derived bulk SiO_2 contents. The remaining two dacites (82-95 and 82-88b) plot as andesites; however, 82-88b does extend into the dacite field with error bars.

5.4. Summary of Classifications

Table 8 summarizes results for each classification scheme to determine if the volcanic samples can be distinguished using thermal infrared spectra, deconvolved mineralogies, and derived mineral and bulk rock chemistries. Samples are divided into basalt, basaltic andesite, andesite, and dacite groups according to their measured bulk chemical classifications. A letter is assigned to each sample representing the rock type determined for that sample using a particular classification scheme. For example, an andesite that is correctly classified as an andesite is assigned the letter "A," while a correctly classified basalt is assigned the letter "B." An andesite that is misclassified as a basalt would also be assigned the letter "B." Samples that classify as basaltic andesites are assigned the letters "BA," and samples that classify as dacites are assigned the letter "D". Letters in parentheses represent samples that change their classification due to their error bars extending into different class fields. For example, a rock designated as "A (BA)" is classified as an andesite based on the location of the data point in a particular scheme; however, the basaltic andesite classification is also possible due to the associated error. Samples without parentheses thus do not change their classification with the addition of error bars. "N/A" indicates that the classification scheme does not have a class designation for a particular rock group or where a particular sample may plot in a scheme. In general, basaltic andesites are likely to be more difficult to distinguish than basalts or andesite due to their intermediate nature.

All basalts, andesites, and dacites are correctly classified in at least two of four discriminant plots. Spectral fields (Figure 13) and derived bulk rock chemistries (Figure 16) are the most accurate classification schemes. All basalts, all andesites, and all dacites

are correctly classified using spectral fields. Derived bulk rock chemistries result in three of eight basalts being clearly classified. Of the remaining five basalts, two accurately plot as basalt but range into the basaltic andesite field with error bars, and two plot as basaltic andesites that range into the basalt field with error bars. Only one basalt is completely misclassified as a basaltic andesite using derived bulk rock chemistries; however, this sample is accurately classified as basalt using spectral fields and derived mineral chemistry. Derived bulk rock chemistries result in six of eleven basaltic andesites being clearly classified. Of the remaining five basaltic andesites not clearly classified, three are classified as basaltic andesite but range into the andesite and basalt fields when error bars are applied, and two are misclassified as basalts. Derived bulk rock chemistries result in three of nine andesites being clearly classified. Of the remaining six andesites not clearly classified, four are classified as andesite but range into the basaltic andesite field with error bars, and two are classified as basaltic andesite but range into the andesite field with error bars. Derived bulk rock chemistries result in two of four dacites being accurately classified. Only one dacite is completely misclassified as an andesite with derived bulk oxide abundance. Thus, using the spectral and derived bulk chemistry classification schemes, most basalts, basaltic andesites, andesites, and dacites can be distinguished. The deconvolved modal mineralogy scheme (Figure 14) is effective in distinguishing basalts and andesites/dacites but not basaltic andesites. The deconvolved mineral chemistry scheme (Figure 15) is not as effective as others because of some andesite samples being misclassified as basalts.

Thus, by utilizing the measured spectra, deconvolved mineral modes, and derived chemical classification schemes, all andesites can be distinguished from basalts.

However, no one classification scheme can be applied to distinguish all samples of each rock type. The multiple steps of classification required to distinguish andesite from basalt reflect the continuum of compositions that exist between volcanic rock types.

6. Implications for Determination of Martian Volcanic Rock Lithologies

This laboratory study addresses the question of whether thermal infrared spectra and derived mineralogical and chemical data of terrestrial basalts, basaltic andesites, andesites, and dacites can be used for petrologic classification. The results of this work are applicable to the study and classification of martian surface compositions. In a companion paper [*Hamilton et al.*, 2001], laboratory spectral data (2 cm^{-1} sampling) are convolved to TES 10 cm^{-1} sampling to ascertain whether adequate results for volcanic rock classification can be obtained with lower spectral resolution, comparable to that obtained from Mars orbit. The techniques and classification schemes developed in this paper are applied in paper 2 [*Hamilton et al.*, 2001] to examine and classify martian surface compositions from *Christensen et al.*, [2000] and *Bandfield et al.* [2000] and to help constrain the surface lithologies of the martian crust.

7. Conclusions

1. Linear deconvolution of thermal infrared emission spectra successfully identifies the primary minerals of terrestrial basalt, basaltic andesite, andesite, and dacite samples.

2. Direct comparisons between bulk modes derived from deconvolution and measured modes from electron microprobe phase mapping reveal slight discrepancies in the absolute abundances of modeled phases (e.g., silica glass phases and quartz). However,

these differences are small, as the vast majority (28 of 32, or 87.5%, for basalt and 34 of 40, or 85%, for andesite/dacite) fall within the estimated error of the deconvolution algorithm.

3. Deconvolved modes of plagioclase end-members may be combined to derive a single weighted average composition that approximates the average plagioclase composition in volcanic rocks. Pyroxene compositions can be similarly modeled and separated into orthopyroxenes, pigeonite, and high-calcium clinopyroxenes.

4. Bulk chemistries of volcanic rocks can be derived by combining the composition (wt % oxides) of deconvolved end-member phases in proportion to their relative abundances in a sample (recalculated to wt %). Most common oxides in silicate mineral phases (SiO_2, Al_2O_3, CaO, FeO, Na_2O, and K_2O) are well modeled relative to measured values. However, MgO and TiO_2 are not as well modeled owing to overestimation of deconvolved olivine and the lack of oxide spectral end-members, respectively.

5. Thermal infrared spectral shapes, deconvolved bulk mineralogies and mineral compositions, and derived bulk rock chemistries can be applied to distinguish andesites/dacites from basalts and basaltic andesites. However, no one classification scheme is effective in accurately classifying all volcanic samples. The multiple steps of classification required to distinguish andesite from basalt reflect the continuum of compositions that exist between volcanic rock types.

References

Adams, J. B., M. O. Smith, and A. R. Gillispie, Imaging spectroscopy: Interpretations based on spectral mixture analysis, in *Remote Geochemical Analysis: Elemental and Mineralogical Compositions*, edited by C. M. Pieters and P. A. Englert, pp. 145–166, Press Syndicate of University of Cambridge, Cambridge, 1993.

Baird, A. K., and B. C. Clark, On the original igneous source of martian fines, *Icarus*, 45, 113–123, 1981.

Baker, M. B., Evolution of lavas at Mt. Shasta Volcano, N. California: An experimental and petrologic study, Ph.D. dissertation, 430 pp., Mass. Inst. of Technol, Cambridge, 1988.

Bandfield, J. L., V. E. Hamilton, and P. R. Christensen, A global view of martian surface compositions from MGS-TES, *Science*, 287, 1626–1630, 2000.

Chayes, F., Distribution of basalt, basanite, andesite and dacite in a normative equivalent of the QAPF double triangle, *Chem. Geol.*, 33, 127–140, 1981.

Christensen, P. R., and S. T. Harrison, Thermal infrared emission spectroscopy of natural surfaces: Application to desert varnish coatings on rocks, *J. Geophys. Res.*, 98, 19,819–19,834, 1993.

Christensen, P. R., H. H. Kieffer, S. C. Chase, and D. D. Laporte, A thermal emission spectrometer for identification of surface composition from Earth orbit, in *Commercial Applications and Scientific Research Requirements for Thermal Infrared Observations of Terrestrial Surfaces*, NASA-EOSAT joint report, pp. 119–132, Earth Obs. Satell. Co., Lanham, Md., 1986.

Christensen, P. R., J. L. Bandfield, V. E. Hamilton, D. A. Howard, M. D. Lane, J. L. Piatek, S. W. Ruff, and W. L. Stefanov, A thermal emission spectral library of rock forming minerals, *J. Geophys. Res.*, 105, 9735–9739, 2000.

Crisp, J., A. B. Kahle, and E. A. Abbott, Thermal infrared spectral character of Hawaiian basaltic glasses, *J. Geophys. Res.*, 95, 21,657–21,669, 1990.

Feely, K. C., and P. R. Christensen, Quantitative compositional analysis using thermal emission spectroscopy: Application to igneous and metamorphic rocks, *J. Geophys. Res.*, 104, 24,195–24,210, 1999.

Gerlach, D. C., and T. L. Grove, Petrology of Medicine Lake Highland volcanics: Characterization of endmembers of magma mixing, *Contrib. Mineral. Petrol.*, 80, 147–159, 1982.

Grove, T. L., R. J. Kinzler, M. B. Baker, N. J. Donnelly, and C. E. Lesher, Assimilation of granite by basaltic magma at Burnt lava flow, Medicine Lake Volcano, northern California; decoupling of heat and mass transfer, *Contrib. Mineral. Petrol.*, 99; 3, 320–343, 1988.

Hamilton, V. E., and P. R. Christensen, Determining the modal mineralogy of mafic and ultramafic igneous rocks using thermal emission spectroscopy, *J. Geophys. Res.*, 105, 9717–9733, 2000.

Hamilton, V. E., P. R. Christensen, and H. Y. McSween Jr, Determination of martian meteorite lithologies and mineralogies using vibrational spectroscopy, *J. Geophys. Res.*, 102, 25,593–26,603, 1997.

Hamilton, V. E., M. B. Wyatt, H. Y. McSween Jr., and P. R. Christensen, Analysis of terrestrial and martian volcanic compositions using thermal emission spectroscopy, 2.

Application to martian surface spectra from the Mars Global Surveyor Thermal Emission Spectrometer, *J. Geophys. Res.*, 106, 14,733-14,746, 2001.

Irvine, T. N., and W. R. Baragar, A guide to the chemical classification of the common volcanic rocks, *Can. J. Earth Sci.*, 8, 523–548, 1971.

Johnson, P. E., M. O. Smith, S. Taylor-George, and J. B. Adams, A semiempirical method for analysis of the reflectance spectra of binary mineral mixtures, *J. Geophys. Res.*, 88, 3557–3561, 1983.

Johnson, P. E., M. O. Smith, and J. B. Adams, Simple algorithms for remote determination of mineral abundances and particle sizes from reflectance spectra, *J. Geophys. Res.*, 97, 2649–2657, 1992.

Kahle, A. B., A. R. Gillespie, E. A. Abbott, M. J. Abrams, R. E. Walker, G. Hoover, and J. P. Lockwood, Mapping and relative dating of Hawaiian basalt flows using multispectral thermal infrared images, *J. Geophys. Res.*, 93, 15,239–15,251, 1988.

Kuno, H., Petrology of Hakone volcano and the adjacent areas, Japan, *Geol. Soc. Am. Bull.*, 61, 957–1014, 1950.

Lambert, R. J., I. K. Marsh, and V. E. Chamberlain, The occurrence of interstitial granite-glass in all formations of the Columbia River Basalt Group and its petrogenetic implications, in Volcanism and Tectonism in the Columbia River Flood-Basalt Province, edited by S. P. Reidel and P. R. Hooper, *Spec. Pap. Geol. Soc. Am.*, 239, 321–332, 1989.

Le Bas, M. J., R. W. Le Maitre, A. Streckeisen, and B. A. Zanettin, Chemical classification of volcanic rocks based on the total alkali-silica diagram, *J. Petrol.*, 27, 745–750, 1986.

Leighty, R. S., Neogene tectonism and magmatism across the Basin and Range-Colorado Plateau boundary, central Arizona, Ph.D. dissertation, 1019 pp., Ariz. State Univ., Tempe, 1997.

Lindsley, D. H., Pyroxene thermometry, *Am. Mineral.*, 68, 477–493, 1983.

Milam, K.A., H.Y. McSween, Jr., V.E. Hamilton, and P.R. Christensen, Assessing the accuracy of deconvolved plagioclase compositions from TES data, *LPSC XXXIII*, #1868, 2002.

McSween, H. Y., Jr., What we have learned about Mars from SNC meteorites, *Meteoritics*, 29, 757–779, 1994.

McSween, H. Y., Jr., and K. Keil, Mixing relationships in the martian regolith and the composition of globally homogeneous dust, *Geochim. Cosmochim. Acta.*, 64, 2155–2166, 2000.

McSween, H. Y., Jr., et al., Chemical, multispectral, and textural constraints on the composition and origin of rocks at the Mars Pathfinder landing site, *J. Geophys. Res.*, 104, 8679–8715, 1999.

Mustard, J. F., and J. M. Sunshine, Seeing through the dust: martian crustal heterogeneity and links to the SNC meteorites, *Science*, 267, 1623–1626, 1995.

Mustard, J. F., S. Murchie, S. Erard, and J. M. Sunshine, In situ compositions of martian volcanics: Implications for the mantle, *J. Geophys. Res.*, 102, 25,605–25,615, 1997.

Press, W. H., B. P. Flannery, S. A. Teukolsky, and W. T. Fettering, *Numerical Recipes in C: The Art of Scientific Computing*, 1st ed., pp. 517-539, Cambridge Univ. Press, New York, 1988.

Ramsey, M. S., Quantitative analysis of geological surfaces: A deconvolution algorithm for mid-infrared remote sensing data, Ph.D. dissertation, 276 pp., Ariz. Sate Univ., Tempe, 1996.

Ramsey, M. S., and P. R. Christensen, Mineral abundance determination: Quantitative deconvolution of thermal emission spectra, *J. Geophys. Res.*, 103, 577–596, 1998.

Ramsey, M. S., and J. H. Fink, Estimating silicic lava vesicularity with thermal remote sensing: A new technique for volcanic mapping and monitoring, *Bull. Volcanol.*, 61, 32–39, 1999.

Rieder, R., et al., The chemical composition of martian soils and rocks returned by the mobile alpha proton X-ray spectrometer: Preliminary results from the X-ray mode, *Science,* 278, 1771–1774, 1997.

Ruff, S. W., P. R. Christensen, P. W. Barbera, and D. L. Anderson, Quantitative thermal emission spectroscopy of minerals: A laboratory technique for measurement and calibration, *J. Geophys. Res.*, 102, 14,899–14,913, 1997.

Salisbury, J. W., L. S. Walter, N. Vergo, and D. M. D'Aria, *Infrared (2.1–25 μm) Spectra of Minerals*, 267 pp., Johns Hopkins Univ. Press, Baltimore, Md., 1991a.

Salisbury, J. W., D. M. Aria, and E. Jarosewich, Midinfrared (2.5– 13.5 μm) reflectance spectra of powdered stony meteorites, *Icarus*, 92, 280–297, 1991b.

Singer, R. B., and H. Y. McSween Jr., The igneous crust of Mars: Compositional evidence from remote sensing and the SNC meteorites, in *Resources of Near-Earth Space*, edited by J.S. Lewis, M. S. Matthews, and M. L. Guerrieri, pp. 709–736, Univ. of Ariz. Press, Tucson, 1993.

Taylor, L. A., A. Patchen, D. H. S. Taylor, J. G. Chambers, and D. S. McKay, X-ray digital imaging and petrography of lunar mare soils: Data input for remote sensing calibrations, *Icarus*, 124, 500–512, 1996.

Thomson, J. L., and J. W. Salisbury, The mid-infrared reflectance of mineral mixtures (7–14 μm), *Remote Sens. Environ.*, 45, 1–13, 1993.

Walter, L. S., and J. W. Salisbury, Spectral characterization of igneous rocks in the 8– to 12–μm region, *J. Geophys. Res.*, 94, 9203–9213, 1989.

Wright, T. L., and R. S. Fiske, Origin of the differentiated and hybrid lavas of Kilauea volcano, Hawaii, *J. Petrol.*, 12, 1–65, 1971.

Appendix

Table 1: Major and Minor Element Analyses of Basalts, Basaltic Andesites, Andesites, and Dacites (Wt. % Oxides)

Sample	Reference [a]	SiO_2	TiO_2	Al_2O_3	Fe_2O_3[b]	FeO[b]	MnO	MgO	CaO	Na_2O	K_2O	P_2O_5	Total
Basalts													
Med. Lake High.	[1]												
79-35i*		47.68	0.71	17.74	9.72	-	0.16	9.35	11.74	2.30	0.09	0.06	99.55
79-3b*		50.11	1.10	20.86	9.10	-	0.13	4.06	10.54	3.27	0.47	0.18	99.82
Kilauea volcano	[2]												
HCC4E*		50.77	2.79	14.16	3.17	8.50	0.18	6.45	10.38	2.30	0.51	0.27	99.48
HCC4A*		50.77	2.79	14.16	3.17	8.50	0.18	6.45	10.38	2.30	0.51	0.27	99.48
Deccan Traps	[3]												
WAR-R1049		49.54	2.05	12.67	-	13.15	0.00	6.15	9.13	2.76	0.43	0.00	95.88
Columbia River	[4]												
CRB-5		50.60	3.62	12.70	16.18	-	0.21	4.27	8.29	2.46	1.21	0.59	100.13
Arizona	[3]												
RSL-95-23		50.80	1.56	14.80	-	9.92	0.00	7.00	10.32	3.00	0.96	0.00	98.36
RSL-94-41		50.80	0.94	17.50	-	8.72	0.00	7.10	9.75	3.30	0.89	0.00	99.00
Basaltic Andesites													
Columbia River	[4]												
CRB-4		51.71	2.82	13.25	14.06	-	0.20	4.20	8.01	2.75	1.34	0.61	98.95
CRB-2		52.05	3.20	12.89	14.54	-	0.20	3.97	8.04	2.65	1.41	0.64	99.59
CRB-6		55.04	2.39	13.76	12.27	-	0.20	3.37	6.90	3.07	1.87	0.49	99.36
Med. Lake High.	[1]												
79-24c		52.94	0.80	18.54	7.94	-	0.13	6.55	9.29	3.14	0.71	0.16	100.21
79-38k		54.20	0.93	17.48	8.42	-	0.12	5.65	8.67	3.32	0.99	0.17	99.93
79-38g*		54.20	0.93	17.48	8.42	-	0.12	5.65	8.67	3.32	0.99	0.17	99.93
79-37j		54.93	1.10	17.17	8.68	-	0.14	4.53	8.11	3.81	0.90	0.22	99.59
79-4d		56.31	0.66	16.68	7.08	-	0.12	6.26	8.43	2.73	1.46	0.09	99.82
Arizona	[3]												
RSL94-36		53.10	1.57	15.00	-	10.30	0.00	7.90	8.77	3.10	0.60	0.00	100.34
RSL94-8		53.90	1.00	16.20	-	8.00	0.00	5.60	8.72	3.40	1.31	0.00	98.13
RSL94-12		55.00	1.27	15.20	-	8.31	0.00	7.30	7.66	3.30	1.22	0.00	99.26

Table 1: Major and Minor Element Analyses of Basalts, Basaltic Andesites, Andesites, and Dacites (Wt. % Oxides) Continued

Sample	Reference [a]	SiO_2	TiO_2	Al_2O_3	Fe_2O_3[b]	FeO[b]	MnO	MgO	CaO	Na_2O	K_2O	P_2O_5	Total
Andesites													
Med. Lake High.	[1] [5]												
82-5		56.80	0.66	16.40	6.77	-	0.12	5.87	8.05	3.31	1.54	0.12	99.64
79-39d*		57.15	1.17	16.03	7.53	-	0.11	4.29	7.27	3.33	1.82	0.52	99.20
79-9g		57.66	1.44	16.45	8.49	-	0.14	2.75	6.10	4.80	1.34	0.34	99.51
82-69b		57.80	0.63	16.30	6.54	-	0.12	5.62	7.77	3.28	1.65	0.11	99.82
Hakone volcano	[4]												
Hk-1		59.52	1.01	16.79	8.64	-	0.16	2.14	6.20	3.21	0.86	0.15	98.68
Hk-3*		59.52	1.01	16.79	8.64	-	0.16	2.14	6.20	3.21	0.86	0.15	98.68
Hk-5*		59.52	1.01	16.79	8.64	-	0.16	2.14	6.20	3.21	0.86	0.15	98.68
Mount Shasta	[6]												
82-102		60.61	0.65	16.97	1.49	3.57	0.09	4.15	6.79	3.91	1.23	0.16	99.62
82-85		61.00	0.66	16.86	0.76	3.86	0.08	3.80	5.83	4.37	1.81	0.30	99.33
Dacites													
Mount Shasta	[6]												
85-2b		62.67	0.64	16.75	0.18	3.83	0.07	3.36	6.28	4.07	1.15	0.18	99.18
82-88b		62.98	0.58	16.74	1.60	2.55	0.07	2.79	5.12	4.65	1.93	0.28	99.29
82-98		63.78	0.60	16.65	1.37	2.87	0.08	3.20	5.50	4.05	1.56	0.18	99.84
82-95		63.95	0.61	16.05	1.79	2.59	0.08	3.17	5.05	3.88	2.21	0.18	99.56

[a] [1] Gerlach and Grove, 1982; [2] Wright and Fiske, 1971; [3] Hamilton and Christensen, 2000; [4] This study; [5] Grove et al., 1988; [6] Baker, 1988. [b] Total iron reported as Fe_2O_3 and/or FeO. *Samples with outcrop or volcanic flow measured bulk chemistry.

Table 2: Concentration Criteria Used to Classify Minerals and Glasses

Phase	Defining Criteria *
Plagioclase	38-76% Si, 17-50 % Al, 4-26 % Ca, < 4 % K
Quartz	> 95 % Si, < 3 % K, < 2 % Al
Olivine	38-57 % Si, 18-55 % Mg, < 2 % Ca
Augite	46-75 % Si, 14-33 % Ca, 5-20 % Mg
Pigeonite	55-75 % Si, 3-12 % Ca, 10-25 % Mg
K-Feldspar	14-30 % K
Orthopyroxene	55-75 % Si, < 3 % Ca, 10-30 % Mg
Silica Glass	> 80 % Si, < 3 % K, < 25 % Al
Si-K_2O Glass	55-95 % Si, 2-25 % K

* These "concentrations" are in terms of percentage of spectrum as provided by the X-ray imaging software. The values are similar to the oxide weight percentages for given elements (e.g., 30% Al ~ 39 wt.% Al_2O_3).

Table 3: Major Element Analyses of Glasses Added to Mineral Library (Wt. % Oxides)

	Quenched Hawaiian Basalt	Silica-K_2O Glass	Silica Glass
SiO2	50.2 (0.3)*	77.9	99.9
TiO2	2.69 (0.12)	0	0
Al2O3	13.2 (0.5)	12.6	0
Cr2O3	0.03 (0.03)	0	0
MgO	6.29 (0.18)	0	0
CaO	10.9 (0.2)	0	0
MnO	0.17 (0.05)	0	0
FeO	11.4 (0.3)	0	0
Na2O	2.29 (0.05)	3.90	0
K2O	0.47 (0.03)	5.67	0
Total	97.6 (0.5)	100	99.9

* Numbers in parentheses refer to standard deviations of mean analyses.

Table 4: End-member Mineral Compositions Used in Deconvolution (Wt. % Oxides)

	SiO_2	TiO_2	Al_2O_3	$FeO^{(T)}$	MnO	MgO	CaO	Na_2O	K_2O	P_2O_5	Cr_2O_3	Total
Feldspars:												
Albite WAR-5851	63.03	0.01	19.67	5.51	0.02	0.47	1.37	8.50	0.22	0.01	0.63	99.44
Oligoclase WAR-5804	60.08	0.01	22.29	0.17	0.01	0.01	4.01	8.48	0.71	0.06	0.01	95.84
Andesine BUR-240	53.85	0.12	27.09	0.59	0.01	0.07	9.51	5.55	0.37	0.10	0.02	97.28
Labradorite WAR-4524	52.62	0.11	27.74	2.50	0.02	0.14	10.90	5.01	0.42	0.03	0.04	99.53
Labradorite WAR-RGAND01	49.85	0.05	28.03	3.09	0.03	0.68	13.04	3.46	0.22	0.01	0.22	98.68
Bytownite WAR-5859	48.35	0.04	31.54	1.56	0.01	0.26	14.68	2.89	0.09	0.01	0.12	99.55
Anorthite BUR-340	44.84	0.01	35.01	0.37	0.00	0.00	18.25	0.94	0.00	0.00	0.00	99.42
Anorthite WAR-5759	41.54	0.03	29.50	9.20	0.03	2.69	15.40	1.13	0.08	0.01	0.98	100.59
Silica:												
Quartz BUR-4120	100.00	0.00	0.00	0.00	0.00	0.00	0.00	0.00	0.00	0.00	0.00	100.00
Silica glass[a]	99.99	0.00	0.00	0.00	0.00	0.00	0.00	0.00	0.00	0.00	0.00	99.99
Silica-K_2O glass[a]	77.87	0.00	12.55	0.00	0.00	0.00	0.00	3.90	5.67	0.00	0.00	99.99
Pyroxenes:												
Orthopyroxene HS-9.4b	57.87	0.02	0.99	6.87	0.17	34.86	0.67	0.00	0.00	0.00	0.00	101.45
Orthopyroxene NMNH-93527	51.84	0.35	5.28	13.78	0.23	26.76	1.46	0.07	0.00	0.00	0.00	99.77
Clinopyroxene WAR-5780	54.14	0.02	0.51	2.56	0.06	17.54	24.25	0.45	0.00	0.00	0.00	99.53
Clinopyroxene HS-119.4b	52.87	0.02	0.92	10.20	0.29	11.91	24.08	0.65	0.00	0.00	0.00	100.94
Clinopyroxene DSM-HED01	49.96	0.01	0.06	14.14	7.99	4.32	22.80	0.11	0.00	0.00	0.00	99.39
Clinopyroxene WAR-6474	50.60	0.18	2.35	12.58	0.30	9.96	21.13	2.00	0.00	0.00	0.00	99.10
Clinopyroxene BUR-620	50.51	0.11	1.69	16.19	0.73	7.58	21.51	1.91	0.00	0.00	0.00	100.23
Clinopyroxene NMNH-9780	51.00	0.20	1.55	16.52	0.46	9.42	20.49	0.33	0.02	0.00	0.00	99.99
Pigeonite $Wo_{10}En_{36}Fs_{54}$33,34[a,b]	50.49			32.59		12.20	4.71					

Table 4: End-member Mineral Compositions Used in Deconvolution (Wt. % Oxides) Continued

	SiO_2	TiO_2	Al_2O_3	$FeO^{(T)}$	MnO	MgO	CaO	Na_2O	K_2O	P_2O_5	Cr_2O_3	Total
Olivines:												
Forsterite AZ-01	38.47	0.01	0.09	9.57	0.13	48.88	0.14	0.03	0.01	0.01	0.00	97.34
Fayalite WAR-RGFAY01	31.11	0.06	0.00	59.75	1.30	7.71	0.09	0.00	0.00	0.00	0.00	100.02
Amphiboles:												
Mg-hastingsite HS-115.4b	45.12	0.24	9.94	8.31	0.09	18.69	11.73	2.20	0.78	0.01	0.16	97.27
Actinolite WAR-0354	54.00	0.04	2.07	6.89	0.23	20.03	11.48	0.99	0.06	0.01	0.28	96.08
Serpentines:												
Antigorite HS-8.4b	42.28	0.01	1.21	3.79	0.06	38.50	0.02	0.01	0.01	0.00	0.00	85.89
Lizardite 83-145B	40.49	0.01	1.18	6.30	0.11	38.81	0.03	0.01	0.01	0.01	0.00	86.96

[a] Synthetic samples. [b] Chemistry determined from Wo En Fs values provided by D. Lindsley.

Table 5: Electron Microprobe Bulk Mineralogy of Basalt, Andesite, and Dacite.

Sample	Plagioclase	Si-K_20 glass	Si glass	Quartz	Opx	Pigeonite	High-Ca Px	Olivine	Total
Basalts									
79-35i	68	1					16	14	99
79-3b	76	5			1	5	8	1	96
HCC4E	48	12				4	31	3	98
HCC4A	48	10	1			5	29	3	96
Andesites									
79-39d	46	38	1		2	4	5	1	97
Hk-1	53	18	17	2	1	3	3		97
Hk-3	56	12	12	2	5	8	3		98
Hk-5	53	10	14	1	8	3	6	1	96
Dacite									
82-98	39	42	6	1	4	2	3		97

Table 6: Deconvolved Bulk Mineralogy of Basalt, Basaltic Andesite, Andesite, and Dacite.

Sample	Plagioclase	Si-K_20 glass	Si glass	Quartz	Opx	Pigeonite	High-Ca Px	Olivine	Amphibole	Serpentine
Basalts										
79-35i	71						7	22		1
79-3b	78				1		10	6		4
HCC4E	52	1				25	19	2		
HCC4A	57	5				7	18			14
WAR-R1049	49	5	1		6	16	16	1		7
CRB-5	40	12			3	32	10	3		
RSL-95-23	63	6				12	12	7		
RSL-94-41	62		2			17	10	10		
Basaltic Andesites										
CRB-4	43	10	1			30	13	4		
CRB-2	36	14	1		3	33	12	2		
CRB-6	31	19	2			39	4	4	1	
79-24c	42	10					13	13		22
79-38k	63	7				24	4	2		
79-38g	71			1			16	2		10
79-37i	69	8	2		1	14	4	2		
79-4d	64	12	2		1		13	5		5
RSL-94-36	45	10				26	11	8		1
RSL-94-8	66	4				14	11	4		2
RSL-94-12	54	9	1		4	20	7	4		

Table 6: Deconvolved Bulk Mineralogy of Basalt, Basaltic Andesite, Andesite, and Dacite. Continued

Sample	Plagioclase	Si-K_20 glass	Si glass	Quartz	Opx	Pigeonite	High-Ca Px	Olivine	Amphibole	Serpentine
Andesites										
82-5	53	29			6		2	9		2
79-39d	42	32			8		1	9	6	2
79-9g	70		9			7	8	6		
82-69b	55	27			7		1	10		
Hk-1	51		9	6	7	13	8	6	1	
Hk-3	55		7	5	12	5	9	6		2
Hk-5	53		8	5	8	18	3	6		
82-102	71	1	5	3		12	5	2		
82-85	58	20	4	1	6		7	4		1
Dacites										
85-2b	66		15	10	1		4	4		
82-88b	37	21	9	2			16	6		9
82-98	46		20	7	5	7	6	8		1
82-95	79		2	9			3	7		

Table 7: Major Mineralogy and Bulk Chemistry Error Analysis

	Plagioclase	Si-K_20 glass	Si glass	Quartz	Opx	Pigeonite	High-Ca Px	Olivine
Mean Absolute Difference	4.0	12.0	4.0	2.0	2.0	7.0	6.0	5.6
*Standard Deviation	2.9	12.2	4.8	2.4	3.1	6.9	3.7	2.4

	SiO_2	TiO_2	Al_2O_3	FeO	MgO	CaO	Na_2O	K_2O
Mean Absolute Difference	1.8	1.3	2.1	1.8	2.6	0.9	0.4	0.5
Mean Relative Difference	3.2	94.7	13.0	24.2	74.5	12.4	12.3	44.1
*Standard Deviation	1.4	0.9	1.5	1.2	2.6	0.7	0.4	0.4

* Standard deviation is of the mean absolute difference.

Table 8: Summary of Volcanic Rock Classifications [a]

Samples	Classification Schemes			
	Spectral Fields[b]	Modeled Modal Mineralogy[c]	Derived Mineral Chemistry[d]	Derived Bulk Rock Chemistry[e]
Basalts				
79-35i	B	B (N/A)	B	B
79-3b	B	B	B	B
HCC4E	B	B	B	B (BA)
HCC4A	B	B	B	B
WAR-R1049	B	B	B	BA (B)
CRB-5	B	B (N/A)	B	BA
RSL-95-23	B	B	B	BA (B)
RSL-94-41	B	B (N/A)	B	B (BA)
Basaltic Andesites				
CRB-4	N/A	B (N/A)	B	BA
CRB-2	N/A	N/A (B)	B	BA
CRB-6	N/A	N/A (A)	B	BA (A)
79-24c	N/A	B (N/A)	B	B
79-38k	N/A	N/A (B)	B	BA
79-38g	N/A	B	B	B
79-37i	N/A	N/A (B)	B (A)	BA
79-4d	N/A	N/A (B)	A (B)	BA
RSL-94-36	N/A	B (N/A)	B	BA (B)
RSL-94-8	N/A	B	B	BA (B)
RSL-94-12	N/A	B (N/A)	B	BA

Table 8: Summary of Volcanic Rock Classifications [a] Continued

Samples	Classification Schemes			
	Spectral Fields[b]	Modeled Modal Mineralogy[c]	Derived Mineral Chemistry[d]	Derived Bulk Rock Chemistry[e]
Andesites				
82-5	A	A (N/A)	B (A)	A (BA)
79-39d	A	A	A (B)	A (BA)
79-9g	A	B (N/A)	A	A
82-69b	A	A (N/A)	B (A)	BA (A)
Hk-1	A	N/A (B)	B	A
Hk-3	A	B (N/A)	B	A (BA)
Hk-5	A	N/A	B	BA (A)
82-102	A	N/A (B)	A (B)	A (BA)
82-85	A	A (N/A)	A (B)	A
Dacites				
85-2b	D	A (N/A)	D (A)	D
82-88b	D	N.A.	A	A (D)
82-98	D	A (N/A)	A	D
82-95	D	N.A.	A (D)	A

[a] A, andesite; B, basalt; BA, basaltic andesite; D, dacite. These refer to the classification of a sample based on the location of the data point in a particular scheme. Letters in parentheses represent samples that change their classification due to error bars extending into different class fields. N/A indicates that a classification scheme does not have a class designation for a particular rock group or where a particular sample may plot in a scheme.

[b] See Figure 13.

[c] See Figure 14.

[d] See Figure 15.

[e] See Figure 16.

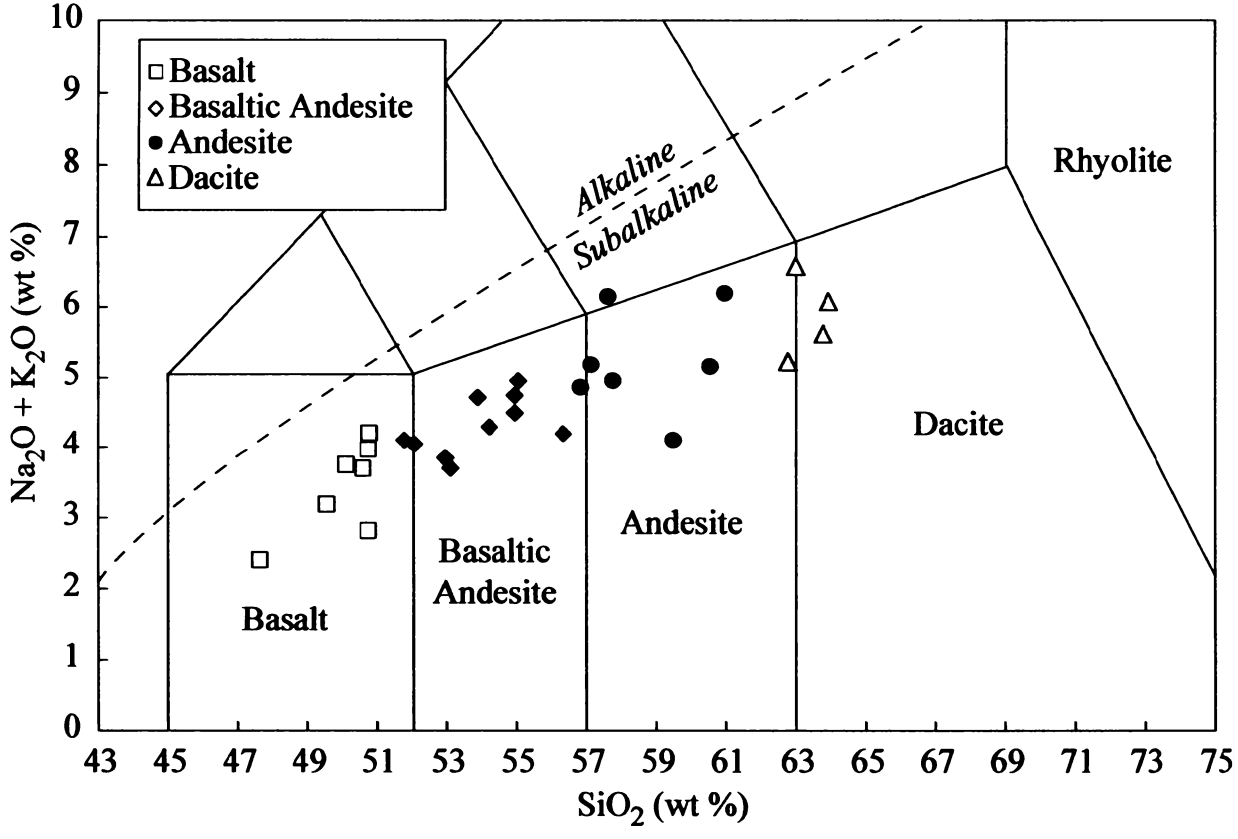


Figure 1. Chemical compositions of subalkaline volcanic rocks examined in this study. Symbols indicate the measured chemical classification name for each volcanic rock.

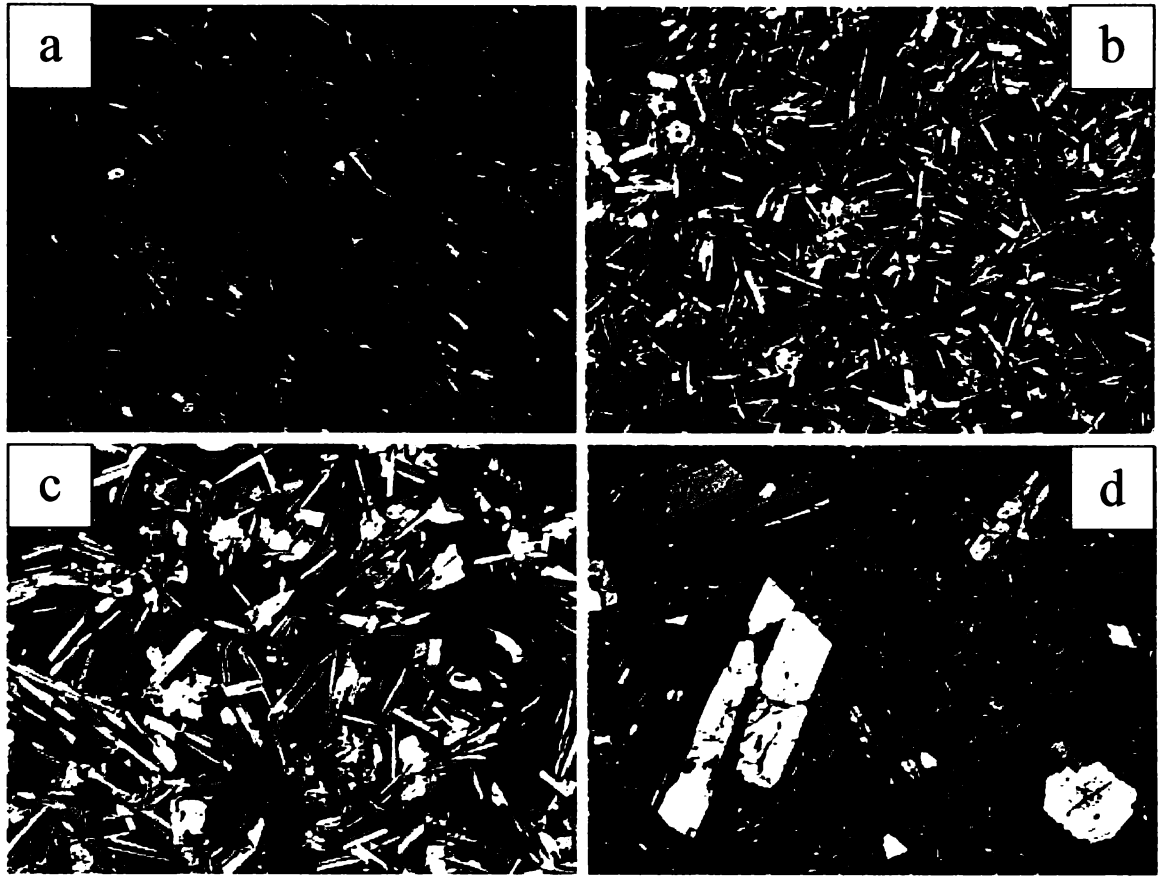


Figure 2. Crossed polar photomicrographs (3.4 mm across) of volcanic rocks displaying variable textures. (a) Glassy basaltic andesite with plagioclase and pyroxene microlites (Medicine Lake Highland). (b) Intersertal-subophitic basalt with plagioclase phenocrysts in a groundmass of plagioclase and pyroxene microlites and glass (Medicine Lake Highland). (c) Fine-grained, hypocrystalline basalt with plagioclase and clinopyroxene phenocrysts in a groundmass of plagioclase and glass (Kilauea). (d) Porphyritic andesite with phenocrysts of plagioclase and orthopyroxene in a groundmass of plagioclase microlites and glass (Hakone).

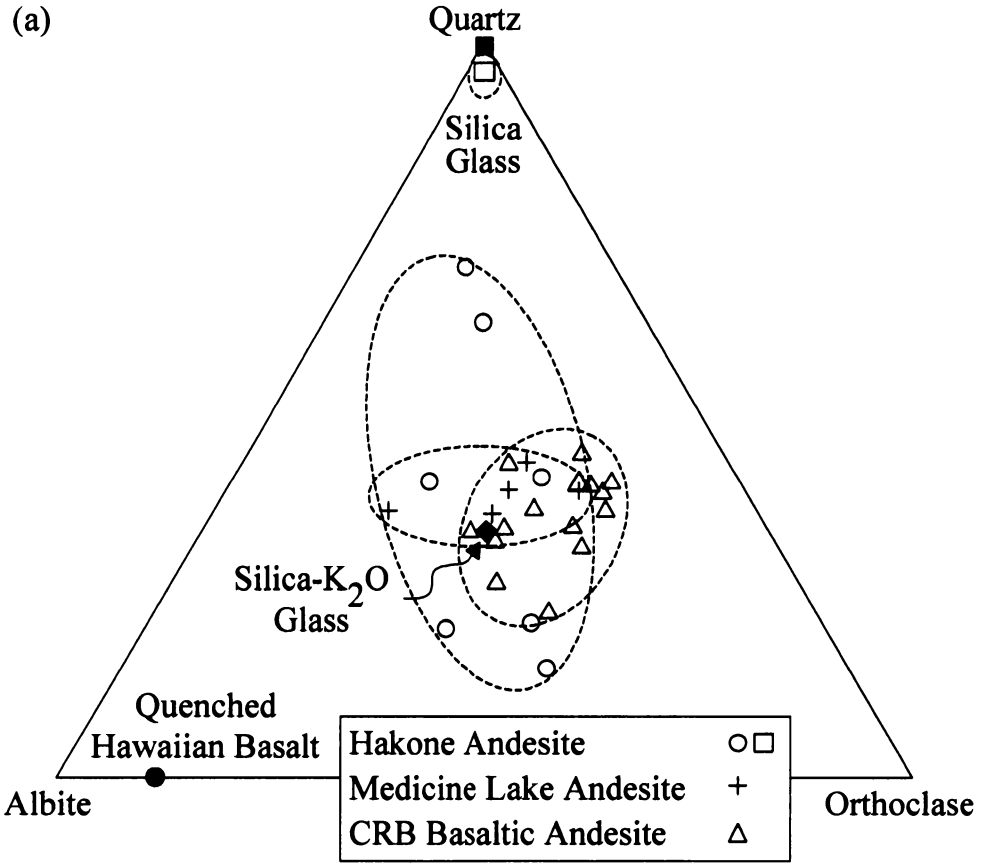


Figure 3. Normative recalculation of microprobe analyses of interstitial glasses in Hakone and Medicine Lake andesite (this work) and Columbia River flood basalt [*Lambert et al.*, 1989] (a). Also shown are glass compositions (solid symbols) added to the mineral library of phases: quenched Hawaiian basalt, silica-K_2O glass, and silica glass.

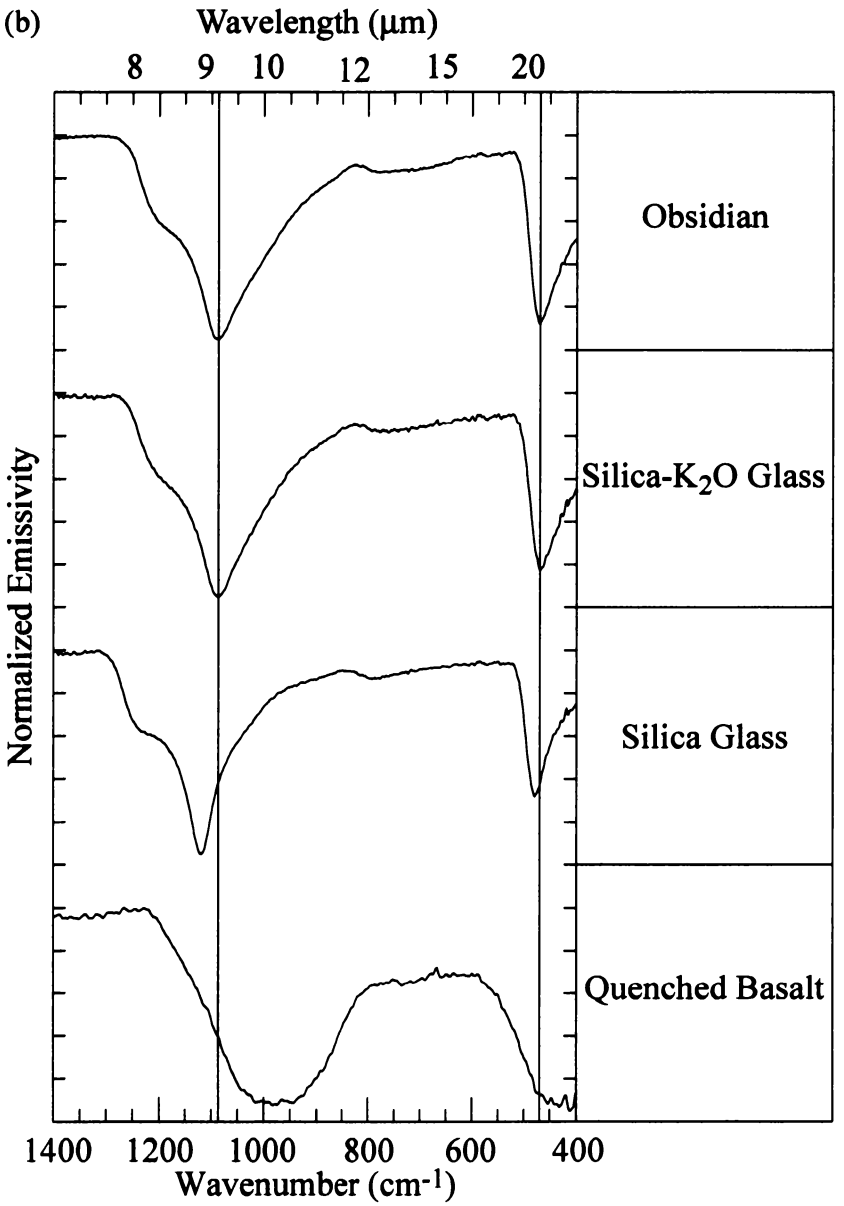


Figure 3 Continuned. Measured normalized emissivity spectra of obsidian, silica-K_2O glass, silica glass, and quenched basalt (b). Variations in the spectral shape and location of absorption features (as indicated with vertical lines passing through spectra) are a reflection of the different chemical compositions of the glasses.

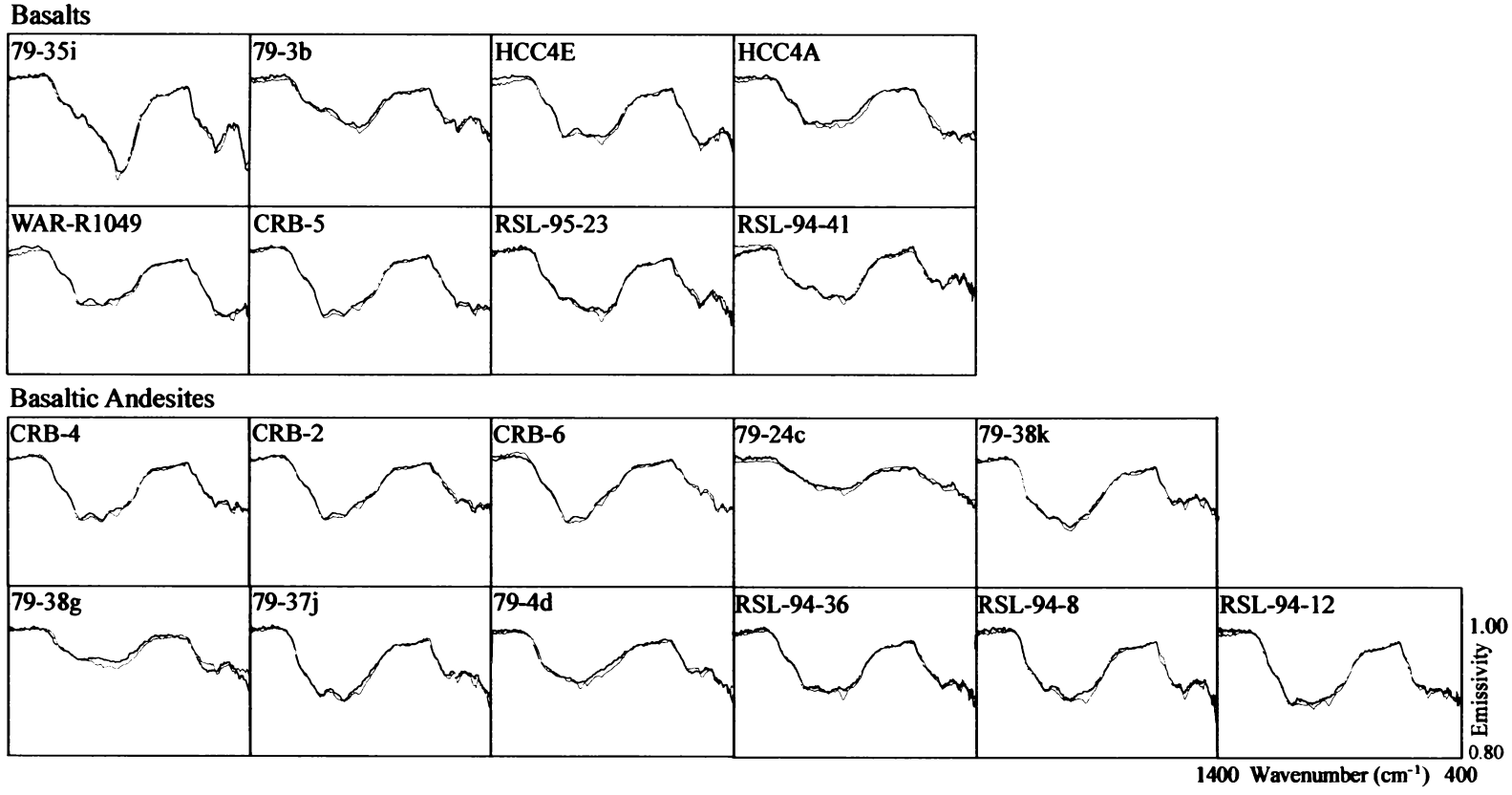


Figure 4. Measured (black) and modeled (red) emissivity spectra of basalt and basaltic andesite. Spectral fits produced by the linear deconvolution algorithm are extremely good, suggesting major rock phases are well represented in the end-member library and that they provide good fits to the rock types in this study.

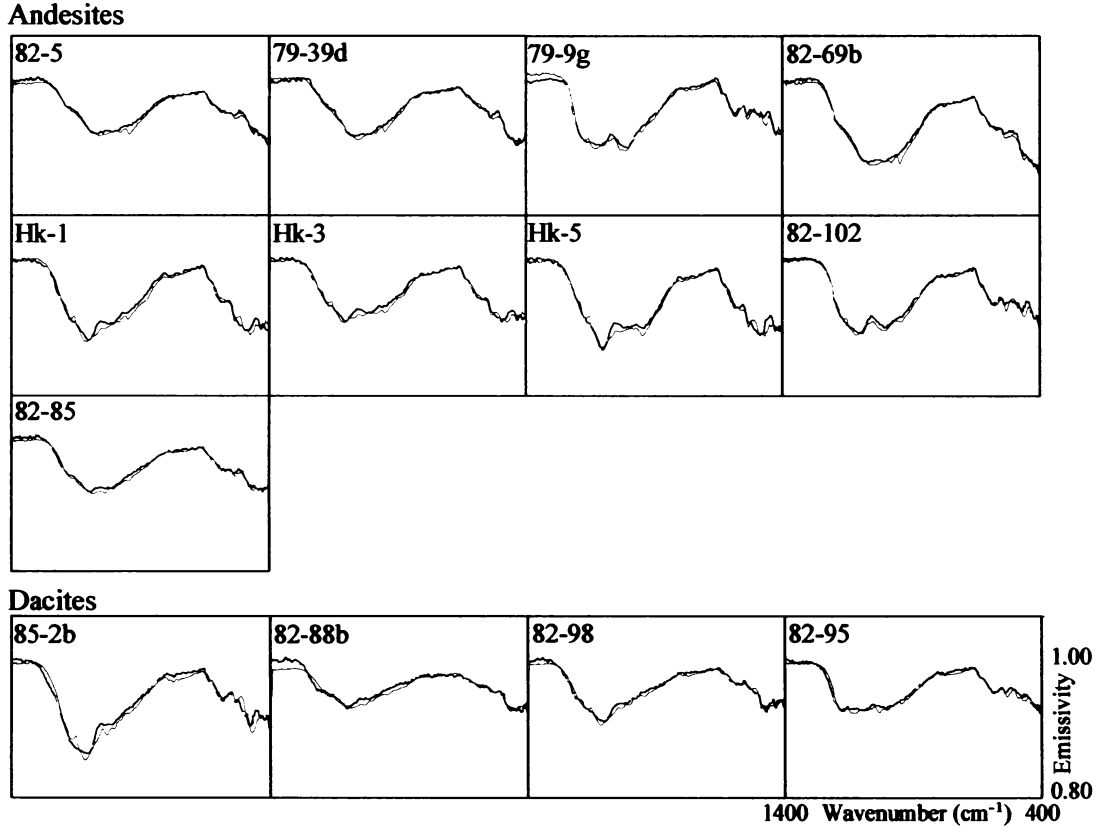


Figure 5. Measured (black) and modeled (red) emissivity spectra of andesite and dacite. Spectral fits produced by the linear deconvolution algorithm are again very good.

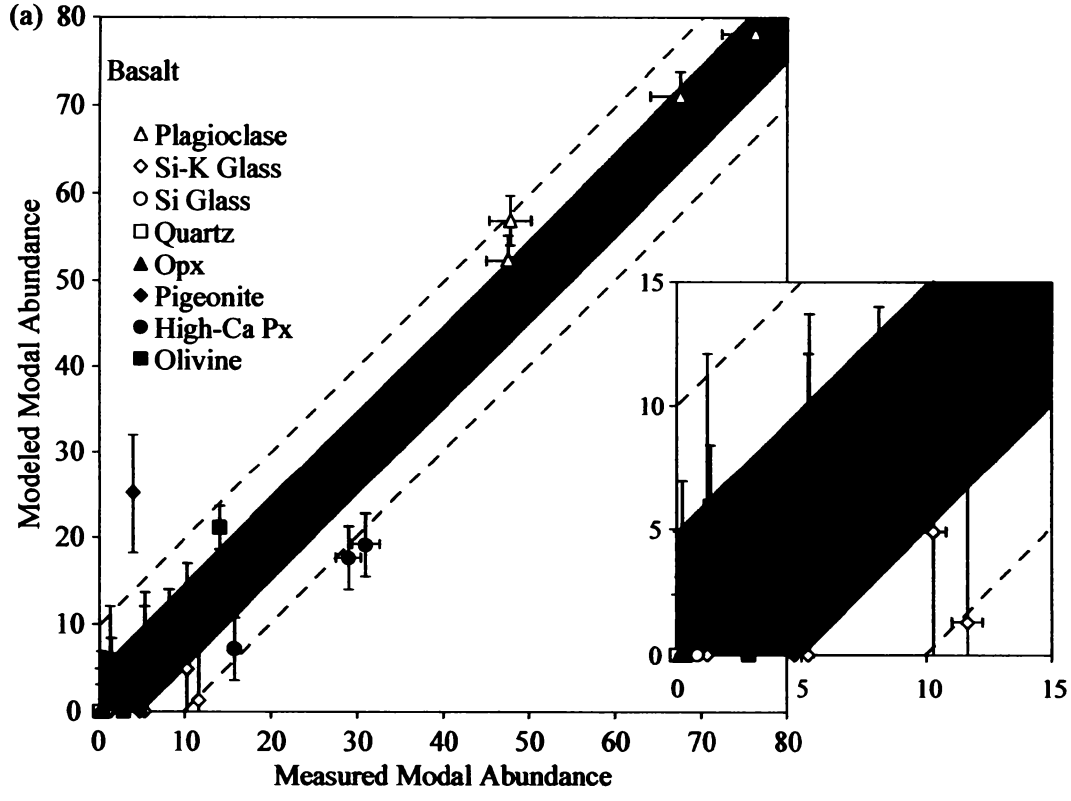


Figure 6. Comparison of electron microprobe (measured) and deconvolved bulk mineralogies for (a) basalt, and (b) andesite/dacite. Smaller boxes are enlargements of lower left corners of larger boxes. Errors for modeled phases are 1σ standard deviations of the absolute differences between modeled and measured mineral phases (Table 7). Error for measured phases are a relative ±5 vol % of the amount measured [*Taylor et al.*, 1996].

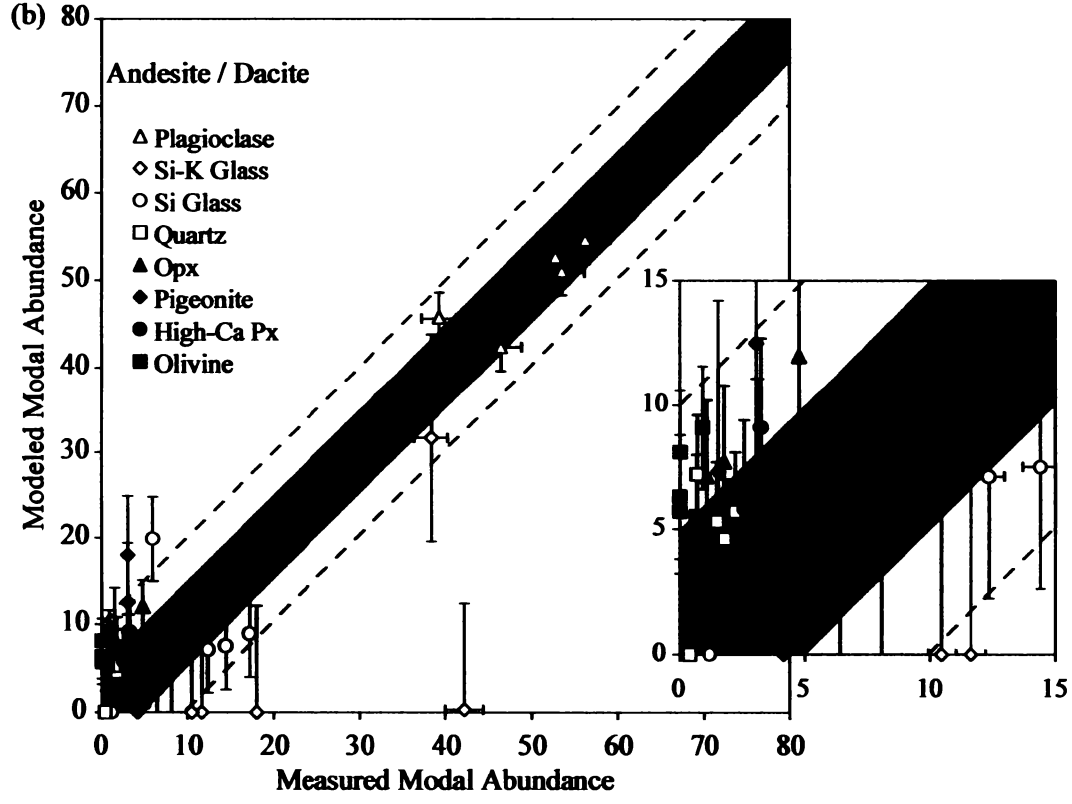


Figure 6 Continued. Comparison of electron microprobe (measured) and deconvolved bulk mineralogies for (a) basalt, and (b) andesite/dacite. Smaller boxes are enlargements of lower left corners of larger boxes. Errors for modeled phases are 1σ standard deviations of the absolute differences between modeled and measured mineral phases (Table 7). Error for measured phases are a relative ±5 vol % of the amount measured [*Taylor et al.*, 1996].

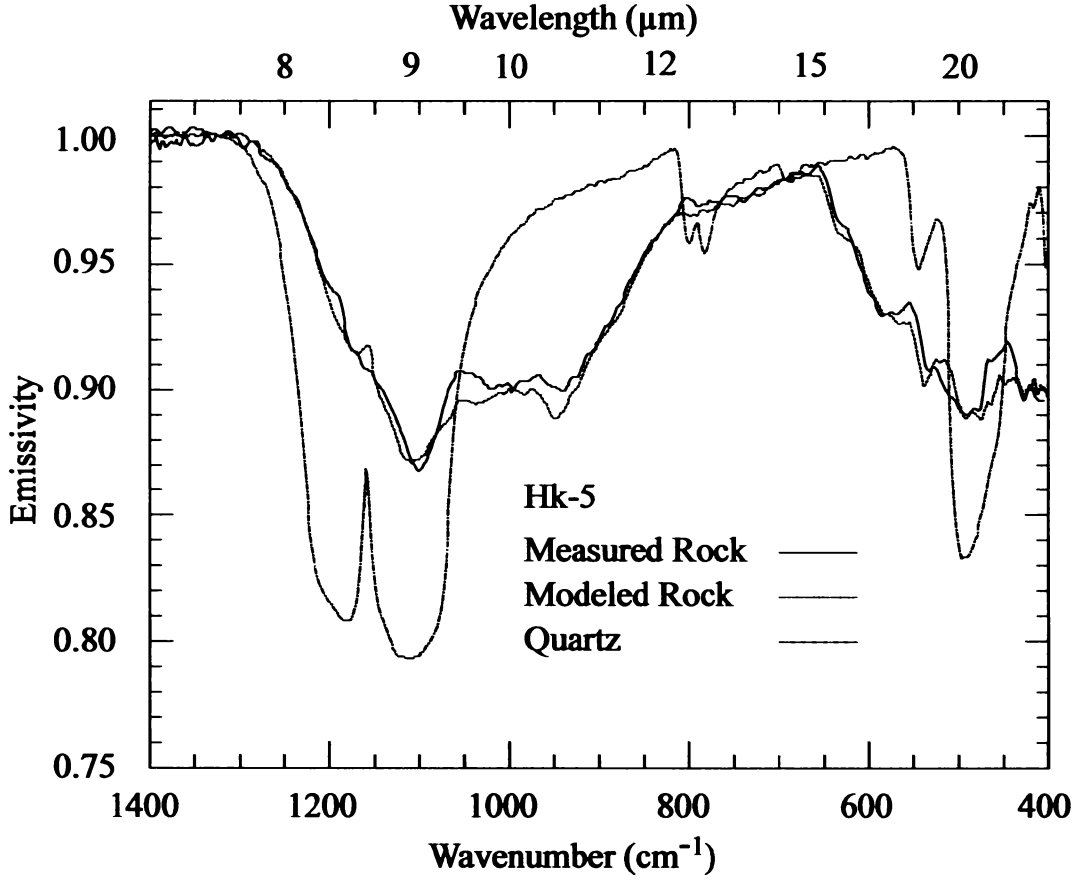


Figure 7. Measured and modeled emissivity spectra of Hakone andesite sample Hk-5 and quartz end-member showing misfit between measured and modeled spectra at 1150 cm^{-1}. The same misfit peak due to overestimated quartz can be seen in the modeled spectra for Hakone andesites Hk-1 and Hk-3 and Cascades samples 82-95, 82-98, 82-102, and 85-2b.

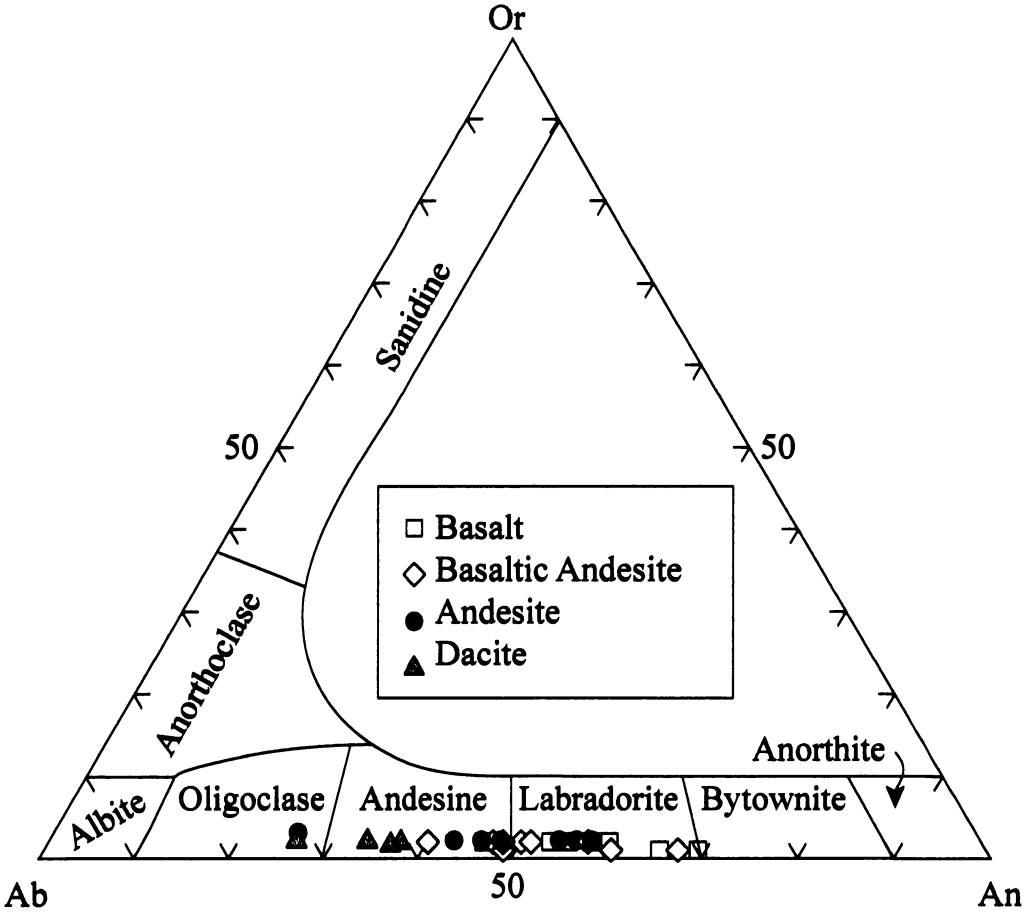


Figure 8. Or-Ab-An ternary diagram showing deconvolved feldspar compositions (mol % An) for basalt, basaltic andesite, andesite, and dacite. Symbols indicate volcanic rock type as determined by measured chemical analyses.

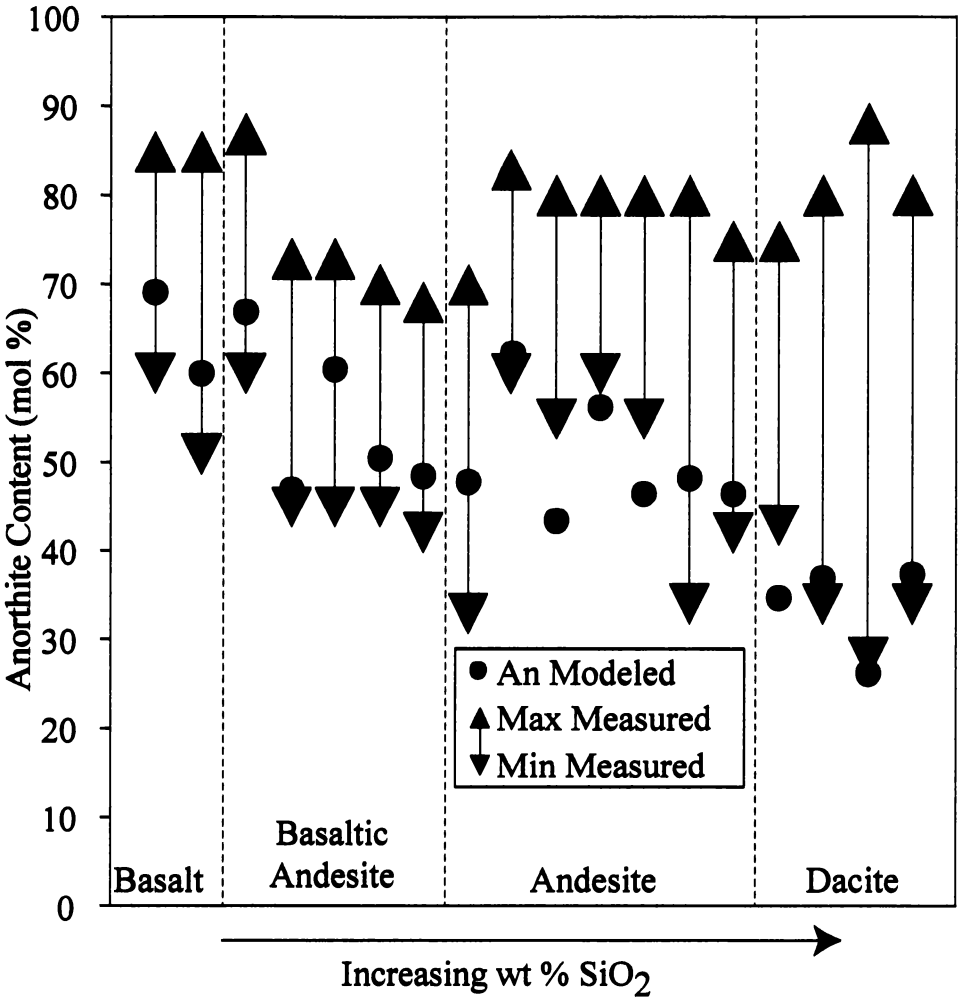


Figure 9. Deconvolved and maximum and minimum measured mol % An values in plagioclase for basalt, basaltic andesite, andesite, and dacite. Deconvolved plagioclase probably reflects the average of total plagioclase chemistry in a rock, in which phenocryst rims and groundmass are volumetrically more abundant than phenocryst cores. Samples shown are basalts, 79-35i and 79-3b; basaltic andesites, 79-24c, 79-38k, 79-38g, 79-37j, and 79-4d; andesites, 79-39d, 79-9g, Hk-1, Hk-3, Hk-5, 82-102, and 82-85; and dacites, 85-2b, 82-88b, 82-98, and 82-95.

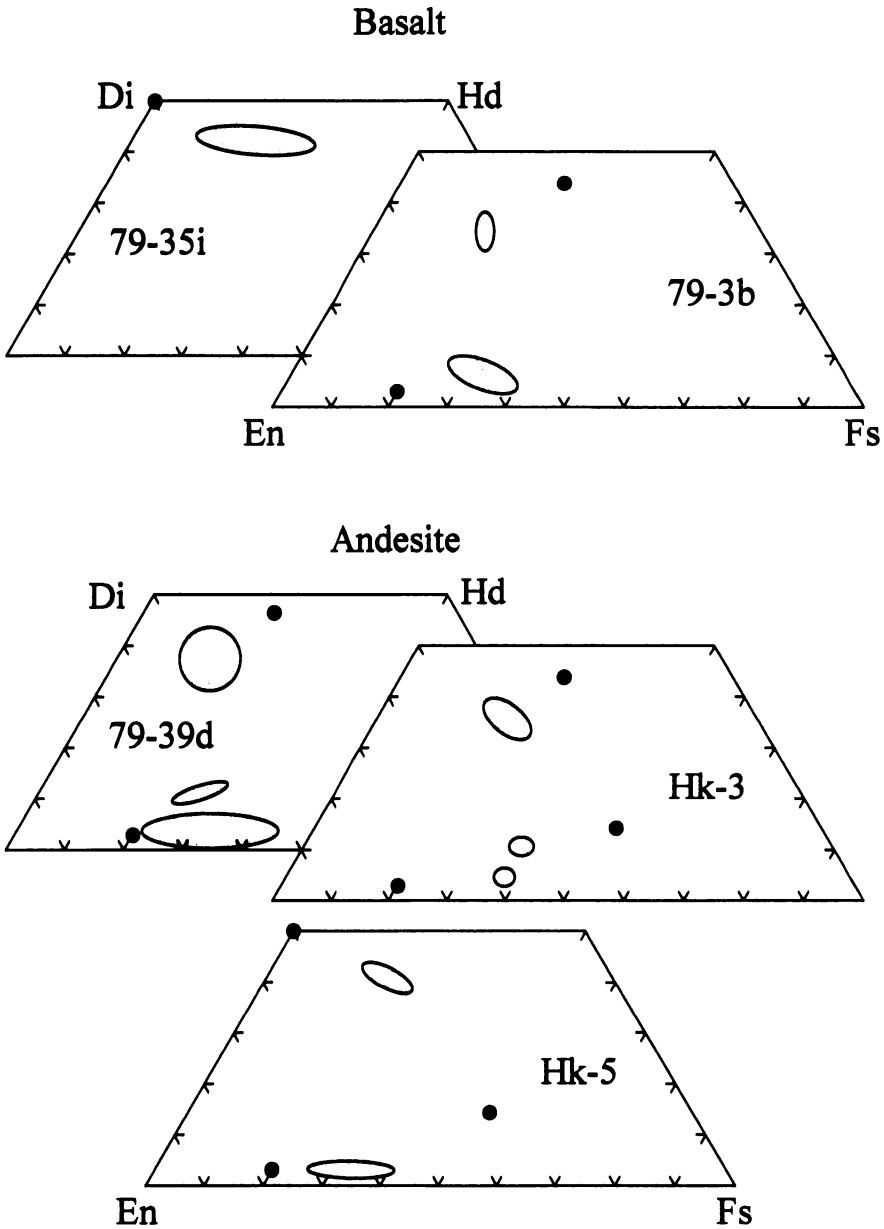


Figure 10. Deconvolved (solid dots) and measured (shaded ovals) pyroxene compositions for basalts (79-35i and 79-3b) and andesites (79-39d, Hk-3, and Hk-5) in the diopside (Di)-enstatite (En)-hedenbergite (Hd)-ferrosilite (Fs) system. For basalts and andesites, when orthopyroxenes and clinopyroxenes are measured, they are also modeled.

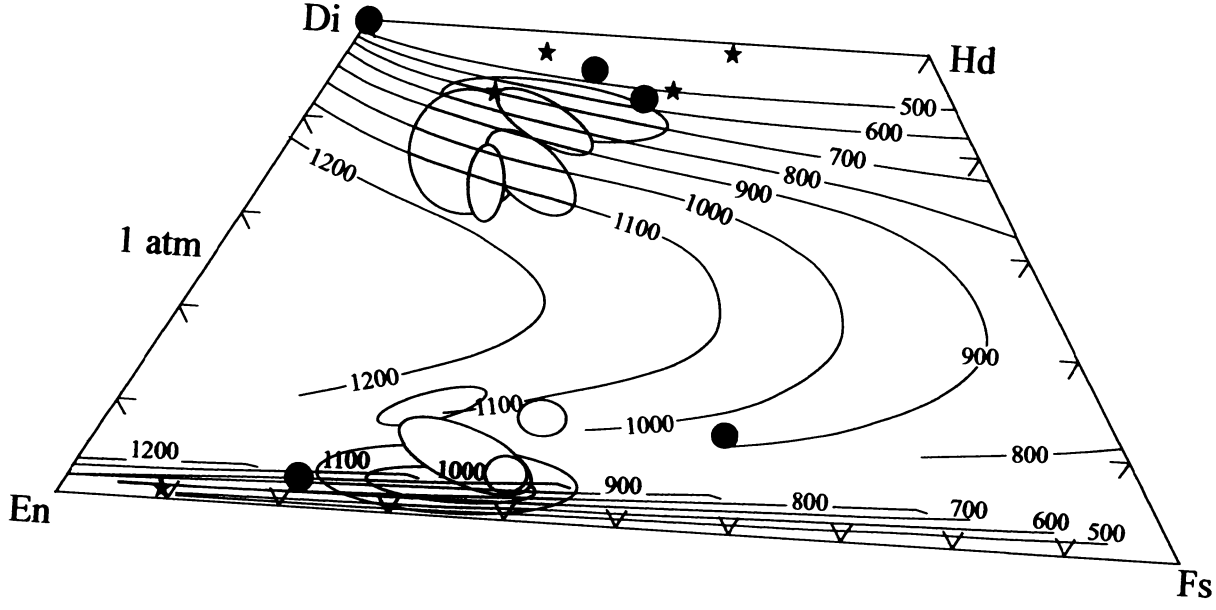


Figure 11. Isotherms for pyroxene compositions in the Di-En-Hd-Fs system at atmospheric pressure [*Lindsley*, 1983]. Deconvolved clinopyroxenes are from plutonic rocks, and they display higher calcic compositions (reflecting lower equilibration temperatures) than measured clinopyroxenes from volcanic rocks.

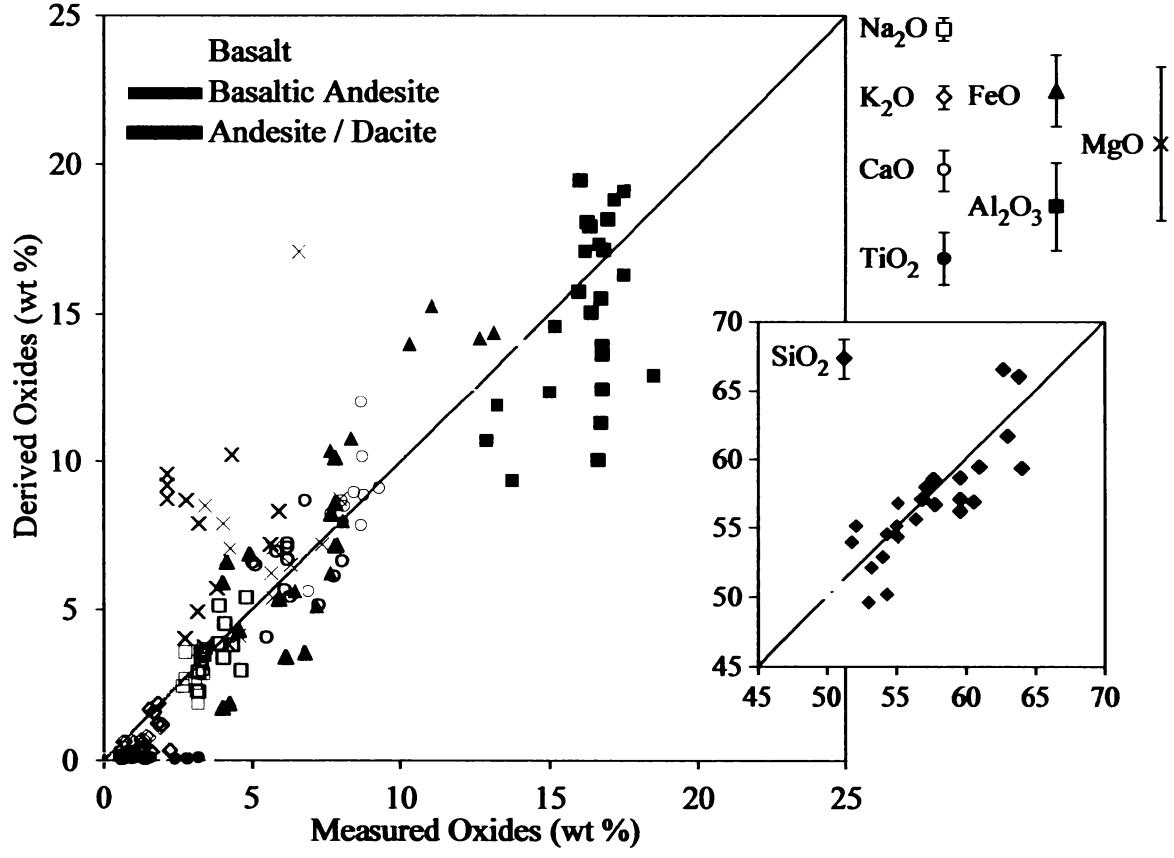


Figure 12. Measured versus derived oxide data (wt %) for all basalt, basaltic andesite, andesite, and dacite rocks. Overall, derived oxide contents exhibit good correlations with measured values. Silica data are shown in the smaller box. Error bars are 1 σ standard deviations of the absolute differences between each derived and measured oxide abundance (Table 7).

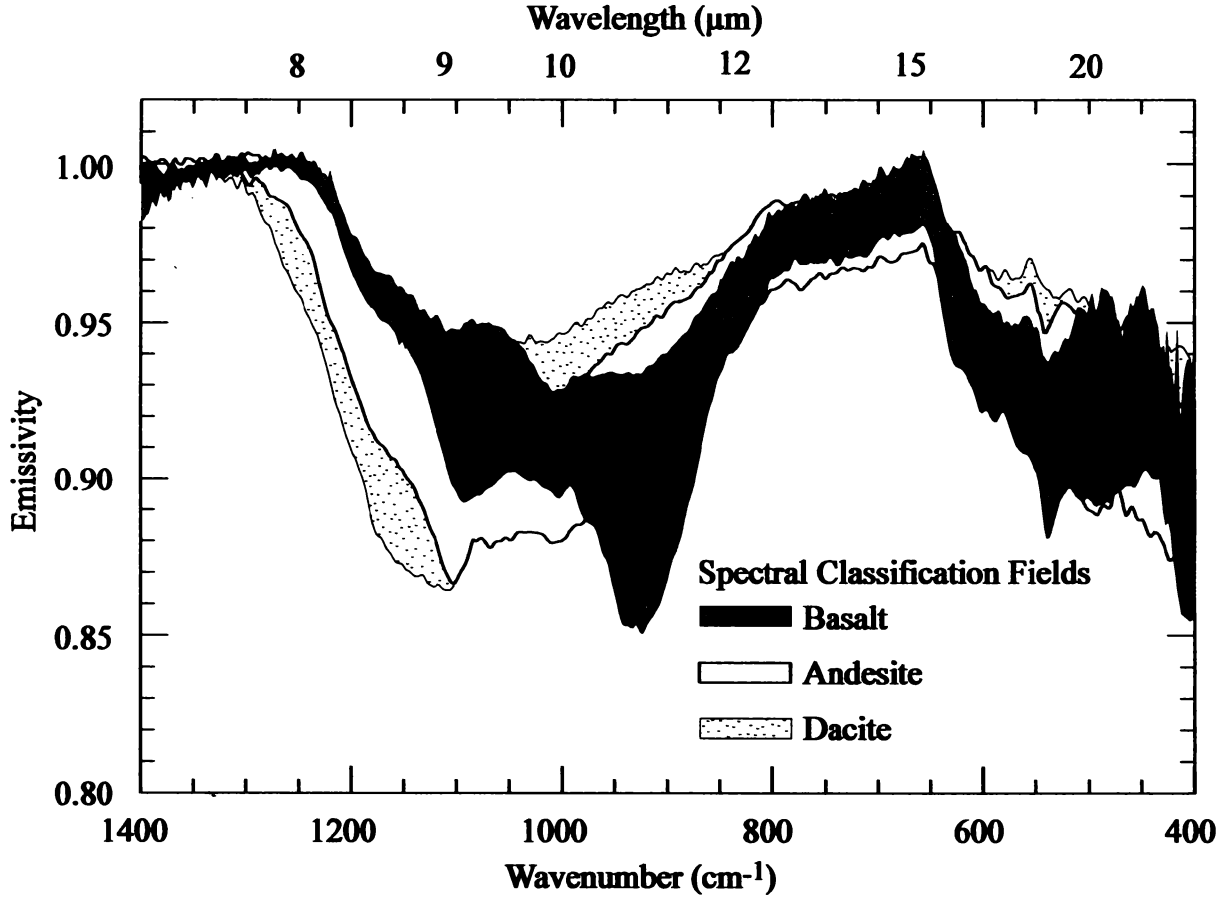


Figure 13. Overlapping but distinct composite spectral fields for basalt (shaded), andesite (open), and dacite (dotted). The spectral fields are not defined by single rock spectra but, instead, by portions of several rock spectra that delineate maximum and minimum spectral ranges.

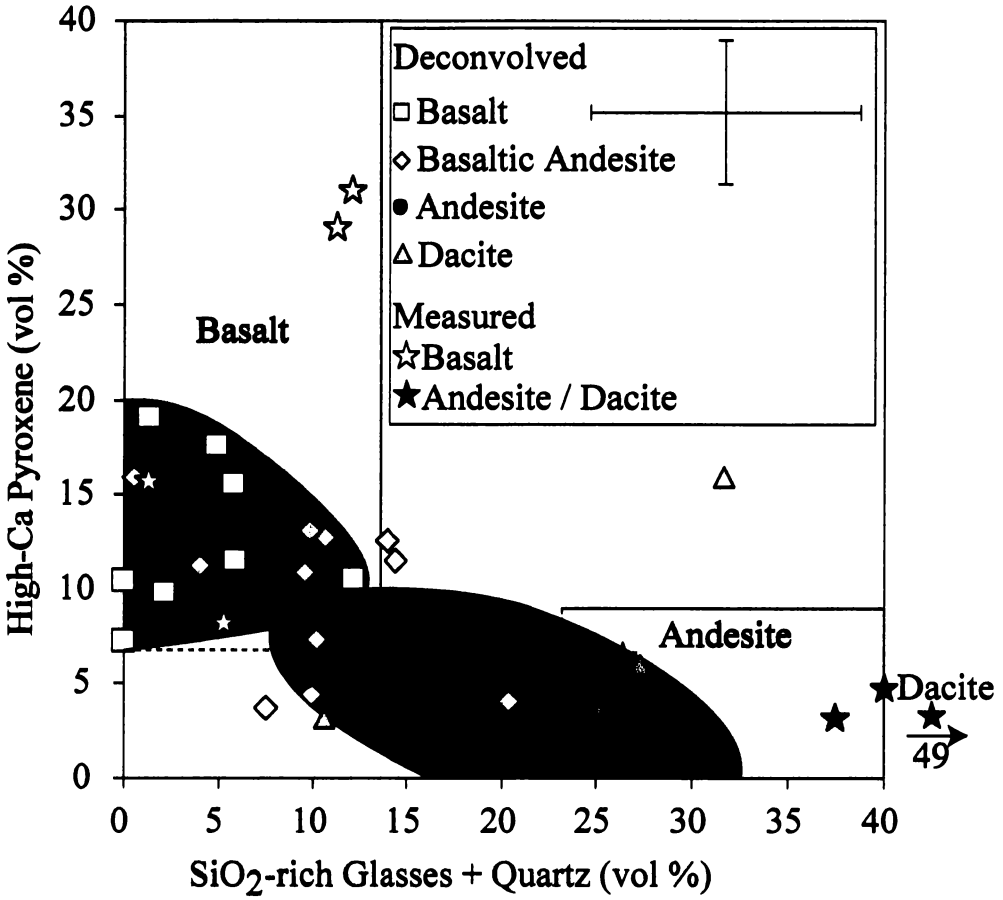


Figure 14. Measured mineralogy classification scheme for distinguishing andesite/dacite from basalt, using SiO_2-rich glasses (silica and silica-K_2O) + quartz versus high-calcium pyroxene (augite + diopside). Deconvolved mineral abundances of basalts and andesites that plot in their respective fields are well classified. Error bars are taken from 1σ standard deviations for modeled mineral abundances listed in Table 7. Differing symbols indicate the chemical classification of each sample based on its measured bulk chemistry.

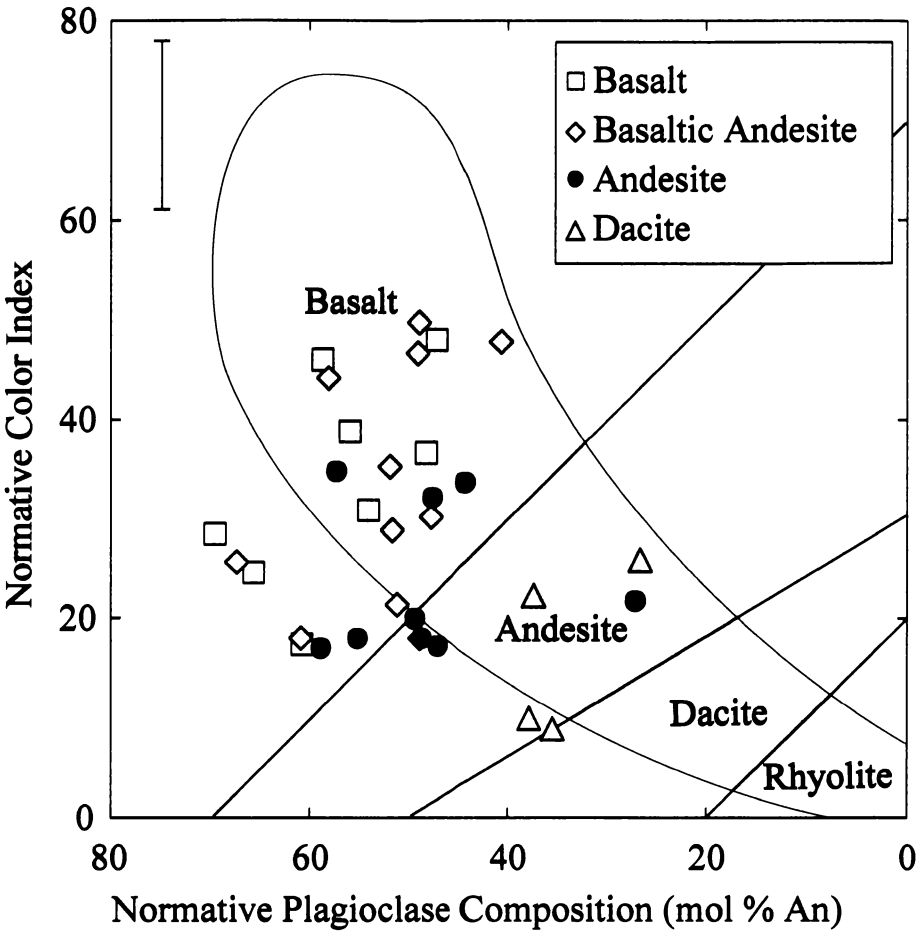


Figure 15. Normative plagioclase composition (mol % An) versus normative color index (modal olivine + orthopyroxene + clinopyroxene) for separating subalkaline volcanic rocks [*Irvine and Baragar*, 1971]. Deconvolved plagioclase compositions and color indexes are plotted. Symbols indicate the measured chemical classification name for each volcanic rock. The shaded field represents typical volcanic compositions. Error bar for normative color index is the 1σ standard deviation of modeled phases from Table 7. No error calculation is possible for normative plagioclase compositions (see text for discussion). Basalts and basaltic andesites consistently plot within the basalt field, but some andesites do as well.

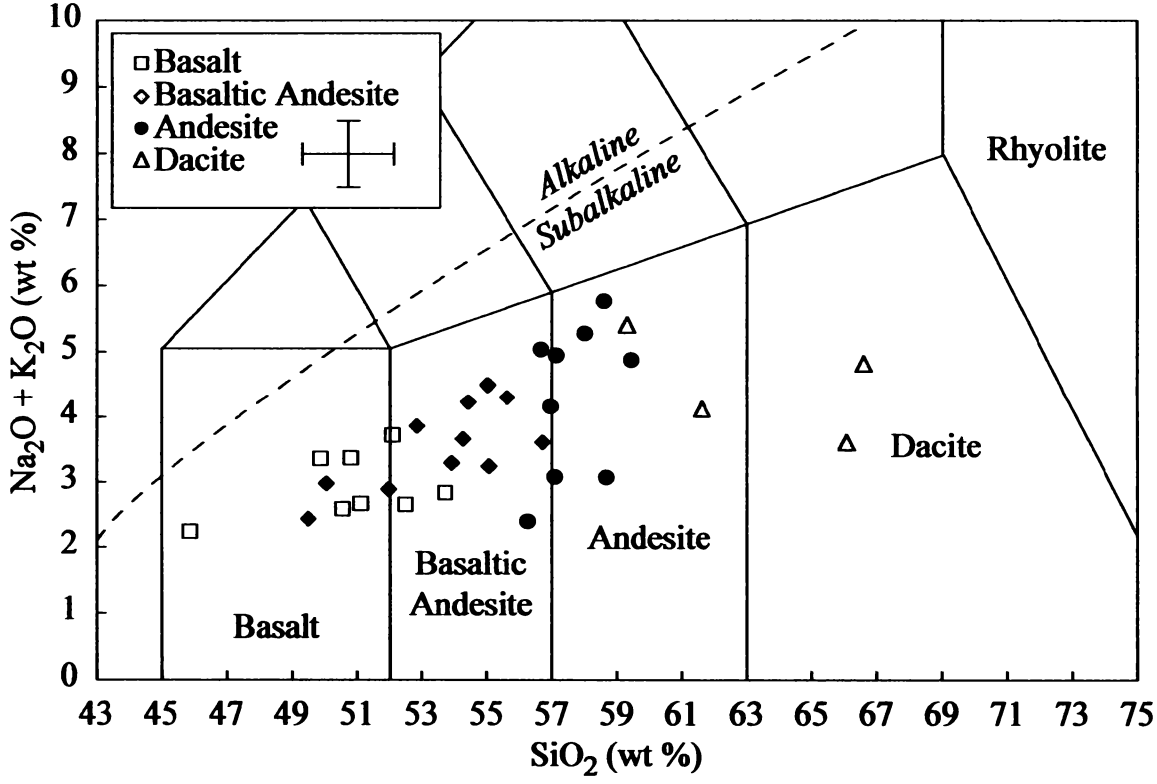


Figure 16. Derived silica versus alkalis superimposed on the chemical classification scheme for volcanic rocks [*Le Bas et al.*, 1986]. Symbols indicate the measured chemical classifi-cation name for each volcanic rock. Error bars are the 1 σ standard deviations for SiO_2 and $Na_2O + K_2O$ from Table 7. All modeled basalts are distinguished from andesite but mixed with basaltic andesite.

Part 2

Analysis of terrestrial and martian volcanic compositions using thermal emission spectroscopy: 2. Application to martian surface spectra from the Mars Global Surveyor Thermal Emission Spectrometer

This chapter is a revised version of a paper by the same name published in the *Journal of Geophysical Research* in 2001 by Victoria E. Hamilton, Michael B. Wyatt, Harry Y. McSween Jr., and Philip R. Christensen:

Hamilton, V.E., Wyatt, M.B., McSween, H.Y. Jr., Christensen, P.R., and Taylor, L.A. Analysis of terrestrial and martian volcanic compositions using thermal emission spectroscopy: 2. Application to martian surface spectra from the Mars Global Surveyor Thermal Emission Spectrometer *JGR 106*, 14,733-14,746 (2001).

Abstract

Atmospherically corrected thermal infrared spectra of large regions of the martian surface from the Mars Global Surveyor Thermal Emission Spectrometer (MGS TES) previously have been interpreted to represent two general spectral classes. One class represents a basalt to basaltic andesite composition, and the other class a basaltic andesite to andesite composition. We have performed new linear deconvolutions of the two martian surface type spectra with an end-member set tailored to represent volcanic rock types. Our preparatory study of laboratory spectra of terrestrial volcanic rocks (acquired at 2 cm^{-1} sampling), convolved to TES spectral sampling (10 cm^{-1}), shows little degradation in deconvolution results when compared to results acquired using the higher spectral resolution data, indicating that the deconvolution technique is valid for analyzing data at TES resolution. Our spectral fits to the martian data agree well with previous models and do not exhibit any notable deviations from the martian spectra that would indicate the absence of any significant end-members in our model. Modal mineralogies

obtained with these new spectral fits also compare favorably (within the previously stated uncertainties) to prior results. The newly derived modal mineralogies are used with new and traditional classification schemes for volcanic igneous rocks (introduced in a companion paper) to classify the martian compositions. Our results substantiate the previously proposed hypothesis that these two spectral classes on the martian surface represent volcanic compositions with distinguishable differences in silica content ranging from basalt to andesite.

1. Introduction

As described in a companion paper [*Wyatt et al.*, 2001] (henceforth referred to as Paper I), modal mineralogies are difficult to obtain for volcanic igneous rocks, which are usually fine-grained. Therefore, volcanic rocks such as basalt and andesite are typically distinguished and named based upon bulk silica and alkali oxide contents [*LeBas et al.*, 1986]. However, although bulk chemistries of rocks are straightforward to acquire when a hand sample is available, they are much more difficult to obtain if the sample of interest can only be measured using remote sensing techniques.

Currently in martian orbit, the Mars Global Surveyor Thermal Emission Spectrometer (MGS TES) is acquiring thermal infrared spectra of Mars for the purpose of mapping surface geology. Because thermal infrared emissivity spectra (including those returned by the TES) are typically interpreted via linear deconvolution [*Hamilton et al.*, 1997; *Ramsey and Christensen*, 1998; *Feely and Christensen*, 1999; *Hamilton and Christensen*, 2000; *Christensen et al.*, 2000*a*; 2000*b*; *Bandfield et al.*, 2000*a*], a technique which provides modal mineralogies rather than chemistries, classification schemes for

volcanic rocks based on mineralogy, or chemistry derived from mineralogy, are necessary. Paper I details the use of a specially-selected end-member set for the linear deconvolution of thermal infrared spectra of 32 terrestrial volcanic samples, examines the accuracy of deconvolved modal mineralogies and chemistries, and discusses the use of the deconvolution results with several traditional and new classification schemes for sample identification. Although no single classification scheme is 100% accurate in classifying all samples, two or more schemes used in concert can be used to classify a rock based on its thermal infrared spectrum [*Wyatt et al.*, 2001].

In this work, we examine the effects of reducing the spectral resolution of the terrestrial rock sample data (to that of the TES instrument) on the modeled spectra, modal mineralogies, and chemistries. We then present new linear deconvolution analyses of the two martian surface type spectra of *Bandfield et al.* [2000*a*] based on the end-member set presented in Paper I. Finally, we discuss the identification and discrimination of the martian spectra based on the new linear deconvolution results, using the classification techniques described by *Wyatt et al.* [2001].

2. Data and Methods

2.1. Laboratory Rock and Mineral Spectra

Thermal infrared (2000 – 400 cm^{-1}, or ~5 – 25 μm) emission spectra of 32 terrestrial volcanic rocks were acquired at 2 cm^{-1} sampling with Arizona State University's (ASU) Mattson Cygnus 100 FTIR interferometric spectrometer [*Ruff et al.*, 1997]. Although the TES instrument covers an additional portion of the spectrum, from 400 – 200 cm^{-1} (25-50 μm), we were unable to cover this region in the laboratory with

the Mattson instrument. At the time the present work was completed, ASU's Thermal Emission Spectroscopy lab had just purchased a new spectrometer that will permit coverage of the full TES wavelength range, and we anticipate using this new spectrometer to update our study. Details of the sample mineralogies and chemistries, and spectral data acquisition and calibration are presented in Paper I [*Wyatt et al.*, 2001]. For this study the terrestrial rock spectra were convolved to the exact 10 cm^{-1} sampling of the TES. Similarly, end-member mineral spectra from the ASU spectral library (also described in Paper I) [*Christensen et al.*, 2000*c*] were convolved to TES resolution prior to their use in linear deconvolution models of the terrestrial and martian spectra.

2.2. TES Martian Surface Spectra

TES spectra of the martian surface shown in this study are the "surface type 1" and "surface type 2" spectra from *Bandfield et al.* [2000*a*] and represent the averages of four to seven regional, low-albedo locations. Detailed descriptions of the methodology used for separating the surface and atmospheric components in TES-measured spectra are provided by *Bandfield et al.* [2000*a*; 2000*b*] and *Smith et al.* [2000]. Although *Bandfield et al.* [2000a] describe the bulk mineralogy of martian dark regions in terms of two primary components, additional local-scale variations on the surface have been identified [e.g., *Christensen et al.*, 2000*b*; *Hoefen et al.*, 2000; *Clark and Hoefen*, 2000; *Christensen et al.*, 2001; *Hamilton et al.*, 2001 that were not identified in the locally averaged spectra, and it is likely that further variations will become apparent as the entire TES dataset is analyzed in detail. Small-scale chemical or spatial variations are not addressed here. As new and revised results are presented, we will examine them in the context of our classification schemes.

TES data used in the derivation of the surface type 1 and 2 spectra were limited to those with warm surface temperatures > 270K, low dust and water-ice opacities (<0.3 and <0.1, respectively), and low albedo (<0.15) to ensure a high surface signal to noise ratio [*Bandfield et al.*, 2000a]. These constraints also help to minimize possible uncertainties such as incomplete atmospheric removal or particle size effects. By limiting these potential sources of error, we focus on the effects that different spectral resolutions (laboratory 2 cm^{-1} and TES 10 cm^{-1}) may have on derived rock compositions.

Initial examinations of the martian surface spectra do in fact show general matches to laboratory spectra of both particulate rock samples and linear mixtures of minerals, with no evidence for unusual particle size or environmental effects [*Christensen et al.*, 2000*a*]. However, martian surface materials analyzed by *Bandfield et al.*, [2000*a*] are thought to be sand-sized particulates [*Christensen et al.*, 2000*a*;], not bedrock, so their spectral contrast will be less than that exhibited by our laboratory rock samples [*Ruff*, 1998; *Hamilton*, 1998; *Hamilton and Christensen,* 2000]. Thus, only for qualitative spectral shape comparison of the martian surface spectra and laboratory spectra (e.g., Figure 4 below), we have contrast enhanced the TES spectra by 40% to simulate solid rock spectra using the procedure of *Ruff*, [1998] and *Hamilton and Christensen*, [2000]. Note that contrast enhancement is a cosmetic change equally affecting the entire spectrum – it does not change the shape of spectral features, and was not applied to the deconvolved TES spectra. These similarities support comparisons of well-constrained martian surface spectra with thermal emission spectra of terrestrial volcanic rocks.

Further support for such comparisons comes from pre-launch and in-flight calibration and instrument-related error studies of the TES instrument. A complete

description of the TES calibration and instrument-related errors is described in *Christensen* [1999] and *Christensen et al.* [2000a]. The absolute accuracy of TES spectra was determined at pre-launch to be ~ 4 x 10^{-8} W cm^{-2} sr^{-1}/cm^{-1} from ~ 300 to 1400 cm^{-1} [*Christensen*, 1999]. For a surface temperature of 280 K, this error corresponds to an absolute temperature error of 0.5 K [*Christensen et al.*, 2000a] and is mapped into a smoothly varying offset in the emissivity spectrum that varies from 0.001 at 400cm^{-1} to a maximum of 0.004 at 920 cm^{-1} to essentially 0 at 1300 cm^{-1} [*Christensen et al.*, 2000a]. This subtle curvature has a negligible effect on the derivation of modeled surface compositions [*Christensen et al.*, 2002]. Systematic errors in radiance can occur due to the calibration process where noise in the space and reference observations maps into the calibrated planet spectra as a function of the instrument temperature and the temperature difference between the scene and the instrument. This noise is reduced by acquiring and averaging three consecutive observations of both space and the reference surface. The instrument temperature has varied from 275 to 290 K over the course of the mission, and the surface temperatures of the spectra used for compositional analyses are >275 K [*Christensen et al.*, 2002]. For this combination of temperatures the resulting systematic calibration error is ~1 x 10^{-8} W cm^{-2} sr^{-1}/cm^{-1} (less than the pre-flight calibration error) between 300 and 1400 cm^{-1} [*Christensen et al.*, 2002].

2.3. Linear Deconvolution

The linear deconvolution technique for emission spectra is fully described by *Ramsey and Christensen* [1998] and its application to the present work is outlined in Paper I (section 3.3). Briefly stated, the spectrum of a rock is a linear combination of the spectra of the mineral-phases composing the rock, in proportion to their abundance

[*Lyon*, 1965; *Christensen et al.*, 1986; *Crown and Pieters*, 1987; *Thomson and Salisbury*, 1993]. A linear deconvolution algorithm uses a library of pure mineral spectra ("end-members") to perform a linear least-squares fit to the spectrum of an unknown mixture, such as a rock [*Ramsey and Christensen*, 1998]. Upon obtaining a fit to the unknown spectrum, the algorithm supplies the user with a model-derived spectrum and the specific end-members used in the fit along with the percentage of the model represented by each end-member. The percentages are based on areal abundances (as measured by the spectrometer) and are thus comparable to percentages obtained by viewing a rock in thin section; therefore, percentages are reported as vol %. The quality of the fit and resultant mineralogy can be judged by the degree of difference between the model-derived spectrum and the unknown spectrum and by the root-mean-square (RMS) error value provided as part of the output of the algorithm [*Ramsey and Christensen*, 1998; *Hamilton et al.*, 1997; *Feely and Christensen*, 1999; *Hamilton and Christensen*, 2000]. However, because RMS error values are valid only for comparing deconvolution runs for a given sample, not the fits of different samples [*Hamilton and Christensen*, 2000; *Christensen et al.*, 2000], we have determined a more robust measure of uncertainty by calculating the standard deviation of the absolute differences between measured and modeled abundances [*Wyatt et al.,* 2001]. Commonly, a blackbody end-member (unit emissivity at all wavelengths) is included in the end-member set to account for differences in spectral contrast between the end-members and the mixture spectrum [*Hamilton et al.*, 1997; *Feely and Christensen*, 1999; *Hamilton and Christensen*, 2000]. The addition of a blackbody end-member does not change spectral shape – it only changes spectral contrast uniformly across a spectrum. Deconvolution results are typically normalized to remove

any blackbody percentage so that mineral phases sum to ~100 vol %; this is how modal abundances are presented in this work. This normalization is only valid if none of the compositional components are completely spectrally featureless in the spectral region used.

2.4. Calculation of Bulk Oxides from Deconvolution Results

Bulk oxides for unknown spectra can be derived by summing the known chemistries of the end-members used in the best-fit model in proportion to their modeled abundance [*Ruff*, 1998; *Hamilton*, 1998; *Hamilton and Christensen*, 2000] The uncertainties associated with modeled bulk oxides derived from 10 cm^{-1} data were determined by calculating the one-sigma standard deviation of the absolute differences between the measured and modeled bulk oxide values [*Wyatt et al.*, 2001]; these are the uncertainties shown on all plots. Oxide values are generally reported to two significant figures but typically have associated uncertainties at the hundredths of a percent level that vary by oxide. Using these known values for each end-member, it is possible to calculate oxides from deconvolution results to two significant figures; however, we are of the opinion that the uncertainties in the original measured values do not support reporting of more than one significant figure. Absolute abundances of different oxides in silicate rocks are widely variable, but in a consistent fashion across all rocks (e.g., SiO_2 is typically ~45 – 75% of a rock whereas Na_2O+K_2O is typically only ~1 – 8%). Therefore, we also report relative uncertainties (i.e., the absolute difference divided by the measured value, multiplied by 100). Relative uncertainties are best used for determining the oxides with the greatest percentage error of the absolute quantity. Uncertainties in the deconvolved modes that might influence calculated oxide abundances are not taken into

account because it is impossible to predict how variation in one or more modes would affect the modeled abundances or compositions of the remaining phases.

3. Deconvolution of Terrestrial Volcanic Compositions at Reduced Spectral Resolution

The Thermal Emission Spectrometer has selectable 5 or 10 cm^{-1} spectral sampling [*Christensen et al.*, 1992]. We resampled our laboratory rock spectra to the 10 cm^{-1} sampling of the TES and redeconvolved them to ascertain whether or not adequate results for rock classification could still be obtained with data acquired at a spectral resolution comparable to that of the lowest resolution TES data. All laboratory spectra shown in this paper are at 10 cm^{-1} sampling, and all model-derived data shown in the figures are from the lower-resolution deconvolution unless otherwise stated. It is important to note that this reduction in spectral sampling does not provide an exact comparison to remotely acquired data in that the signal-to-noise ratio (SNR) of the lab data is higher than that of the TES and no significant atmospheric component needed to be removed; however, instrumental uncertainties [*Christensen et al.*, 2000*a*], sources of error associated with the atmospheric correction techniques [*Smith et al.*, 2000; *Bandfield et al.*, 2000*b*], and the limits of the deconvolution technique [*Ramsey and Christensen*, 1998] are extremely well-known and have been used to apply a ~10-15 vol % uncertainty to the modal mineralogies obtained from TES surface spectra [*Christensen et al.*, 2000*a*; *Bandfield et al.*, 2000*a*].

Modeled spectra, modal mineralogies, and bulk rock chemistries obtained by deconvolution of the 10 cm^{-1} laboratory data show very little change from the results

obtained at higher spectral resolution. Figure 1 shows example plots of several measured and modeled terrestrial basalt, basaltic andesite, andesite, and dacite spectra. These spectra may be compared to the laboratory-resolution measured and modeled spectra of the same rocks in Figures 4 and 5 of Paper I. Virtually no difference in the quality of the model fits is observable in the reduced-resolution data.

Figure 2 compares the deconvolved modal mineralogies of the terrestrial rocks obtained at 2 cm^{-1} and 10 cm^{-1} sampling (modes have been normalized to remove blackbody components ranging from 13 – 74% [*Wyatt et al.*, 2001]). Table 1 shows the microprobe-measured modes and the 2 cm^{-1} and 10 cm^{-1} sampling modeled modes. The uncertainty associated with the 2 cm^{-1} deconvolution results as compared to microprobe-measured modes is discussed in Paper I and is calculated in the same way for the 10 cm^{-1} data (see section 2.3 above). The one-sigma standard deviation for the 10 cm^{-1} data varies by mineral group from 2.3 to 12.2 vol % (Table 2); these are virtually the same values that were calculated for the 2 cm^{-1} data [*Wyatt et al.*, 2001], which demonstrates that convolution to 10 cm^{-1} spectral sampling does not noticeably alter the uncertainty associated with the derived mineralogy. Therefore, as in the case of the 2 cm^{-1} data (see Paper I), the greatest uncertainties in the 10 cm^{-1} data are associated with the silica phases and pigeonite.

Modal abundances obtained from 10 cm^{-1} data commonly differ slightly from those obtained with 2 cm^{-1} data, but generally not by more than 5 vol % (absolute). A few outliers are present (Figure 2), most notably three points that represent five cases in which pigeonite or clinopyroxene phases that were identified in 2 cm^{-1} data were not identified in the 10 cm^{-1} data. For two of these points, the abundance of pigeonite

determined from data acquired at 2 cm^{-1} sampling was less than 10 vol %, which is at or below the detectability limits usually associated with data acquired at 10 cm^{-1} data [*Bandfield et al.*, 2000*a*; *Hamilton and Christensen*, 2000]. One of the rock samples has deconvolved mineralogies at both 2 and 10 cm^{-1} sampling that include significant amounts of weathering products; this sample simply may not be modeled very accurately in either case as only a few weathering products were included in the end-member set. Finally, in the last two cases, pigeonite was not detected in the 10 cm^{-1} data at ~12 vol % (2 cm^{-1} data), but the clinopyroxene content was higher in the 10 cm^{-1} data, suggesting that the spectrum was still best modeled with a calcium-bearing pyroxene. Despite these few outlier points, the similarity in the 2 cm^{-1} and 10 cm^{-1} results indicates that the degradation of spectral resolution does not significantly alter the derived mineralogies. Therefore, we expect that the chemistries derived from both datasets also will be similar.

In fact, chemistries derived from the 10 cm^{-1} spectra are very similar to those derived using the 2 cm^{-1} data. Table 2 shows the uncertainties in the 10 cm^{-1} data compared to the same values for the 2 cm^{-1} data. As an example of the consistency of our results, we have plotted the SiO_2 contents derived from the 2 cm^{-1} and 10 cm^{-1} laboratory samples against the rocks' known SiO_2 abundances in Figure 3. The minimum and maximum absolute difference between 2 and 10 cm^{-1} modeled values are 0.1 and 2.3 wt %, respectively, with an average of only 0.5 wt %. Although bulk SiO_2 content is the most highly derived (model-dependent) measure of composition in our studies, it is also one of the most accurate in terms of classifying the rocks [*Wyatt et al.*, 2001]. Therefore, it is a good measure of the similarity and accuracy of the high- and low resolution model results. As in the case of the 2 cm^{-1} data, the worst relative errors are observed for TiO_2

(95%) and MgO (85%) (Table 2); however, neither of these oxides is used in any of our classification schemes.

In summary, degradation of the laboratory rock spectra to the spectral sampling of the TES instrument does not significantly alter the mineralogies and chemistries derived by linear deconvolution of the spectra. This result demonstrates that the traditional and new classification schemes of *Wyatt et al.* [2001] are valid for the interpretation of TES-resolution data. The following discussion examines new deconvolution results for the TES martian surface spectra in the context of the classification schemes discussed in Paper I.

4. Martian Surface Compositions

Christensen et al. [2000*a*] identified a basaltic surface component in Cimmeria Terra and *Bandfield et al.* [2000*a*] identified two primary martian lithologies on a global scale, one basaltic to basaltic andesite (surface type 1), and another resembling basaltic andesite to andesite (surface type 2). The two martian surface compositions are split in their distribution roughly along the planetary dichotomy that separates the ancient, heavily cratered crust in the south from younger plains in the north [*Bandfield et al.*, 2000*a*].

Because the results of *Christensen et al.* [2000*a*] and *Bandfield et al.* [2000*a*] were based on deconvolutions that used different sets of mineral end-member spectra than those used in this study, and may not be directly comparable, we have deconvolve the surface spectra obtained by *Bandfield et al.* [2000*a*] with the end-member set presented in Paper I. The results we obtain differ slightly from those obtained with other

end-member sets; however, this approach allows us to make the most consistent comparison to the terrestrial data provided in Paper I. Furthermore, we will be able to provide an example of the minor variability that can be expected in deconvolution results in cases in which different end-member sets are used to deconvolve the same unknown spectrum.

It is important to note that the deconvolved mineralogies reported by *Christensen et al.* [2000*a*], *Bandfield et al.* [2000*a*], and the derived mineralogies and chemistries presented here are based on preliminary derivations of martian surface spectra, which are themselves regional averages and may not represent local variability of the martian surface. Detailed analysis of martian surface spectra and deconvolved mineralogies and derived chemistries using different spectral end-member sets is ongoing.

4.1. Spectral Classification

Figure 4 shows the overlapping composite spectral fields for distinguishing basalt and andesite, as described in Paper I, defined by terrestrial rock spectra at 10 cm^{-1} sampling. The spectral field shapes are nearly identical to those obtained with the 2 cm^{-1} data (see Figure 13 of Paper I); there is slightly less detail in small spectral curves and peak shapes, but the overall spectral shapes are not noticeably different. Also included in Figure 4 are the martian surface spectra derived by *Bandfield et al.* [2000*a*]. The surface type 1 spectrum lies within the field defined by terrestrial basalts (the small deviation near 1250 cm^{-1} is due to a residual atmospheric CO_2 isotope band). The surface type 2 spectrum plots within or very near the terrestrial andesite field; locations where spectrum plots outside the andesite field fall within the field if the standard deviation of the surface type 2 spectrum is considered [*Bandfield et al.*, 2000*a*].

Christensen et al. [2000*a*] and *Bandfield et al.* [2000*a*] based the initial assessments of their spectra on comparisons to the shapes of two of our samples, WAR-R1049 (basalt) and 79-39d (andesite, see *Hamilton and Christensen* [2000] and *Wyatt et al.* [2001] for details regarding these samples). The similarities between the martian spectra and the lab sample spectra were cited as supporting the two differing compositions reported by *Bandfield et al.* [2000*a*].

4.2. Deconvolution of Martian Surface Mineralogies

Bandfield et al. [2000*a*] obtained modal mineralogies for their martian surface spectra using a library of mineral end-members that represented a wide variety of phases. This wide variety minimized the chances that any major phases would be missed in the first deconvolution of these martian spectra. The resulting model fit indicated that the martian surface spectra were representative of volcanic igneous rocks, composed primarily of feldspars, pyroxenes, and glasses, with additional evidence for some sheet silicates. To apply our classification schemes to martian data, we have performed a new deconvolution of the martian surface spectra using our end-member set, which is tailored to the deconvolution of subalkaline volcanic compositions [*Wyatt et al.*, 2001]. This end-member set includes an expanded range of feldspars, pyroxenes, and glasses compared to *Bandfield et al.*, [2000a]. For consistency with previous work [*Bandfield et al.*, 2000*a*; *Christensen et al.*, 2000*a*], our model fits were performed over the spectral region from ~1280 – 400 cm^{-1}, and the region dominated by atmospheric CO_2 absorption (~825 – 507 cm^{-1}) was excluded. The results presented here for the martian data should be viewed with additional sources of uncertainty in mind, such as those associated with atmospheric removal, that we cannot quantify with our laboratory data.

4.2.1. Modeled spectra

The martian surface spectra and our modeled spectra are compared in Figure 5. The model fits are very good, with RMS values comparable (0.002) to those obtained by *Bandfield et al.* [2000*a*]. Our model spectra do not follow the martian surface spectra quite as closely as the Bandfield et al. models due to the fact that the Bandfield et al. fits used a greater number of end-members, with several end-members at very small abundances. These low-abundance end-members commonly are included in the fit because they can minimize slight and/or local variations between the model and the measured spectrum [*Feely and Christensen*, 1999; *Hamilton and Christensen*, 2000]. However, there are no major deviations from the measured spectrum in our modeled spectrum that would indicate any significant components are inaccurately modeled.

4.2.2. Modal Mineralogy

Modes obtained for the two martian spectra are shown in Table 3, along with the results of *Christensen et al.* [2000*a*] (Cimmeria Terra) and *Bandfield et al.* [2000*a*] for comparison (modes have been normalized to remove blackbody components of 47 vol % [*Christensen et al.*, [2000*a*], and 41/57 vol % [this work]; blackbody percentages were not provided in *Bandfield et al.* [2000*a*]). Our results agree very well with the results of *Bandfield et al.* [2000*a*], typically well within the 10-15 vol % uncertainties of their model. Thus, our results also suggest that these two surface spectra represent compositions with distinctly differing mineralogies. The most significant deviation between the two models is in the deconvolved feldspar mode for the more andesitic (surface type 2) martian surface spectrum – we estimate ~15 vol % more feldspar than was estimated in the previous study (which is still within the uncertainty of *Bandfield et*

al., [2000*a*]). One possible explanation for this difference is that Bandfield et al. emphasize the abundances of major modes, which only sum to 85 vol %. The remaining modes are not discussed as they consist of end-members fit to the martian spectrum at less than ~5 vol % and are not believed to be dependable individually because they are at or below the detection limits of the linear deconvolution technique [*Ramsey and Christensen*, 1998; *Feely and Christensen*, 1999; *Hamilton and Christensen*, 2000]. It is therefore probable that the difference in the modeled feldspar modes between these two studies is due to the difference in the end-member sets used. Due to the reduced number of non-igneous phases in our end-member set (e.g. clays, oxides, etc.), our model fits cannot include a variety minor end-members at low abundances in the same way that the end-member set used by Bandfield et al. did. As a result, the remaining (major) phases will show some reorganization and differences in the absolute abundance of each mineral group.

Although the deconvolution results of *Christensen et al.* [2000*a*] are for a spectrum representing only Cimmeria Terra (not shown here), we show their deconvolution results in Table 3 for general comparison with the results of *Bandfield et al.* [2000*a*] and this work. (Spectra from Cimmeria Terra are included in the surface type 1 of *Bandfield et al.* [2000*a*].) The results of our deconvolution of the basaltic (surface type 1) martian spectrum lie within 5 – 10 vol % of the modes obtained by *Christensen et al.* [2000*a*] for the Cimmeria Terra spectrum, which is broadly similar, although not identical, in shape to the *Bandfield et al.* [2000*a*] surface type 1 spectrum. Therefore, the results of all three studies are similar, regardless of the end-member set used and the number of end-members available.

Figure 6 shows the martian data points on the mineralogy classification diagram from Paper I along with the measured and derived terrestrial volcanic rock mineralogies. The modes obtained from terrestrial data convolved to 10 cm^{-1} sampling show no significant variations from data derived at 2 cm^{-1} sampling (compare to Paper I, Figure 14). Slight differences are observed in the positions of some samples, but not to the extent that any rocks are reclassified; similarly self-consistent results were obtained by *Feely and Christensen* [1999] and *Hamilton and Christensen* [2000] in their examinations of reduced-resolution deconvolution results. Mineral abundances derived from our models of the martian surface spectra fall in the basalt and andesite fields, and are consistent with the classifications based on the spectral fields in Figure 4. Even though the deconvolutions of martian data presented by *Christensen et al.* [2000*a*] and *Bandfield et al.* [2000*a*] were performed with different end-member sets, their modal results also fall in these fields (within their uncertainties), resulting in the same classifications. These results give additional support to the basalt-basaltic andesite and basaltic andesite-andesite martian surface compositions described by *Bandfield et al.* [2000*a*], as well as to applying terrestrial volcanic classification schemes from deconvolved mineralogies for distinguishing martian surface compositions.

Our modal mineralogy (and bulk chemistry) classifications assume that glass phases identified in the deconvolution are primary volcanic phases (as they are known to be in the terrestrial samples). Based on currently available information (including the lack of significant quantities of weathering products), by Occam's Razor, our interpretation is the simplest explanation of glass formation that explains the observations. If similar glasses can be demonstrated to form by secondary processes,

such as oxidation [e.g., *Minitti et al.*, 2000] or acid-sulfate weathering [e.g., *Morris et al.*, 2000], and identical spectra and derived mineralogies can be obtained from samples affected by these conditions, new criteria for classifying glass-bearing surface types may be necessary.

4.3. Normative Plagioclase Composition versus Color Index

Hamilton and Christensen [2000] and *Wyatt et al.* [2001] have demonstrated that approximate solid solution compositions for plagioclase feldspar and pyroxenes may be obtained from linear deconvolution results by taking the weighted average composition of the feldspar or pyroxene end-members used in the best fit model. The underlying assumption is that there is no single end-member spectrum that best represents the spectral character of the feldspar or pyroxene phase in the mixture spectrum; the use of several end-members within a solid solution series thus approximates the spectral signature of an intermediate composition not available in the end-member set or represents zonation in the phase [*Hamilton et al.*, 1997; *Hamilton and Christensen*, 2000]. Results are typically accurate to within 10 – 15 Mg# or An# for mafic and ultramafic samples [*Hamilton and Christensen*, 2000] and are demonstrated to generally lie within or near the minimum and/or maximum (core and rim) microprobe-measured compositions for the mafic to silicic volcanic rocks in Paper I. Figure 7 shows a comparison of the average feldspar An# determined from the datasets at 2 and 10 cm^{-1} sampling, and the values are shown in Table 4; the derived compositions at both resolutions are very similar, typically within 0 – 5 An#. In the few cases that are different by more than 5 An#, the deconvolved values are nearly always within the core and rim values measured by electron microprobe (Table 4). Uncertainties associated with

the modeled An# cannot be calculated as the volumetric average composition is not known, only the minimum and maximum An#.

Below we present the classification of our terrestrial samples and the two martian spectra based on normative plagioclase composition (100*An/(An+Ab)) versus color index (modal olivine + orthopyroxene + clinopyroxene) [*Irvine and Baragar*, 1971]. Ongoing work by *Hamilton et al.* [2000] examines the solid solution compositions of feldspar and pyroxene derived from deconvolution of martian data as a function of the end-member set utilized and provides some indication of the variability possible in the derived average composition.

Figure 8 shows normative color index versus the deconvolved normative plagioclase compositions from the martian surface spectra and the terrestrial volcanic rocks (at 10 cm^{-1} sampling) of Paper I. The uncertainty associated with normative color index was calculated in the same manner as the uncertainties in Table 2, using the sum of the mafic phases. Uncertainties for derived normative plagioclase composition cannot be calculated because we know only the range of An values, not the average compositions. As discussed in Paper I, this classification scheme is somewhat ambiguous for the terrestrial rocks in that andesites are not always accurately classified (basaltic andesites are not distinguished in this scheme), but basalts are usually correctly classified. In the case of the martian data, the two data points are plainly distinguishable, with the martian surface type 1 spectrum plotting in the shaded basalt field, and the surface type 2 spectrum plotting in the unshaded portion of the basalt field. Surface type 2 is not clearly classified using this scheme, however, this is not unexpected based on the results obtained with terrestrial samples.

4.4. Derived Bulk Chemistries of the Martian Surface

Modal mineralogies obtained from linear deconvolution of midinfrared spectra can be converted to bulk chemistries by combining the chemistries of the spectral library end-members used in the best fit in proportion to their modeled abundances [*Hamilton*, 1998; *Ruff*, 1998; *Hamilton and Christensen*, 2000; *Wyatt et al.*, 2001]. The model-derived bulk SiO_2 and alkalis (Na_2O+K_2O) then can be plotted on the classification diagram of *Le Bas et al.* [1986] to classify unknown samples. It is important to note, however, that model-derived chemistries are not directly representative of the chemistries of the unknown spectra; they are dependent on and represent the composition of a comparable sample composed of the exact minerals contained in the end-member set and are thus subject to slight variability as a function of the end-members selected.

Figure 9 shows model-derived silica versus alkalis for the 32 terrestrial volcanic rocks of Paper I plotted on the chemical classification scheme for volcanic rocks [*Le Bas*, 1986] with our model-derived silica and alkali contents of the martian surface spectra. Chemistries obtained from the modes derived in the present work place the *Bandfield et al.* [2000*a*] surface type 1 in the basaltic andesite category and surface type 2 in the andesite category. These results are consistent with the results of *Bandfield et al.* [2000*a*].

4.5. Summary of classifications

The results of the four classification schemes are summarized in Table 5. Martian surface type 1 is classified as a basalt in three out of four cases, and surface type 2 is classified as an andesite in three out of four cases. This degree of consistency among the classification schemes is comparable to that obtained with terrestrial samples [*Wyatt et*

al., 2001]. These assignments agree very well with the compositional determinations of *Bandfield et al.* [2000*a*] and *Christensen et al.* [2000*a*] for surface types 1 and 2 and Cimmeria Terra.

The impact of significant abundances of weathering and alteration products is not addressed by this study, so further work (Part 3) is planned to investigate the impact of surface and intimate weathering and alteration phases on the determination of bulk mineralogy, chemistry, and classification. Also, the addition of data in the 400 – 200 cm^{-1} (25 - 50 μm) region will allow for a more accurate analogy to TES data and potentially will provide even better results.

5. Comparison to Martian Meteorite Compositions and Previous Results

The TES-based mineralogical results presented here and elsewhere [*Bandfield et al.*, 2000*a*; *Christensen et al.*, 2000*a*] indicate that the majority of martian dark regions are broadly characterized by surface materials that are basaltic and andesitic in character. These results do not attempt to address local scale variations in composition and thus do not preclude the existence of such variations. These spectra do not match known martian meteorite spectra, are consistent with some interpretations of previously acquired data from various instruments, and are inconsistent with other previous interpretations. When considering such comparisons, it is also important to remember that different techniques are sensitive to different characteristics of the martian surface and do not provide the same types of mineralogical information; thus, some discrepancies are likely, and are not necessarily problematic.

5.1. Comparison to Martian meteorite compositions

Martian (or SNC) meteorites represent lithologies ranging from basalt or lherzolite (shergottites) to clinopyroxenite (nakhlites), orthopyroxenite (ALH84001), and dunite (Chassigny). Meteorites from and within each class have clearly distinguishable thermal infrared emission spectra [*Hamilton et al.*, 1997; *V. E. Hamilton,* unpublished data]. The two primary surface spectral types measured by TES are not similar in shape to emission spectra of any of the martian meteorites [*Bandfield et al.*, 2000*a*; *Christensen et al.*, 2000*a*] and the mineralogies derived from the TES spectra are not very similar to those of the martian meteorites [*Hamilton et al.*, 2002] (summarized by *Meyer* [1998] and numerous references therein), despite the fact that surface type 1 is basaltic (as are most shergottites). We believe that this result is entirely consistent with what is known about martian meteorites, as there are several reasons why the meteorites and their spectra should not necessarily be observed in wide distribution on the surface of Mars. First, the plutonic/cumulate nature of many of the meteorites suggests that their source regions may be at some modest depth below the surface and may not be visible at the uppermost surface, regardless of location and dust cover (see below). Second, clustering of cosmic ray exposure data suggest that a small number of craters may be responsible for all 14 martian meteorites. The nakhlites and Chassigny share one ejection age, and the shergottites may exhibit two to three (and possibly as few as one) ejection ages on an area representing only ~15% of the martian volcanic surface area [*Nyquist et al.*, 1998 and references therein; *Treiman*, 1995]. Therefore, all of the martian meteorites may represent as few as three ejection events (ALH84001, the nakhlites and Chassigny, and then the shergottites) if the shergottites were all ejected simultaneously [*Nyquist et al.*,

1998]. Furthermore, the likelihood of these ejection sites being clearly visible at large areal scales is decreasing as dynamical considerations of cratering events are revised. Work by *Gladman* [1997] and *Head and Melosh* [2000] has reduced the minimum crater diameter of the martian meteorite parent craters to 3 km, which is coincident with the approximate spatial resolution of the TES instrument, and below the resolution of most previous orbital instruments and telescopes (none of which have conclusively identified martian meteorites or their source regions on Mars). Based on the above reasons, it is not clear how representative of the uppermost martian surface these meteorites really are, and we probably should not assume or expect that they are ubiquitous on the surface of the planet.

The TES experiment has clearly and convincingly demonstrated its ability to measure silicate and oxide minerals on the surface of Mars [*Bandfield et al.*, 2000*a*; *Christensen et al.*, 2000*a*; 2000*b*]. Because the spectra of the meteorites do not match the regional average spectra of the martian surface [*Bandfield et al.*, 2000*a*; *Christensen et al.*, 2000*a*], it is reasonable to conclude that if martian meteorite lithologies are presently exposed at the surface, they may be either limited in their areal extent or could be covered by dust. This conclusion differs from those of some previous studies [*Singer and McSween*, 1993; *Mustard et al.*, 1997] that suggested basaltic shergottites might be common on the martian surface, based on visible and near-infrared (VNIR) spectra. Martian meteorites (with the exception of ALH84001) represent relatively young rocks. Geologic mapping suggests that most of the youngest rocks on Mars are in the Tharsis region [*Scott and Tanaka*, 1986]; visible images, radar, and thermal inertia data clearly demonstrate that Tharsis is among the dustiest regions on the planet as summarized by

Simpson et al. [1992] and *Christensen and Moore* [1992]. If the meteorites' parent craters and/or units are located in Tharsis, they are quite probably covered by a thick mantle of dust that will be impenetrable to most remote sensing instruments. In fact, many bedrock units on the surface of Mars, including the source units of the martian meteorites, may be covered by areally extensive layers of subsequently deposited materials (e.g., dust, duricrust, or basaltic and andesitic sands) that prevent identification of bedrock lithologies. Despite all of these reasons that may help to explain why the martian meteorites' source regions have not yet been located, TES data are still being searched for the locations of the parent regions, and local variability may provide clues to the source regions of these meteorites [e.g., *Hamilton et al.*, 2001].

5.2. Comparison to Previous Remote Sensing Results

Previous remotely acquired measurements have led to a variety of interpretations of the mineralogic composition of martian dark regions. Visible and near infrared spectroscopic data of some dark regions are characterized by ~1 and 2-μm absorptions that are commonly attributed primarily to the presence of ferrous (Fe^{2+}) iron in the form of pyroxene and hematite (both nanophase and crystalline) [e.g., *Adams and McCord*, 1969; *Singer et al.*, 1979; *Morris et al.*, 1989; *Mustard et al.*, 1993]. Based on the observation of such features, spectral signatures in Phobos-2 ISM spectra of Syrtis Major have been interpreted to represent two-pyroxene basalts similar to SNC meteorites [*Mustard and Sunshine*, 1995]. *Calvin* [1998] suggested a different perspective that attributes the observed signatures in dark regions to lesser amounts of pyroxene plus dark altered minerals that are more consistent with the observation of a 3-μm water band in intermediate to low albedo regions. Telescopic spectra of Acidalia Planitia by *Merényi et*

al. [1996] do not exhibit a 1-μm pyroxene band (consistent with the presence of high-Ca pyroxene, olivine, mafic glass, or coatings), nor do 12-point spectra acquired by the Imager for Mars Pathfinder (which was located in a relatively bright region) [*Smith et al.*, 1997; *McSween et al.*, 1999]. In fact, recent refinements of the APXS data acquired by Mars Pathfinder south of Acidalia Planitia indicate a silica content of ~58 wt % for soil-free rock [*Foley et al.*, 2000], which is equivalent to a low-silica andesite. Thermal infrared (~8 – 14 microns) telescopic spectra of Acidalia Planitia analyzed by *Moersch et al.* [1997] were found to be comparable to a glassy terrestrial basalt; however, the description of the terrestrial sample as "basalt" was based on petrographic analysis, not sample chemistry, and thus the term may not accurately reflect the true composition of the sample, which could be more silicic [*J. Moersch*, pers. comm., 2001].

Our work further refines the interpretations of *Bandfield et al.* [2000*a*] and *Christensen et al.* [2000*a*], which indicate the presence of basaltic and andesitic materials in martian dark regions. Current interpretations of the mineralogies represented by TES data are less consistent with some of the studies above, and more consistent with others. TES-derived mineralogies for both surface types do not include low-calcium pyroxenes (orthopyroxene and/or pigeonite) at abundances above the current detectability limit for large regional averages [*Bandfield et al.*, 2000*a*; *Christensen et al.*, 2000*a*; this work]. However, small amounts of low-Ca pyroxenes were included in our best fit model of the surface type 1 spectrum and in the fit of *Bandfield et al.* [2000*a*] (8 and 5 vol %, respectively), hinting that such a component might be real, perhaps in the form of smaller local enrichments rather than as a ubiquitous component in the regional average. Additional work with individual spectra in smaller regions may provide greater

confidence in the presence of this phase. Previous data also suggest that martian surfaces may be dark and altered [*Calvin*, 1998]; TES-derived mineralogies include small amounts (~5 – 15 vol %) of sheet silicates [*Bandfield et al.*, 2000*a*; *Christensen et al.*, 2000*a*; this work]. These abundances are also at or below current detectability limits, but as in the case of low-Ca pyroxene, further studies may be able to place better constraints on the possible presence of these phases. Telescopic and in situ analyses of intermediate to dark regions in the northern hemisphere are suggestive of lesser amounts of pyroxene and more silicic (or glassy) compositions that are consistent with TES-derived mineralogies for surface type 2. In fact, the most current estimate of the silica and alkali content of the soil-free rock at the Mars Pathfinder landing site (SiO_2 = ~57.8 wt %, $Na_2O + K_2O$ = 3.7 wt %) [*Foley et al.*, 2000] is quite close to the composition derived in the present work (SiO_2 = 58.2 wt %, $Na_2O + K_2O$ = 4.1 wt %). *Merényi et al.* [1996] observed that compositional differences in their data generally corresponded to the global crustal dichotomy of Mars, an observation to one previously made for the two TES surface types [*Bandfield et al.*, 2000*a*]. The mineralogies derived from TES data thus reflect a continuum that spans many of the previously suggested compositions for martian dark regions. Further work with smaller averages or individual spectra will surely shed light on the more subtle local variations in composition and may identify regions where some of the minerals subdued in the regionally averaged spectra are present in greater abundances.

6. Conclusions

1. Convolution of terrestrial laboratory data to the lowest spectral resolution of the TES instrument does not produce significantly degraded deconvolution results: modeled spectra provide similarly good matches to the measured spectra, modal mineralogies obtained at low (10 cm^{-1}) spectral sampling typically do not differ significantly from those obtained at high (2 cm^{-1}) spectral sampling, and bulk chemistries derived from data at reduced spectral sampling are virtually identical to those obtained from data at high spectral sampling. These results demonstrate the feasibility of using similar techniques and classification schemes for the interpretation of terrestrial laboratory samples and TES-resolution data.
2. Two distinctly different TES martian surface spectra [*Bandfield et al.*, 2000*a*] lie within spectral envelopes that distinguish basaltic and andesitic compositions [*Wyatt et al.*, 2001], further supporting previous results indicating that these spectra represent surfaces with different mineralogies and chemistries.
3. A limited end-member set tailored to the identification of volcanic igneous rocks provides deconvolution results (modal mineralogies) for martian spectra that are comparable to those obtained with the larger end-member sets of *Christensen et al.* [2000*a*] and *Bandfield et al.* [2000*a*]. Therefore, an iterative approach to deconvolution, starting with a large set of varied end-members and working down to a smaller set of end-members that exploits solid solution variability, is justifiable.
4. The two primary martian surface types of *Bandfield et al.* [2000*a*] are easily distinguished and classified here by their modal mineralogy as basaltic (surface

type 1) and andesitic (surface type 2). Local-scale variations in the composition of the martian surface were not examined, but should also be distinguishable and classifiable if the variations are greater than our uncertainties. The spectra are also easily distinguished, although one (surface type 2) is not as easily classified, by their normative plagioclase composition and color index. These results are consistent with results obtained for terrestrial rock samples [*Wyatt et al.*, 2001], and suggest that the plagioclase composition vs. color index classification scheme should not be considered as strongly as other schemes when classifying high-silica samples. (High-silica samples can be identified by other means, such as their spectral shape and derived mineralogy.)

5. Bulk chemistries derived from our deconvolution of martian surface spectra classify the two surface types as basaltic andesite and andesite, in general agreement with the results of previous workers [*Christensen et al.*, 2000*a*; *Bandfield et al.*, 2000*a*].
6. In summary, the surface type 1 martian spectrum is classified as basalt in three out of four classification schemes (the bulk chemistry scheme indicates a composition of basaltic andesite for surface type 1); we believe that this spectrum most likely represents a high-silica basaltic composition. The surface type 2 martian spectrum is classified as andesite in three out of four classification schemes. This spectrum's mineral chemistry (color index vs. plagioclase composition) plots outside the fields defined by terrestrial igneous rocks. However, this scheme is less reliable than the others in classifying deconvolved silica-rich samples [*Wyatt et al.*, 2001]; therefore, we believe that this spectrum is

most consistent with an andesitic composition. These compositional refinements are in agreement with previously published results [*Bandfield et al.*, 2000*a*; *Christensen et al.*, 2000*a*].

References

Adams, J. B. and T. B. McCord, Mars: Interpretation of spectral reflectivity of light and dark regions, *J. Geophys. Res., 74*, 4851-4856, 1969.

Bandfield, J. L., V. E. Hamilton, and P. R. Christensen, A global view of Martian surface compositions from MGS-TES, *Science, 287*, 1626-1630, 2000*a*.

Bandfield, J. L., P. R. Christensen, and M. D. Smith, Spectral dataset factor analysis and end-member recovery: Application to analysis of Martian atmospheric particulates, *J. Geophys. Res., 105*, 9573-9587, 2000*b*.

Calvin, W. M., Could Mars be dark and altered?, *Geophys. Res. Lett., 25*, 1597-1600, 1998.

Christensen, P. R. and H. J. Moore, The martian surface layer, in *Mars*, edited by H. H. Kieffer et al., pp. 686-729, Univ. of Arizona Press, Tucson, 1992.

Christensen, P. R., H. H. Kieffer, S. C. Chase, and D. D. Laporte, A thermal emission spectrometer for identification of surface composition from Earth orbit, in *Commercial Applications and Scientific Research Requirements for Thermal Infrared Observations of Terrestrial Surfaces, NASA-EOSAT Joint Report,* pp. 119-132, Earth Obs. Satell. Co., Lanham, Md., 1986.

Christensen, P. R., D. L. Anderson, S. C. Chase, R. N. Clark, H. H. Kieffer, M. C. Malin, J. C. Pearl, J. Carpenter, N. Bandiera, F. G. Brown, and S. Silverman, Thermal Emission Spectrometer Experiment: Mars Observer Mission, *J. Geophys. Res., 97*, 7719-7734, 1992.

Christensen, P.R., Calibration report for the Thermal Emission Spectrometer (TES) for the Mars Global Surveyor Mission, Mars Global Surveyor Project, Jet. Propul. Lab., Pasadena, Calif., 1999.

Christensen, P. R., J. L. Bandfield, M. D. Smith, V. E. Hamilton, and R. N. Clark, Identification of a basaltic component on the Martian surface from Thermal Emission Spectrometer data, *J. Geophys. Res.*, *105*, 9609-9621, 2000*a*.

Christensen, P. R., J. L. Bandfield, R. N. Clark, K. S. Edgett, V. E Hamilton, T. Hoefen, H. H. Kieffer, R. O. Kuzmin, M. D. Lane, M. C. Malin, R. V. Morris, J. C. Pearl, R. Pearson, T. L. Roush, S. W. Ruff, and M. D. Smith, Detection of crystalline hematite mineralization on Mars by the Thermal Emission Spectrometer: Evidence for near-surface water, *J. Geophys. Res., 105*, 9623 – 9642, 2000*b*.

Christensen, P. R., J. L. Bandfield, V. E. Hamilton, D. A. Howard, M. D. Lane, J. L. Piatek, S. W. Ruff, and W. L. Stefanov, A thermal emission spectral library of rock forming minerals, *J. Geophys. Res., 105*, 9735-9739, 2000*c*.

Christensen, P. R., R. V. Morris, M. D. Lane, J. L. Bandfield, and M. C. Malin, Martian hematite mineral deposits: Remnants of water-driven processes on early Mars, *J. Geophys. Res., 2001.*

Christensen, P. R., J. L. Bandfield, V. E. Hamilton, S. W. Ruff, H. H. Kieffer, T. N. Titus, M. C. Malin, R. V. Morris, M. D. Lane, R. L. Clark, B. M. Jakosky, M. T. Mellon, J. C. Pearl, B. J. Conrath, M. D. Smith, R. T. Clancy, R. O. Kuzmin, T. Roush, G. L. Mehall, N. Gorelick, K. Bender, K. Murray, S. Dason, E. Greene, S. Silverman, M. Greenfield, The Mars Global Surveyor Thermal Emission

Spectrometer experiment: Investigation description and surface science results, *J. Geophys. Res.*, 2002

Clark, R.N. and T. M. Hoefen, Spectral feature mapping with Mars Global Surveyor thermal emission spectra: Mineral implications, *Bull. Am. Astron. Soc., 32*, 1118, Abstract 62.02, 2000.

Crown, D. A., and C. M. Pieters, Spectral properties of plagioclase and pyroxene mixtures and the interpretation of lunar soil spectra, *Icarus, 72,* 492-506, 1987.

Feely, K. C. and P. R. Christensen, Quantitative compositional analysis using thermal emission spectroscopy: Application to igneous and metamorphic rocks, *J. Geophys. Res., 104*, 24,195-24,210, 1999.

Foley, C. N., T. E. Economou, W. Dietrich, and R. N. Clayton, Chemical composition of martian soil and rocks: Comparison of the results from the alpha, proton, and X-ray modes of the Pathfinder APXS, *Meteorit. Planet. Sci., 35*, 55-56, 2000.

Gladman, B., Destination: Earth. Martian meteorite delivery, *Icarus, 130*, 228-246, 1997.

Hamilton, V. E., Thermal infrared emission spectroscopy of the pyroxene mineral series and pyroxene-bearing lithologies, Ph.D. dissertation, 214 pp., Ariz. State Univ., Tempe, 1998.

Hamilton, V. E. and P. R. Christensen, Determining the modal mineralogy of mafic and ultramafic igneous rocks using thermal emission spectroscopy, *J. Geophys. Res., 105*, 9717-9733, 2000.

Hamilton, V. E., P. R. Christensen, and H. Y. McSween Jr., Determination of Martian meteorite lithologies and mineralogies using vibrational spectroscopy, *J. Geophys. Res., 102*, 25,593-26,603, 1997.

Hamilton, V. E., Bandfield, J. L., and P. R. Christensen, The mineralogy of martian dark regions from MGS TES data: Preliminary determination of pyroxene and feldspar compositions, in *Lunar and Planetary Science XXXI*, Abstract #1824, Lunar and Planetary Institute, Houston (CD-ROM), 2000.

Hamilton, V. E., P. R. Christensen, H. Y. McSween, Jr., R. N. Clark, and T. M. Hoefen, Spectral variations in MGS TES data of Nili Fossae: A possible source region for SNC meteorites on Mars?, in *Lunar and Planetary Science XXXII*, Abstract #2184, Lunar and Planetary Institute, Houston (CD-ROM), 2001.

Hamilton, V. E., P. R. Christensen, H. Y. McSween, Jr., Global constraints on martian meteorite source regions, Deconvolutions of MGS-TES data using SNC meteorites as end-members, *Lunar and Planetary Science XXXIII*, Abstract #1937, Lunar and Planetary Institute, Houston (CD-ROM), 2002.

Head, J. N., and H. J. Melosh, Launch velocity distribution of the martian clan meteorites, in *Lunar and Planetary Science XXXI*, Abstract #1937, Lunar and Planetary Institute, Houston (CD-ROM), 2000.

Hoefen, T.M., R. N. Clark, J. C. Pearl, M. D. Smith, Unique spectral features in Mars Global Surveyor thermal emission spectra: Implications for surface mineralogy in Nili Fossae, *Bull. Am. Astron. Soc., 32*, 1118, Abstract 62.03, 2000.

Irvine, T. N. and W. R. Baragar, A guide to the chemical classification of the common volcanic rocks, *Can. J. Earth Sci., 8*, 523-548, 1971.

Le Bas, M. J., R. W. Le Maitre, A. Streckeisen, and B. A. Zanettin, Chemical classification of volcanic rocks based on the total alkali-silica diagram, *J. Petrol., 27*, 745-750, 1986.

Lyon, R. J. P., Analysis of rock spectra by infrared emission (8 – 25 μm), *Econ. Geol., 60*, 715 – 736, 1965.

McSween, H. Y., Jr., and 19 others, Chemical, multispectral, and textural constraints on the composition and origin of rocks at the Mars Pathfinder landing site, *J. Geophys. Res., 104*, 8679-8715, 1999.

Merényi, E., R. B. Singer, and J. S. Miller, Mapping of spectral variations on the surface of Mars from high spectral resolution telescopic images, *Icarus, 124*, 280-295, 1996.

Meyer, C., *Mars meteorite compendium – 1998*, Office of the Curator, JSC Pub. #27672, Rev. A, 237 pp., 1998.

Minitti, M. E., M. J. Rutherford, and J. F. Mustard, The effects of oxidation on spectra of SNC-like basalts: Applications to Mars remote sensing, in *Lunar and Planetary Science XXXI*, Abstract #1282, Lunar and Planetary Institute, Houston (CD-ROM), 2000.

Moersch, J. E., T. L. Hayward, P. D. Nicholson, S. W. Squyres, J. Van Cleve, and P. R. Christensen, Identification of a 10-μm silicate absorption feature in the Acidalia region of Mars, *Icarus, 126*, 183-196, 1997.

Morris, R. V., D. G. Agresti, H. V. Laver, Jr., H. A. Newcomb, T. D. Shelfer, and A. V. Murali, Evidence for pigmentary hematite on Mars based on optical, magnetic, and Mössbauer studies of superparamagnetic (nanocrystalline) hematite, *J. Geophys. Res., 94*, 2760-2778, 1989.

Morris, R. V., T. Graff, M. D. Lane, D. C. Golden, C. S. Schwandt, T. D. Shelfer, D. W. Ming, S. A. Mertzman, J. F. Bell III, J. Crisp, and P. R. Christensen, Acid sulfate alteration products of a tholeiitic basalt: Implications for interpretation of martian

thermal emission spectra, in *Lunar and Planetary Science XXXI*, Abstract #2014, Lunar and Planetary Institute, Houston (CD-ROM), 2000.

Mustard, J. F. and J. M. Sunshine, Seeing through the dust: Maritan crustal heterogeneity and links to the SNC meteorites, *Science, 267*, 1623-1626, 1995.

Mustard, J. F., S. Erard, J.-P. Bibring, J. W. Head, S. Hurtrez, Y. Langevin, C. M. Pieters, and C. J. Sotin, The surface of Syrtis Major: Composition of the volcanic substrate and mixing with altered dust and soil, *J. Geophys. Res., 98*, 3387-3400, 1993.

Mustard, J. F., S. Murchie, S. Erard, and J. Sunshine, In situ compositions of martian volcanics: Implications for the mantle, *J. Geophys. Res., 102*, 25,605-25615, 1997.

Nyquist, L. E., D. D. Bogard, D. H. Garrison, and Y. Reese, A single-crater origin for martian shergottites: Resolution of the age paradox?, in *Lunar and Planetary Science XXIX*, Abstract #1688, Lunar and Planetary Institute, Houston (CD-ROM), 1998.

Ramsey, M. S. and P. R. Christensen, Mineral abundance determination: Quantitative deconvolution of thermal emission spectra, *J. Geophys. Res.*, *103*, 577-596, 1998.

Ruff, S. W., Quantitative thermal infrared emission spectroscopy applied to granitoid petrology, Ph.D. dissertation, 234 pp., Ariz. State Univ., Tempe, 1998.

Ruff, S. W., P. R. Christensen, P. W. Barbera, and D. L. Anderson, Quantitative thermal emission spectroscopy of minerals: A laboratory technique for measurement and calibration, *J. Geophys. Res.*, *102*, 14899-14913, 1997.

Scott, D. H. and K. L. Tanaka, *Geologic Map of the Western Equatorial Region of Mars, scale 1:15,000,000.* U. S. G. S. Misc. Inv. Series Map I-1802-A, 1986.

Simpson, R. A., J. K Harmon, S. H. Zisk, T. W. Thompson, and D. O. Muhleman, Radar determination of Mars surface properties, in *Mars*, edited by H. H. Kieffer et al., pp. 652-685, Univ. of Arizona Press, Tucson, 1992.

Singer, R. B. and H. Y. McSween, Jr., The igneous crust of Mars: Compositional evidence form remote sensing and the SNC meteorites, in *Resources of near-Earth space*, edited by J. S. Lewis, M. S. Matthews, and M. L. Guerrieri, pp. 709-736, Univ. of Arizona Press, Tucson, 1993.

Singer, R. B., T. B. McCord, R. N. Clark, J. B. Adams, and R. L. Huguenin, Mars surface composition from reflectance spectroscopy: A summary, *J. Geophys. Res., 84*, 8415-8426, 1979.

Smith, M. D., J. L. Bandfield, and P. R. Christensen, Separation of atmospheric and surface spectral features in Mars Global Surveyor Thermal Emission Spectrometer (TES) spectra, *J. Geophys. Res., 105*, 9589-9607, 2000.

Smith, P. H. and 28 others, Results from the Mars Pathfinder Camera, *Science, 278*, 1758-1765, 1997.

Thomson, J. L. and J. W. Salisbury, The mid-infrared reflectance of mineral mixtures (7-14 μm), *Remote Sens. Environ., 45*, 1-13, 1993.

Treiman, A. H., S≠NC: Multiple source areas for maritan meteorites, *J. Geophys. Res., 100*, 5329-5340, 1995.

Wyatt, M. B., V. E. Hamilton, H. Y. McSween, Jr., P. R. Christensen, and L. A. Taylor, Analysis of terrestrial and martian volcanic compositions using thermal emission spectroscopy: I. Determination of mineralogy, chemistry, and classification strategies, *J. Geophys. Res., 106*, 14,711-14,732 (2001).

Appendix

Table 1. Measured and Modeled Modal Mineralogies of Laboratory Samples

Sample & Phases	Meas vol %[a]	Mod. vol% $2cm^{-1}$	Mod. vol% $10cm^{-1}$
79-35i			
Feldspar	68	71	71
Silica phases	1	0	0
Low-Ca pyroxene	0	0	0
Pigeonite	0	0	0
High-Ca pyroxene	16	7	8
Olivine	14	21	20
HCC4E			
Feldspar	48	52	47
Silica phases	12	1	0
Low-Ca pyroxene	0	0	1
Pigeonite	4	25	25
High-Ca pyroxene	31	19	22
Olivine	3	2	2
79-39d			
Feldspar	46	42	36
Silica phases	39	32	37
Low-Ca pyroxene	2	8	6
Pigeonite	4	0	0
High-Ca pyroxene	5	1	0
Olivine	1	9	9

Sample & Phases	Meas vol %[a]	Mod. vol% $2cm^{-1}$	Mod. vol% $10cm^{-1}$
79-3b			
Feldspar	76	78	75
Silica phases	5	0	0
Low-Ca pyroxene	1	1	2
Pigeonite	5	0	0
High-Ca pyroxene	8	10	10
Olivine	1	6	7
HCC4A			
Feldspar	48	57	54
Silica phases	11	5	5
Low-Ca pyroxene	0	0	0
Pigeonite	5	7	12
High-Ca pyroxene	29	18	16
Olivine	3	0	0
HK-1			
Feldspar	53	51	50
Silica phases	37	15	15
Low-Ca pyroxene	1	7	9
Pigeonite	3	13	12
High-Ca pyroxene	3	8	7
Olivine	0	6	6

Table 1. Measured and Modeled Modal Mineralogies of Laboratory Samples

Sample & Phases	Meas vol %[a]	Mod. vol% 2cm^{-1}	Mod. vol% 10cm^{-1}
HK-3			
Feldspar	56	55	53
Silica phases	26	12	12
Low-Ca pyroxene	5	12	13
Pigeonite	8	5	5
High-Ca pyroxene	3	9	9
Olivine	0	6	6
82-98			
Feldspar	39	46	46
Silica phases	49	27	31
Low-Ca pyroxene	4	5	8
Pigeonite	2	7	0
High-Ca pyroxene	3	6	4
Olivine	0	8	8

Sample & Phases	Meas vol %[a]	Mod. vol% 2cm^{-1}	Mod. vol% 10cm^{-1}
HK-5			
Feldspar	53	53	51
Silica phases	25	13	13
Low-Ca pyroxene	8	8	8
Pigeonite	3	18	19
High-Ca pyroxene	6	3	3
Olivine	1	6	6

[a]Feature scan (microprobe) modes are from *Wyatt et al*. [2001]

Table 2. Uncertainties Associated with Derived Modal Abundances and Bulk Oxides

Phase	Standard Deviation (vol %)		Oxide	Standard Deviation		Relative Uncertainty (%)	
	2 cm^{-1}	10 cm^{-1}		2 cm^{-1}	10 cm^{-1}	2 cm^{-1}	10 cm^{-1}
Plagioclase	2.8	3.1	SiO_2	1.4	1.5	3.2	3.5
Si-K_2O Glass	12.1	12.2	TiO_2	0.9	0.9	94.7	95.0
Si Glass	4.9	5.2	Al_2O_3	1.5	1.7	13	11.3
Quartz	2.4	3.1	FeO(T)	1.2	1.2	24.2	25.3
Opx	3.1	3.3	MgO	2.6	2.4	74.5	85.2
Pigeonite	6.9	6.9	CaO	0.7	0.8	12.4	13.5
High-Ca Px	3.6	3.7	Na_2O	0.4	0.4	12.3	14.4
Olivine	2.5	2.3	K_2O	0.4	0.4	44.1	46.8
Silica phases[a]	7.2	7.2	Na_2O+K_2O	0.5	0.5	n/a	n/a

[a] Silica phases includes Si-K_2O glass, Si glass, and quartz; the standard deviation was calculated based on the sum of the knowns as if they were a single phase

Table 3. Modal Mineralogies Derived from Martian Surface Spectra

Mineral Group	Cimmeria Terra / Surface Type 1 -- Basaltic			Surface Type 2 -- Andesitic	
	Christensen et al.	*Bandfield et al.*	This work	*Bandfield et al.*	This work
Feldspar	45	50	55	35	49
Clinopyroxene	26	25	21	(10)	
Glass			(9)	25	28
Sheet silicate	(15)	(15)	(5)	(15)	(8)
Orthopyroxene		(5)	(8)		(8)
Amphibole			(2)	(6)	(4)
Olivine	(12)			(3)	(3)
# Endmembers Available:	59	45	29	45	29
# Endmembers Used:	not stated	12	9	12	7

Numbers in parenthesis are modeled at or below detection limits of ~10-15 vol % as stated by *Christensen et al.* [2000] and *Bandfield et al.* [2000]

Table 4. Measured and Modeled Average Feldspar Composition

Sample	Measured An#[a]	Modeled An# 2 cm^{-1}	Modeled An# 10 cm^{-1}
Basalts			
79-35i	60-85	69	69
79-3b	51-85	60	63
HCC4E	N/A	58	58
HCC4A	N/A	65	67
WAR-1049	54[b]	55	56
CRB-5	N/A	46	56
RSL-95-23	N/A	53	52
RSL-94-41	N/A	47	44
Basaltic Andesites			
CRB-4	N/A	48	48
CRB-2	N/A	48	49
CRB-6	N/A	40	41
79-24c	60-87	67	67
79-38k	45-73	47	49
79-38g	45-73	60	67
79-37j	45-70	50	49
79-4d	42-68	48	47
RSL-94-36	N/A	57	61
RSL-94-8	N/A	51	50
RSL-94-12	N/A	51	53

Sample	Measured An#[a]	Modeled An# 2 cm^{-1}	Modeled An# 10 cm^{-1}
Andesites			
82-5	N/A	58	60
79-39d	33-70	48	62
79-9g	60-83	26	22
82-69b	N/A	54	57
HK-1	55-80	43	42
HK-3	55-80	46	46
HK-5	60-80	56	56
82-102	34-80	48	49
82-85	42-75	46	47
Dacites			
85-2b	43-75	34	37
82-88b	34-80	37	39
82-95	34-80	37	39
82-98	28-88	26	20

[a] *Wyatt et al.*, [2001]. [b] *Hamilton and Christensen* [2000]
N/A indicates no information available.

Table 5. Summary of Classification Results for Martian Spectra

	Classification Schemes			
Sample	Spectral Fields	Modal Mineralogy	Mineral Chemistry	Bulk Rock Chemistry
Surface Type 1	B	B	B	BA
Surface Type 2	A	A	B	A

B - Basalt, BA - Basaltic Andesite, A - Andesite

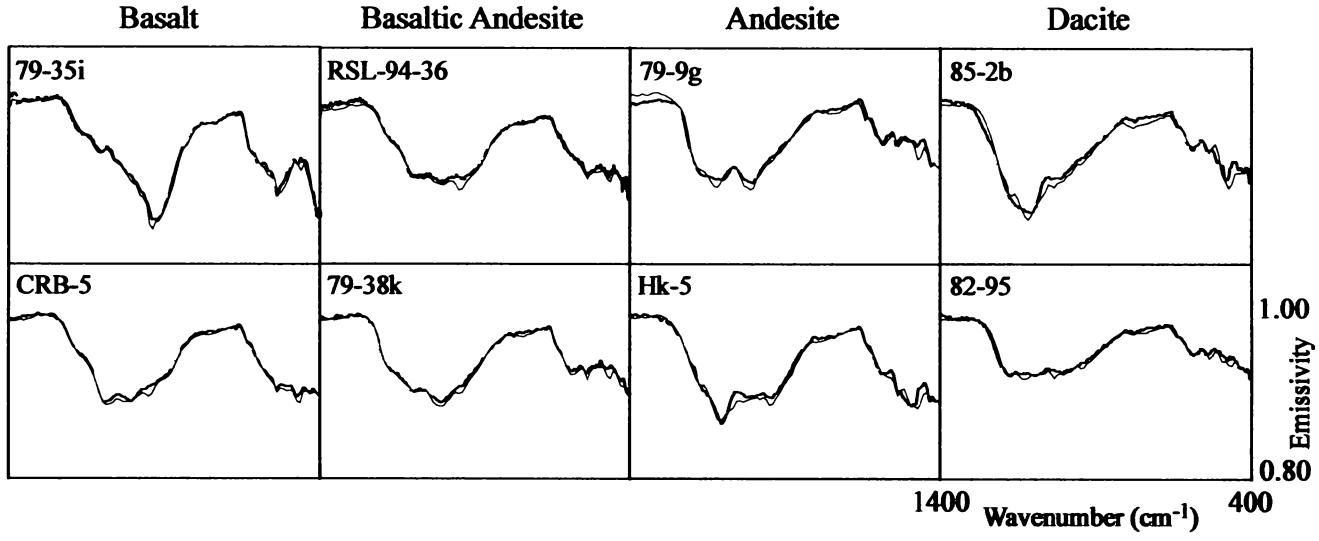


Figure 1. Example measured (black) and modeled (red) terrestrial rock spectra at 10 cm^{-1} spectral sampling.

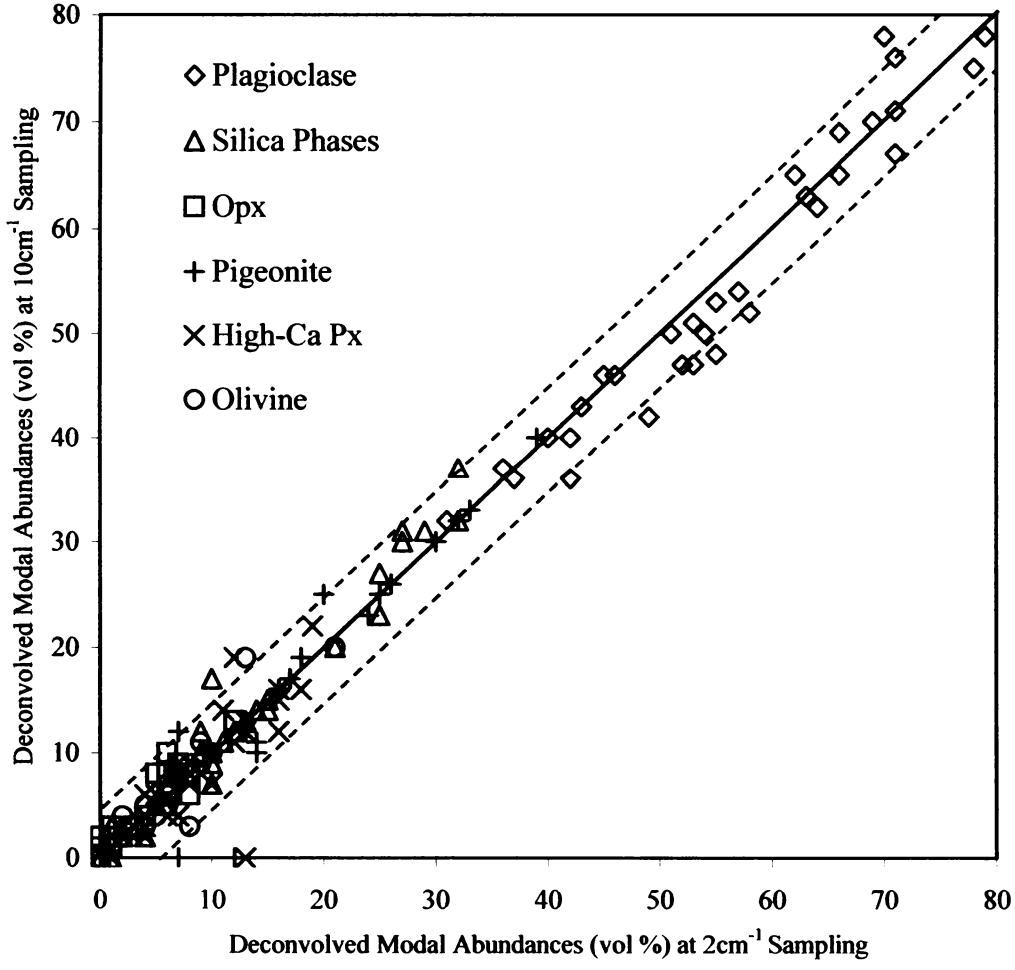


Figure 2: Scatterplot of mineral abundances deconvolved from terrestrial rocks spectra at 2 versus 10 cm^{-1} spectral sampling. Dashed lines enclose points that deviate < 5 vol% from the 1:1 line. Some plot points represent modes for more than one sample. Uncertainties for each phase are listed in Table 2.

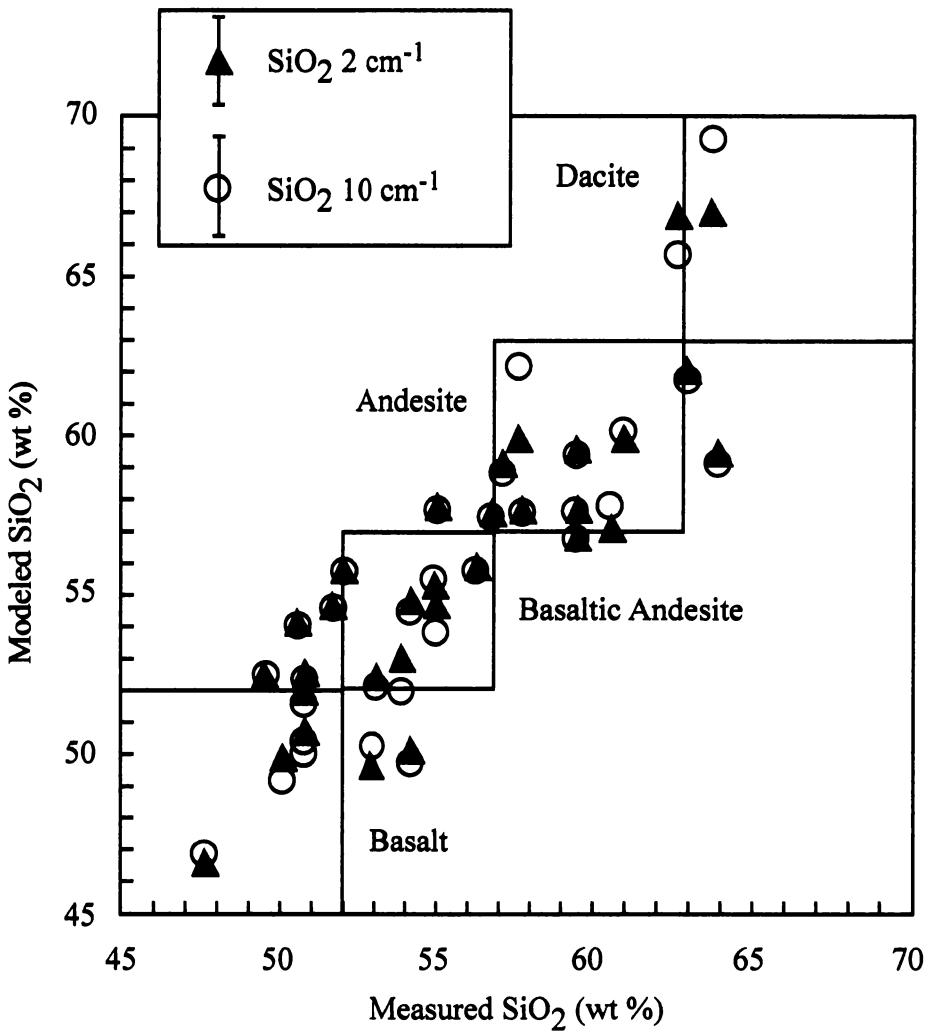


Figure 3: Scatterplot of measured versus modeled wt % SiO_2 for all terrestrial rocks at 2 and 10 cm^{-1} spectral sampling.

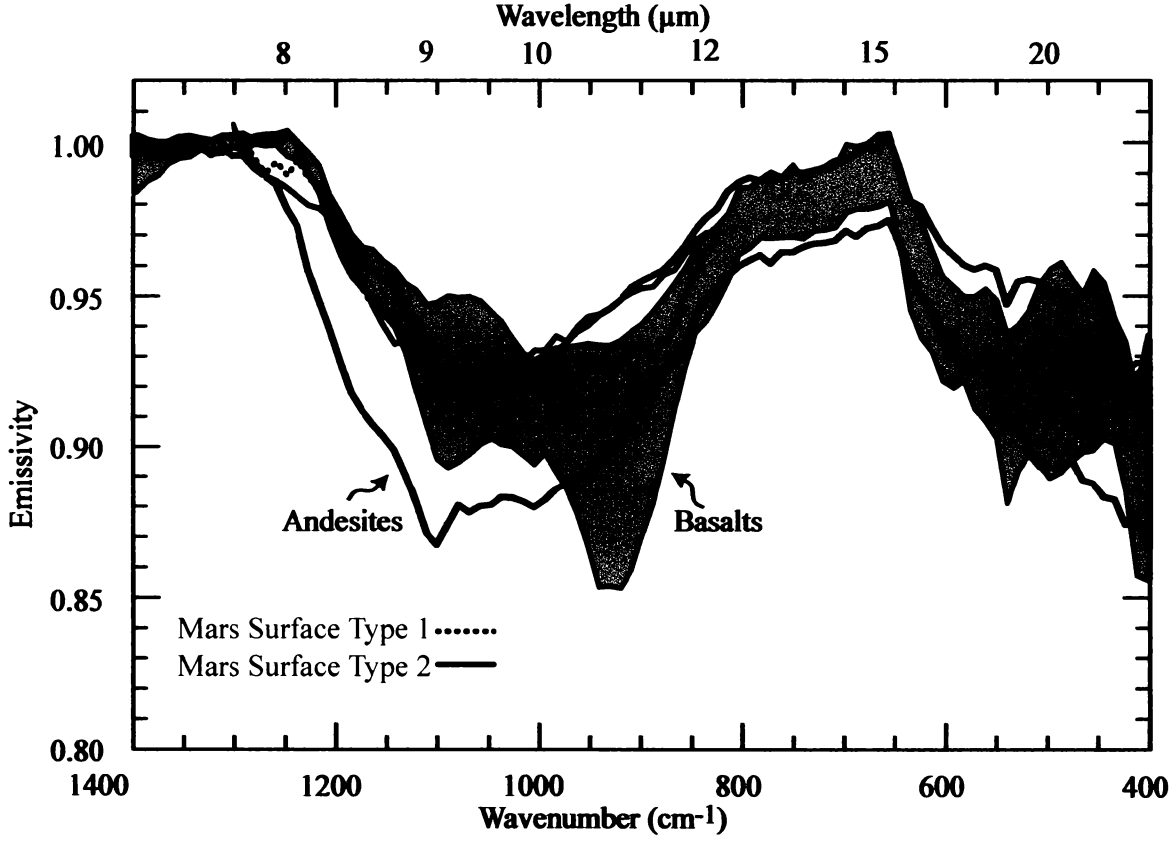


Figure 4. Martian surface spectra acquired by TES [*Bandfield et al.*, 2000a] overlaid on the spectral field classification diagram. Fields are defined by spectra of terrestrial rocks at 10 cm^{-1} sampling. Basaltic rocks fall within the grey shaded zone and andesitic rocks lie between the black lines (the dacite fields in Figure 13 of Part I are not shown for clarity). Martian spectra are contrast enhanced for visual comparison only (see text for discussion).

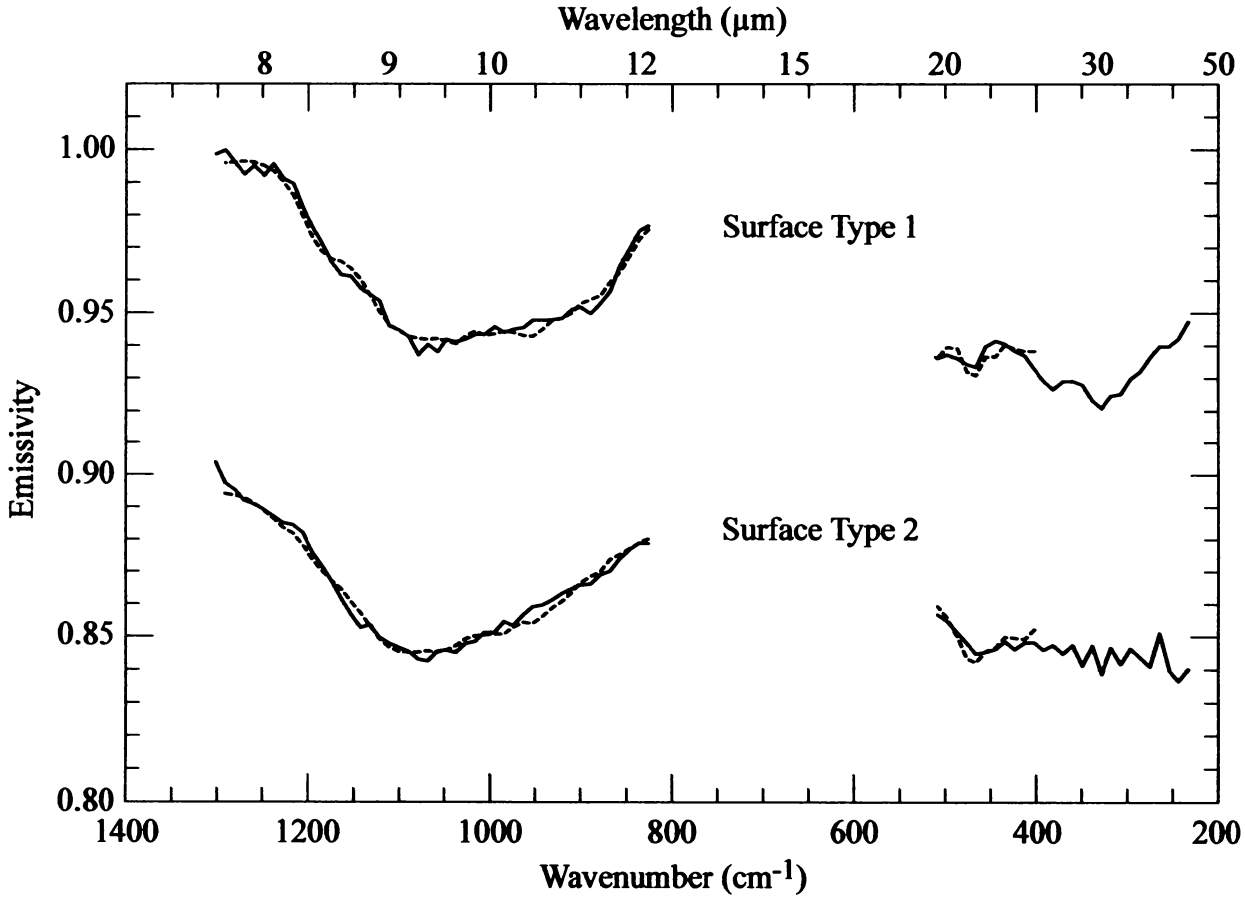


Figure 5. TES martian surface spectra (solid) [*Bandfield et al.*, 2000a] and modeled spectra (dotted) derived using the end-member set described in Part 1 [Wyatt et al., 2001]. Spectra are offset 0.1 for clarity and are not contrast enhanced.

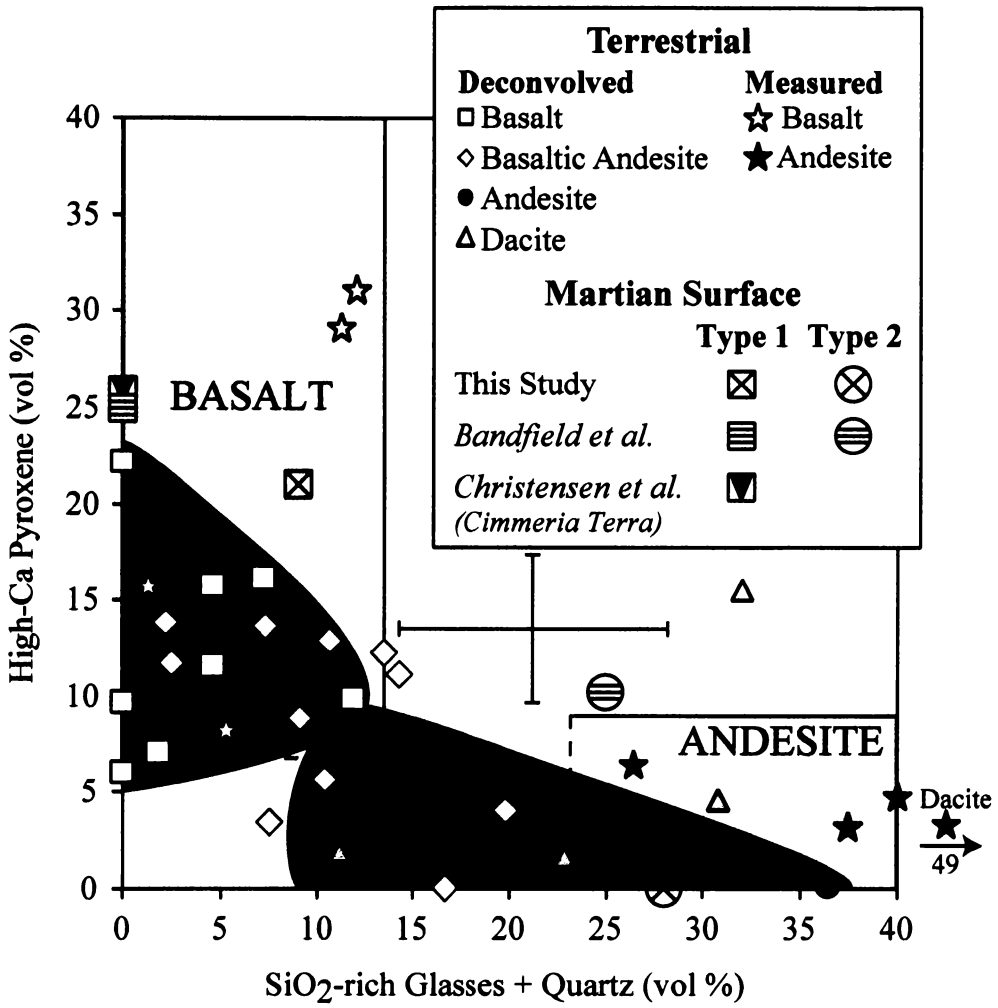


Figure 6. Modal mineralogy classification diagram from Part 1 [*Wyatt et al.*, 2001]. Terrestrial data points indicate modes derived from spectra at 10 cm^{-1} sampling. Stars represent samples with microprobe-measured modes. Error bars represent the one-sigma uncertainties listed in Table 2 for high-Ca pyroxene and silica phases. The dark shaded fields represent basaltic and andesitic fields defined based only on deconvolution results of terrestrial samples and do not take into account their measured mineralogy.

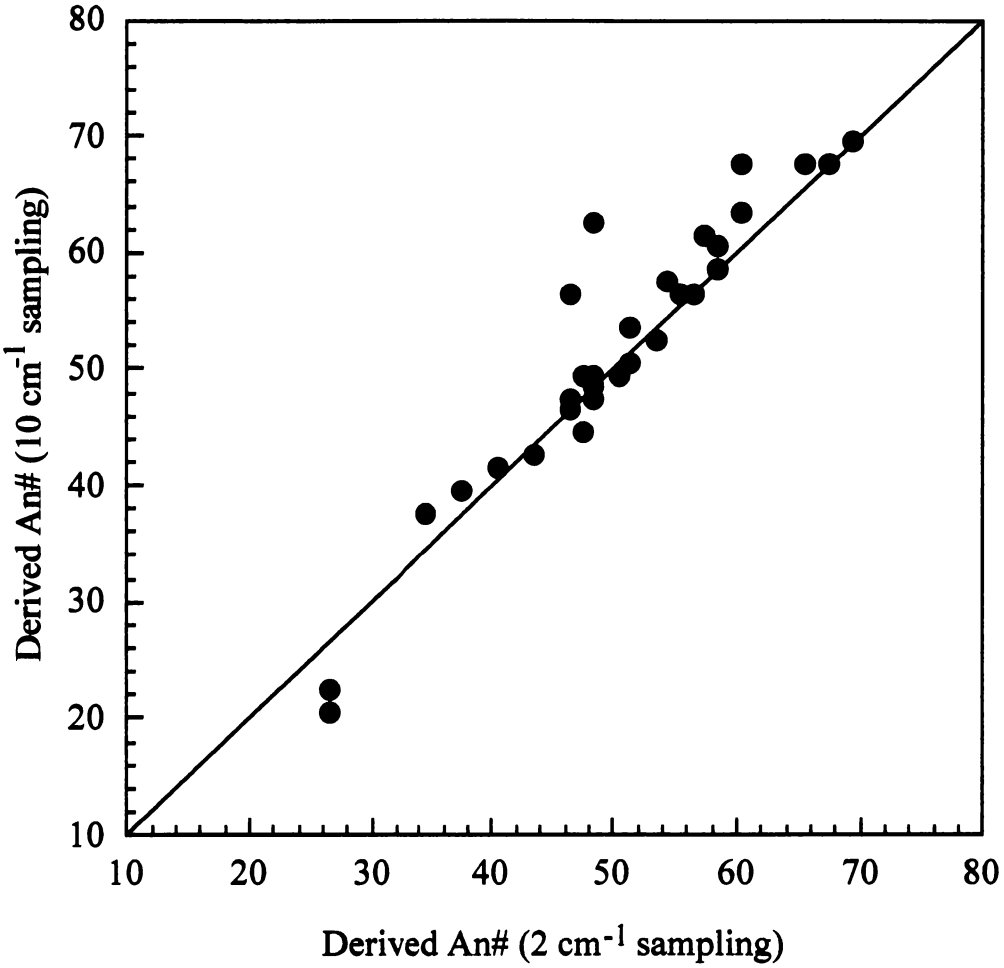


Figure 7. Comparison of average plagioclase An# derived from deconvolution of terrestrial spectra at 2 and 10 cm^{-1} sampling.

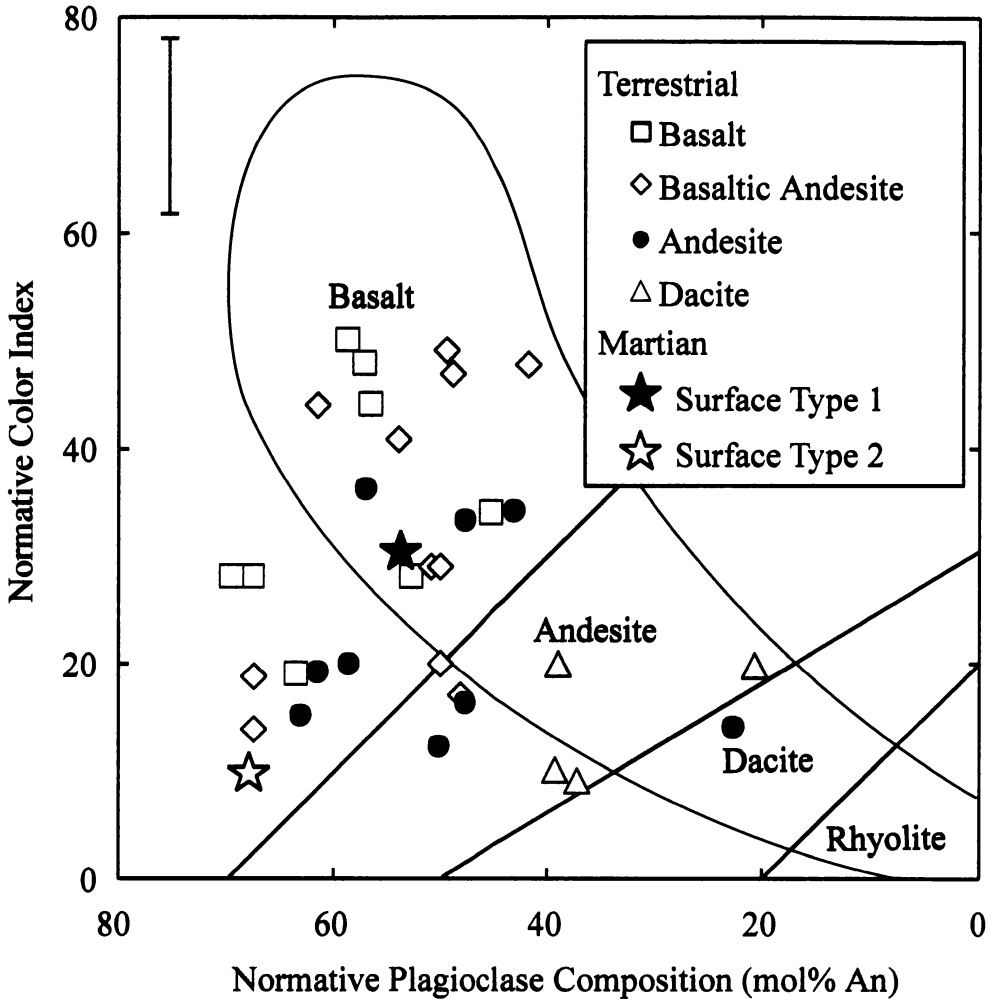


Figure 8. Normative plagioclase composition versus normative color index (both modeled) for 32 terrestrial rocks and martian spectra (note that symbols for martian spectra are different than in Figure 6). The shaded field represents typical terrestrial volcanic compositions [*Irvine and Baragar*, 1971]. The error bar associated with normative color index is based on the one-sigma standard deviation of the sum of the mafic phases.

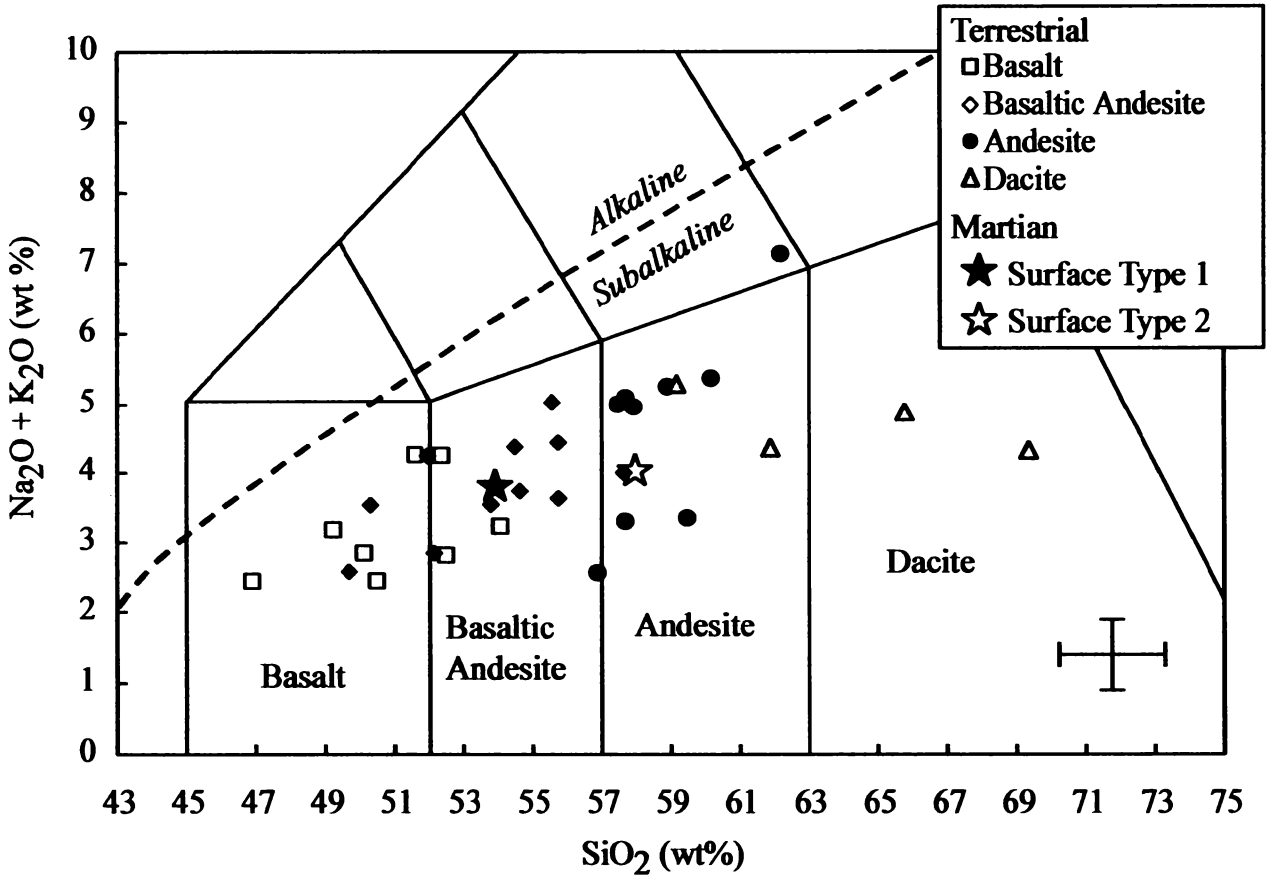


Figure 9. Chemical classification diagram showing model-derived chemistries for terrestrial 10 cm^{-1} data and martian spectra (stars). Symbols are the same as in Figure 8. Error bars represent the uncertainties for silica and alkalis listed in Table 2.

Part 3

Spectral evidence for weathered basalt as an alternative to andesite in the northern lowlands of Mars

This chapter is a revised version of a paper by the same name in press in the journal *Nature* in 2002 by Michael B. Wyatt and Harry Y. McSween Jr.

Wyatt, M.B. and McSween, H.Y., Jr. Spectral evidence for weathered basalt as an alternative to andesite in the northern lowlands of Mars. *Nature*, *in press*, (2002).

Abstract

Mineral abundances derived from analysis of remotely sensed thermal emission data from Mars have been interpreted to indicate that the surface is composed of basalt (Surface Type 1) and andesite (Surface Type 2) [*Bandfield et al.*, 2000]. The global distributions of basalt and andesite are divided roughly along the planetary dichotomy which separates ancient, heavily cratered crust in the southern hemisphere from younger lowland plains in the north [*Bandfield et al.*, 2000]. The existence of such a large volume of andesite is difficult to reconcile with existing knowledge of the geologic evolution of the planet. Here we reinterpret martian surface rock lithologies using mineral abundances from *Bandfield et al.* [2000] and new mineralogies derived from a spectral end-member set representing minerals common in unaltered and low-temperature aqueously altered basalts. The new formulations maintain the dominance of unaltered basalt in the southern highlands, but indicate the northern lowlands can be interpreted as weathered basalt. The coincidence between locations of altered basalt and a suggested northern ocean basin implies that lowland plains materials may be basalts weathered under submarine conditions and/or weathered basaltic sediments transported into this depocenter.

1. Introduction

The identification of basalt on Mars from TES observations [*Bandfield et al.*, 2000; *Christensen et al.*, 2000] agrees with visible/near-infrared spectroscopic observations of low albedo regions [*Mustard et al.*, 1997]. The identification of andesite on Mars from TES observations [*Bandfield et al.*, 2000] is consistent with chemical analyses of rocks by Mars Pathfinder [*Rieder et al.*, 1997]. Additional calibrations using a variety of unweathered terrestrial volcanic rocks have demonstrated the fidelity with which thermal emission data can distinguish basalt and andesite [*Wyatt et al.*, 2001], and *Hamilton et al.* [2001] applied these results to support the identification of basaltic and andesitic martian surface compositions.

The large expanse of andesite in the northern plains as suggested by *Bandfield et al.* [2000] is however difficult to explain. On Earth, andesite forms mostly at subduction zones, where water released from descending slabs promotes mantle melting. However, there is no evidence for subduction on Mars. Although andesite can also be produced during fractionation of basaltic magma, this process is inefficient and could not account for a large volume of andesite [*McSween et al.*, 1999]. Less fractionation is required for hydrous basaltic melts to reach the composition of andesite, and evidence exists that some martian basaltic meteorites contained water [*McSween et al.*, 2001]. In this case, however, the northern plains should consist of comparable amounts of andesite and basalt.

The observed geographic concentration of martian andesite within the northern lowlands [*Bandfield et al.*, 2000] suggests an alternative mechanism for their formation. Previous abstracts have indicated that weathered or oxidized basaltic glass is spectrally

similar to andesitic glass [*Noble and Pieters*, 2001; *Minitti et al.*, 2000]. Here, we explore whether Surface Type 2 (andesite) might be reinterpreted as basalt weathered in a submarine environment. The northern lowlands lie, for the most part, below the 0-km elevation datum, and lakes or oceans, possibly fed by large outflow channels originating in the southern highlands, may have occupied this region [*Head et al.*, 1999]. Deconvolved mineral abundances from *Bandfield et al.* [2000] and new mineralogies derived from TES data and terrestrial basalts using a spectral end-member set representing minerals common in unaltered and low-temperature aqueously altered basalts are used to reclassify martian surface lithologies.

2. Results

Figures 1a and 1b compare spectral fits and modeled mineral abundances produced by linear deconvolutions of Surface Types 1 and 2 spectra (see methods). *Bandfield et al.* [2000] used 45 spectral end-members [*Christensen et al.*, 2000] representing igneous, sedimentary, and metamorphic minerals, whereas *Hamilton et al.* [2001] used a narrower range of 29 mineral spectra representing mostly unweathered basalts and andesites. Our 39 spectral end-members represent minerals common in unaltered and low-temperature aqueously altered basalts [*Thompson*, 1983] (Table 1). One of the primary differences between the *Bandfield et al.* [2000] and *Hamilton et al.* [2001] spectral end-member sets and the end-member set used here is the omission of a high-silica glass phase [*Wyatt et al.*, 2001] in this study (see methods). A similar difference involving K-feldspar occurs between the end-member set used by *Hamilton et al.* [2001] compared to *Bandfield et al.* [2000] and this study (see methods). Also shown

in Figures 1a and 1b are one-sigma standard deviations for martian surface spectra (each martian spectrum is an average of four to seven regional locations of selected spectra) as determined by *Bandfield et al.* [2000].

Spectral fits produced by linear deconvolution of the Surface Type 1 spectrum show low RMS values of 0.0018 [*Bandfield et al.*, 2000], 0.0026 [*Hamilton et al.*, 2001], and 0.0018 (this study). Modeled mineral abundances for the three end-member sets (Figure 1a, Table 2) are all characterized by high values of plagioclase and pyroxene, and low values of weathering products (clays, sulfates, and carbonates). The low RMS values and similar modeled mineral abundances derived from different endmember sets indicate these modes accurately reflect the Surface Type 1 composition. The modeled mineral abundances, and the broad, slightly squared shape absorption between ~800-1200 cm^{-1} characteristic of Surface Type 1, are representative of unweathered basaltic compositions [*Bandfield et al.*, 2000; *Christensen et al.*, 2000; *Wyatt et al.*, 2001; *Hamilton et al.*, 2001]

Analogous spectral fits of the Surface Type 2 spectrum show low RMS values of 0.0009 [*Bandfield et al.*, 2000], 0.0023 [*Hamilton et al.*, 2001], and 0.0014 (this study). However, modeled mineral abundances differ, resulting in an ambiguous description of the Surface Type 2 composition (Figure 1b, Table 2). The results of *Bandfield et al.* [2000] and *Hamilton et al.* [2001] are characterized by high modeled abundances of plagioclase and high-silica glass and low abundances of pyroxene and weathering products. Modeled abundances in this study are characterized by plagioclase with appreciable alteration minerals (clays and K-feldspar) and lesser pyroxene. The well modeled spectra indicate that each of the different mineral modes is equally valid for

describing the Surface Type 2 spectrum. Modeled mineral abundances from *Bandfield et al.* [2000] and *Hamilton et al.* [2001], and the slightly V-shaped absorption between ~800-1200 cm^{-1} characteristic of Surface Type 2, are representative of andesite [*Bandfield et al.*, 2000; *Wyatt et al.*, 2001; Hamilton et al., 2001]. Higher abundances of clays and K-feldspar, and lower abundances of pyroxenes for Surface Type 2 as modeled in this study, are characteristic of altered basalt [*Thompson*, 1983].

Modeled mineral abundances supporting a weathered basalt composition are largely a result of clays replacing high-silica glass. Absorption features between 500-550 cm^{-1} in laboratory spectra distinguish clays modeled in this study (Fe-smectite and Ca-montmorillonite) from high-silica glass (Figure 2a); however, the CO_2 atmosphere of Mars is largely opaque is this spectral region, limiting its usefulness for analysis of surface compositions. The spectral regions of high-silica glass and clays used for analysis of martian surface compositions are very similar in their overall spectral shape and positions of spectral features.

Despite this ambiguity, conclusions from deconvolved TES spectra concerning other rock-forming minerals are thought to be robust, as numerous different end-member sets have been examined to determine the uniqueness of these model solutions [*Bandfield et al.*, 2000; *Hamilton et al.*, 2001; this study]. The differences between modeled abundances of major rock-forming minerals for the Surface Type 2 spectrum using different end-member sets are within stated uncertainties [Table 2]. Furthermore, the small variations in modeled abundances that exist for igneous minerals do not change interpretations of rock types. The only possible substitution between phases that does not cause the RMS error between modeled and measured spectra to be unacceptably high is

Fe-smectite plus Ca-montmorillonite versus high-silica glass. Clays and glasses lack the long-range order in crystal structure compared to major rock forming silicate minerals (feldspars and pyroxenes), which is a controlling factor in the relative strength, number, and wavelength positions of spectral absorptions. For feldspars and pyroxenes, spectral absorptions are unique at several points, however for some clays and glasses spectral absorptions are not as diagnostic, allowing for their substitution. Future work is needed to understand better the degree of substitution and spectral effects of varying crystallinity in poorly crystalline phases over a range of chemical compositions. While this demonstrates the ambiguity in distinguishing andesite and weathered basalt, we do not believe any other geologically plausible lithologies fit the Surface Type 2 spectrum.

Figure 2b shows spectra of the fresh cut and weathered surfaces of a Columbia River Flood Basalt (CRB sample 4 [*Wyatt et al.*, 2001; *Hamilton et al.*, 2001]) re-sampled to TES spectral resolution compared to Surface Type 1 and 2 spectra, respectively. Because martian surface spectra analyzed by TES are thought to be dominated by sand-sized particles [*Christensen et al.*, 2000; *Bandfield et al.*, 2000] rather than bedrock, a blackbody component (which does not affect spectral shape) was added to each terrestrial sample to account for band depth particle size effects. The spectrum of the fresh cut CRB surface displays a broad, slightly squared shape absorption between ~800-1200 cm^{-1} similar to the Surface Type 1 spectrum while the spectrum of the natural CRB surface displays a more V-shaped absorption similar to the Surface Type 2 spectrum. Spectral fits produced by linear deconvolution of the fresh cut CRB surface spectrum show low RMS values (.0020 [*Bandfield et al.*, 2000], .0025 [*Hamilton et al.*, 2001], .0031 this study) and deconvolved mineral abundances are characterized by high

values of plagioclase and pyroxene, and low values of weathering products (Table 3), similar to Surface Type 1. Spectral fits produced by linear deconvolution of the natural CRB surface spectrum show analogous low RMS values (.0023 [*Bandfield et al.*, 2000], .0034 [*Hamilton et al.*, 2001], .0030 this study). However, modeled mineral abundances for the natural CRB surface using the end-member sets of *Bandfield et al.* [2000] and *Hamilton et al.* [2001] are characterized by high abundances of plagioclase, pyroxene, and high-silica glass, whereas abundances in this study are characterized by plagioclase with appreciable alteration minerals and lesser pyroxene (Table 3), similar to the ambiguous mineralogic characterization of Surface Type 2.

Microscopic examination of the fresh cut and natural CRB surfaces agrees best with deconvolved mineral abundances from *Bandfield et al.* [2000] in which a combination of plagioclase, pyroxene, high-silica glass, and clays comprises the sample's modal mineralogy. A decrease in pyroxene and increase in clay abundances is expected on a natural surface as pyroxenes are typically weathered to clays. However, an increase in the abundance of high-silica volcanic glass on a natural surface is not expected as such a phase is also easily weathered. The increase in modeled high-silica glass from the fresh cut to natural CRB surface might indicate the formation of amorphous silica alteration products which are spectrally similar to high-silica glass. The original interpretation of the high-silica glass spectral end-member phase as a primary volcanic glass may be too limited, as it could also represent an amorphous high-silica alteration product.

Figure 3 compares the global distribution of Surface Types 1 and 2, as determined by *Bandfield et al.* [2000] and global topography determined from MOLA data [*Smith et al.*, 1999] in hemispherical north and south stereographic polar projections. The highest

concentrations of Surface Type 1 (green) in the southern highlands and Surface Type 2 (red) in the northern lowlands coincide roughly with the planetary dichotomy, although there is some mixing of surface types across this divide. Blue pixels on TES composition maps represent regions covered by fine-grained bright dust which blankets the surface and prohibits spectral analysis of sand and rock compositions. Also shown on the north polar projections is a white line defining contacts previously interpreted as shorelines [*Parker et al.*, 1989] which approximate an equipotential line [*Head et al.*, 1999]. Surface Type 2 compositions in the northern hemisphere are distributed almost entirely within the proposed shorelines where they are not spectrally obscured by dust cover. Surface Type 2 compositions in the southern hemisphere may be due to similar alteration processes, but the lack of geographic concentrations does not support a large southern hemisphere body of liquid water.

3. Discussion

Linear deconvolution of the Surface Type 2 spectrum by *Bandfield et al.* [2000] and this study requires some clay/sheet silicates be modeled at or above the TES detectability limit [*Christensen et al.*, 2000]. The high abundance of modeled alteration products in this study results from the spectral similarities and substitution of clays for high-silica glass at TES spectral resolution. High abundances of well crystalline phyllosilicates in low-albedo regions are not supported by Near-Infrared Spectrometer Mapper (ISM) data [*Murchie et al.*, 2000]; however, poorly crystalline palagonite has been proposed as a component in bright martian soil [*Murchie et al.*, 1993]. We note that ISM data only covered ~20% of the martian equatorial region, which is dominated by

unweathered basaltic compositions as determined by TES data. Comparison of ISM data with weathered basalt compositions in the northern hemisphere is thus not possible. *Merényi et al.* [1996] did observe northern regions from high spectral resolution telescopic images and noted that weaker mafic mineral bands could be explained by a higher glass content. This is generally analogous to the increased glass content determined by *Bandfield et al.* [2000] (interpreted here as a possible alteration product) to explain differences in the Surface Type 1 and 2 spectra. The mineralogies determined by *Bandfield et al.* [2000] and this study for Surface Type 2 can thus both be interpreted as representing weathered basalt.

A martian crust dominated by basalt containing augite and pigeonite (Table 3) is in agreement with visible/near-infrared spectroscopic observations of low albedo regions that suggest surface materials may be similar to shergottite meteorites [*Mustard et al.*, 1997]. Analysis of depressions ("ghost craters") in the lowlands indicate that the basement there is of Noachian age [*Frey et al.*, 2001], like the southern highlands, so it is plausible that the entire planet had an ancient basaltic crust that was altered where water ponded. This hypothesis may also explain the absence of andesite among martian meteorites, because either this material might exist as weathering rinds or more thoroughly weathered rocks might not survive impact ejection. *McSween and Keil* [2000] compared compositions of martian soils and concluded that the global dust formed by weathering of basalts rather than andesites.

4. Conclusions

Although the existence of andesite on Mars remains a viable hypothesis, linear deconvolution of martian thermal infrared spectra, spectral matching with terrestrial volcanic rocks, and the geographic distribution of the Surface Type 2 spectrum suggest that martian northern lowland plains materials are basalts weathered under submarine conditions and/or sediments derived from weathered basalt and deposited in this basin.

References

Bandfield, J. L., Hamilton, V. E., & Christensen, P.R. A global view of martian surface compositions from MGS-TES. *Science* 287, 1626 (2000).

Christensen, P. R. et al. Identification of a basaltic component on the martian surface from Thermal Emission Spectrometer data. *JGR* 105, 9609 (2000).

Christensen, P. R. et al. A thermal emission spectral library of rock forming minerals. *JGR* 105, 9735 (2000).

Frey, H. V. et al., A very large population of likely buried impact basins in the northern lowlands of Mars revealed by MOLA data. *LPSC XXXII, CD #1680* (2001).

Hamilton, V. E. et al. Analysis of terrestrial and martian volcanic compositions using thermal emission spectroscopy: II. Application to martian surface spectra from the Mars Global Surveyor Thermal Emission Spectrometer. *JGR* 106, 14,733 (2001).

Head, J. W. et al. Possible ancient oceans on Mars; evidence from Mars Obriter laser altimeter data. *Science* 286, 2134 (1999).

McSween, H. Y., Jr. et al. Chemical, multispectral, and textural constraints on the composition and origin of rocks at the Mars Pathfinder landing site. *JGR* 104, 8679 (1999).

McSween, H. Y., Jr. & Keil, K. Mixing relationships in the martian regolith and the composition of globally homogenous dust. *GCA* 64, 2155 (2000).

McSween, H. Y., Jr. et al. Geochemical evidence for magmatic water within Mars from pyroxenes in the Shergotty Meteorite. *Nature* 409, 487 (2001).

Merényi, E.,Singer, R. B., & Miller, J. S., Mapping of spectral variations on the surface of Mars from high spectral resolution telescopic images. *Icarus* 124, 280-295 (1996).

Minitti, M. E., Rutherford, M. J., & Mustard, J. F. The effects of oxidation on spectra of SNC-like basalts: Application to Mars remote sensing. *LPSC XXXI, CD #1282* (2000).

Murchie, S. et al. Spatial variations in the spectral properties of bright regions on Mars. *Icarus* 105, 454 (1993).

Murchie, S., Kirkland, L., Erard, S., Mustard, J., & Robinson, M., Near-infrared spectral variations of martian surface materials from ISM imaging spectrometer data. *Icarus* 147, 444-471 (2000).

Mustard, J. F., Murchie, S., Erard, S., & Sunshine, J. M. In situ compositions of martian volcanics: Implications for the mantle. *JGR* 102, 25,605 (1997).

Noble, S. K. & Pieters, C. M. Type 2 terraine: compositional constraints on the martian lowlands. *LPSC XXXII, CD #1230* (2001).

Parker, T. J. et al. Transitional morphology in the west Deuteronilus Mensae region of Mars: implications for modification of the lowland/upland boundary. *Icarus* 82, 111 (1989).

Rieder, R. et al. The chemical composition of martian soils and rocks returned by the mobile alpha proton X-ray spectrometer: Preliminary results from the X-ray mode. *Science* 278, 1771 (1997).

Smith, D. E. et al. The global topography of Mars and implications for surface evolution. *Science* 284, 1495 (1999).

Thompson, G., in *Hydrothermal Processes at Seafloor Spreading Centers*, P. A. Rona, K. Bostrom, L. Laubier, K. L. Smith, Jr., Eds. (Plenum Press, New York, 1983), pp. 225-278.

Wyatt, M. B. et al. Analysis of terrestrial and martian volcanic compositions using thermal emission spectroscopy: I. Determination of mineralogy, chemistry, and classification strategies. *JGR* 106, 14,711 (2001).

Appendix

Methods

Linear deconvolutions using three spectral end-member sets [Christensen et al., 2000] (*Bandfield et al.* [2000], *Hamilton et al.* [2001], and this study) were run for each martian surface spectrum. Algorithm outputs include a best-fit model spectrum for each martian surface spectrum, percentage of each mineral end-member used, and a root-mean-square (RMS) error value (average error over the entire spectrum). The RMS value indicates goodness of fit for a particular model iteration for the same martian spectrum, rather than a comparison between fits of the two martian spectra. Spectral fitting for both methods was constrained to 1280-400 cm^{-1}, although TES data cover the wavenumber range of 1650-200 cm^{-1}. The atmospheric correction used to derive the TES surface spectra used in this study did not include the high wavenumber range of TES data due to numerous water vapor and minor CO_2 features. Furthermore, there are no fundamental silicate features in the 1650-1400 cm^{-1} region. Similar to *Bandfield et al.* [2000], the deconvolution algorithm also did not use the 400-200 cm^{-1} spectral range. Residual atmospheric water vapor rotational bands are apparent in both the Martian surface spectra as well as in the ASU mineral library end-member spectra. This restricted wavenumber range prevents the deconvolution algorithm from attempting to fit water vapor features instead of surface mineralogy.

Accurate deconvolution is largely dependent on spectral end-member sets representing an appropriate range of compositions in the mixture. The high-silica glass phase (77.9% SiO_2, 12.6% Al_2O_3, 3.90% Na_2O, 5.67% K_2O) not included in the end-member set used in this study has been interpreted by *Bandfield et al.* [2000] and *Hamilton et al.* [2001] as representing a primary volcanic glass. High-silica volcanic

glasses are often not present in high abundances in unweathered basalts, compared to andesites, and typically alter to clays in a weathering environment. For these reasons, we have excluded this volcanic glass phase in our end-member set that is designed to represent basalts and low-temperature aqueously altered basalts. K-feldspar is not included in the *Hamilton et al.* [2001] spectral end-member set as it is not typically found in unweathered basalt and andesite. K-feldspar is however included by *Bandfield et al.* [2000] to represent possible mineralogies in a larger suite of igneous, metamorphic, and sedimentary rock types and in this study as a possible alteration product [*Thompson*, 1983].

Table 1: Mineral library spectral end-member set used for the deconvolution of martian Surface Type 1 and 2 spectra in this study.

Feldspars	Pyroxenes	Clay / Sheet Silicate	Other
Albite WAR-5851	Bytownite WAR-1384	Muscovite WAR-5474	Fayalite WAR-RGFAY01
Oligoclase WAR-5804	Enstatite Hs-9.4B	Biotite BUR-840	Forsterite AZ-01
Andesine BUR-240	Bronzite NMNH-93527	Phlogopite HS-23.3B	Actinolite HAS-116.4B
Labradorite WAR-RGAND01	Diopside WAR-6474	Serpentine Hs-8.4B	Magnesiohornblende WAR-0354
Labradorite WAR-4524	Hedenbergite DSM-HED01	Serpentine BUR-1690	Anhydrite ML-S9
Anorthite WAR-5759	Augite (low-Ca) WAR-6474	Antigorite NMNH-47108	Gypsum ML-S6
Anorthite BUR-340	Augite (low-Ca) BUR-620	Ca-montmorillonite STx-1s	Calcite C27
Anorthoclase	Augite (low-Ca) NMNH-9780	Nontronite WAR-5108s	Dolomite C17
Microcline1	Pigeonite	Saponite ASU-SAP01	
Microcline BUR-3460A		Illite IMt-2	
		Fe-smectite SWa-1s	
		Chlorite WAR-1924	

Table 2: Modeled mineral abundances retrieved by deconvolution for martian Surface Type 1 and 2 spectra.

	Surface Type 1			Surface Type 2		
Mineral Group [a]	Bandfield et al.	Hamilton et al.	This work	Bandfield et al.	Hamilton et al.	This work
Feldspars [b]	49	55	33	33	49	39
Pyroxenes [c]	29	29	41	(10)	(8)	16
High-Silica Glass		(9)		23	28	
Clay / Sheet Silicate [d]	17	(5)	(14)	17	(8)	31
Other [e]	(6)	(2)	(12)	17	(7)	(14)

[a] Numbers in parentheses are modeled at or below detection limits of ~10-15 vol.%.

[b] Feldspars dominated by plagioclase in modeled results, except Surface Type 2 (This work) with 14 vol.% modeled K-feldspar.

[c] Pyroxenes dominated by high-calcium clinopyroxene in modeled results, except Surface Type 1 (This work) with 21 vol.% modeled pigeonite.

[d] Clay / Sheet Silicate in Surface Type 2 dominated by Fe-Smectite and Ca-Montmorillonite in this work and Fe-Smectite in Bandfield *et al*[1].

[e] Comprised of individual phases (e.g. carbonate, sulfate) modeled well below detection limits of ~10-15 vol.%.

Table 3: Modeled mineral abundances retrieved by deconvolution for Columbia River Basalt (CRB) fresh cut and natural (weathered) surfaces.

CRB-4[5,6]	CRB fresh cut			CRB natural surface		
Mineral Group [a]	Bandfield et al.	Hamilton et al.	This work	Bandfield et al.	Hamilton et al.	This work
Feldspars [b]	49	49	50	49	48	39
Pyroxenes [c]	23	38	45	(15)	17	26
High-Silica Glass	(15)	(11)		22	26	
Clay / Sheet Silicate[d]	1		(2)	(11)	(3)	25
Other [e]	(14)	(3)	(4)	(5)	(6)	(12)

[a] Numbers in parentheses are modeled at or below detection limits of ~10-15 vol.%.

[b] Feldspars dominated by plagioclase in modeled results, except CRB natural surface (This work) with 19 vol.% modeled K-feldspar.

[c] Pyroxenes dominated by high-calcium clinopyroxene and pigeonite in CRB fresh cut and high-calcium pyroxene only in CRB natural surface

[d] Clay / Sheet Silicate in CRB natural surface dominated by Ca-Montmorillonite and serpentine in this work and nontronite in Bandfield *et al*[1].

[e] Comprised of individual phases (e.g. carbonate, sulfate) modeled well below detection limits of ~10-15 vol.

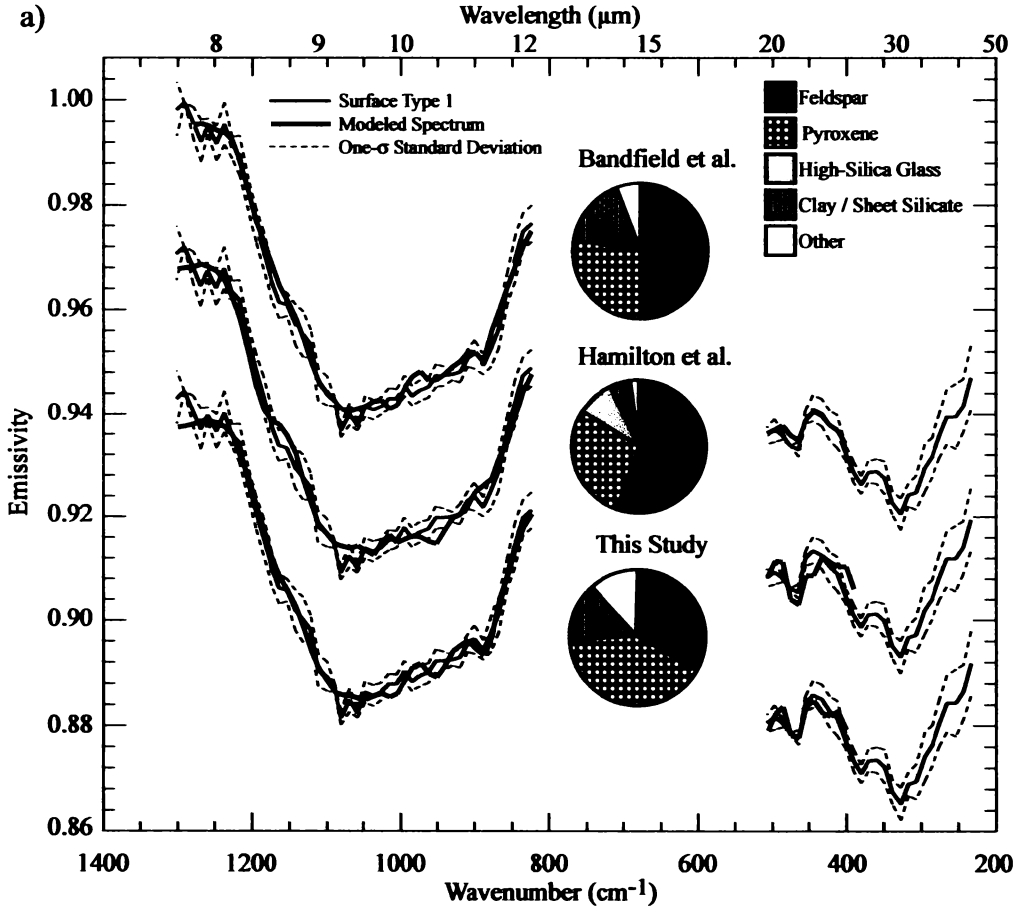


Figure 1: Comparison of martian surface spectra and modeled spectral fits. (a) Martian Surface Type 1 and (b) Type 2 spectra and modeled spectral fits (offset by .028 emissivity for clarity) and mineral abundances produced by linear deconvolution from Bandfield et al., Hamilton et al. and this study (Table 2). The detection limit for mineral abundances deconvolved from TES spectra is 10-15 vol. % [Christensen et al., 2000]. Mineral abundances for Surface Type 2 are characteristic of either andesitic or weathered basaltic compositions.

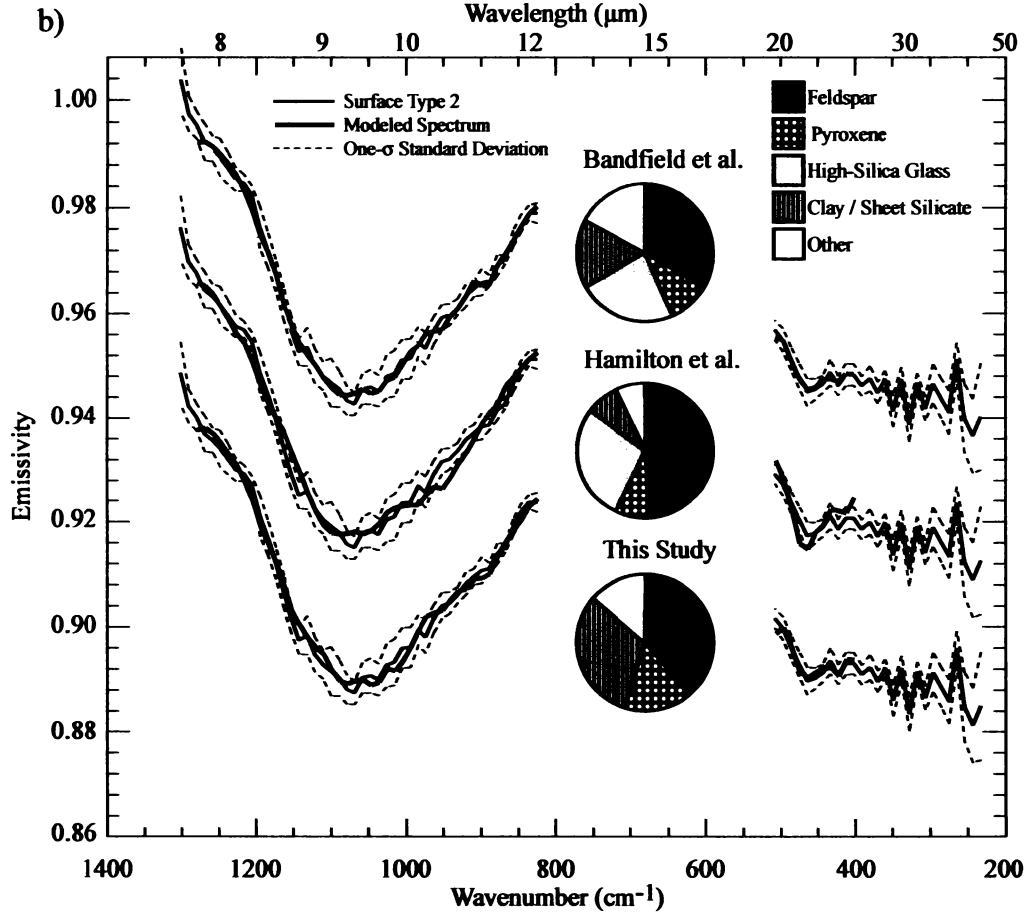


Figure 1 Continued: Comparison of martian surface spectra and modeled spectral fits. (a) Martian Surface Type 1 and (b) Type 2 spectra and modeled spectral fits (offset by .028 emissivity for clarity) and mineral abundances produced by linear deconvolution from Bandfield et al., Hamilton et al. and this study (Table 2). The detection limit for mineral abundances deconvolved from TES spectra is 10-15 vol. % [Christensen et al., 2000]. Mineral abundances for Surface Type 2 are characteristic of either andesitic or weathered basaltic compositions.

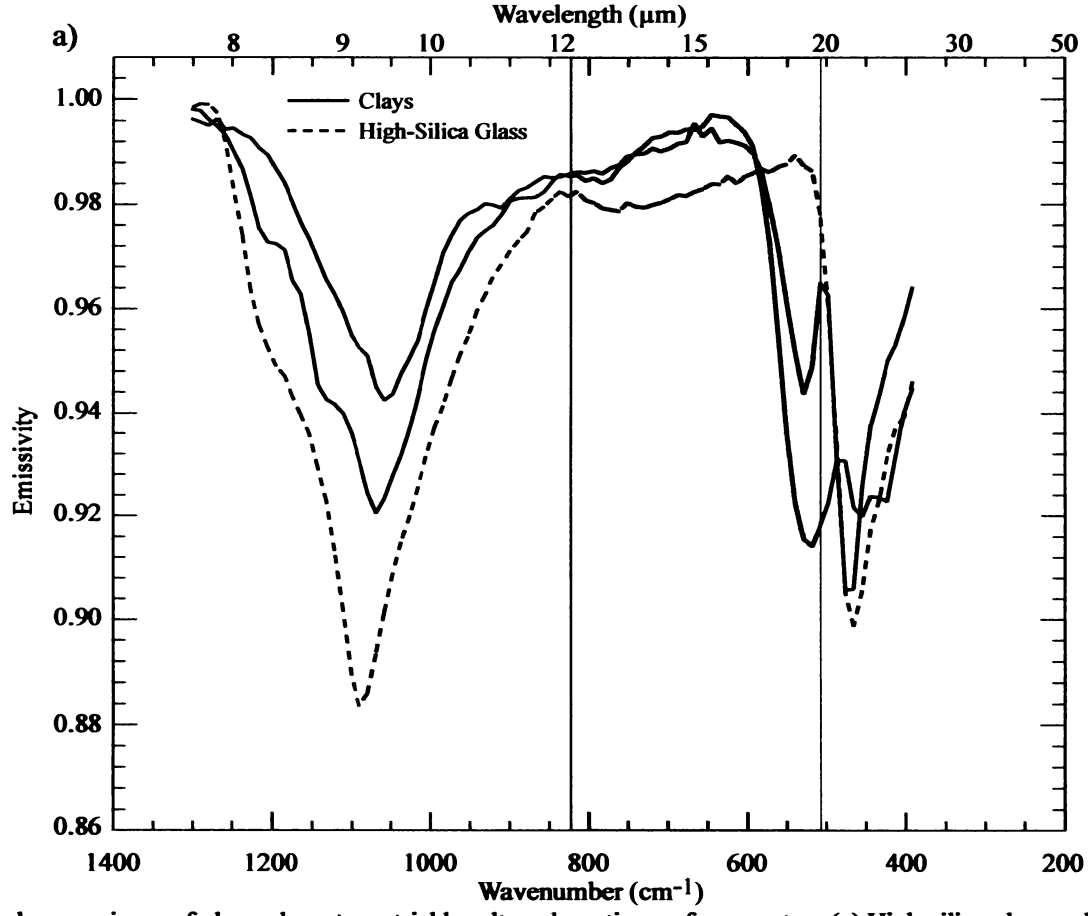


Figure 2: Spectral comparisons of glass, clays, terrestrial basalt, and martian surface spectra. (a) High-silica glass and two clays (Fe-Smectite and Ca-Montmorillonite), and (b) fresh-cut and weathered surface of a CRB sample [Wyatt et al., 2001; Hamilton et al., 2001] compared to Surface Type 1 and 2 spectra, respectively (offset by .06 emissivity for clarity). Blackbody was added to each terrestrial rock sample to account for band depth particle size effects.

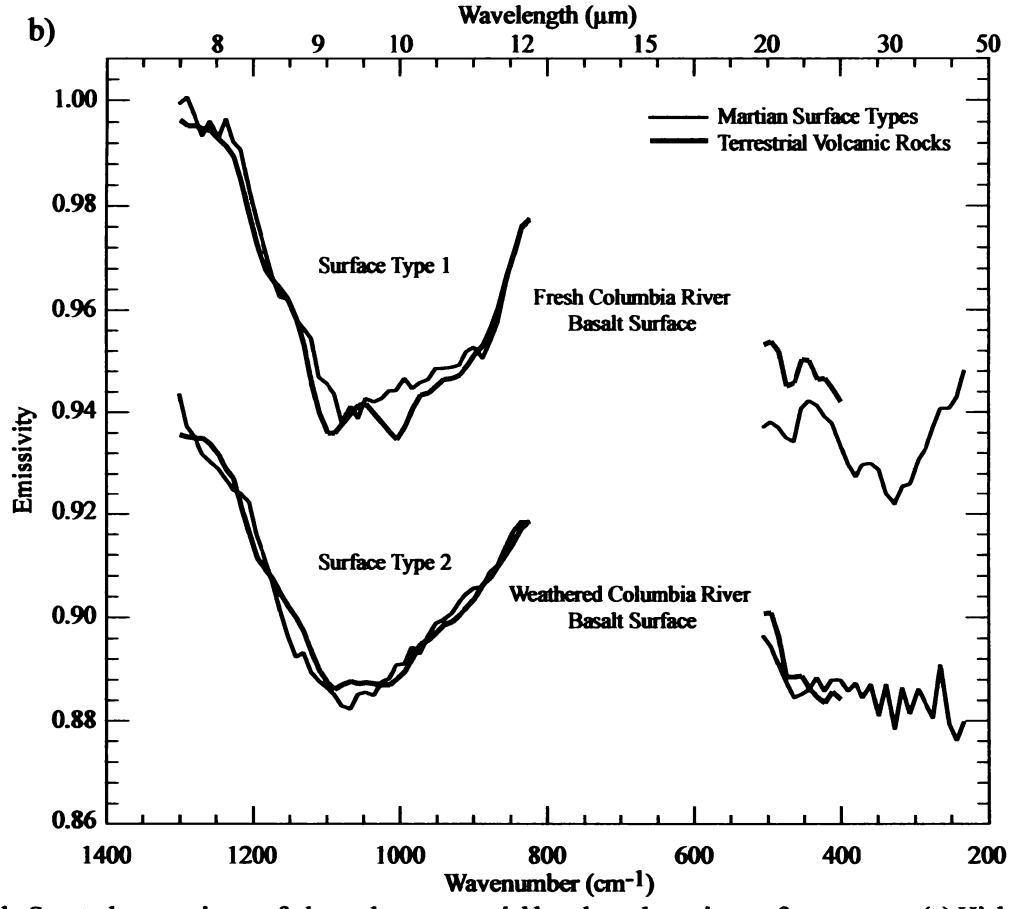


Figure 2 Continued: Spectral comparisons of glass, clays, terrestrial basalt, and martian surface spectra. (a) High-silica glass and two clays (Fe-Smectite and Ca-Montmorillonite), and (b) fresh-cut and weathered surface of a CRB sample [Wyatt et al., 2001; Hamilton et al., 2001] compared to Surface Type 1 and 2 spectra, respectively (offset by .06 emissivity for clarity). Blackbody was added to each terrestrial rock sample to account for band depth particle size effects.

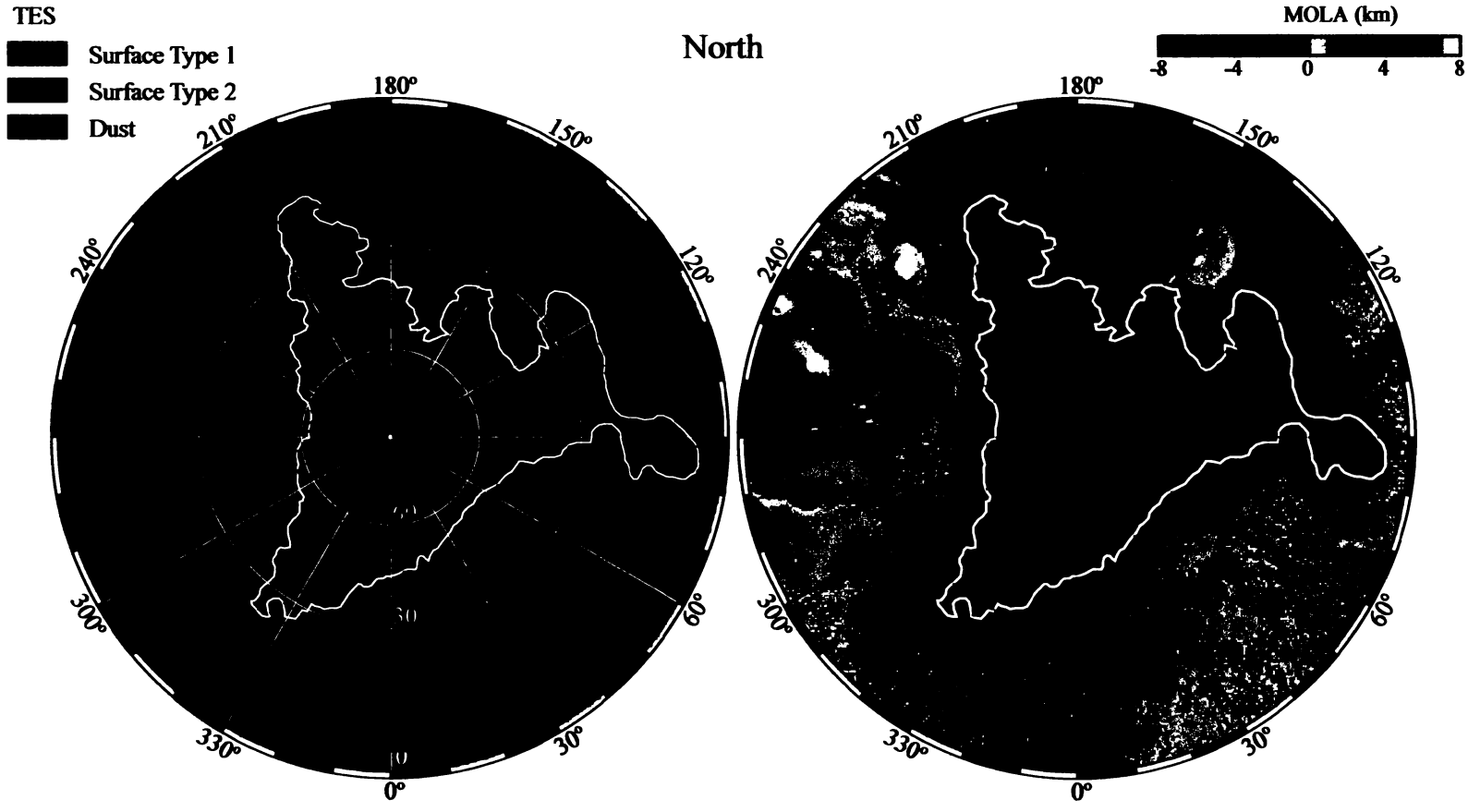


Figure 3: Global distribution of Surface Types 1 and 2 as determined by Bandfield et al. and global topography determined from MOLA data [Smith et al., 1999]. Surface Type 2 compositions in the northern hemisphere map closely to a proposed ocean basin [Parker et al., 1989], as delineated by elevation and a possible shoreline (white line) [Head et al., 1999].

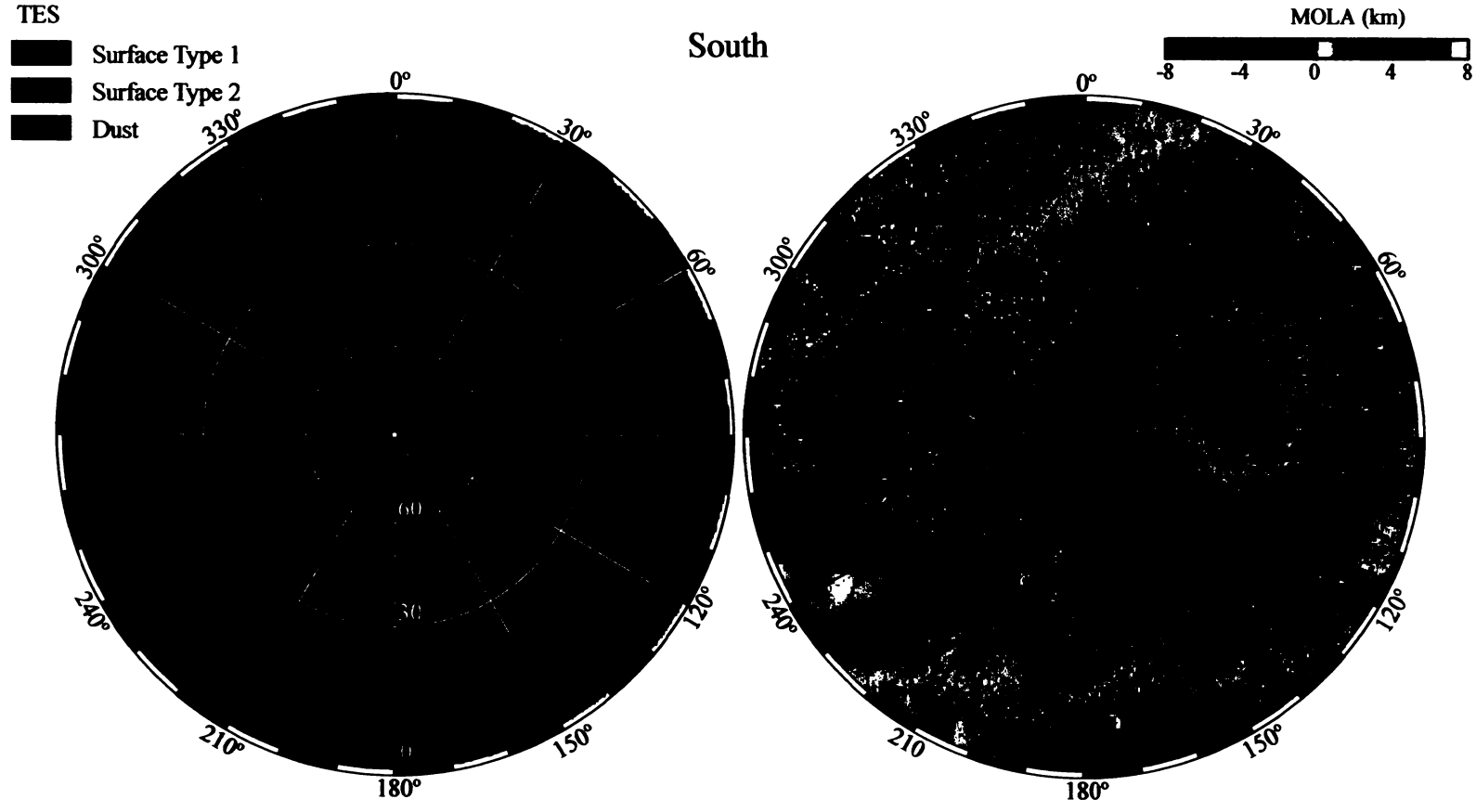


Figure 3 Continued: Global distribution of Surface Types 1 and 2 as determined by Bandfield et al. and global topography determined from MOLA data [Smith et al., 1999]. Surface Type 2 compositions in the northern hemisphere map closely to a proposed ocean basin [Parker et al., 1989], as delineated by elevation and a possible shoreline (white line) [Head et al., 1999].

Part 4

Analysis of Surface Compositions in the Oxia Palus Region on Mars from Mars Global Surveyor Thermal Emission Spectrometer Observations

This chapter is in preparation to be submitted to the *Journal of Geophysical Research* in 2002 by Michael B. Wyatt, Joshua L. Bandfield, Harry Y. McSween Jr., Jeffrey Moersch, and Phillip R. Christensen.

Abstract

We examine the distribution of Thermal Emission Spectrometer (TES) derived surface compositions in the Oxia Palus region on Mars through high-spatial resolution mapping and integration with Mars Orbiter Camera (MOC) and Mars Orbiter Laser Altimeter (MOLA) datasets. We also fit the basalt-andesite [*Bandfield et al.*, 2000] and basalt-weathered basalt [*Wyatt and McSween*, 2002] interpretations of TES Surface Type 1 and Type 2 materials into multiple working hypotheses to describe the origin of surface materials in local and regional scales. Local regions of interest include volcanic/sedimentary materials in southern Acidalia Planitia, low-albedo crater floors and wind streaks in western Arabia Terra, and the channel outflow deposits of the Mars Pathfinder (MP) landing site in Chryse Planitia. Regionally, Surface Type 1 materials dominate the low-albedo southern highlands and Surface Type 2 materials dominate the low-albedo northern lowlands. A mixing/transition from Surface Type 1 to Type 2 compositions is observed in the low-albedo regions of southern Acidalia Planitia. This gradational boundary may represent either (1) an influx of basaltic sediment from the southern highlands, deposited on and mixed with andesitic volcanics; (2) an influx of water-transported basaltic sediment from the southern highlands that was altered and later

deposited as a thin sedimentary veneer; or (3) different degrees of weathering of basalt marking the geographic extent of submarine alteration of basaltic crust. Evaluation of the models on local to regional to global scales supports the "wet" transport and/or indigenous coastal marine models involving basalt and weathered basalt. Both hypotheses fit within the existing geologic scenarios describing the sedimentary and volcanic history of the Oxia Palus region, and are also consistent on a global-scale. Deconvolved TES spectra of low albedo intracrater materials in western Arabia Terra reveal both Surface Type 1 and 2 compositions within individual craters where complete TES coverage is available. Surface Type 1 compositions form a central core in dark features on crater floors while Surface Type 2 compositions form a surrounding arc on the dark downwind sides of crater walls. The transition between these compositions appears to occur near the floor-wall interface within some impact craters. The compositional transition coincides with decreasing thermal inertia values that are interpreted to reflect decreasing particle sizes, possibly controlled by mineralogic differences between a largely unweathered basalt component and an andesite/altered basalt component. Intracrater floor materials are interpreted as eolian sediment blown into impact craters. Intracrater wall materials are interpreted as either eolian sediment sorted by particle size, or eroded material from in-place crater wall lithologies. Surface Type 1 and 2 compositions are also observed in adjacent low albedo wind streaks; however, a mixing trend is not as evident as within the impact craters. There does not appear to be a discernable compositional difference across (east-west) dark wind streak material and the often observed bright red deposits along their margins. This distribution may support both deflation and erosional models for the formation of wind streaks. The

Mars Pathfinder landing site and Ares and Tiu Valles source regions are sufficiently blanketed by fine-grained dust to prohibit the analysis of surface rock compositions. Despite the fact that the MP site is one of the rockiest places on the planet and that dust apparently covers only the upper surfaces of rocks, spectral observations at multiple emission angles remain obscured by dust in the atmosphere.

1. Introduction

Atmospherically corrected thermal emissivity data [*Bandfield et al.*, 2000a; *Smith et al.*, 2000] from the Mars Global Surveyor (MGS) Thermal Emission Spectrometer (TES) have been used to identify two unique global-scale surface lithologies [*Bandfield et al.*, 2000b; *Christensen et al.*, 2000a]. Surface Type 1 and Type 2 spectral units are divided roughly along the planetary dichotomy which separates ancient, heavily cratered crust in the southern hemisphere from younger lowland plains in the north [*Bandfield et al.*, 2000b; *Rogers et al.*, 2001]. The Surface Type 1 spectral end-member is characterized by high abundances of plagioclase and pyroxene and is interpreted as largely unweathered basalt [*Christensen et al.*, 2000a; *Bandfield et al.*, 2000b; *Hamilton et al.*, 2001]. The Surface Type 2 spectral end-member has been interpreted both as andesite with high modal plagioclase and volcanic glass and low modal pyroxene [*Bandfield et al.*, 2000b; *Hamilton et al.*, 2001] and as partly weathered basalt with high modal plagioclase and alteration phases (clays and silica coatings) and low modal pyroxene [*Wyatt and McSween*, 2002].

The Oxia Palus quadrangle on Mars is unique in that it encompasses the geographic and compositional transition between the southern highlands and northern

lowlands and Surface Type 1 and 2 lithologies, as well as past spacecraft landing sites that may provide ground truth for spectral interpretations from orbit. In this study, we examine the distribution of TES-derived Surface Type 1 and 2 materials in Oxia Palus through high-spatial resolution mapping, and integrate Mars Orbiter Camera (MOC) and Mars Orbiter Laser Altimeter (MOLA) datasets for a detailed description of the martian surface. The diversity of observable landforms in Oxia Palus, which reflect both active geologic processes and remnants of paleoclimate effects, have made this one of the most studied regions on Mars. Features of interest within Oxia Palus for this study include volcanic/sedimentary materials in southern Acidalia Planitia, low-albedo crater floors and wind streaks in western Arabia Terra, and the channel outflow deposits of the Mars Pathfinder (MP) landing site in Chryse Planitia. We also attempt to fit the basalt and andesite/weathered basalt interpretations of the TES surface types into multiple working hypotheses to describe the origin of surface materials on local and regional scales.

2. Geologic Setting

Within the Oxia Palus quadrangle (0-45W longitude, 0-30N latitude), the northern lowland terrains of Chryse and Acidalia Planitiae are bounded by the southern highland terrains of Xanthe and Arabia Terrae (Figure 1, MOC Composite Image). Relative ages of northern lowland materials based on the crater-density stratigraphy of *Tanaka* [1986] range from Late Noachian to Early Amazonian while older southern highland materials range in age from Middle Noachian to Early Hesperian. In ascending stratigraphic order, the exposed surface units within the Oxia Palus quadrangle are (1) the Middle to Late Noachian southern-cratered terrain, (2) the Hesperian-aged Vastitas Borealis Formation,

a unit interpreted to be degraded lava flows and sediments, (3) Hesperian-aged outflow channel deposits at the margins of the lowlands in Chryse Planitia, (4) and various local Amazonian-aged plains units [*Head et al.*, 2002].

Northern Lowlands: Chryse Planitia makes up the southern portion of a basin with elevations ranging from 0 to -2000 m (relative to geoid) and grades north into Acidalia Planitia with elevations decreasing to -4000 m. Several large outflow channels (Ares, Simud, and Tiu Valles) empty into Chryse Planitia and eventually grade into broad relatively smooth plains further north in Acidalia Planitia. The MP landing site was selected in Chryse Planitia partly because of the expected high rock abundances [*Edgett*, 1997] in the Ares and Tiu Valles outflow deposits. High rock abundances at the landing site were confirmed by Imager for Mars Pathfinder (IMP) observations that showed the area to be strewn with large boulders, although with significant amounts of surface dust coatings [*Rieder et al.*, 1997a]. Chryse and Acidalia Planitiae landforms and surface materials have been variously interpreted as subaerially emplaced mass flows [*Tanaka*, 1997], coastal marine [*Parker et al.*, 1993], and residual sedimentary deposits [Head et al., 2002]. A curved dashed white line displayed in Figure 1 marks the extent of a proposed ancient shoreline for a large standing body of water in southern Acidalia Planitia [*Parker et al.*, 1993; *Head et al.*, 1999]. A curved solid white line in Figure 1 marks the southern extent of the Vastitas Borealis Formation [*Head et al.*, 2002]

Southern Highlands: Xanthe Terra is part of the heavily cratered highlands and is cut by long systems of grabens in the Valles Marineris system of canyons to the west. Arabia Terra has numerous impact craters with large low-albedo wind streaks emanating from low-albedo splotches on crater floors. Most models for the formation of dark

intracrater splotches involve the entrapment of sand-sized particles that can be transported into, but not out of, craters by wind [e.g. *Arvidson*, 1974; *Christensen*, 1983; *Thomas*, 1984]. Several hypotheses exist for the origin of adjacent low-albedo wind streaks. Some models interpret them to be a result of saltation and traction [e.g. *Arvidson*, 1974; *Thomas et al.*, 1981], consisting of sandy material deflated from adjacent dark intracrater deposits, or others the result of material being stripped from the surface revealing a darker substrate [e.g. *Soderblom et al.*, 1978]. More recent models have proposed that streaks form by the deposition of fine dark silt from plumes of suspended material [*Thomas and Veverka*, 1986]. This view is now supported by MOC observations that suggest the dark materials are mantle deposits of fine-grained sediment deflated from adjacent crater floors, not sand-sized particles [*Edgett*, 2002].

The Sinus Meridiani and Aram Chaos hematite regions in Terra Meridiani identified by TES also occur partly within the Oxia Palus quadrangle [*Christensen et al.*, 2000; *Christensen et al.*, 2002]. A range of possible mechanisms for the formation of coarse-grained, crystalline hematite on Mars was critically examined by Christensen et al. [2000], with a favored interpretation proposed as in-place sedimentary units composed primarily of basaltic sediment with ~10-15% crystalline gray hematite.

3. Datasets

3.1 Thermal Emission Spectrometer

Thermal infrared spectral observations by the TES instrument cover the wavelength range from 1700 to 200 cm^{-1} (~6 to 50 μm) at 10 or 5 cm^{-1} sampling [*Christensen et al.*, 1992]. A complete description of the TES instrument, radiometric

calibration, and instrument-related errors is found in *Christensen et al.* [2001]. Spectra used for analysis of surface compositions were collected from the start of the mapping orbit dataset up to orbit 5317 (ock 7000, L_s 104-352). The orbit range is restricted due to an anomaly, possibly caused from vibrations with the MGS spacecraft, that causes a sporadic minor feature to appear in TES spectral data at ~1000 cm^{-1} in orbits after 5317. Only data at 10 cm^{-1} sampling is examined in this study, which is approximately 99% of the total data collected from this orbit range. Spectra are limited to those with surface temperatures > 250K, dust extinctions of < 0.18 (1075 cm^{-1} opacity of approximately 0.3), and water ice extinctions of < 0.1 (800 cm^{-1} opacity of approximately 0.15) to ensure a high surface signal to noise ratio [*Bandfield et al.*, 2000a]. A data restriction of emission angles < 30° is applied everywhere except the MP landing site, when higher multiple emission angles are examined in an effort to analyze rock surfaces with less bright dust coverings. Multiple emission angle observations, or emission phase functions (EPF), are taken with the TES pointing mirror at several angles in the fore and aft direction during orbit passes creating a mosaic of the targeted surface. Fine-grained dust closely resembles a featureless blackbody spectrum in the wavelengths studied and can mask underlying rock compositions from analysis if sufficient coverings are present [*Crisp and Bartholomew*, 1992].

TES emissivity spectra are linearly deconvolved using average global martian surface and atmospheric spectral end-members [*Bandfield et al.*, 2000a; *Smith et al.*, 2000; *Bandfield et al.*, 2000b] to derive surface compositions in Oxia Palus. The least squares fit algorithm, output results, and method used are fully described in *Ramsey and Christensen* [1998], *Bandfield et al.* [2000a], *Christensen et al.* [2000a], and *Smith et al.*

[2000]. The Surface Type 1 and 2 [*Bandfield et al.*, 2000b] spectral end-members, mixtures of the two units, and hematite [*Christensen et al.*, 2000c] have been demonstrated to represent accurately the surface composition of all major low-albedo regions on Mars covered by TES [*Bandfield et al.*, 2000b].

Concentrations of Surface Type 1 and 2 materials, derived from the linear deconvolution of individual TES emissivity spectra, are binned and averaged into maps of 8 and 16 pixels/degree for regional and high-resolution views respectively. One square pixel in a TES high-resolution composition map represents approximately a 3.7 km by 3.7 km area at the martian equator. Each measured TES spectrum represents the average emissivity of an approximate 3 km by 9 km footprint on the martian surface. Surface concentrations from overlapping TES spectra are averaged within the TES composition maps to improve the signal to noise ratio. The elongated pixel dimension for measured TES spectra is due to the final mapping orbit of MGS being reversed relative to the martian surface because of a damaged solar panel that caused an extended aerobraking phase. Image motion compensation was originally designed to compensate for the MGS orbit direction; however, it does not produce the intended result when stepping the targeting mirror in a direction opposite that which was originally intended. Averaging derived surface compositions from TES emissivity spectra from different orbits raises the possibility that different atmospheric conditions were present during data collection. However, data are filtered to exclude extreme atmospheric conditions (dust storms, ice clouds) and atmospheric components have been demonstrated by *Bandfield et al.* [2000a] to combine in an extremely linear manner.

To better understand the physical nature of surface materials, we also examine thermal inertia values derived from TES bolometric thermal radiance (5.1 to 150 μm) measurements. Thermal inertia is the primary factor controlling the amplitude of the diurnal variation of surface temperature, and is most strongly dependent on the thermal conductivity of the surface materials. Thermal inertia is defined as a combination of thermal conductivity k, density ρ, and heat capacity c :

$$I \equiv \sqrt{k\rho c} \quad (1)$$

Thermal inertia depends primarily on the average particle size of the grains comprising the surface, the size and abundance of rocks on and near the surface, and the degree of induration of duricrust. Low-albedo regions comprise about 50% of the martian surface and have thermal inertias and spectral contrasts expected for sand-sized particles [e.g. *Kieffer et al.*, 1977; *Presley and Christensen.*, 1997], enabling detailed analysis of surface compositions. For a complete description of how thermal inertia is calculated, see *Mellon et al.* [2000].

3.2 Mars Orbiter Camera

MOC narrow angle (NA) and wide angle (WA) images are obtained at spatial resolutions of 1.5 to 6 m/pixel and 240 to 7500 m/pixel respectively. A description of the MOC instrument is detailed by *Malin and Edgett* [2001]. Available images for this study were acquired between September 1997 and December 2001, and all images were obtained with the MGS spacecraft in a nadir-viewing orientation. WA mosaics are provided courtesy of NASA/JPL/Malin Space Science Systems and provide the context for NA images that are used for high-resolution detailed mapping.

3.3 Mars Orbiter Laser Altimeter

MOLA topography data are used to create digital topographic maps and 3-D shaded relief images of the martian surface in Oxia Palus. For a complete description of the MOLA instrument, analytical techniques, and instrument-related errors, see *Zuber et al.* [1992]. MOLA data are binned in a ~500 m/pixel grid [courtesy M. Carr, MOLA Science Team] and are used as a base map for overlaying TES compositional maps and MOC NA and WA images.

3.4 Dataset Registration

The TES, MOC, and MOLA datasets are all defined by latitude and longitude coordinates. When these datasets are translated to a map projection, each dataset will also be defined in a Cartesian coordinate system as described by the selected projection. Map projected TES compositional images, MOC composite images, and MOLA Digital Elevation Maps (DEMs) are aligned in ArcView (ESRI) based on their Cartesian coordinates. In ArcView, for raster datasets, this is expressed by the top left pixel location and the pixel dimension in map units (i.e. meters). Each dataset can then be overlain and merged together within the ArcView software interface. Changes to map locations can also be done manually to compensate for any small offsets in registration of map-projected images.

4. Distribution of TES Surface Compositions

4.1 Regional View

Figure 2 shows the regional distribution of Surface Type 1 (green) and 2 (red) lithologies in Oxia Palus derived from linear deconvolution of TES emissivity spectra.

Blue pixels on the TES composition map represent areas covered by fine-grained bright dust which sufficiently blankets the surface to prohibit spectral analysis of sand and rock compositions. The "concentration" of fine dust was determined not from linear deconvolution, but instead by using the derived TES dataset index parameter "long-wavelength depth" which distinguishes between light and dark regions. This parameter has proven useful in mapping where coarse particles are located on the martian surface, and hence where fine dust is absent, and correlates very well with albedo and thermal inertia [*Bandfield*, 2000c]. Yellow pixels indicate mixing of Surface Type 1 and 2 materials, whereas black stripes and pixels indicate a lack of surface coverage data.

Surface Type 1 dominates the southern highlands of Xanthe Terra and southern Arabia Terra, and Surface Type 2 dominates northern Acidalia Planitia. Both surface types coincide well with observed low-albedo regions, despite the higher uncertainty with Surface Type 2 due to random and systematic noise inherent in this spectral signature [*Bandfield et al.*, 2000a]. A mixing/transition from Surface Type 1 to Surface Type 2 (south to north) compositions is observed in low-albedo regions marking the southern extent of Acidalia Planitia and northeastern extent of Chryse Planitia.

The MP Landing site (marked with an X in Figure 2) is located in an area that appears to be mostly covered by fine grained dust, near the Surface Type 1 and Type 2 transition in southern Acidalia Planitia. This initial regional TES observation agrees with Mars Pathfinder IMP observations of the landing site showing that the tops of rocks, and surfaces in between rocks, are largely covered by fine-grained dust [*McSween et al.*, 1997]. Ares and Tiu Valles show a similar covering of fine-grained dust. Low-albedo crater floors and wind streaks in western Arabia Terra, however, show strong

concentrations of Surface Type 1 and 2 materials even at a regional scale (outline of box in Figure 2).

4.2 Southern Acidalia Planitia

The mixing/transition from Surface Type 1 to Surface Type 2 (south to north) compositions in the low-albedo regions of southern Acidalia Planitia is focused on in Figure 3. Two gray-scale TES maps (16 pixels/degree) show the concentrations of Surface Type 1 and Type 2 materials in panels (A) and (B) respectively. Panel (C) is a gray-scale MOLA shaded relief image sampled at 500 m/pixel and panel (D) is a mosaic of MOC images of the same area. Superimposed on all panel images is a curved dashed line marking the extent of a proposed ancient shoreline for a large standing body of water in southern Acidalia Planitia [*Parker et al.*, 1993; *Head et al.*, 1999] and a curved solid line marking the southern extent of the Vastitas Borealis formation [*Head et al.*, 2002]. The images in Figure 3 extend north of 30°N, which marks the northern extent of the Oxia Palus quadrangle, to show the distribution of surface materials in a greater area of Acidalia Planitia. Red boxes indicate locations of TES surface spectra shown in Figure 4.

Panel (A) in Figure 3 clearly shows the narrow extent of Surface Type 1 materials in southern Acidalia Planitia while Panel (B) shows the range of Surface Type 2 materials across nearly all of Acidalia Planitia. Surface Type 1 materials are located predominately south of the proposed shoreline and the Vastitas Borealis formation while Surface Type 2 materials dominate to the north with some crossover of the shoreline. A comparison between panels (A) and (B) with the MOLA map in panel (C) shows that Surface Type 1 materials in the mixing/transition zone occur mainly near the highlands/lowlands

transition while Surface Type 2 materials are concentrated in the northern lowlands of Acidalia Planitia.

Figure 4 compares average TES surface spectra for materials at the southern extent of the mixing/transition band with materials to the north (Figure 3 Red Boxes). Also shown in Figure 4 are the Surface Type 1 and 2 spectral end-members from *Bandfield et al.* [2000], offset by 0.02 emissivity for comparison purposes. Within the southern portion of the mixing band, surface components contain a broad, flat absorption between ~800-1000 cm^{-1} and absorption through ~200-500 cm^{-1}. In the northern transition surface components contain a more V-shaped absorption between ~800-1000 cm^{-1} and more uniform slope between ~200-500 cm^{-1}. Linear deconvolution of these spectra using the Surface Type 1 and 2 end-members reveal the surface spectrum from the southern portion of the band is dominated by a Surface Type 1 component (~ 60 vol %), but with a significant contribution of Surface Type 2 material (~ 40 vol %). The reverse is seen to the north, where the surface spectrum is dominated by a Surface Type 2 component (~ 66 vol %) with a significant contribution of Surface Type 1 material (~ 34 vol %).

4.3 Low-Albedo Crater Floors and Wind Streaks

Deconvolved TES spectra of low albedo intracrater materials in western Arabia Terra reveal both Surface Type 1 and 2 compositions within individual craters where complete TES coverage is available. Surface Type 1 compositions form a central core in dark features on crater floors while Surface Type 2 compositions form a surrounding arc on the dark downwind sides of crater walls. The transition between these compositions appears to occur near the floor-wall interface within some impact craters. Surface Type 1

and 2 compositions are also observed in the adjacent low albedo wind streaks; however, a mixing trend is not as evident as within the impact craters. There does not appear to be a discernable compositional difference across (east-west) dark wind streak material and the often observed bright red deposits along their margins.

Figure 5 shows a composite MOC image (A), a TES compositional map (B), and a TES thermal inertia map (C) of Radau and Marth craters, which are outlined by a white box in the MOC composite image of Figure 1 and TES regional view of Figure 2. Radau Crater (17.1°N, 4.8°W: 114.5 km diameter) and Marth Crater (13.0°N, 3.5°W: 98.4 km diameter) are representative of many large impact craters in western Arabia Terra that have both an intracrater low albedo feature on part of the southern crater floor and an adjacent dark wind streak that extends southward from the dark material (Fig. 1). The Radau Crater composition image (Fig. 5B) clearly shows the core of Surface Type 1 (green) and surrounding arc of Surface Type 2 (red) in the intracrater low albedo feature. The Marth Crater composition image shows the Surface Type 1 core and part of the Surface Type 2 rim; however, some dark rim material is not covered by TES observations. The thermal inertia map of Marth Crater (Fig. 5C) shows higher values for Surface Type 1 materials (~ 400-550 $J/m^2Ks^{1/2}$) compared to Surface Type 2 materials (~ 300-400 $J/m^2Ks^{1/2}$). The thermal inertia map of Radau Crater (Fig. 5C) partly shows an edge of high thermal inertia material in the low-albedo crater floor, but TES coverage is incomplete. Higher thermal inertias may be interpreted as representing a coarser particle size compared to lower thermal inertias if materials are unconsolidated sediments.

Figure 6 shows a composite MOC image of Radau Crater (southward looking) with superimposed TES composition pixels draped over MOLA topography. The core of

Surface Type 1 and arc of Surface Type 2 materials on the crater floor and walls are clearly observed. Also shown in Figure 6 is a NA MOC image across the crater floor/wall interface with a schematic cross section of MOLA topography and TES compositions. The location of the NA MOC image on the MOC composite image is shown in the Radau Crater inset figure. The transition from Surface Type 1 to Surface Type 2 compositions occurs near the crater floor/wall interface and is correlated with a transition from low-albedo dune materials to low-moderate albedo dune-free materials. The absence of dunes in wall materials, and lower measured thermal inertias, may be interpreted as representing finer particle sizes compared to the higher thermal inertia dune material on crater floors.

Figure 7 shows average TES surface spectra for materials within the low-albedo Radau impact crater floor and the slope of crater walls compared to Surface Type 1 and 2 spectral end-members from *Bandfield et al.* [2000], which are offset by 0.02 emissivity. Within the impact crater floors, surface components contain a broad, flat absorption between ~800-1000 cm^{-1} and absorption through ~200-500 cm^{-1} very similar to the Surface Type 1 endmember. Along the impact crater walls, the surface components contain a V-shaped absorption between ~800-1000 cm^{-1} and more uniform slope through ~200-500 cm^{-1} similar to the Surface Type 2 end-member. Linear deconvolution of crater floor and wall spectra using the Surface Type 1 and 2 end-members confirm the general comparison of spectral features. Impact crater floor materials are almost entirely dominated by a Surface Type 1 component (~ 75-100 vol %), whereas impact crater wall materials are dominated by Surface Type 2 material (~ 75-100 vol %).

4.4 Mars Pathfinder Landing Site and Source Regions

The MP landing site is among the rockiest locations on the planet; however, nearly all of the rocks have significant amounts of surface dust mantles [*McSween et al.*, 1997a]. For this reason, MP offers an ideal opportunity to test whether rock compositions can be resolved in dust-covered regions. Furthermore, the APXS analyses of rocks having andesitic compositions [*Rieder et al.*, 1997a; *McSween et al.*, 1999] offers groundtruth data for interpreting mineralogies and chemistries derived from thermal infrared spectra measured from orbit.

Figure 8 shows a composite MOC image of Chryse Planitia with the MP landing site and arrows indicating flow directions in the Ares and Tiu Valles outflow channels [*Tanaka*, 1997]. The image is not centered on the MP landing site because the goal of this analysis is to determine whether compositional information can be obtained from both the landing site and its source region to the south. Superimposed on the composite MOC image are boxes representing averaged and binned TES composition pixels at 3.7 km by 3.7 km. At a high-resolution scale, TES coverage of the martian surface in this region is not complete with data that pass the data filters used in this study. Figure 9A shows a high-resolution MOC NA image of the landing site, with a higher resolution part of the WA mosaic from Figure 8 for reference, and Figure 9B shows an average TES surface spectrum of the MP landing site compared to the Surface Type 1 and 2 spectral endmembers which are offset by 0.02 emissivity. Also shown in Figure 9B are average spectra of the Ares and Tiu Valles source regions.

The landing site and source region spectra show much shallower spectral absorptions compared to the Surface Type 1 and 2 spectra. While there are some spectral

absorption features observed in the landing site and source regions spectra, their depth is too small to have confidence in any linear deconvolution results. The tops of rocks and intervening ground surfaces at the landing site were observed to be covered by bright fine-grained dust. The apparent spectral roll-off feature at ~ 1150 cm^{-1} observed in the MP spectra in Figure 9B is a typical result of fine particle size effects [*Christensen et al.*, 2000a]. The fine-grained surface dust, which closely resembles a featureless blackbody spectrum, thus appears to be sufficiently abundant to obscure analysis of rock compositions from TES observations.

The TES instrument is capable of making emission phase function (EPF) observations by using a pointing mirror to measure a surface at various emission angles along an orbital track. Such measurements could potentially enable TES to observe the sides of rocks at the Mars Pathfinder landing site, instead of only the top surfaces which are covered by fine-grained dust. The sides of rocks at the landing site were observed by the IMP camera to have lower albedos compared to the tops of rocks, and were targeted by the Alpha Proton X-Ray Spectrometer (APXS) instrument for chemical analyses of dust free surfaces.

Figure 10 is a plot of albedo vs ICK (Incremental Counter Keeper) for an EPF mosaic of the MP landing site. ICK is the sequential numbering scheme for observations of the TES interferometer and the counter begins at zero at the night-side equator crossing. With increasing ICK, the five data clusters in Figure 10 correspond to different emission angle measurements from forward facing emission observations of 46° and 26°, to one nadir observation, followed by reverse facing emission angle observations of 26° and 46°. Figure 10 shows that EPF observations at higher emission angles do not result

in a significant decrease in surface albedo (note vertical scale), i.e. a greater spectral contribution by non-mantled rock surfaces. This is possibly due to the increased amount of atmospheric dust observed with increasing emission angle observations through thicker portions of the martian atmosphere. The composition of atmospheric and surface dust is still very uncertain, which makes their removal from EPF observations difficult. For this reason, EPF observations of the MP landing site cannot be used to analyze sides of rocks at this time.

5. Discussion

The distributions of Surface Type 1 and 2 materials, combined with the basalt [*Christensen et al.*, 2000a; *Bandfield et al.*, 2000b; *Hamilton et al.*, 2001] and andesite [*Bandfield et al.*, 2000b; *Hamilton et al.*, 2001] or weathered basalt interpretations [*Wyatt and McSween,* 2002], allow for multiple working hypotheses to describe the origins of these materials. In the following sections we re-interpret the mixing/transition of Surface Type 1 and 2 materials in southern Acidalia Planitia and low-albedo impact crater floors and adjacent wind streaks in western Arabia Terra, and attempt to fit TES observations to models describing the sedimentary and igneous history of Oxia Palus.

5.1 Southern Acidalia Planitia

In the following discussion, we examine three geologic models involving transport of material and/or in-place aqueous alteration to describe the observed transition from Surface Type 1 to Type 2 materials in southern Acidalia Planitia. The transport models are "dry" or "wet" and require the movement of material from the southern highlands to northern lowlands via large outflow channels in Chryse Planitia. The "dry"

transport model is analogous to the subaerially emplaced mass flow model proposed by *Tanaka* [1997] that does not involve or require water as a means for mass movement. The "wet" transport model is analogous to the residual sedimentary deposit model proposed by *Head et al.* [2002] that involves the deposition of water and sedimentary material in the northern basin and the subsequent loss of water and formation of a residual sedimentary layer. The third geologic model is an indigenous aqueous-alteration hypothesis; analogous to a coastal marine model proposed by *Parker et al.* [1993] that involves the alteration of in-place volcanic materials beneath an ancient northern ocean. Figure 11 illustrates all three geologic models that are described in detail in the following sections.

Mixture of Basalt and Andesite: Subaerially emplaced "dry" mass flows [*Tanaka*, 1997] could explain the observed mixing band of Surface Type 1 and Type 2 compositions if interpreted as basalt and andesite. Surface Type 1 material transported to southern Acidalia Planitia by large outflow channels in Chryse Planitia originated toward the southern highlands, which is dominated by basaltic materials (Figure 11). The basalt-dominated mixing band marking the southern extent of Acidalia Planitia could represent the maximum extent of sediment transport from these channels. In this scenario, the andesite in central Acidalia is interpreted as regionally indigenous volcanic material that was partly covered and mixed with basaltic sand transported from the south (Figure 11). Transported basaltic materials would thus also dominate the dust-covered region between this band and the basalt-dominated southern highlands.

Mixture of Basalt and Weathered Basalt: Residual sedimentary "wet" deposits [*Head et al.*, 2002] and/or indigenous coastal marine sediments [*Parker et al.*, 1993]

could explain the observed mixing band of Surface Type 1 and 2 compositions if interpreted as basalt and weathered basalt. Figure 11 shows the extent of the Hesperian Vastitas Borealis Formation in southern Acidalia Planitia, which has been interpreted as a thin veneer of residual sediment deposited on top of older Hesperian ridged material [*Head et al.*, 2002]. The Vastitas Borealis formation occupies about 45% of the entire northern lowlands [*Tanaka and Scott*, 1987] and has been proposed by *Head et al.* [2002] to represent material transported to the north by large volumes of water. Also shown in Figure 11 are geomorphic contacts previously interpreted as ancient shorelines [*Parker et al.*, 1993]. The elevations of these contacts been examined with high-resolution MOLA data and found to approximate an equipotential line [*Head et al.*, 1999], supporting the hypothesis of an ancient ocean basin.

In a "wet" deposit model, Surface Type 1 material originating in the basalt-dominated southern highlands was transported to southern Acidalia Planitia by floods that carved the large outflow channels in Chryse Planitia. The transported basaltic material was altered where water ponded, and was later deposited as a thin residual veneer (Vastitas Borealis Formation) when the water was lost. Figure 11 shows that the Vastitas Borealis formation contact coincides very well with the transition between Surface Type 1 basalt and Type 2 weathered basalt.

In an indigenous coastal marine model, the transition between the two surface types marks the southern extent of submarine alteration of indigenous basalt caused by large bodies of standing water in the northern lowlands. Shoreline contacts in Chryse and Acidalia Planitiae (Figure 11) also coincide very well with the transition zone between Surface Type 1 basalt and Type 2 weathered basalt. The basalt-dominated band and large

volume of weathered basalt in central Acidalia are both interpreted in this scenario as indigenous materials reflecting a progression of more advanced alteration of basalt towards deeper water levels.

The transport model does not directly address the presence or absence of long-term, large standing bodies of water (oceans?) in the northern lowlands. It does, however, provide possible insight into the origin of some unusual surface properties in the region. The northern lowlands, including southern Acidalia Planitia, are extremely smooth at several scale lengths, comparable to abyssal plains on Earth [e.g. *Smith et al.*, 1998; *Aharonson et al.*, 1998; *Head et al.*, 2002]. The emplacement of aqueously altered outflow channel deposits could provide a mode of formation for this smoothing [*Head et al.*, 2002]. This explanation does not preclude the presence of oceans, as they could have existed prior to material transport (Noachian [e.g. *Clifford and Parker*, 2001]). However, in this case, sediment transported into pre-existing large bodies of water and later deposited would result in a similar thin veneer of altered material (Vastitas Borealis formation).

In summary, the basalt and andesite/weathered basalt interpretations allow for multiple working hypotheses to describe the origin of the Surface Type 1 and Type 2 mixing/transition in southern Acidalia Planitia. The "dry" transport model and "wet" transport and/or indigenous coastal marine models fit within existing geologic scenarios describing the sedimentary and volcanic history of the region. However, by evaluating these models in a global-scale context, the "dry" transport model is not favored. The "dry" transport model requires Surface Type 2 material in southern Acidalia Planitia to be interpreted as indigenous andesitic materials. At this local to regional scale, the

occurrence of high-silica volcanic materials like andesite can be explained by fractionation of basaltic magma. However, this component in southern Acidalia Planitia extends far beyond the Surface Type 1 and Type 2 mixing/transition region, and covers large portions of the entire northern hemisphere. A large expanse of Surface Type 2, interpreted as andesite, in the northern plains is difficult to explain. On Earth, andesite forms mostly at subduction zones, where water released from descending slabs promotes mantle melting. However, there is no evidence for subduction on Mars. Although andesite can be produced during fractionation of basaltic magma, this process is inefficient and could not account for a large volume of andesite [*McSween et al.*, 1999]. Less fractionation is required for hydrous basaltic melts to reach the composition of andesite [*Minitti and Rutherford*, 2000]; however, if this were the case, the northern plains should consist of comparable amounts of andesite and basalt.

The "wet" transport and/or indigenous coastal marine models involving basalt and weathered basalt both fit within the existing geologic scenarios describing the sedimentary and volcanic history of the Oxia Palus region, and are also consistent on a global-scale. For these reasons, these models are preferred over the "dry" transport model. The northern lowlands lie, for the most part, below the 0-km elevation datum, and lakes or oceans, possibly fed by large outflow channels originating in the southern highlands, may have occupied this region [*Head et al.*, 1999]. The observed geographic concentration of Surface Type 2 within the northern lowlands is thus consistent with indigenous basalt weathered in a submarine environment or basaltic sediment transported into this depocenter and later altered.

5.2 Low-Albedo Intracrater Materials and Wind Streaks

The physical properties of, and genetic link between, low-albedo intracrater materials and wind streaks in Oxia Palus and western Arabia Terra have been the subject of considerable study and debate for three decades [e.g., *Sagan et al.*, 1972; *Arvidson*, 1974; *Peterfreund*, 1981; *Christensen*, 1983; *Thomas*, 1984; *Edgett and Christensen*, 1994; *Edgett and Malin*, 2000]. Most models describing the origin and formation of these features are based on visible observations and thermal inertia measurements. We attempt to fit the TES compositional interpretations of basalt and andesite/weathered basalt for Surface Type 1 and Type 2 materials into various origin hypotheses to provide insight into formational processes.

Low-Albedo Intracrater Materials: Models for the formation of dark intracrater floor material generally involve the entrapment of sand sized particles that can be transported into, but not out of, craters by wind [e.g., *Arvidson*, 1974; *Christensen*, 1983; *Thomas*, 1984]. These features correlate with Surface Type 1 basaltic compositions identified in the low-albedo floors of impact craters [Fig. 6]. Supporting evidence for an eolian origin of these materials comes from Mariner 9, Viking, and MOC high-resolution observations of barchan dune fields [e.g., *Sagan et al.*, 1972; *Arvidson*, 1974; *Peterfreund*, 1981; *Christensen*, 1983; *Thomas*, 1984; *Edgett and Christensen*, 1994; *Edgett and Malin*, 2000]. Observations of a consistent orientation in a downwind direction for many dark intracrater features and high thermal inertia values further support the hypothesis that these materials are eolian in origin, sand sized, and marginally mobile.

High-resolution MOC images have shown that dunes are not observed in low-albedo material covering the southern walls and rims of the same impact craters. This material correlates with Surface Type 2 compositions that form an arc around intracrater Surface Type 1 basaltic floor materials. Sorting of particle sizes blown into craters and up onto crater walls could be controlling the observed spatial distribution of Surface Type 1 and Type 2 materials. The thermal inertia map in Figure 5 clearly shows a decrease in thermal inertia, interpreted as indicating a fining of material, from the center of low-albedo crater floors south to crater walls in Radau and Marth craters. If this is true, fine material on crater walls has to be coarser than dust.

Differences in particle sizes between crater floors and walls could possibly reflect differences in the mineralogies of the respective surfaces. The coarsest basalt material near the center of the crater floor may grade to finer Surface Type 2 material transported further downwind (southward) and partially up crater walls. The deconvolved andesite and weathered basalt mineralogies for Surface Type 2 contain significantly more glass and/or clay compared to Surface Type 1 basaltic materials. Under a physical weathering environment, such as the eolian regime that transported material along the floors and up onto the walls of craters, lithologies containing glass and/or clay (Surface Type 2) will break down into smaller particles compared to lithologies with less modal abundances (Surface Type 1). The mineralogies of the two Surface Types blown into impact craters may thus control their observed distribution.

Another hypothesis to explain the origin of low-albedo impact crater wall material is that Surface Type 2 is being eroded and is cascading downward from layers within crater walls, instead of being transported upward. In this scenario, Surface Type 2

material is indigenous to the crater wall lithology. MOC and MOLA data have been used to show that some crater walls are covered by what appears to be loose, granular material that is at the angle of repose near crater rims [*Edgett and Malin*, 2000]. Furthermore, outcrops and streaks in crater walls have been observed to run down-slope, suggesting that Surface Type 2 material may be eroding and sliding down the slope surface. The andesite interpretation for Surface Type 2 would suggest the existence of in-place andesite layers in crater walls. This model is consistent with the Mars Pathfinder conclusion that the material in this region is andesitic in composition [*Rieder et al.* 1997a; *McSween et al.*, 1999].

The weathered basalt interpretation for Surface Type 2 is also consistent with an indigenous model for material on crater walls. In this scenario, in-place lithologies are altered by sub-aerially emplaced ice and/or water layers and later eroded downwards forming loose material. All material within impact craters is thus originally basalt, as either transported floor material or indigenous wall exposures, with altered basalt forming later and eroding from crater walls.

In summary, it is difficult to trace the origin of Surface Type 1 basalt materials on the floors of impact craters to bedrock exposures because of their mobile nature and eolian origin. It is even more difficult to tie Surface Type 2 compositions (andesite or weathered basalt) to bedrock exposures because of the uncertainty about whether their sources lie inside or outside the craters, or if they represent local or global source compositions.

Low-Albedo Impact Crater Wind Streaks: Several hypotheses exist for the origin of adjacent low albedo wind streaks. Some models interpret them as resulting from

saltation and traction and to consist of sandy material deflated from adjacent dark intracrater deposits [*Arvidson*, 1974; *Thomas*, 1984], or to result from material being stripped from the surface to reveal a darker substrate [e.g., *Soderblom et al.*, 1978]. Conversely, *Thomas and Veverka* [1986] proposed that dark wind streaks formed by the deposition of fine dark silt from plumes of suspended material. This view is now supported by MOC observations that suggest the dark materials are mantle deposits of fine-grained sediment deflated from adjacent crater floors, not sand-sized particles [*Edgett and Malin*, 2000]. Fine-grained particles in wind streaks compared to intracrater material agree with the lack of observed dunes (formed by sand-sized particles) in MOC high-resolution images.

The observation of Surface Type 1 material grading to Surface Type 2 material in wind streaks (Figure 5 and Figure 6) may support a combination of depositional and erosional/remnant models. We will first examine the end-members of depositional and erosional models, and then offer a combination model as an alternative.

In a depositional model, both Surface Type 1 sandy floor material and Surface Type 2 wall material are deflated from within the crater and deposited to form the wind streak. There are two uncertainties with this model. First, if Surface Type 1 sandy floor material is deflated out of the crater, why does it not also cover the intervening crater wall observed as Surface Type 2 material? Second, why are there not dune formations, which form in an eolian environment with sufficient sand supply, in the sandy Surface Type 1 material in the wind streak? It is thus difficult to account for the observed Surface Type 1 and Type 2 distributions using only a depositional model.

In an erosional model, both Surface Type 1 and Type 2 materials would be locally derived and exposed as overlying material is removed. Uncertainties with this model include how to explain either basalt-andesite or basalt-weathered basalt compositional contacts with no prevailing geologic evidence for different lava flows or different amounts of alteration. Also, taking into consideration the global and regional distributions of surface compositions, it seems unlikely that such small-scale heterogeneity exists on Mars.

A model that combines deposition and erosion is more consistent with the observed Surface Type 1 and Type 2 distributions in wind streaks. In this model, Surface Type 2 material is deflated from intracrater walls and deposited on an erosional or protected remnant Type 1 surface in the lee of impact craters. Thermal inertia data indicate that particle sizes in the northern extent of wind streaks, where basaltic surfaces are observed, are smaller compared to the sand-sized basaltic particles in intracrater deposits. This may imply that fine-grained Surface Type 2 materials are mixed with the erosional/remnant Surface Type 1 materials. This may also explain the less evident mixing trend in wind streaks compared to within impact craters. Remnant material corresponding to Surface Type 1 basalt would imply a basalt-dominated region, with Surface Type 2 materials being locally derived and deflated from within impact craters. Wind streaks may thus result from a combination of processes involving deflation of fine-grained Surface Type 2 material from intracrater walls that is then deposited on an erosional or protected older remnant of Surface Type 1 material. This combination model, however, does not provide insight into distinguishing andesite from weathered basalt for Surface Type 2 compositions.

6. Summary

1) The Oxia Palus quadrangle contains the geographic and compositional transition between the southern highlands and northern lowlands and between Surface Type 1 and 2 lithologies.

2) The gradational boundary of Surface Type 1 and 2 materials in Acidalia and Chryse Planitiae may represent either (1) an influx of basaltic sediment from the southern highlands, deposited on and mixed with andesitic volcanics; (2) an influx of water-transported basaltic sediment from the southern highlands that was altered and later deposited as a thin sedimentary veneer; or (3) different degrees of weathering of basalt marking the geographic extent of submarine alteration of basaltic crust. Evaluation of the models on local to regional to global scales supports the "wet" transport and/or indigenous coastal marine models involving basalt and weathered basalt. Both hypotheses fit within the existing geologic scenarios describing the sedimentary and volcanic history of the Oxia Palus region, and are also consistent on a global-scale.

3) Low-albedo intracrater materials grade from Surface Type 1 to Surface Type 2 compositions from crater floors upward onto crater walls. The compositional transition coincides with decreasing thermal inertia values that are interpreted to reflect decreasing particle sizes, possibly controlled by mineralogic differences between a largely unweathered basalt component and an andesite/altered basalt component. Intracrater floor materials are interpreted as eolian sediment blown into impact craters. Intracrater wall materials are interpreted as either eolian sediment sorted by particle size, or eroded material from in-place crater wall lithologies.

4) Low-albedo wind streaks display a compositional gradation of Surface Type 1 to Surface Type 2 in the direction of wind flow; however, the trend is not as evident as within the impact craters. This distribution may support both deflation and erosional models for the formation of wind streaks.

5) The Mars Pathfinder landing site and Ares and Tiu Valles source regions are sufficiently blanketed by fine-grained dust to prohibit the analysis of surface rock compositions. Despite the fact that the MP site is one of the rockiest places on the planet and that dust apparently covers only the upper surfaces of rocks, spectral observations at multiple emission angles remain obscured by dust in the atmosphere.

References

Arvidson, R. E., Wind-blown streaks, splotches, and associated craters on Mars, *Icarus, 21*, 12- 27, 1974.

Bandfield, J. L., P. R. Christensen, and M. D. Smith, Spectral dataset factor analysis and endmember recovery: Application to analysis of Martian atmospheric particulates, *J. Geophys. Res., 105*, 9573-9587, 2000*a*.

Bandfield, J. L., V. E. Hamilton, and P. R. Christensen, A global view of Martian surface compositions from MGS-TES, *Science, 287*, 1626-1630, 2000*b*.

Bandfield, J. L., Isolation and characterization of Martian atmospheric constituents and surface lithologies using thermal infrared spectroscopy, Ph.D. dissertation, 195 pp., Ariz. State Univ., Tempe, 2000.

Christensen, P. R., Eolian intracrater deposits on Mars: Physical properties and global distribution, *Icarus, 56*, 496-518, 1983.

Christensen, P. R., D. L. Anderson, S. C. Chase, R. N. Clark, H. H. Kieffer, M. C. Malin, J. C. Pearl, J. Carpenter, N. Bandiera, F. G. Brown, and S. Silverman, Thermal Emission Spectrometer Experiment: Mars Observer Mission, *J. Geophys. Res., 97* 7719-7734, 1992.

Christensen, P. R., J. L. Bandfield, M. D. Smith, V. E. Hamilton, and R. N. Clark, Identification of a basaltic component on the Martian surface from Thermal Emission Spectrometer data, *J. Geophys. Res., 105*, 9609-9621, 2000*a*.

Christensen, P.R., R.L. Clark, H.H. Kieffer, M.C. Malin, J.C. Pearl, J.L. Bandfield, K.S. Edgett, V.E. Hamilton, T. Hoefen, M.D. Lane, R.V. Morris, R. Pearson, T. Roush, S.W. Ruff, and M.D. Smith, Detection of crystalline hematite mineralization on Mars

by the Thermal Emission Spectrometer: Evidence for near-surface water, *J. Geophys. Res.*, *105*, 9623-9642, 2000c.

Christensen, P. R., J. L. Bandfield, V. E. Hamilton, S. W. Ruff, H. H. Kieffer, T. N. Titus, M. C. Malin, R. V. Morris, M. D. Lane, R. L. Clark, B. M. Jakosky, M. T. Mellon, J. C. Pearl, B. J. Conrath, M. D. Smith, R. T. Clancy, R. O. Kuzmin, T. Roush, G. L. Mehall, N. Gorelick, K. Bender, K. Murray, S. Dason, E. Greene, S. Silverman, M. Greenfield, The Mars Global Surveyor Thermal Emission Spectrometer experiment: Investigation description and surface science results, *J. Geophys. Res.*, 2002

Crisp, J., and M. J. Bartholomew, Mid-infrared spectroscopy of Pahala Ash palagonite and implications for remote sensing studies of Mars, *J. Geophys. Res.*, 97, 14,691-14,699, 1992.

Edgett, K. S., and P. R. Christensen, Rocks and Aeolian features in the Mars Pathfinder landing site region: Viking infrared thermal mapper observations, *J. Geophys. Res., 102*, 4107-4200, 1997.

Edgett, K. S., Low albedo surfaces and eolian sediment:Mars Orbiter Camera views of western Arabia Terra craters and wind streaks, *J. Geophys. Res.*, 2002.

Hamilton, V. E., M. B. Wyatt, H. Y. McSween, Jr., and P. R. Christensen, Analysis of terrestrial and martian volcanic compositions using thermal emission spectroscopy: II. Application to martian surface spectra from the Mars Global Surveyor Thermal Emission Spectrometer, *J. Geophys. Res.*, *106*, 14,733-14,746.

Head, J. W., H. Heisinger, M. A. Ivanov, M. A. Kreslavsky, S. Pratt, and B. J. Thomson, Possible ancient oceans on Mars: Evidence from Mars Orbiter Laser Altimeter data, *Science*, *286*, 2134-2137, 1999.

Head, J. W., M. A. Kreslavsky, and S. Pratt, Northern lowlands of mars: Evidence for widespread volcanic flooding and tectonic deformation in the Hesperian Period, *J. Geophys. Res.* 107, 3-1 – 3-29.

Kieffer, H.H., T.Z. Martin, A.R. Peterfreund, B.M. Jakosky, E.D. Miner, and F.D. Palluconi, Thermal and albedo mapping of Mars during the Viking primary mission, *J. Geophys. Res.*, *82*, 4249-4292, 1977.

Malin, M. C. and K. S. Edgett, The Mars Global Surveyor Mars Orbiter Camera: Interplanetary Cruise through Primary Mission, *J. Geophys. Res.*, *106*, 23429-23570, 2001.

Minitti, M. E. and M. J. Rutherford, Genesis of the Mars Pathfinder "sulfur-free" rock from SNC parental liquids. *Geochim. Cosmochim. Acta*, 14, 2535-2547, 2000.

McSween, H. Y., Jr. et al. Chemical, multispectral, and textural constraints on the composition and origin of rocks at the Mars Pathfinder landing site. *JGR* 104, 8679 (1999).

Parker, T. J., D. S. Gorsline, R. S. Saunders, D. C. Pieri, and D. M. Schneeberger, Coastal geomorphology of the Martian northern plains, *J. Geophys. Res.*, *98*, 11061-11078, 1993.

Presley, M.A., and P.R. Christensen, Thermal conductivity measurements of particulate materials, Part II: Results, *J. Geophys. Res.*, *102*, 6651-6566, 1997.

Ramsey, M.S., and P.R. Christensen, Mineral abundance determination: Quantitative deconvolution of thermal emission spectra, *J. Geophys. Res.*, *103*, 577-596, 1998.

Rieder, R., et al., The chemical composition of Martian soils and rocks returned by the mobile alpha proton X-ray spectrometer: Preliminary results from the X-ray mode, *Science*, *278*, 1771-1774, 1997a.

Rogers, D., P. R. Christensen, and J. L. Bandfield, Mars volcanic surface compositions: distributions and boundaries examined using multiple orbiter datasets, *Lunar Planet. Sci.* [CD-ROM], *XXXII*, abstract 2010, 2001.

Smith, M. D., J. L. Bandfield, and P. R. Christensen, Separation of atmospheric and surface spectral features in Mars Global Surveyor Thermal Emission Spectrometer (TES) spectra, *J. Geophys. Res., 105*, 9589-9607, 2000.

Soderblom, L. A., K. Edwards, E. M. Eliason, E. M. Sanchez, and M. P. Charette, Global color variations on the Martian surface, *Icarus, 34*, 446-464, 1978.

Tanaka, K. L., The stratigraphy of Mars, *Proc. Lunar Planet. Sci. Conf.*, *17th*, *Part 1*, *J. Geophys. Res.*, *91*, suppl., E139-E158, 1986.

Tanaka, K. L., Sedimentary history and mass flow structures of Chryse and Acidalia Planitiae, Mars, *J. Geophys. Res., 102*, 4131-4149, 1997.

Thomas, P., J. Veverka, S. Lee and A. Bloom, Classification of wind streaks on Mars, *Icarus, 45*, 124-153, 1981.

Thomas, P., Martian intracrater splotches: Occurrence, morphology, and colors, *Icarus, 57*, 205- 227, 1984.

Thomas, P., and J. Veverka, Red/violet contrast reversal on Mars: Significance for eolian sediments, *Icarus, 66*, 39-55, 1986.

Wyatt, M. B. and H. Y. McSween, Jr., Weathered basalt as an alternative to andesite, *in press, Nature.*

Zuber, M. T., D. E. Smith, S. C. Solomon, D. O. Muhleman, J. W. Head, J. B. Garvin, J. B. Abshire, and J. L. Bufton, The Mars Observer Laser Altimeter investigation, *J. Geophys. Res.*, *97*, 7781-7798, 1992.

Appendix



Figure 1: Composite MOC image of Oxia Palus quadrangle. Areas of interest include volcanic/sedimentary materials in southern Acidalia Planitia, low-albedo impact crater floors and adjacent wind streaks, and the Mars Pathfinder landing site and Ares and Tiu Valles source regions.

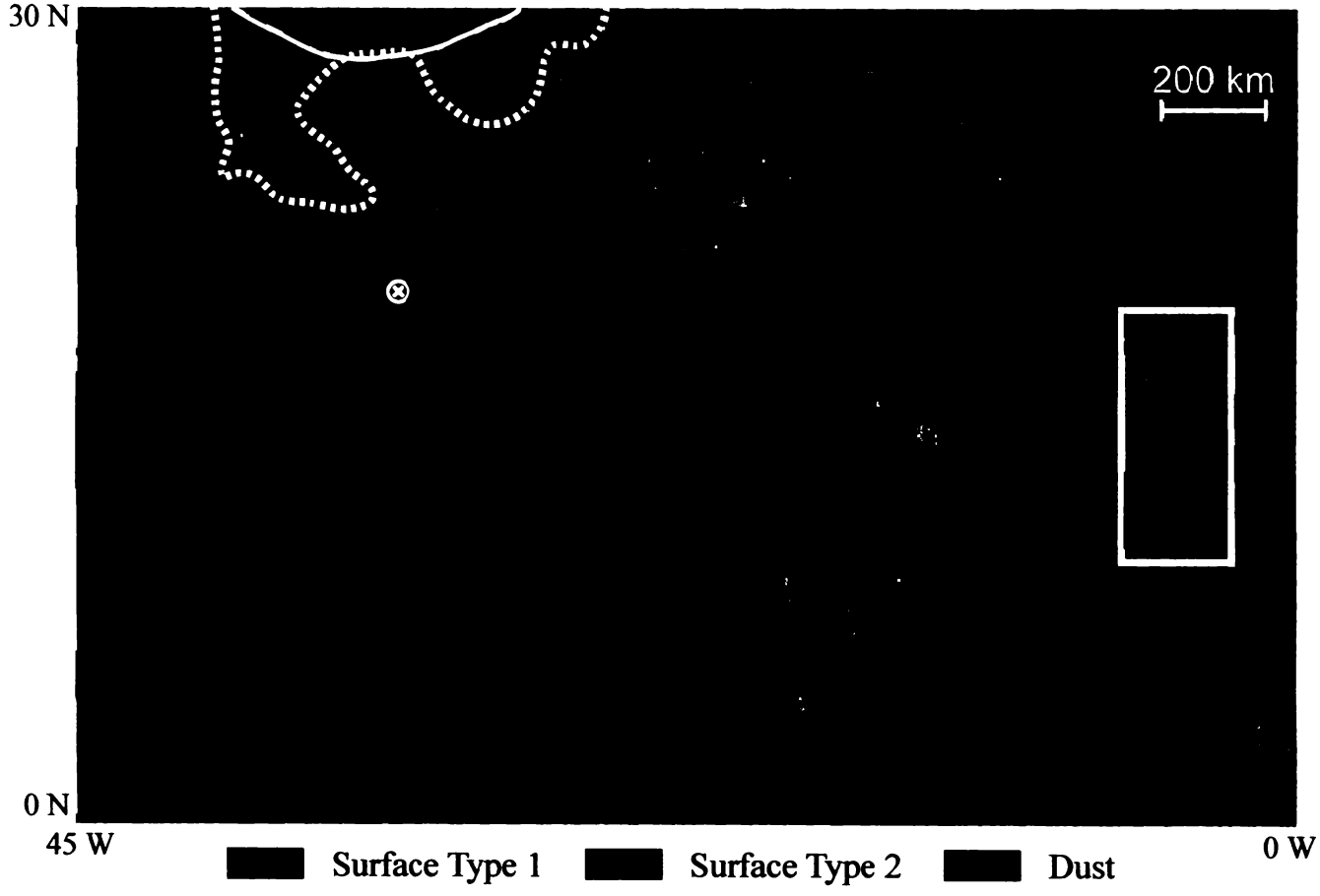


Figure 2: TES compositional map of the Oxia Palus quadrangle binned at 8 pixels/degree. Surface Type 1 (green) dominates the southern highlands, whereas Surface Type 2 (red) dominates the northern lowlands. Blue pixels represent areas covered by fine-grained dust.

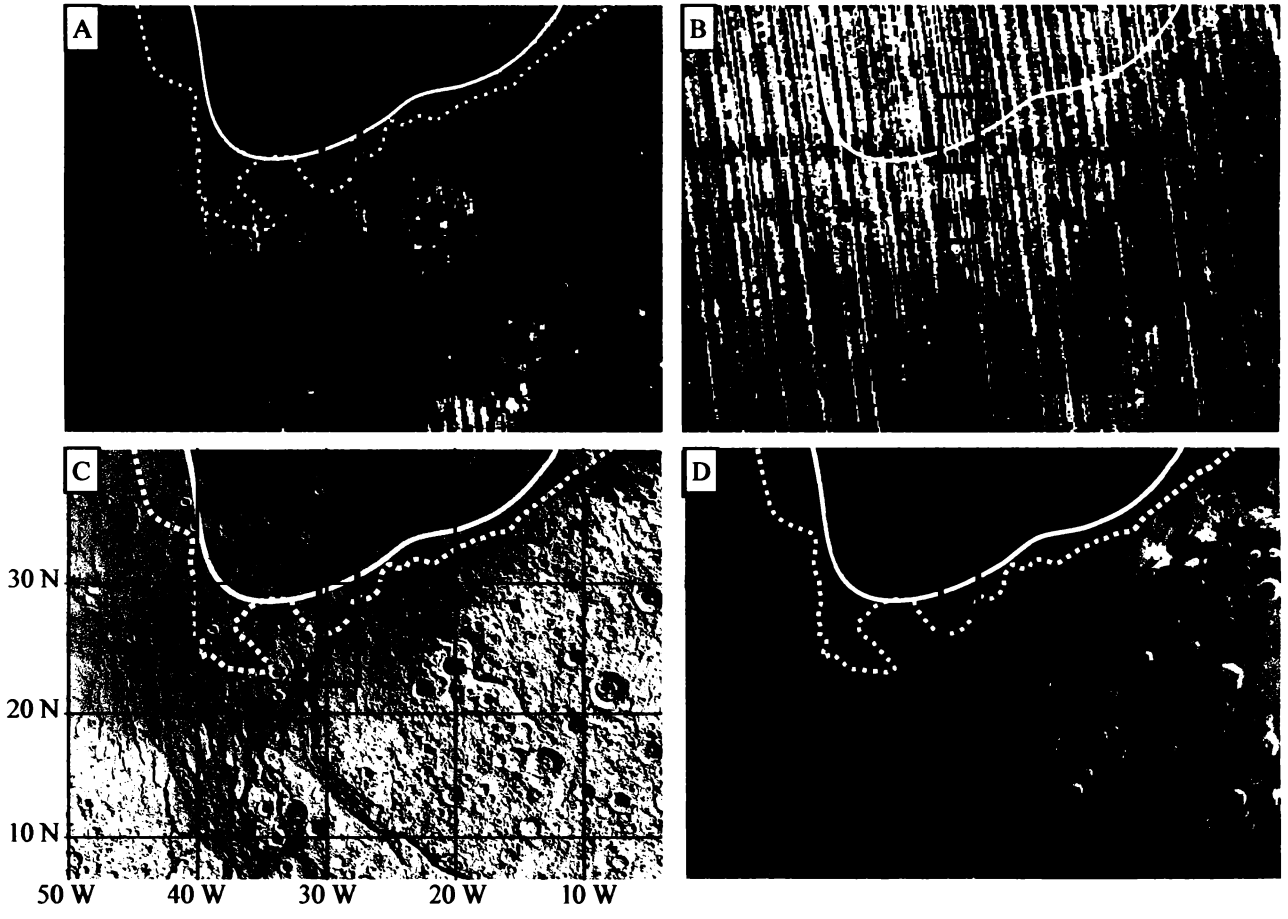


Figure 3: TES compositional maps (Panels A, B), MOLA shaded relief (Panel C), and MOC composite image (Panel D) of the Surface Type 1 and Type 2 transition in southern Acidalia Planitia. Surface Type 1 (bright pixels in Panel A) dominates the southern extent of Acidalia Planitia while Surface Type 2 (bright pixels in Panel B) dominates the northern extent. MOLA topography shows the transition occurs near the northern lowlands-southern highlands boundary. Red boxes indicate locations of spectra shown in Figure 4.

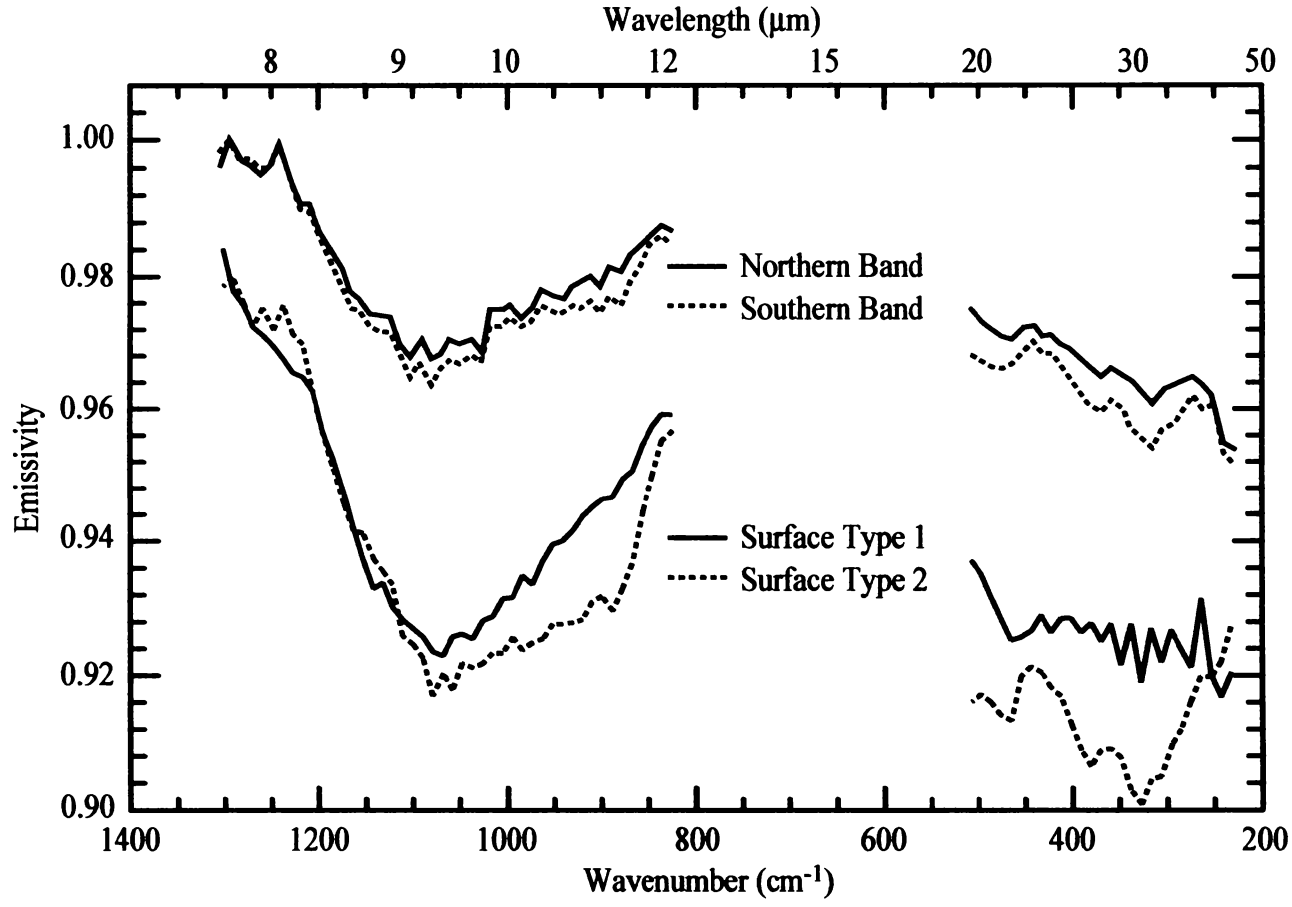


Figure 4: Average atmospherically corrected thermal emissivity spectra of the northern and southern transition bands in Acidalia Planitia compared to Surface Type 1 and Type 2 spectral endmembers. The northern band is dominated by Surface Type 1 components (~60 vol %), whereas the southern band is dominated by Surface Type 2 components (~66 vol %).

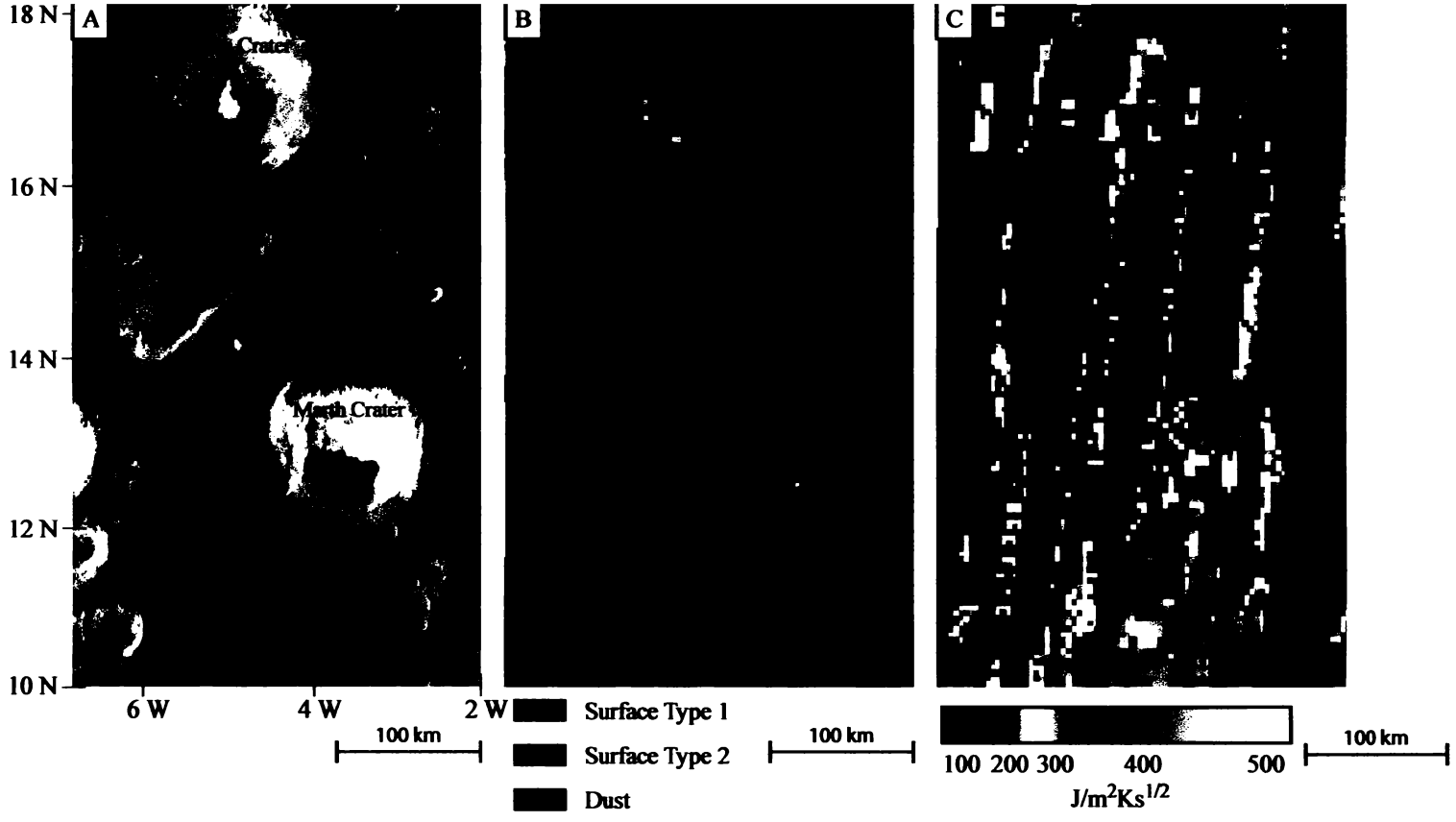


Figure 5: Composite MOC image (Panel A) and TES compositional (Panel B) and thermal inertia (Panel C) maps of Radau and Marth impact craters. Low-albedo intracrater materials display a core of Surface Type 1 material that grades into Surface Type 2 material along impact crater walls. A similar, but less distinct, trend is observed in low-albedo wind streaks in the downwind direction. Surface Type 1 materials generally have higher thermal inertias compared with Surface Type 2 materials, interpreted as reflecting a coarser particle size.



Figure 6: Composite MOC image of Radau Crater (southward looking) with superimposed TES composition pixels draped over MOLA topography. Also shown are NA MOC images across the crater floor/wall interface with a schematic cross section of MOLA topography. The transition from Surface Type 1 to Surface Type 2 compositions occurs near the crater floor/wall interface and is correlated with a transition from low-albedo dune materials to low-moderate albedo dune-free materials.

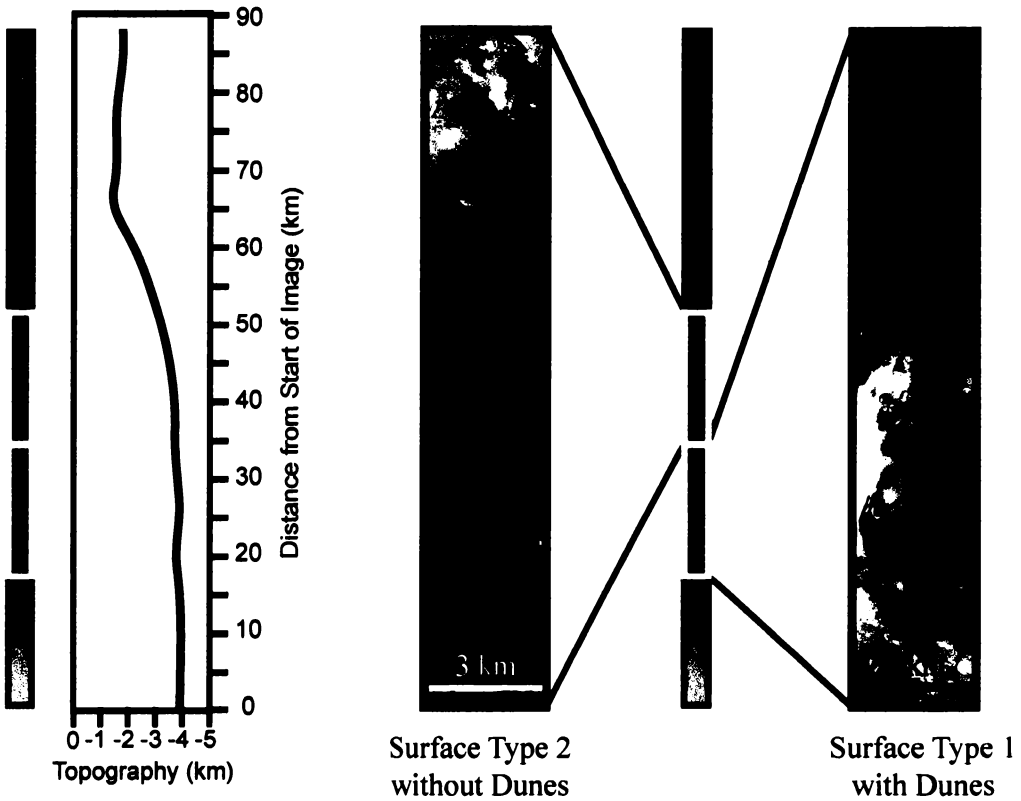


Figure 6 Continued: Composite MOC image of Radau Crater (southward looking) with superimposed TES composition pixels draped over MOLA topography. Also shown are NA MOC images across the crater floor/wall interface with a schematic cross section of MOLA topography. The transition from Surface Type 1 to Surface Type 2 compositions occurs near the crater floor/wall interface and is correlated with a transition from low-albedo dune materials to low-moderate albedo dune-free materials.

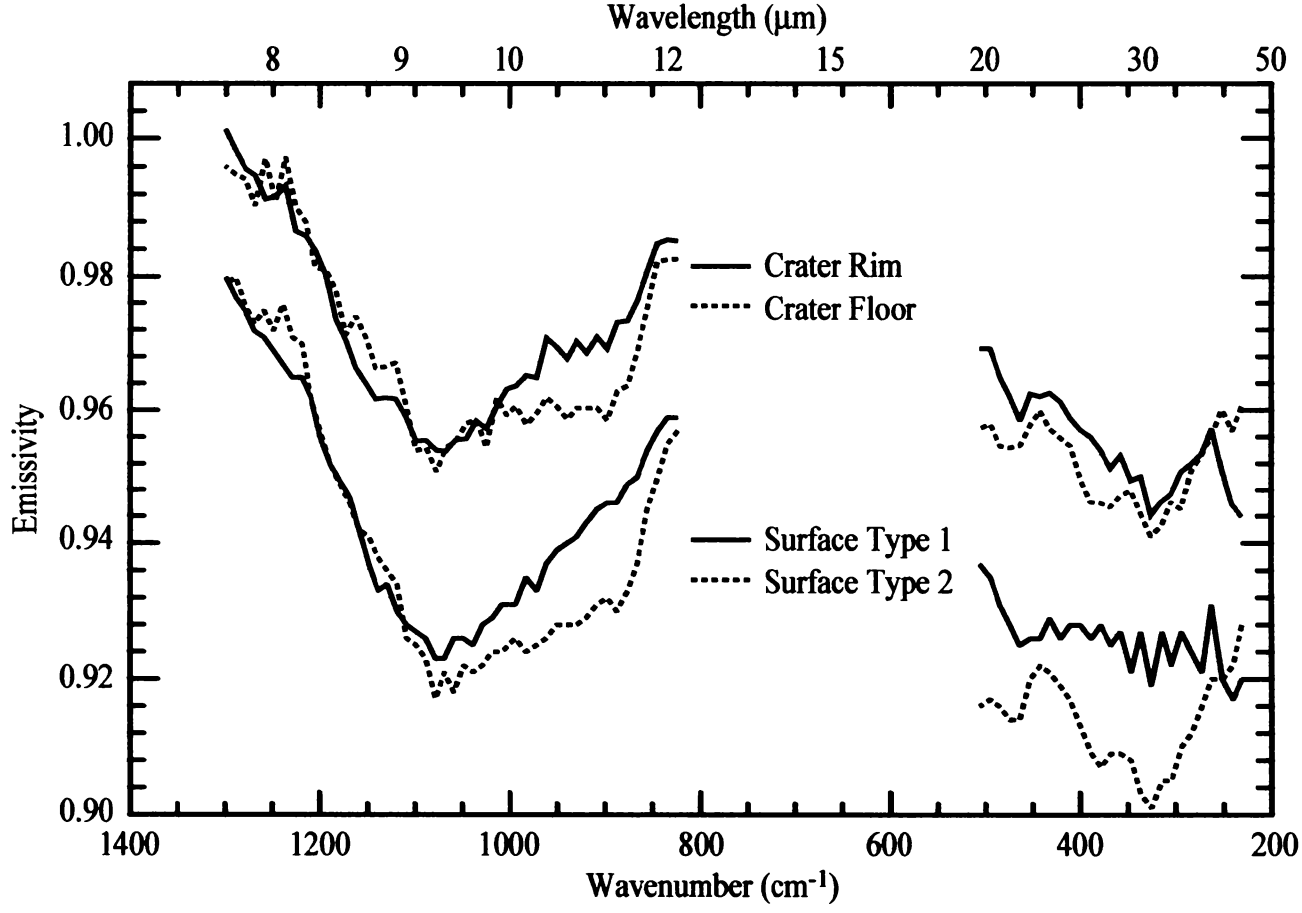


Figure 7: Average atmospherically corrected thermal emissivity spectra of low-albedo intracrater materials compared to Surface Type 1 and Type 2 spectral endmembers. The crater floor is dominated by Surface Type 1 components, wheres crater wall and rim are dominated by Surface Type 2 components.

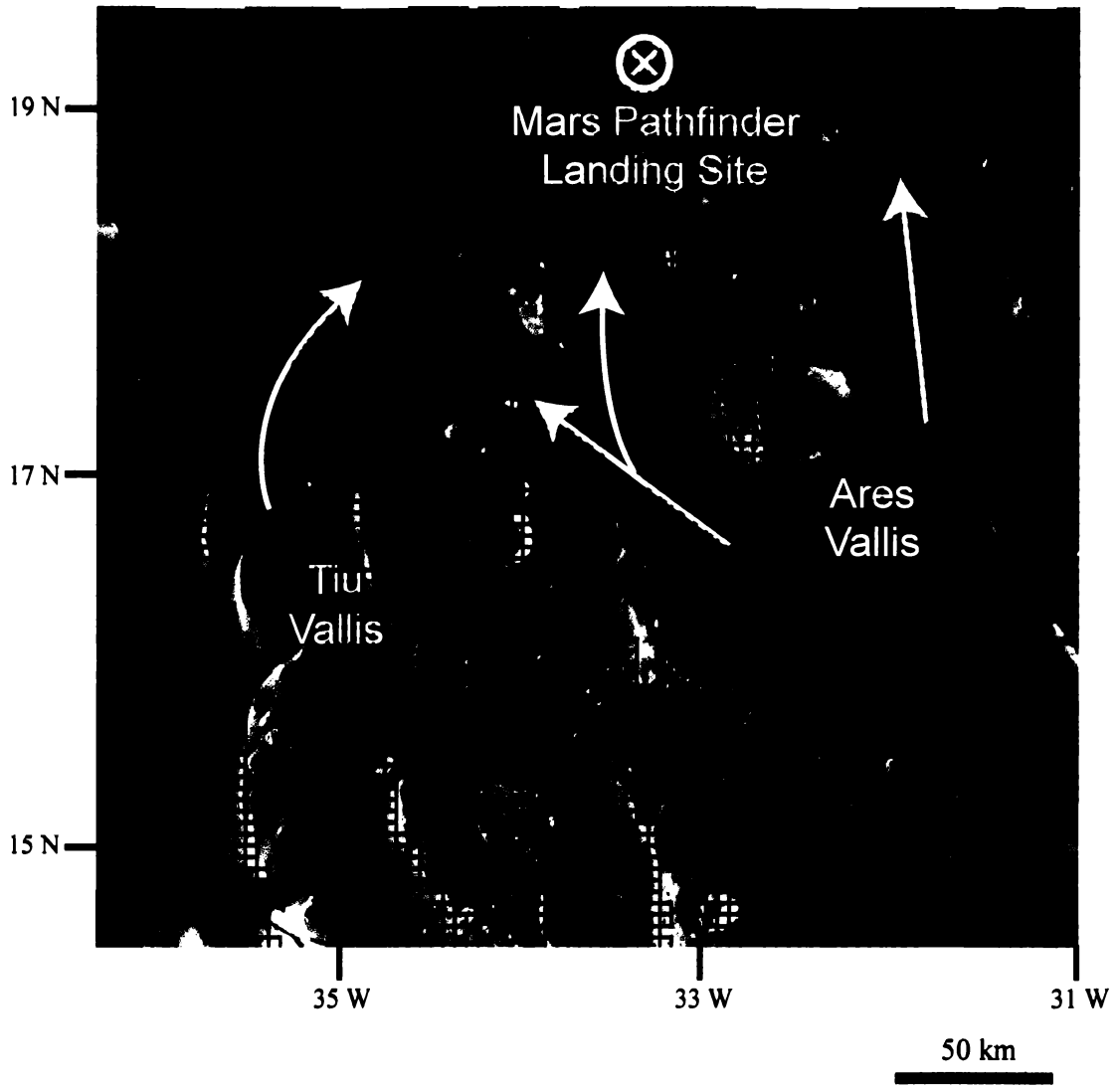


Figure 8: TES 16 pixels/degree compositional coverage superimposed on a composite MOC image of Chryse Planitia with the Mars Pathfinder landing site and Ares and Tiu Valles source regions.

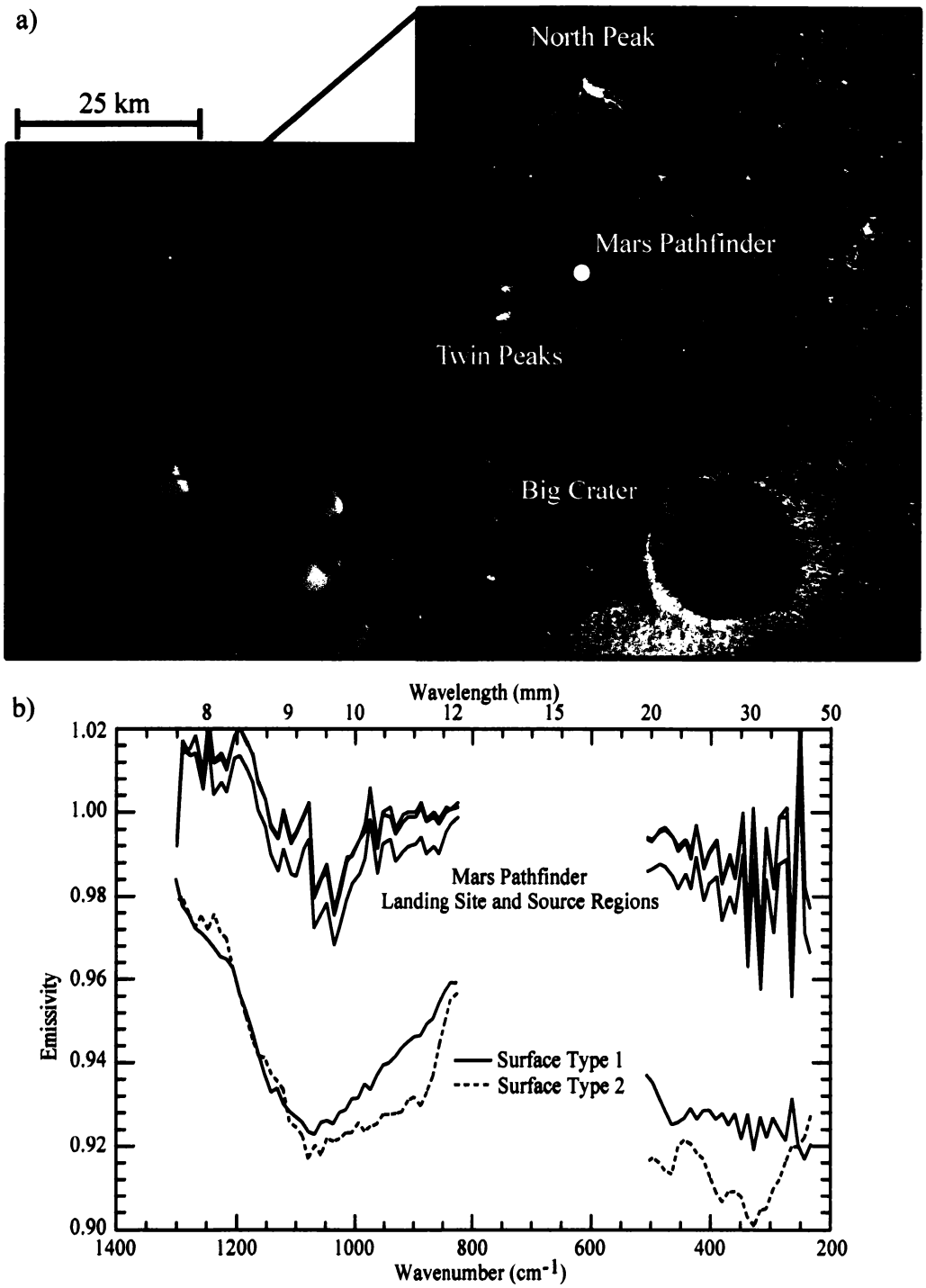


Figure 9: (a) High-resolution NA MOC image of the Mars Pathfinder landing site with (b) thermal emissivity spectra of the landing site and source regions compared to Surface Type 1 and Type 2 spectral end-members. Landing site and source region spectra display very shallow absorptions compared to surface end-members as a result of fine-grained dust cover.

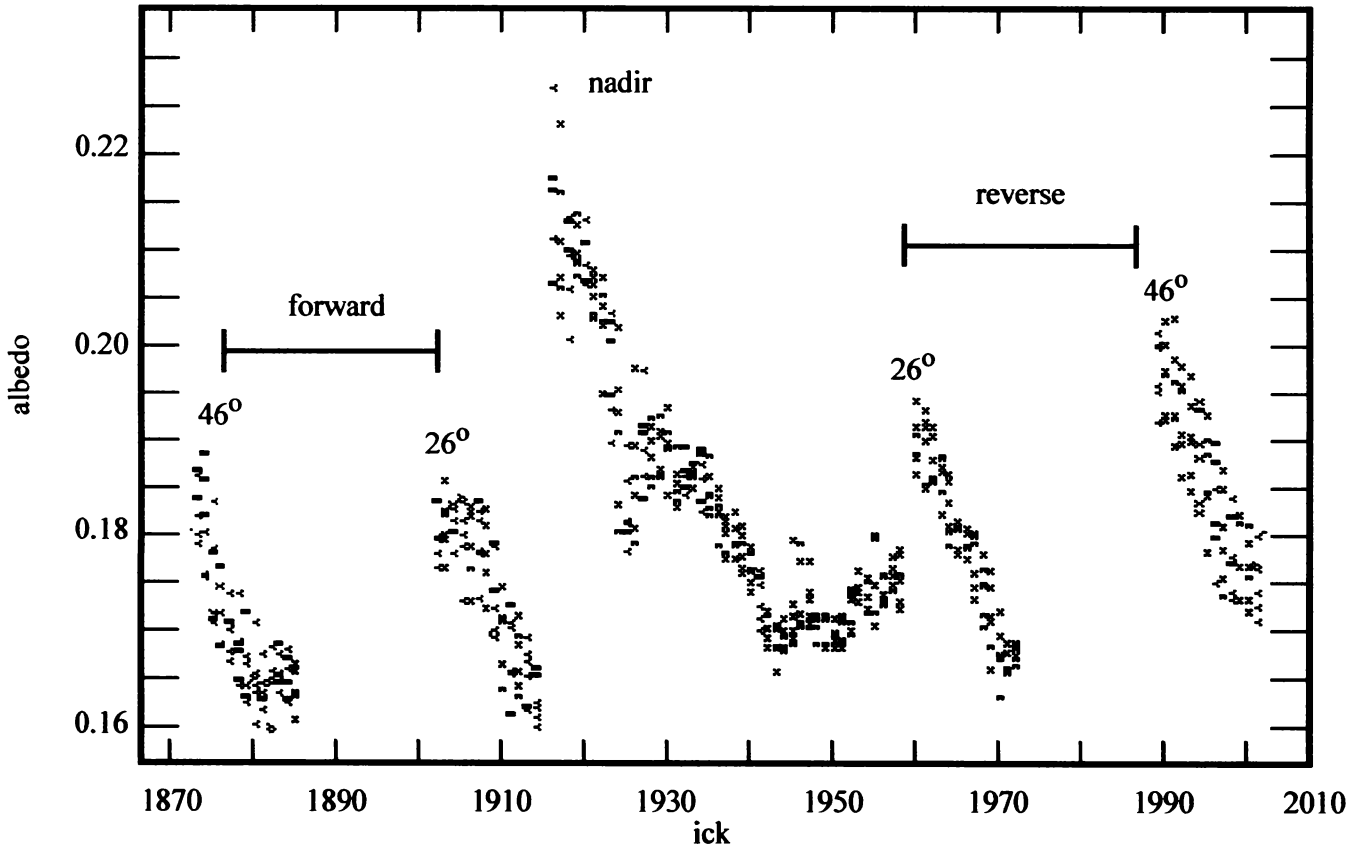


Figure 10: Plot of albedo vs ICK (Incremental Counter Keeper) for an EPF mosaic of the MP landing site. EPF observations at higher emission angles do not result in a significant decrease in surface albedo, i.e. increase in rock observations, at the landing site. This is due to the increased amount of atmospheric dust observed with increasing emission angle observations.

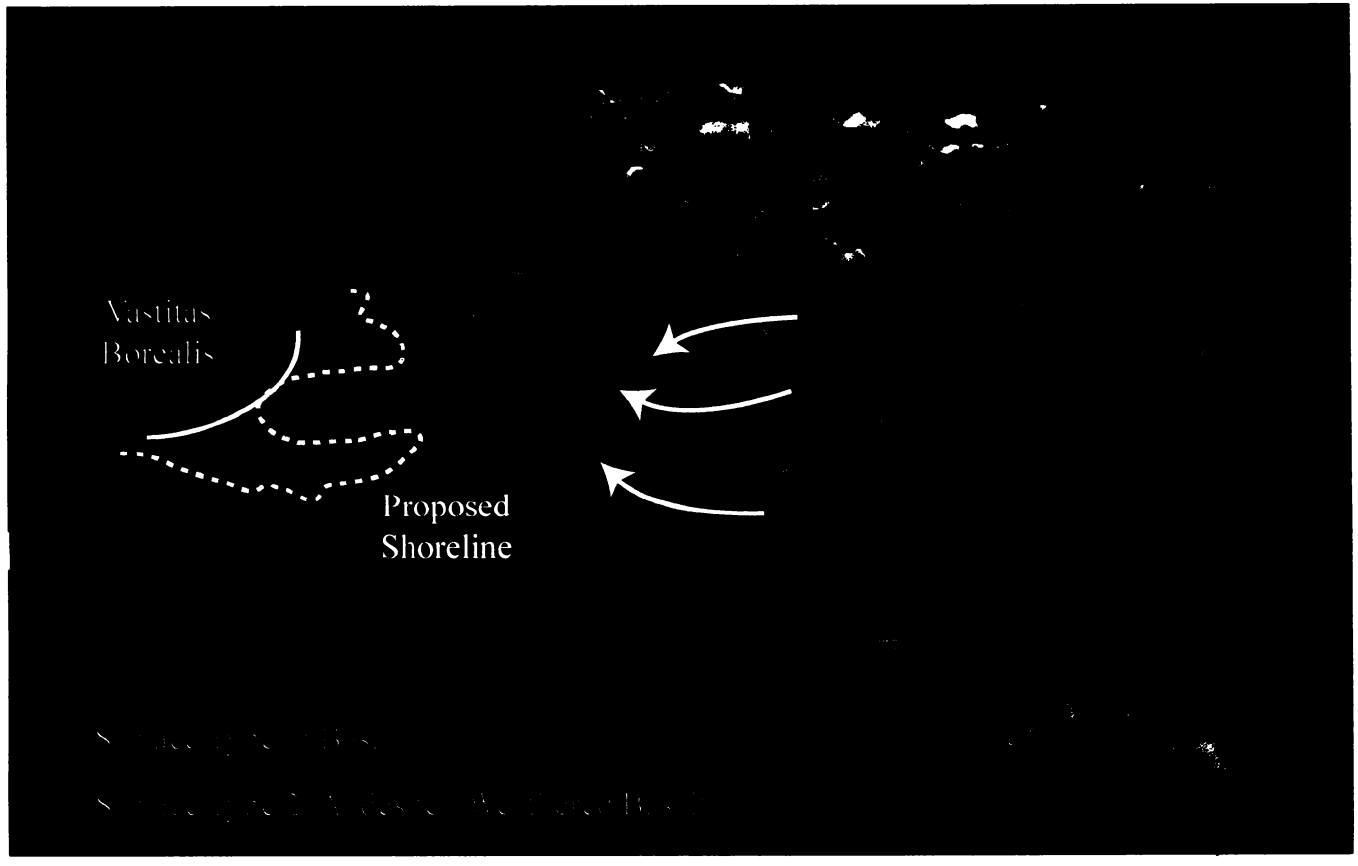


Figure 11: Composite MOC, MOLA, and TES map showing the distribution of Surface Type 1 and Type 2 materials in southern Acidalia Planitia and the southern highlands. Arrows indicate the direction of Surface Type 1 material (Basalt) transported in the "dry" model to southern Acidalia Planitia (over indigenous Surface Type 2 Andesite) by large outflow channels in Chryse Planitia. Curved yellow solid line shows extent of the Vastitas Borealis Formation ("wet" deposit model: Surface Type 2 Weathered Basalt). Curved yellow dashed line shows geomorphic contacts previously interpreted as ancient shorelines (indigenous coastal marine model: Surface Type 2 Weathered Basalt).

Summary

The following reiterates the conclusions from the previous research papers.

Part 1.

1. Linear deconvolution of thermal infrared emission spectra successfully identifies the primary minerals of terrestrial basalt, basaltic andesite, andesite, and dacite samples.

2. Direct comparisons between bulk modes derived from deconvolution and measured modes from electron microprobe phase mapping reveal slight discrepancies in the absolute abundances of modeled phases (e.g., silica glass phases and quartz). However, these differences are small, as the vast majority (28 of 32, or 87.5%, for basalt and 34 of 40, or 85%, for andesite/dacite) fall within the estimated error of the deconvolution algorithm.

3. Deconvolved modes of plagioclase end-members may be combined to derive a single weighted average composition that approximates the average plagioclase composition in volcanic rocks. Pyroxene compositions can be similarly modeled and separated into orthopyroxenes, pigeonite, and high-calcium clinopyroxenes.

4. Bulk chemistries of volcanic rocks can be derived by combining the composition (wt % oxides) of deconvolved end-member phases in proportion to their relative abundances in a sample (recalculated to wt %). Most common oxides in silicate mineral phases (SiO_2, Al_2O_3, CaO, FeO, Na_2O, and K_2O) are well modeled relative to measured values. However, MgO and TiO_2 are not as well modeled owing to overestimation of deconvolved olivine and the lack of oxide spectral end-members, respectively.

5. Thermal infrared spectral shapes, deconvolved bulk mineralogies and mineral compositions, and derived bulk rock chemistries can be applied to distinguish andesites/dacites from basalts and basaltic andesites. However, no one classification scheme is effective in accurately classifying all volcanic samples. The multiple steps of classification required to distinguish andesite from basalt reflect the continuum of compositions that exist between volcanic rock types.

Part 2.

1. Convolution of terrestrial laboratory data to the lowest spectral resolution of the TES instrument does not produce significantly degraded deconvolution results: modeled spectra provide similarly good matches to the measured spectra, modal mineralogies obtained at low (10 cm^{-1}) spectral sampling typically do not differ significantly from those obtained at high (2 cm^{-1}) spectral sampling, and bulk chemistries derived from data at reduced spectral sampling are virtually identical to those obtained from data at high spectral sampling. These results demonstrate the feasibility of using similar techniques and classification schemes for the interpretation of terrestrial laboratory samples and TES-resolution data.

2. Two distinctly different TES martian surface spectra [*Bandfield et al.*, 2000*a*] lie within spectral envelopes that distinguish basaltic and andesitic compositions [*Wyatt et al.*, 2001], further supporting previous results indicating that these spectra represent surfaces with different mineralogies and chemistries.

3. A limited end-member set tailored to the identification of volcanic igneous rocks provides deconvolution results (modal mineralogies) for martian spectra that are

comparable to those obtained with the larger end-member sets of *Christensen et al.* [2000*a*] and *Bandfield et al.* [2000*a*]. Therefore, an iterative approach to deconvolution, starting with a large set of varied end-members and working down to a smaller set of end-members that exploits solid solution variability, is justifiable.

4. The two primary martian surface types of *Bandfield et al.* [2000*a*] are easily distinguished and classified here by their modal mineralogy as basaltic (surface type 1) and andesitic (surface type 2). Local-scale variations in the composition of the martian surface were not examined, but should also be distinguishable and classifiable if the variations are greater than our uncertainties. The spectra are also easily distinguished, although one (surface type 2) is not as easily classified, by their normative plagioclase composition and color index. These results are consistent with results obtained for terrestrial rock samples [*Wyatt et al.*, 2001], and suggest that the plagioclase composition vs. color index classification scheme should not be considered as strongly as other schemes when classifying high-silica samples. (High-silica samples can be identified by other means, such as their spectral shape and derived mineralogy.)

5. Bulk chemistries derived from our deconvolution of martian surface spectra classify the two surface types as basaltic andesite and andesite, in general agreement with the results of previous workers [*Christensen et al.*, 2000*a*; *Bandfield et al.*, 2000*a*].

6. In summary, the surface type 1 martian spectrum is classified as basalt in three out of four classification schemes (the bulk chemistry scheme indicates a composition of basaltic andesite for surface type 1); we believe that this spectrum most likely represents a high-silica basaltic composition. The surface type 2 martian spectrum is classified as andesite in three out of four classification schemes. This spectrum's mineral chemistry

(color index vs. plagioclase composition) plots outside the fields defined by terrestrial igneous rocks. However, this scheme is less reliable than the others in classifying deconvolved silica-rich samples [*Wyatt et al.*, 2001]; therefore, we believe that this spectrum is most consistent with an andesitic composition. These compositional refinements are in agreement with previously published results [*Bandfield et al.*, 2000*a*; *Christensen et al.*, 2000*a*].

Part 3.

1. Although the existence of andesite on Mars remains a viable hypothesis, linear deconvolution of martian thermal infrared spectra, spectral matching with terrestrial volcanic rocks, and the geographic distribution of the Surface Type 2 spectrum suggest that martian northern lowland plains materials are basalts weathered under submarine conditions and/or sediments derived from weathered basalt and deposited in this basin.

Part 4.

1. The Oxia Palus quadrangle contains the geographic and compositional transition between the southern highlands and northern lowlands and between Surface Type 1 and 2 lithologies.

2. The gradational boundary of Surface Type 1 and 2 materials in Acidalia and Chryse Planitiae may represent either (1) an influx of basaltic sediment from the southern highlands, deposited on and mixed with andesitic volcanics; (2) an influx of water-transported basaltic sediment from the southern highlands that was altered and later deposited as a thin sedimentary veneer; or (3) different degrees of weathering of basalt

marking the geographic extent of submarine alteration of basaltic crust. Evaluation of the models on local to regional to global scales supports the "wet" transport and/or indigenous coastal marine models involving basalt and weathered basalt. Both hypotheses fit within the existing geologic scenarios describing the sedimentary and volcanic history of the Oxia Palus region, and are also consistent on a global-scale.

3. Low-albedo intracrater materials grade from Surface Type 1 to Surface Type 2 compositions from crater floors upward onto crater walls. The compositional transition coincides with decreasing thermal inertia values that are interpreted to reflect decreasing particle sizes, possibly controlled by mineralogic differences between a largely unweathered basalt component and an andesite/altered basalt component. Intracrater floor materials are interpreted as eolian sediment blown into impact craters. Intracrater wall materials are interpreted as either eolian sediment sorted by particle size, or eroded material from in-place crater wall lithologies.

4. Low-albedo wind streaks display a compositional gradation of Surface Type 1 to Surface Type 2 in the direction of wind flow; however, the trend is not as evident as within the impact craters. This distribution may support both deflation and erosional models for the formation of wind streaks.

5. The Mars Pathfinder landing site and Ares and Tiu Valles source regions are sufficiently blanketed by fine-grained dust to prohibit the analysis of surface rock compositions. Despite the fact that the MP site is one of the rockiest places on the planet and that dust apparently covers only the upper surfaces of rocks, spectral observations at multiple emission angles remain obscured by dust in the atmosphere.

References

Bandfield, J. L., V. E. Hamilton, and P. R. Christensen, A global view of Martian surface compositions from MGS-TES, *Science*, *287*, 1626-1630, 2000*a*.

Christensen, P. R., J. L. Bandfield, M. D. Smith, V. E. Hamilton, and R. N. Clark, Identification of a basaltic component on the Martian surface from Thermal Emission Spectrometer data, *J. Geophys. Res.*, *105*, 9609-9621, 2000*a*.

Wyatt, M. B., V. E. Hamilton, H. Y. McSween, Jr., P. R. Christensen, and L. A. Taylor, Analysis of terrestrial and martian volcanic compositions using thermal emission spectroscopy: I. Determination of mineralogy, chemistry, and classification strategies, *J. Geophys. Res.*, *106*, 14,711-14,732 (2001).

Future Work

The TES experiment has collected an unprecedented amount of thermal infrared spectral observations to determine and map the composition and distribution of martian surface minerals and rocks from orbit. Parts 1 and 2 of this dissertation evaluate the accuracy to which laboratory and TES thermal infrared spectra (5-25 μm, 2 and 10 cm^{-1} spectral sampling) and model-derived mineral assemblages and chemistries of unweathered terrestrial volcanic rocks can be used for petrologic classification. Parts 3 and 4 of this dissertation apply these results to examine and classify global and regional martian surface compositions and evaluate their distributions in a geologic context. Through this work, and the research of everyone on the MGS-TES team, a new and detailed view of the geologic history of Mars has begun to emerge. As with all experiments, new questions arise with every discovery. This "Future Work" section discusses some of the up-coming robotic orbiter and lander missions to Mars and how their specific objectives will add to our understanding of the post-TES view of Mars, specifically the interpretation of the TES Surface Type 2 component as andesite and/or weathered basalt.

1. 2001 Mars Odyssey

The on-going 2001 Mars Odyssey mission [*Meyer*, 20002; *Saunders et al.*, 2002] is an orbiting spacecraft designed to determine surface mineral and chemical compositions and to detect water and shallow buried ice on Mars. The Thermal Emission Imaging System (THEMIS) will be used to determine the mineralogy and petrology of localized surface deposits using high-resolution (100m/pixel) thermal infrared images

with 10 spectral bands between 6.5 and 14.5 μm [*Christensen et al.*, 2002]. The positions of the infrared bands were selected in part based on results from the TES experiment to distinguish major silicate and carbonate rock-forming minerals and alteration products. THEMIS will also acquire visible-light images with 19m/pixel resolution. The Gamma Ray Spectrometer (GRS) on Odyssey, along with its neutron detector, will determine the abundance and distribution of ~20 primary elements in the martian surface at a spatial resolution of about 300 km by measuring the uniquely identifiable gamma ray signatures of energy emitted by soils and rocks when exposed to cosmic radiation [*Boynton et al.*, 2002]. The calculation of the abundance of hydrogen on Mars will be used to infer the presence or absence of water in the surface since hydrogen is most likely present in the form of water ice and hydrated minerals.

The THEMIS and GRS instruments will be used to evaluate the TES Surface Type 2 interpretation of andesite and/or weathered basalt by combining mineralogic and chemical data of the martian surface. Distinguishing between high-silica glass and clays may prove difficult for THEMIS alone due to the low number of spectral bands compared to TES; however, the high-spatial resolution of THEMIS will allow for detailed mapping of the mineralogy of the martian surface that may indicate localized regions of hydrothermal alteration and/or subaqueous deposition that are below the spatial resolution of TES. THEMIS will also provide high-spatial resolution compositional information between the TES Surface Type 2 spectral unit and possible shoreline morphologies. GRS will be able to detect the abundance of several key elements on the martian surface that may be used to identify igneous or sedimentary lithologies. The abundance of Si on the martian surface, measured via non-elastic scattering or neutron

capture reactions, can be used to distinguish unweathered basalt from andesite; however, this element alone can not unequivocally classify rock types, as it has been shown that volcanic high-silica glasses and alteration high-silica glasses can be chemically similar. Carbon and sulfur concentrations, measured via non-elastic scattering reactions, and chlorine concentrations, measured via neutron capture reactions, may indicate the presence of ancient lake beds or ancient ocean bottoms where significant amounts of salt or evaporates (carbonates, sulfates, chlorides) were collected. Combining these elements with silica may provide insight to distinguishing andesite and weathered basalt. The identification of H in the subsurface on Mars may indicate the presence of water-bearing mineral phases (i.e. clays) or ice particles and can be used to further strengthen arguments about rock compositions. The identification and mapped distribution of mineral phases by THEMIS and chemical elements by GRS in the northern and southern hemispheres of Mars can thus be used in concert to infer the presence of alteration products and to better understand the igneous and sedimentary geologic history of Mars on local to regional scales.

2. 2003 Mars Exploration Rovers

The 2003 twin Mars Exploration Rovers (MER) will carry a sophisticated set of scientific instruments that will allow them to search for markers of past liquid water, analyze the chemistry and mineralogy of soils and rocks, and traverse distances of up to 100 meters a day across the martian surface. The two landing sites for the twin rovers have yet to be decided; however, they will be selected on the basis of results from the Mars Global Surveyor and 2001 Mars Odyssey missions with an emphasis placed on

locations where evidence exists for past liquid water or former lake beds or hydrothermal deposits.

The MER will provide an unprecedented amount of in-situ chemical and mineralogic data of martian soils and rocks. The Athena scientific package on MER contains a visible camera (Pancam) to survey the landing scene and surrounding region and an infrared spectrometer (Mini-TES) to determine mineral abundances in a similar way to the TES instrument. Three more instruments, a microscopic imager, the Mossbauer spectrometer, and the Alpha-Particle-X-Ray spectrometer (APXS), can be placed against rock and soil targets for detailed textural and chemical analyses. The Mossbauer spectrometer is designed to determine the composition and abundance of iron-bearing minerals and will provide information about martian environmental conditions. The APXS will determine the elemental chemistry of rocks and soils to compliment the mineralogical analyses of mini-TES. A Rock Abrasion Tool (RAT) is also part of the Athena package and can be used to scrape away the outer layers of rocks to allow textural, mineralogical, and chemical analyses of rock substrate.

The MER missions should be able to analyze and definitively classify surface compositions of martian soils and rocks. MER should also be able to classify definitively the TES Surface Type 2 composition, if a landing site is chosen where Surface Type 2 compositions are mapped. The ability of the RAT to bore into rocks will allow geologists to determine if alteration surface coatings are present as mineralogical and chemical analyses are made of multiple rock surfaces. Mini-TES should also be able to distinguish between high-silica glass and clays, as the atmospheric pathlength for mini-TES observations is much shorter than TES. A shorter atmospheric path length for mini-TES

results in a more transparent "window" in what is the CO_2 dominated region of TES spectra that obscures analysis of surface compositions. The absorption features between 500-550 cm^{-1} in laboratory spectra that distinguish Fe-smectite and Ca-montmorillonite clays from high-silica glass would thus be observed by mini-TES if present on the surface as rock coatings or alteration products. The textural, mineralogical, and chemical data acquired will provide geologists with a complete set of observations to classify accurately sedimentary and volcanic rocks if present on the surface.

3. 2005 Mars Reconnaissance Orbiter

The 2005 Mars Reconnaissance Orbiter will carry the High Resolution Imaging Science Experiment (Hi-RISE) that will provide visible images of the martian surface at an unprecedented 25-50 cm/pixel spatial resolution, and the Compact Reconnaissance Imaging Spectrometer for Mars (CRISM) that will be able to identify a broad range of minerals at a high 13 m/pixel spatial resolution. CRISM will be a visible to near-infrared hyperspectral mapper that covers the wavelength range from 0.400 to 4.05 μm at 7 nm/channel and is designed to specifically seek evidence of aqueous and hydrothermal deposits. Spectral observations in the near-infrared are sensitive to the electron transitions and lattice molecular vibrational transitions of minerals and can be used to determine chemical and mineralogic compositions. The eventual complete global coverage of CRISM should be able to determine the presence or absence of clays and distinguish between the TES derived Surface Type 1 and Type 2 spectral components.

4. Summary

The TES, THEMIS, GRS, and CRISM global datasets, and the MER in situ textural, mineralogic, and chemical analyses, will represent an unprecedented amount of data for classifying and mapping surface compositions on Mars. The combined datasets will provide a new view of Mars at the visible, near-infrared, thermal infrared, and gamma-ray wavelengths that will be used to shed light on current, and yet to be determined, questions about the Mars.

References

Boynton, W. V., Feldman, W. C., Mitrofanov, I., Trombka, J. I., Arnold, J. R., Englert, P. A. J., Metzger, A. E. R., Reedy, C., Squyres, S. W., d'Uston, C., Wänke, H., Brückner, J., Drake, D. M., Evans, L. G., Starr, R., Shinohara, C., and F. S. Anderson, Expected Performance and Initial Results from the 2001 Mars Odyssey Gamma Ray Spectrometer (GRS) Instrument Suite, *LPSC XXXIII*, Invited Talk, 2002.

Christensen, P. R., Jakosky, B. M., Kieffer, H. H., Malin, M., McSween, H. Y., Jr., Nealson, K., Mehall, G., Silverman, S., and N. Gorelick, Initial Results from the 2001 Mars Odyssey Thermal Emission Imaging System (THEMIS) Investigation, *LPSC XXXIII*, Invited Talk, 2002.

Meyer, M. A., Odyssey Science: Overall Role Within the Mars Program, *LPSC XXXIII*, Invited Talk, 2002.

Saunders, R. S., Plaut, J. J., and M. A. Meyer, Overview of Odyssey Science: Early Results and Plans, *LPSC XXXIII*, Invited Talk, 2002.

VITA

Michael Bruce Wyatt was born on October 1, 1974 in the Philadelphia, Pennsylvania suburb of Meadowbrook. He was raised in nearby Southampton, Pennsylvania for 17 years and graduated from William Tennent High School in Warminster, Pennsylvania in June 1992. In the summer of that year, Michael entered college at the Pennsylvania State University, University Park, where he earned a Bachelor of Science degree in Geosciences in December 1996. In August 1997, he entered the graduate program in Geological Sciences at the University of Tennessee. He completed his Doctor of Philosophy degree in Geology in May 2002.

3238 2553 7
07•24•02 MAB